

***Investigation of Protection
Problems due to Geomagnetically
Induced Currents***

by
Rohitha Prashad Jayasinghe

A Thesis
submitted to the Faculty of Graduate Studies
in partial fulfilment of the requirements for the degree of
Doctor of Philosophy

Department of Electrical and Computer Engineering
University of Manitoba
Winnipeg, Manitoba, Canada.

© October, 1996



**National Library
of Canada**

**Acquisitions and
Bibliographic Services**

**395 Wellington Street
Ottawa ON K1A 0N4
Canada**

**Bibliothèque nationale
du Canada**

**Acquisitions et
services bibliographiques**

**395, rue Wellington
Ottawa ON K1A 0N4
Canada**

Your file Votre référence

Our file Notre référence

The author has granted a non-exclusive licence allowing the National Library of Canada to reproduce, loan, distribute or sell copies of this thesis in microform, paper or electronic formats.

The author retains ownership of the copyright in this thesis. Neither the thesis nor substantial extracts from it may be printed or otherwise reproduced without the author's permission.

L'auteur a accordé une licence non exclusive permettant à la Bibliothèque nationale du Canada de reproduire, prêter, distribuer ou vendre des copies de cette thèse sous la forme de microfiche/film, de reproduction sur papier ou sur format électronique.

L'auteur conserve la propriété du droit d'auteur qui protège cette thèse. Ni la thèse ni des extraits substantiels de celle-ci ne doivent être imprimés ou autrement reproduits sans son autorisation.

0-612-23614-5

**THE UNIVERSITY OF MANITOBA
FACULTY OF GRADUATE STUDIES

COPYRIGHT PERMISSION PAGE**

**INVESTIGATION OF PROTECTION PROBLEMS DUE TO
GEOMAGNETICALLY INDUCED CURRENTS**

BY

ROHITHA PRASHAD JAYASINGHE

**A Thesis/Practicum submitted to the Faculty of Graduate Studies of The University
of Manitoba in partial fulfillment of the requirements of the degree
of
DOCTOR OF PHILOSOPHY**

Rohitha Prashad Jayasinghe 1997 (c)

**Permission has been granted to the Library of The University of Manitoba to lend or sell
copies of this thesis/practicum, to the National Library of Canada to microfilm this thesis
and to lend or sell copies of the film, and to Dissertations Abstracts International to publish
an abstract of this thesis/practicum.**

**The author reserves other publication rights, and neither this thesis/practicum nor
extensive extracts from it may be printed or otherwise reproduced without the author's
written permission.**

*to my parents
and family*

Acknowledgements

I wish to express my deep appreciation to Professor Peter McLaren for suggesting this topic as well as his counsel, guidance, patience and encouragement during the course of this work.

The author is indebted to Professor Rohan Lucas at the University of Moratuwa and Dr. Dennis Woodford of the Manitoba HVDC Centre for their suggestions in transformer modelling.

Dr. Thilak Siyambalapitiya of the Ceylon Electricity Board is thanked for his encouragement to do higher studies and arranging the opportunity to do so.

Tom Molinski of Manitoba Hydro is also thanked for providing the recorded waveforms in the Dorsey–Forbes–Chisago system. The author also wishes to thank Tom Gouldsbrough for his valuable input as an advisor to this project from Manitoba Hydro.

Financial support from the Manitoba Hydro, the University of Manitoba and the National Sciences and Engineering Research Council are also acknowledged.

This acknowledgement would be incomplete without thanking the author's wife and parents for their continuous support, understanding and encouragement in all ways.

Abstract

Geomagnetically Induced Currents (GIC), flowing in power systems during Solar Magnetic Disturbances (SMD), can cause severe offset saturation of power system transformers. Continuous saturation of transformers can result in transformer overheating, and cause harmonic currents to be injected into the system. Relay and protection systems are affected by harmonic currents passing through the system.

A considerable amount of study has been done using analog and/or digital simulations of transformer half-cycle saturation to predict the transformer response to DC excitation. These methods used simplified transformer core models to represent the excitation-flux relationships.

This thesis includes the development of an accurate transformer core model. The accuracy of the model is validated by comparing the recorded waveforms during GIC events with the simulated waveforms using the model. Then the model is used to investigate the other system quantities at different GIC conditions. As well, the performance of several protection schemes under GIC are evaluated. The study is performed using an electromagnetic transients simulation program.

Table of Contents

Acknowledgements	i
Abstract	ii
Table of Contents	iii
List of Figures	vi
List of Tables	x
1. Introduction	1
1.1 Geomagnetically Induced Currents	1
1.1.1 The origin and cyclic nature	1
1.1.2 Interaction with power systems	2
1.2 Effect on power systems	3
1.3 Vulnerability of power systems	5
1.4 Modelling of GIC	6
1.4.1 Estimation of GIC	6
1.5 Scope of the thesis	6
2. Modelling	8
2.1 Transformers	8
2.1.1 Transformer modelling in EMTF	10
2.1.2 Ideal transformer model in EMTDC	11
2.1.3 Transformer core	13
2.1.3.1 Saturation characteristics	15
2.1.3.2 Core losses	21
2.1.4 Overall model for the transformer core	22
2.1.5 Different transformer configurations	22
2.1.5.1 Single phase units	23
2.1.5.2 Three phase conventional transformers	24
2.1.5.3 Three phase five limb transformers	28
2.1.5.4 Three phase three limb transformers	29
2.2 Transmission lines	30
2.2.1 Bergeron model	30
2.2.2 Marti model	34
2.2.3 Mutually coupled transmission lines	38
2.3 Simulation of earth surface potential	38
3. Validity of the models	40
3.1 Response of the transformer core	40
3.2 Initial simulations	42
3.2.1 delta–star three single phase bank model	43
3.2.2 star–star three single phase bank model	44
3.2.3 three phase conventional star–star transformer	47
3.2.4 three phase conventional delta–star transformer	48
3.2.5 three phase five limb star–star transformer	51

3.2.6	three phase five limb delta–star transformer	52
3.2.7	three phase three limb star–star transformer	55
3.2.8	three phase three limb delta–star transformer	56
3.3	Comparison with recorded events	59
3.3.1	Event on September 10, 1992	59
3.3.2	Event on October 5, 1993	62
3.4	Conclusions	64
3.4.1	Susceptibility of different transformer configurations to GIC	64
3.4.2	Differences in recorded and simulated waveforms	64
4.	Dorsey–Forbes–Chisago 500kV system	66
4.1	Description of the system	66
4.2	Worst case scenario	69
4.3	Simulations at different conditions	70
4.3.1	A typical high power flow	71
4.3.1.1	Waveforms in 500kV side	72
4.3.2	A typical low power flow	75
4.3.2.1	Waveforms on the 500kV side	77
4.4	Effect of GIC on distortions and harmonics	80
4.5	Effect of power flow on harmonics	82
4.6	Conclusions	84
5.	Dorsey–Forbes–Chisago after series compensation	86
5.1	Description of the system	86
5.2	Simulations under different conditions	89
5.2.1	A typical low power flow	91
5.2.1.1	Waveforms on the 500kV side	93
5.2.1.2	Waveforms on the 230kV side	95
5.2.1.3	Current waveforms in 230kV Feeders	98
5.2.2	A typical high power flow	100
5.2.2.1	Waveforms in 500kV side	102
5.2.2.2	Current waveforms in 230kV Feeders	104
5.3	Conclusions	106
6.	Protection Considerations	108
6.1	Current in harmonic filters	108
6.1.1	High Pass Filter Currents	108
6.1.1.1	Before series compensation at Maximum recorded ESP	108
6.1.1.2	After series compensation at maximum predicted ESP	111
6.1.2	Current in tuned filters	114
6.1.2.1	Before series compensation at maximum recorded ESP	114
6.1.2.2	After series compensation at maximum predicted ESP	120
6.1.3	Summary	125
6.2	Instrument transformer response	126
6.2.1	Current transformer response	127
6.2.2	Voltage transformer response	132
6.3	Sequence network problems	132
6.4	Transformer differential protection	139
7.	Conclusions	143
	References	148
A.	Flow Charts	151
A–1	Algorithm for calculating the non–linear current in the core	151

B. More details on Dorsey–Forbes–Chisago before compensation	153
B-1 Waveforms in 230kV side – high power flow	153
B-2 Waveforms in 230kV side – low power flow	154
B-3 Effect of GIC on Distortions and Harmonics – voltage waveforms	156
B-4 Effect of Power Flow on Harmonics – Waveforms at other GIC Levels	158
C. More details on Dorsey–Forbes–Chisago after series compensation	160
C-1 Waveforms in the 230kV side – High Power Flow	160
C-2 Current Waveforms in 230kV Feeders at High Power Flow – Current flowing to Drayton	163

List of Figures

Figure 1 .1 : Cyclic Nature of Geomagnetic Activity	2
Figure 1 .2 : ESP between grounded Y transformer neutrals and the resultant GIC in transmission lines.	3
Figure 1 .3 : The shift of operating point on the magnetization characteristics	4
Figure 2 .1 : Generation of harmonics due to the non-linearity of the transformer core	9
Figure 2 .2 : Two mutually coupled windings	11
Figure 2 .3 : Power series curve representation of magnetization characteristics	17
Figure 2 .4 : Conversion of rms values into instantaneous values	20
Figure 2 .5 : Basic Model for the Transformer Core	22
Figure 2 .6 : Final Model of the Transformer Core	22
Figure 2 .7 : Shell form and Core form Single Phase Transformers	23
Figure 2 .8 : Single Phase Model of a Transformer	24
Figure 2 .9 : Three phase conventional transformer core configuration	24
Figure 2 .10 : Equivalent magnetic circuit of the three phase conventional transformer	25
Figure 2 .11 : Equivalent Circuit for 3 phase Conventional Transformer	27
Figure 2 .12 : Three phase Five limb transformer core configuration	28
Figure 2 .13 : Equivalent Circuit for 3 phase 5 limb Transformer	29
Figure 2 .14 : Three phase Three limb transformer core configuration	29
Figure 2 .15 : Equivalent Circuit for 3 phase 3 limb Transformer	30
Figure 2 .16 : A lossless transmission line	31
Figure 2 .17 : Norton representation of the lossless transmission line	32
Figure 2 .18 : Development of Norton representation for a lossy transmission line ..	32
Figure 2 .19 : Norton representation of the lossless transmission line	33
Figure 2 .20 : Frequency dependence model in the time domain	35
Figure 2 .21 : Equivalent circuit in the time domain	37
Figure 2 .22 : Norton representation of the frequency dependent transmission line ..	37
Figure 3 .1 : Test system used to investigate the response of the core model	40
Figure 3 .2 : Transformer core current referred to the 230 kV side at no load conditions	41
Figure 3 .3 : Flux Linkage – Current loop referred to the 230 kV side during no load condition	41
Figure 3 .4 : Transformer core current referred to 230 kV side during energization of the transformer	42
Figure 3 .5 : System used in initial simulations	42
Figure 3 .6 : Line Currents and Phase Voltages in the three single phase bank of delta-star transformer for 100A GIC.	44
Figure 3 .7 : Line Currents and Phase Voltages in the three single phase bank of star-star transformer for 100A GIC.	45
Figure 3 .8 : Fourier Analysis of the line current on the 500 kV side of a single phase bank of a 3 phase transformer for star-star configuration	46
Figure 3 .9 : Fourier Analysis of the line current on the 500 kV side of a single phase bank of a 3 phase transformer for delta-star configuration	46
Figure 3 .10 : Line Currents and Phase Voltages in the three phase conventional star-star transformer for 100A GIC.	48
Figure 3 .11 : Line Currents and Phase Voltages in the three phase conventional delta-star transformer for 100A GIC.	49
Figure 3 .12 : Fourier Analysis of the line current on 500 kV side of a 3 phase conventional star-star transformer	50

Figure 3 .13 : Fourier Analysis of the line current on 500 kV side of a three phase delta–star conventional transformer	50
Figure 3 .14 : Line Currents and Phase Voltages in the three phase five limb star–star transformer for 100A GIC	52
Figure 3 .15 : Line Currents and Phase Voltages in the three phase five limb delta–star transformer for 100A GIC	53
Figure 3 .16 : Fourier Analysis of the line current on 500 kV side of a three phase five limb star–star transformer	54
Figure 3 .17 : Fourier Analysis of the line current on 500 kV side of a three phase five limb delta–star transformer	54
Figure 3 .18 : Line Currents and Phase Voltages in the three phase three limb star–star transformer for 100A GIC.	56
Figure 3 .19 : Line Currents and Phase Voltages in the three phase three limb delta–star transformer for 100A GIC.	57
Figure 3 .20 : Fourier Analysis of the line current on 500 kV side of a three phase three limb star–star transformer	58
Figure 3 .21 : Fourier Analysis of the line current on 500 kV side of a three phase three limb delta–star transformer	58
Figure 3 .22 : Recorded line current on 500 kV side at Dorsey	59
Figure 3 .23 : Simulated line current on 500 kV side at Dorsey	60
Figure 3 .24 : Recorded voltage waveform on 500 kV side at Dorsey	61
Figure 3 .25 : Simulated voltage waveform on 500 kV side at Dorsey	61
Figure 3 .26 : Recorded line current on 500 kV side	62
Figure 3 .27 : Simulated line current on 500 kV side	62
Figure 3 .28 : Harmonic composition of recorded and simulated current waveforms	63
Figure 4 .1 : Single line diagram of Dorsey–Forbes–Chisago system	67
Figure 4 .2 : Geographical layout of the 500 kV transmission line	69
Figure 4 .3 : Voltage waveforms on 500 kV side of Dorsey at high power flow	73
Figure 4 .4 : Fourier analysis of 500 kV voltage waveforms at high power flow	73
Figure 4 .5 : Current waveforms on 500 kV side of Dorsey at high power flow	74
Figure 4 .6 : Fourier analysis of 500 kV current waveforms at high power flow	75
Figure 4 .7 : Voltage waveform on 500 kV side of Dorsey at low power flow	77
Figure 4 .8 : Fourier analysis of 500 kV voltage waveforms at low power flow	78
Figure 4 .9 : Current waveforms on 500 kV side of Dorsey at low power flow	78
Figure 4 .10 : Fourier analysis of 500kV current waveforms at low power flow	79
Figure 4 .11 : Fourier analysis of 500 kV side currents with a typical high power flow	80
Figure 4 .12 : Fourier analysis of 500 kV side currents with a typical low power flow	80
Figure 4 .13 : THD Factor of 500 kV side currents	81
Figure 4 .14 : Fourier analysis of 500 kV side currents at Dorsey with 105A GIC per phase	82
Figure 4 .15 : Fourier analysis of 500 kV side phase voltages at Dorsey with 105A GIC per phase	82
Figure 4 .16 : Harmonic Distortion of current with the Load Flow	83
Figure 4 .17 : Harmonic Distortion of voltage with the Load Flow	84
Figure 5 .1 : Single line diagram of Dorsey–Forbes–Chisago system after series compensation	87
Figure 5 .2 : Geographical layout of the 500 kV transmission line	89
Figure 5 .3 : Voltage waveform on 500 kV side of Dorsey at low power flow	93
Figure 5 .4 : Current waveforms on 500 kV side of Dorsey at low power flow	93
Figure 5 .5 : Fourier analysis of 500kV side voltage waveforms at low power flow .	94
Figure 5 .6 : Fourier analysis of 500kV side current waveforms at low power flow .	95
Figure 5 .7 : Voltage waveforms on the 230 kV side of Dorsey at low power flow ..	96

Figure 5 .8 : Current waveforms on the 230 kV side of Dorsey at low power flow ..	96
Figure 5 .9 : Fourier analysis of 230kV voltage waveforms at Dorsey at low power flow	97
Figure 5 .10 : Fourier analysis of 230kV side current waveforms at Dorsey at low power flow	97
Figure 5 .11 : Current on Dorsey–Drayton line at Dorsey at low power flow	98
Figure 5 .12 : Current on Dorsey–Moranville line at Dorsey at low power flow	98
Figure 5 .13 : Fourier analysis of current flowing to Drayton at low power flow	99
Figure 5 .14 : Fourier analysis of current flowing to Moranville at low power flow ..	100
Figure 5 .15 : Voltage waveforms on 500 kV side at high power flow	102
Figure 5 .16 : Current waveforms on 500 kV side of Dorsey at high power flow ...	102
Figure 5 .17 : Fourier analysis of 500kV voltage waveforms at high power flow ...	103
Figure 5 .18 : Fourier analysis of 500kV current waveforms at high power flow	104
Figure 5 .19 : Current on Dorsey–Moranville line at Dorsey at high power flow	105
Figure 5 .20 : Fourier analysis of current flowing to Moranville at high power flow ..	106
Figure 6 .1 : High Pass Filter current at Dorsey with 105A GIC per phase and with a high power flow	109
Figure 6 .2 : High Pass Filter current at Dorsey with 105A GIC per phase and with a low power flow	109
Figure 6 .3 : Fourier analysis of high pass filter current waveforms at 105A GIC per phase on 500kV side	110
Figure 6 .4 : High Pass Filter current at Dorsey with a high power flow	112
Figure 6 .5 : High Pass Filter current at Dorsey at low power flow	112
Figure 6 .6 : Fourier analysis of currents in high pass filter	113
Figure 6 .7 : 13th Harmonic Filter current at Dorsey with 105A GIC per phase and with a high power flow	114
Figure 6 .8 : 13th Harmonic Filter current at Dorsey with 105A GIC per phase and with a low power flow	115
Figure 6 .9 : Fourier analysis of currents in 13th harmonic filter before compensation	115
Figure 6 .10 : 5th Harmonic Filter current at Dorsey with 105A GIC per phase and with a high power flow	116
Figure 6 .11 : 5th Harmonic Filter current at Dorsey with 105A GIC per phase and with a low power flow	117
Figure 6 .12 : Fourier analysis of currents in 5th harmonic filter before compensation	117
Figure 6 .13 : 13th Harmonic Filter current at Dorsey with 105A GIC per phase and with a high power flow	120
Figure 6 .14 : 13th Harmonic Filter current at Dorsey	121
Figure 6 .15 : Fourier analysis of currents in 13th harmonic filter after compensation	121
Figure 6 .16 : 5th Harmonic Filter current at Dorsey with 105A GIC per phase and with a high power flow	122
Figure 6 .17 : 5th Harmonic Filter current at Dorsey	123
Figure 6 .18 : Fourier analysis of currents in 5th harmonic filter after compensation	123
Figure 6 .19 : CT Response for 105A GIC per phase, low power case	127
Figure 6 .20 : Magnitude of the harmonics in current waveforms at low power flow	128
Figure 6 .21 : Phase of the harmonics in current waveforms at low power flow	128
Figure 6 .22 : Flux Density of the CT for 105A GIC per phase, low power case	129
Figure 6 .23 : Core current of the CT for 105A GIC per phase, low power case	129
Figure 6 .24 : CT Response for 105A GIC per phase high power case	130
Figure 6 .25 : Magnitude of the harmonics in current waveforms at high power flow	130
Figure 6 .27 : Phase of the harmonics in current waveforms at high power flow	131
Figure 6 .28 : Flux Density of the CT for 105A GIC per phase, high power case ...	131

Figure 6 .29 : Core current of the CT for 105A GIC per phase high power case	132
Figure 6 .30 : A Simple Negative Sequence Filter	133
Figure 6 .31 : Positive Sequence Output for 315A GIC high power case	134
Figure 6 .32 : Negative Sequence Output for 105A GIC per phase, high power case	135
Figure 6 .33 : Zero Sequence Output for 105A GIC per phase, high power case	136
Figure 6 .34 : Positive Sequence Output for 315A GIC low power case	136
Figure 6 .35 : Negative Sequence Output for 105A GIC per phase, low power case	137
Figure 6 .36 : Zero Sequence Output for 105A GIC per phase, low power case	138
Figure 6 .37 : Effect of positive sequence harmonics on positive sequence filter	139
Figure 6 .38 : Effect of negative sequence harmonics on positive sequence filter	139
Figure 6 .39 : Transformer differential current seen from CT for 105A GIC per phase, high power case	140
Figure 6 .40 : Transformer differential current seen from CT for 105A GIC per phase, low power case	140
Figure 6 .41 : Fourier analysis of differential current at high power flow	141
Figure 6 .42 : Fourier analysis of differential current at low power flow	141
Figure A –1 : Simplified Flow Chart for Calculating Non-Linear Current	152
Figure B –1 : Voltage waveforms on 230 kV side at high power flow	153
Figure B –2 : Fourier analysis of 230 kV side voltage waveform at high power flow	154
Figure B –3 : Voltage waveform on 230 kV side at low power flow	155
Figure B –4 : Fourier analysis of 230kV side voltage waveform at low power flow	155
Figure B –5 : Fourier analysis of 500 kV side phase voltages with a typical high power flow	156
Figure B –6 : Fourier analysis of 500 kV side phase voltages with a typical low power flow	157
Figure B –7 : THD Factor of 500 kV side phase voltages	157
Figure B –8 : Fourier analysis of 500 kV side currents with 150A GIC	158
Figure B –9 : Fourier analysis of 500 kV side currents with 400A GIC	158
Figure B –10 : Fourier analysis of 500 kV side phase voltages with 150A GIC	159
Figure B –11 : Fourier analysis of 500 kV side phase voltages with 400A GIC	159

List of Tables

Table 4 .1 : Pre-GIC system conditions for high power flow study – 500kV side . . .	70
Table 4 .2 : Pre-GIC system conditions for low power flow study – 500kV side	70
Table 4 .3 : System conditions after saturation for high power flow	71
Table 4 .4 : Reactive Power Flow at Dorsey for high power flow	72
Table 4 .5 : Details on the 500kV side phase voltage	73
Table 4 .6 : Details on the 500kV side line current	74
Table 4 .7 : System conditions after saturation for high power flow	76
Table 4 .8 : Reactive Power Flow at Dorsey	76
Table 4 .9 : Details on the 500kV side phase voltage	77
Table 4 .10 : Details on the 500kV side line current	79
Table 5 .1 : Pre-GIC system conditions for low power flow study – 500kV side	90
Table 5 .2 : Pre-GIC system conditions for low power flow study – 230kV side	90
Table 5 .3 : Pre-GIC system conditions for high power flow study – 500kV side . . .	91
Table 5 .4 : Pre-GIC system conditions for high power flow study – 230kV side . . .	91
Table 5 .5 : Post-GIC system conditions for low power flow study – 500kV side . . .	92
Table 5 .6 : Post-GIC system conditions for low power flow study – 230kV side . . .	92
Table 5 .7 : The details on the 500 kV side voltage at Dorsey after saturation	94
Table 5 .8 : The details on the 500 kV side current at Dorsey after saturation	94
Table 5 .9 : The details on the 230 kV side voltage after saturation	96
Table 5 .10 : The details on the 230 kV side current at Dorsey after saturation	97
Table 5 .11 : The details on the current flowing to Drayton after saturation	99
Table 5 .12 : The details of the current flowing to Moranville after saturation	99
Table 5 .13 : Post-GIC system conditions for high power flow study – 500kV side . .	101
Table 5 .14 : Post-GIC system conditions for high power flow study – 230kV side . .	101
Table 5 .15 : The details on the 500 kV side voltage after saturation	103
Table 5 .16 : The details on the 500 kV side current after saturation	103
Table 5 .17 : The details on the current flowing to Moranville after saturation	105
Table 6 .1 : Analysis of high pass filter currents at different power flows before series compensation	111
Table 6 .2 : Analysis of high pass filter currents at different power flows after series compensation	113
Table 6 .3 : Analysis of currents through the tuned harmonic filters for a high power flow	118
Table 6 .4 : Analysis of currents through the tuned harmonic filters for a low power flow	119
Table 6 .5 : Apparent increase of rms magnitudes when based on peak values	120
Table 6 .6 : Analysis of currents though the tuned harmonic filters for a high power flow	124
Table 6 .7 : Analysis of currents though the tuned harmonic filters for a low power flow	124
Table 6 .8 : Apparent increase of rms magnitudes when based on peak values	125
Table B – 1 : Details on the 230 kV side phase voltage at high power flow	154
Table B – 2 : Details on the 230 kV side phase voltage at low power flow	155
Table C – 1 : The details on the 230 kV side voltage after saturation	161
Table C – 2 : The details on the 230 kV side current after saturation	161
Table C – 3 : The details on the current flowing to Drayton after saturation . . .	163

Chapter 1

Introduction

1.1 GEOMAGNETICALLY INDUCED CURRENTS

1.1.1 THE ORIGIN AND CYCLIC NATURE

The sun is continuously discharging a thin plasma of protons and electrons into interplanetary space which is known as solar wind. The solar wind is affected by three categories of solar phenomena: solar flares, coronal holes and disappearing filaments.[1][2]

When one of those phenomena cause fluctuations in the solar wind, then the interaction of the solar wind with the earth's magnetic field can produce auroral currents, or electrojets which follow circular paths around the earth's geomagnetic poles at altitudes of 100km or more.

These auroral currents disturb the earth's normally dormant magnetic field and when the disturbances are of sufficient severity they are termed Geomagnetic Storms. On average, solar activity, which is measured by the number of sunspots in a month, follows

an 11-year cycle. Figure 1.1 shows both the Number of geomagnetically disturbed days per year and the sunspot number measured between 1932 and 1986 [3][4]. Figure 1.1 clearly shows the cyclic nature of geomagnetic activity with a period of roughly 11 years.

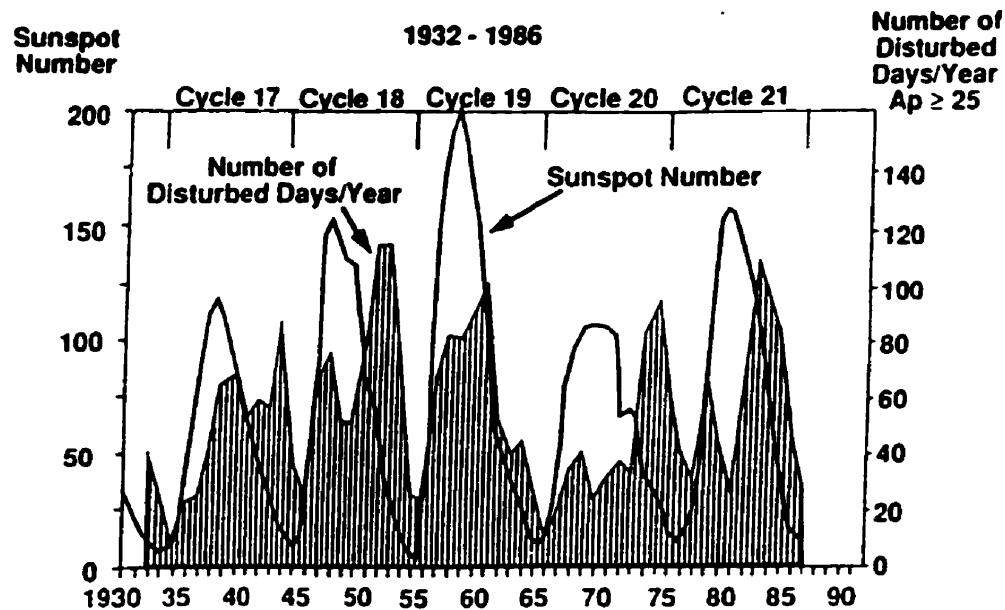


Figure 1.1 : Cyclic Nature of Geomagnetic Activity

1.1.2 INTERACTION WITH POWER SYSTEMS

During Geomagnetic storms, a potential difference is induced on the surface of the earth due to the earth's geomagnetic field fluctuations. The resulting earth surface potential (ESP) acts as a voltage source applied between the grounded neutrals of wye connected transformers or auto-transformers that may be located at opposite ends of a long transmission line as shown in Figure 1.2. This ESP produces a current, known as Geomagnetically Induced Current (GIC), through the grounded neutrals of transformers or auto-transformers and flowing along the transmission line.

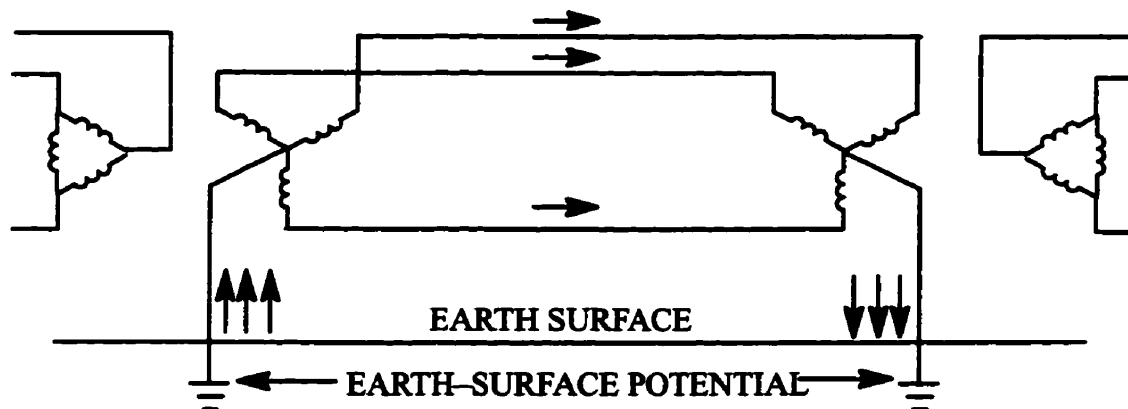


Figure 1 .2 : ESP between grounded Y transformer neutrals and the resultant GIC in transmission lines.

The magnitude of the per-phase GIC can be many times larger than the RMS ac magnetizing current of the transformer. The GIC has a frequency of millihertz and appears as a quasi-dc in comparison to the normal power system frequencies.

1.2 EFFECT ON POWER SYSTEMS

The first known written report of the adverse effects of magnetic storms on electric power systems was made by W. F. Davidson in 1940 [4][5]. The report was based on information obtained from 22 electric utility companies in North America for the magnetic storm of March 24, 1940.

Geomagnetically Induced Current enters the transformer through its grounded neutral and flows along its windings. This builds up a dc flux and shifts the operating point on the transformer magnetization characteristics away from the origin, as shown in Figure 1 .3 , saturating only in one half of each cycle. This effect is known as half cycle saturation of a transformer. The half cycle saturation is the source of nearly all the operating and equipment problems caused by GIC's during magnetic storms.

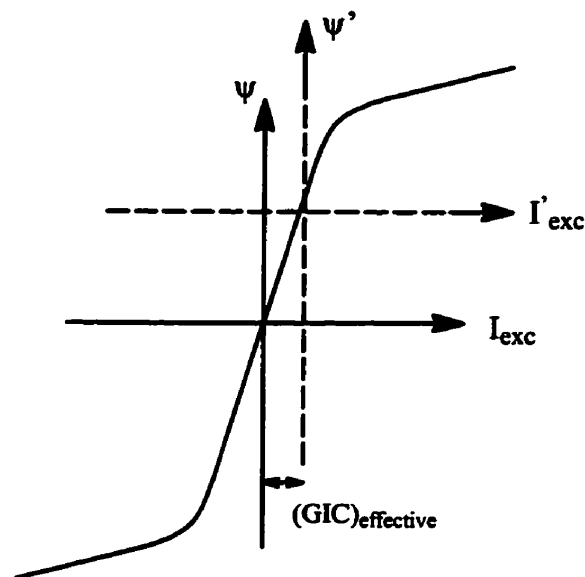


Figure 1 .3 : The shift of operating point on the magnetization characteristics

The consequences of transformer half cycle saturation can be classified as follows [3][4]:

1. Generation of both odd and even harmonics in transformers.

This may result in several adverse effects on the power system.

- (a). Shunt capacitor banks are seen as low impedance paths for the higher harmonics. This will cause a major portion of the harmonic currents to go through capacitor banks. Since some protection schemes could see this as an overload, it is possible to trip out capacitor banks due to overload protection.
- (b). The undesired operation of other protective relays that may respond to sequence voltages or currents but are not frequency selective. Undesired operations can be of three types; detection of fault where none exists, failure to detect a fault and failure to detect a fault in an adequate time period.

2. An increase in reactive power drawn by transformers.

Some of the adverse effects due to this increase can be:

- (a). Intolerable system voltage depressions.
- (b). Unusual swings in active and reactive power flow along transmission lines
- (c). Problems with generator reactive power limits in some instances.

3. A possible drastic leakage flux effect in the transformer with resulting excessive localized heating which could result in the following:

- (a). Increase in losses
- (b). Degradation of insulation

The complete blackout of the Hydro-Quebec system during a GIC event on March 13th 1989 is an example of how disastrous the effects of GIC can be [2][6]. During this geomagnetic storm excessive harmonics flowed into static voltampere reactive compensators, which provide rapid voltage regulation. The capacitive legs of the Static VAR Compensator's (SVC) act as a sink to the harmonics. The harmonics quickly loaded the capacitors to such an extent that protective systems sensed a false overload and took the SVC off-line to prevent equipment damage. This caused severe voltage regulation problems and subsequently the entire Hydro-Quebec network collapsed.

1.3 VULNERABILITY OF POWER SYSTEMS

Normally the GIC which flows in the power system is proportional to the ESP impressed between neutral grounding points. The ESP in turn, varies with the distance between grounding points. Today's power systems have very long transmission lines and inter-connections between regional power grids are becoming very common. Thus the distances between grounding points has increased, leading to a greater likelihood of significant GIC levels.

1.4 MODELLING OF GIC

The power system model for the flow of GIC is basically a dc conducting path model through the station ground mat resistances, the transformer windings, and the interconnecting transmission line network. While there are similarities between the path taken by GIC and zero sequence currents in a power system, there are also important differences in the connective topology representing transformers in the two instances[7]. The GIC transformer models are not concerned with leakage reactance values, but only with paths through the transformer that could be followed by dc current.

In simulation of GIC in an electromagnetic transient simulation package, GIC has to be simulated as a dc potential difference between two substations rather than an injected dc current through the grounding points in the substation.

1.4.1 ESTIMATION OF GIC

During a geomagnetic storm, the portions of the earth which experience an appreciable time rate of change of the geomagnetic field will have induced ESP. Analytical methods have been developed to estimate the ESP based on geomagnetic field fluctuation data and a multi-layered earth conductivity model [8]. Towle et. al.[9] proposed a method by modelling ionospheric current as a gaussian distributed current sheet above the earth and dividing the surface of the earth into different earth resistivity regions. The resulting ESP at each power system substation is then calculated. Rackliffe et. al.[10] quantified the GIC on a power system by a simulated magnetohydrodynamic–electromagnetic pulse.

1.5 SCOPE OF THE THESIS

This study is aimed at modelling the transformer core to represent the saturation characteristics and transformer losses accurately and develop the model to represent different core configurations.

The Dorsey–Forbes–Chisago 500kV system is taken as a case study and an evaluation of some protection schemes are carried out under GIC conditions. The effects of GIC on this system after series compensating the 500kV lines are also studied. The capacitors in series block the d.c. path in the 500 kV line and restrict the GIC into the parallel 230 kV lines.

The study is primarily based on modelling transformers and evaluating some protection schemes. Maximum recorded GIC current levels and predicted maximum GIC current levels are used for the study. The maximum predicted value used in the thesis was based on calculations done assuming an uniform electric field model that is not considered realistic today. However, at the time levels were chosen, there was no other information available.

Chapter 2

Modelling

2.1 TRANSFORMERS

To assess the power system response in the presence of GIC, a simulation package such as EMTDC[11] has to be used but several improvements are necessary before it is entirely suitable. It is clear that simulation results are going to depend very much on how the transformers are modelled since the effects on the power system due to GIC are due primarily to transformer half cycle saturation.

The way the transformer core, including saturation characteristics, eddy current losses and hysteresis losses, is modelled is very important since the cause of harmonic generation are in fact the non-linearities of the core of the transformer. This is further illustrated by figure 2.1 .

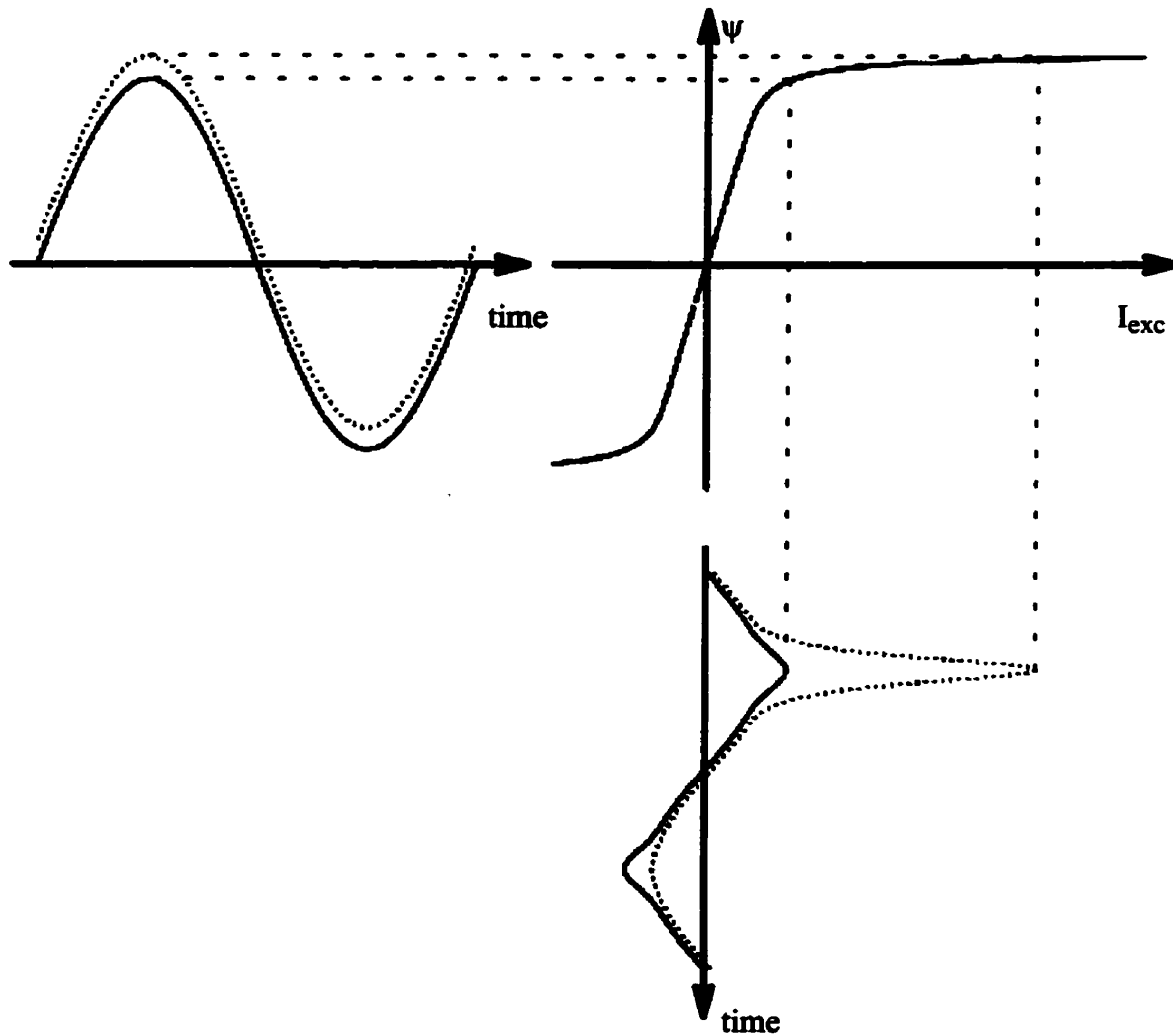


Figure 2 .1 : Generation of harmonics due to the non-linearity of the transformer core

GIC appears as a quasi-dc current giving rise to a dc flux, provided a low reluctance path exists for dc flux. This will drive the transformer into half cycle saturation. A three phase three limb transformer is an example where there is no low reluctance path for dc flux, therefore exhibit no significant effects. This is an example of how different core models behave in different ways in response to the GIC. Before going into details of transformer modelling let us first understand how the transformers are represented in simulation packages such as EMTP[12] and EMTDC[11].

2.1.1 TRANSFORMER MODELLING IN EMTP

In principle, any N winding transformer can be described as N coupled coils.

And it can be represented by the following equation for the a.c. steady state

$$V_i = \sum_{k=1}^N Z_{ik} I_k \quad \text{or} \quad [V]_{n \times 1} = [Z]_{n \times n} [I]_{n \times 1} \quad (2.1)$$

and for the transient state

$$v_i = \sum_{k=1}^N R_{ik} i_k + \sum_{k=1}^N L_{ik} \frac{di_k}{dt} \quad \text{or} \quad [v]_{n \times 1} = [R]_{n \times n} [i]_{n \times 1} + [L]_{n \times n} \frac{d}{dt} [i]_{n \times 1} \quad (2.2)$$

The matrix Z in equation 2.1 is symmetric. Elements of that matrix can be measured in no load tests. If coil k is energized and all other coils are open circuited, then the measured values of I_k and $V_1 \dots V_n$ produce the k th column of the matrix Z .

$$Z_{ik} = \frac{V_i}{I_k} \quad (2.3)$$

Unfortunately the short circuit input impedances which describe the more important transfer characteristics of the transformer are insignificant in such no load measurements. Large transformers are tightly coupled with a coupling coefficient very close to unity making it impossible to calculate short circuit impedance with a reasonable accuracy[12].

Thus matrix Z is calculated in a different way. Let the transfer characteristics be expressed in the form of voltage drops between coil i and a reference N . Then,

$$V_i - \frac{w_i}{w_N} V_N = \sum_{k=1}^N \left(Z_{ik} - \frac{w_i}{w_N} Z_{Nk} \right) I_k \quad (2.4)$$

where w_i is the number of turns in coil i .

Because the exciting magnetomotive force (m.m.f.) is negligible for the short circuit test, we have m.m.f. balance,

$$\sum_{k=1}^N w_k I_k = 0 \quad (2.5)$$

Combining equations 2.4 and 2.5 and eliminating I_N ,

$$V_i - \frac{w_i}{w_n} V_N = \sum_{k=1}^{N-1} Z_{ik}' I_k \quad 1 \leq i \leq (N-1) \quad (2.6)$$

or $[V']_{(n-1) \times 1} = [Z']_{(n-1) \times (n-1)} [I]_{(n-1) \times 1}$

The elements of Z' can be found directly from short circuit test data [12].

Then the matrix Z' is inverted

$$[I]_{(n-1) \times 1} = [Y']_{(n-1) \times (n-1)} [V']_{(n-1) \times 1} \quad (2.7)$$

and by adding equation 2.5 and re-arranging

$$[I]_{n \times 1} = [Y]_{n \times n} [V]_{n \times 1} \quad (2.8)$$

2.1.2 IDEAL TRANSFORMER MODEL IN EMTDC

To understand how ideal transformers are modelled in EMTDC [11], let us first understand the theory of mutual coupling. To simplify the study let us consider two mutually coupled windings as shown in Figure 2.2.

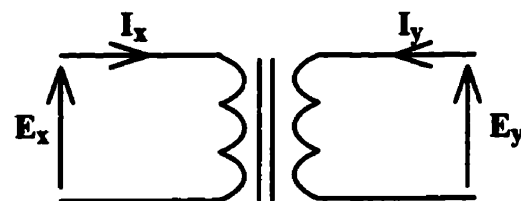


Figure 2.2 : Two mutually coupled windings

The voltages across the first and second windings are E_x and E_y respectively whereas the currents going into the windings are I_x and I_y . The self inductances of the windings x and y are denoted as L_{xx} and L_{yy} respectively whereas mutual inductance between the two windings is denoted as $M_{xy} = M_{yx} = M$. Equation 2.9 can be written to describe this circuit.

$$\begin{bmatrix} E_x \\ E_y \end{bmatrix} = \begin{bmatrix} L_{xx} & M \\ M & L_{yy} \end{bmatrix} \frac{d}{dt} \begin{bmatrix} I_x \\ I_y \end{bmatrix} \quad (2.9)$$

In order to solve for the currents, the inductance matrix needs to be inverted.

$$p \begin{bmatrix} I_x \\ I_y \end{bmatrix} = \frac{1}{\Delta} \begin{bmatrix} L_{yy} & -M \\ -M & L_{xx} \end{bmatrix} \begin{bmatrix} E_x \\ E_y \end{bmatrix} \quad (2.10)$$

where $p = \frac{d}{dt}$

$$\Delta = L_{xx}L_{yy} - M^2 = L_{xx}L_{yy}(1 - k_{xy}^2)$$

$$k_{xy} = \frac{M}{\sqrt{L_{xx}L_{yy}}}$$

The coupling coefficient $k = 1$ when the windings are ideally coupled. In a practical power transformer $k \cong 1$, but $k < 1$ which enables the inverse of the inductance matrix to be finite. For closely coupled coils, turns ratio 'a' is defined as shown below.

$$a = \frac{E_1}{E_2} = \sqrt{\frac{L_{xx}}{L_{yy}}} \quad (2.11)$$

L_{xx} and L_{yy} can be determined by doing standard open circuit tests on the two windings. For example when winding y is open circuited,

$$\begin{aligned} I_y &= 0 \\ E_x &= L_{xx} \frac{d}{dt} I_x \end{aligned} \quad (2.12)$$

If the applied voltage E_x is assumed to be sinusoidal, with rms voltage V_x , and an angular frequency of ω , and if it produces a rms current of I_x then,

$$L_{xx} = \frac{V_x}{\omega I_x} \quad (2.13)$$

Similarly the mutual inductance between coils x and y can be found by shorting coil y and applying a rms voltage V_x to coil x so that rated rms current I_x flows in coil x. Then

$$\begin{aligned}
E_y &= 0 \\
E_x &= L_{xx} pI_x + M_{xy} pI_y \\
0 &= M_{xy} pI_x + L_{yy} pI_y \\
E_x &= (L_{xx} - \frac{M_{xy}^2}{L_{yy}}) pI_x = L_{xx}(1 - k_{xy}^2) pI_x \\
\frac{V_x}{I_x} &= \omega L_{xx}(1 - k_{xy}^2)
\end{aligned} \tag{2.14}$$

since k_{xy} is very close to one,

$$\begin{aligned}
\frac{V_x}{I_x} &= 2\omega L_{xx}(1 - k_{xy}) \\
&= X_{L_{xy}}
\end{aligned} \tag{2.15}$$

Hence,

$$\begin{aligned}
k_{xy} &= 1.0 - \frac{X_{L_{xy}}}{2\omega L_{xx}} \\
\text{and } M_{xy} &= k_{xy} \sqrt{L_{xx} L_{yy}}
\end{aligned} \tag{2.16}$$

From equations 2.13, 2.15 and 2.16 when the rated voltages of the windings, MVA rating of the transformer, leakage reactances between windings and the frequency are given, one can calculate the inductance matrix.

From equation 2.10 the inverse of the matrix can be written as follows by substituting 'a' and letting $k_{xy} = 1$ within the matrix

$$\begin{aligned}
\begin{bmatrix} L_{xx} & M_{xy} \\ M_{xy} & L_{yy} \end{bmatrix}^{-1} &= \frac{1}{L_{xx} L_{yy} (1 - k_{xy}^2)} \begin{bmatrix} L_{yy} & -M_{xy} \\ -M_{xy} & L_{xx} \end{bmatrix} \\
&= \frac{1}{\omega X_{L_{xy}}} \begin{bmatrix} 1 & -a \\ -a & a^2 \end{bmatrix}
\end{aligned} \tag{2.17}$$

2.1.3 TRANSFORMER CORE

When an ideal transformer is modelled, iron core non linearities and winding resistances are not represented. These have to be added separately. The most prominent iron

core non linearity is the saturation followed by eddy current loss and hysteresis loss [13],[14]. The simplest and most commonly used method to represent core losses is to add a shunt resistance across one winding. For most of the studies using EMTP or EMTDC, core and winding losses can be neglected because of the little significance to the result [11]. But for studying the effects of GIC, where the cause of the problem is the non-linearity of the core, the transformer core has to be modelled accurately.

Many studies including transformers do require saturation to be adequately modelled. It can be represented in either of two ways;

1. Varying inductance
2. non-linear current source across a winding

If the saturation is modelled by the varying inductance method the conductance matrix corresponding to that particular subsystem has to be re-computed and inverted again whenever there is a change in the inductance. The advantage of using a non linear current source is that there is no requirement for re-computation and inversion of the conductance matrix but the voltage available for calculation of current is one time step old and hence some sort of prediction is used to get the present voltage.

In most of the models representing the saturation, non linearity is represented as a combination of several linear sections. EMTDC uses a combination of a curve and a straight line section [11]. This kind of representation is quite adequate for most of the studies. But for studying the effects of GIC, where the results are highly dependent on transformer saturation characteristics, it is not sufficient.

As for core losses, Swift has shown that eddy current losses are greater than hysteresis losses and eddy current effect can be closely approximated in a linear way for power system transients [13].

2.1.3.1 SATURATION CHARACTERISTICS

There are several models in use but almost all of them are only accurate up to a certain degree of saturation. Representation of magnetization characteristics over a wide range having a smooth variation of incremental permeability is feasible only by representing the saturation as a non-linear current source. The variable inductance method will not be feasible as this will force a repeated number of computations and inversions of the conductance matrix.

Then the problem is finding a suitable mathematical expression which gives the magnitude of the non-linear current. There were several attempts to represent the magnetization characteristics as a polynomial series, rational fraction polynomial series[15] or a non-integer power series[16]. Although polynomial series and rational fraction polynomial give a fairly good representation, incremental permeability is not represented accurately even giving rise to negative values. The non-integer power series method proposed by Lucas[16] ensures a smooth and realistic variation of incremental permeability.

The magnetization curve of transformer steel has a low incremental permeability at low magnetizing fields, increasing to a peak value and then decreasing as saturation is increased. Lucas has shown that field intensity H can be expressed by a power curve of flux density B of the form given by

$$H = \sum K_i B^{\alpha_i} \quad \text{with } K_i > 0 \text{ and } \alpha_i > 0 \text{ for all } i \quad (2.18)$$

Alternatively this may be expressed in terms of flux linkage λ and magnetizing current i_m at time $t = n \Delta t$ as in equation 2.20 .

$$\frac{N i_{m,n}}{l} = \sum K_i \left(\frac{\lambda_n}{NA} \right)^{\alpha_i} \quad \text{with } K_i > 0 \text{ and } \alpha_i > 0 \text{ for all } i$$

where

- N = Number of turns
- l = mean length of the flux path
- A = cross sectional area of the core

$$(2.19)$$

This simplifies to,

$$i_{m,n} = \sum k_i \lambda_n^{\alpha_i} \quad \text{with } k_i > 0 \text{ and } \alpha_i > 0 \text{ for all } i$$

$$\text{where} \quad k_i = \frac{l}{N} \frac{K_i}{(NA)^{\alpha_i}} \quad (2.20)$$

The coefficients K_i and hence k_i are deliberately chosen to be positive to ensure that both H and incremental permeability $\frac{dB}{dH}$ vary smoothly without oscillations. The indices α_i need not be integers but are chosen to be integers for convenience. The first index α_1 is really a decimal fraction close to half which represents the ankle region of the magnetization characteristics[17]. Since the ankle region is not of great importance for this study α_1 is chosen as unity for ease of computation.

The coefficient K_1 is calculated by plotting $\log B$ vs. $\log H$ and then applying a least square method for the initial region. After solving K_1 for $\alpha_1 = 1$, the rest of the indices α_i and coefficients K_i can be found by using logarithmic plots [16]. Typically 3 terms of the power curve give a very good representation over a wide range of values.

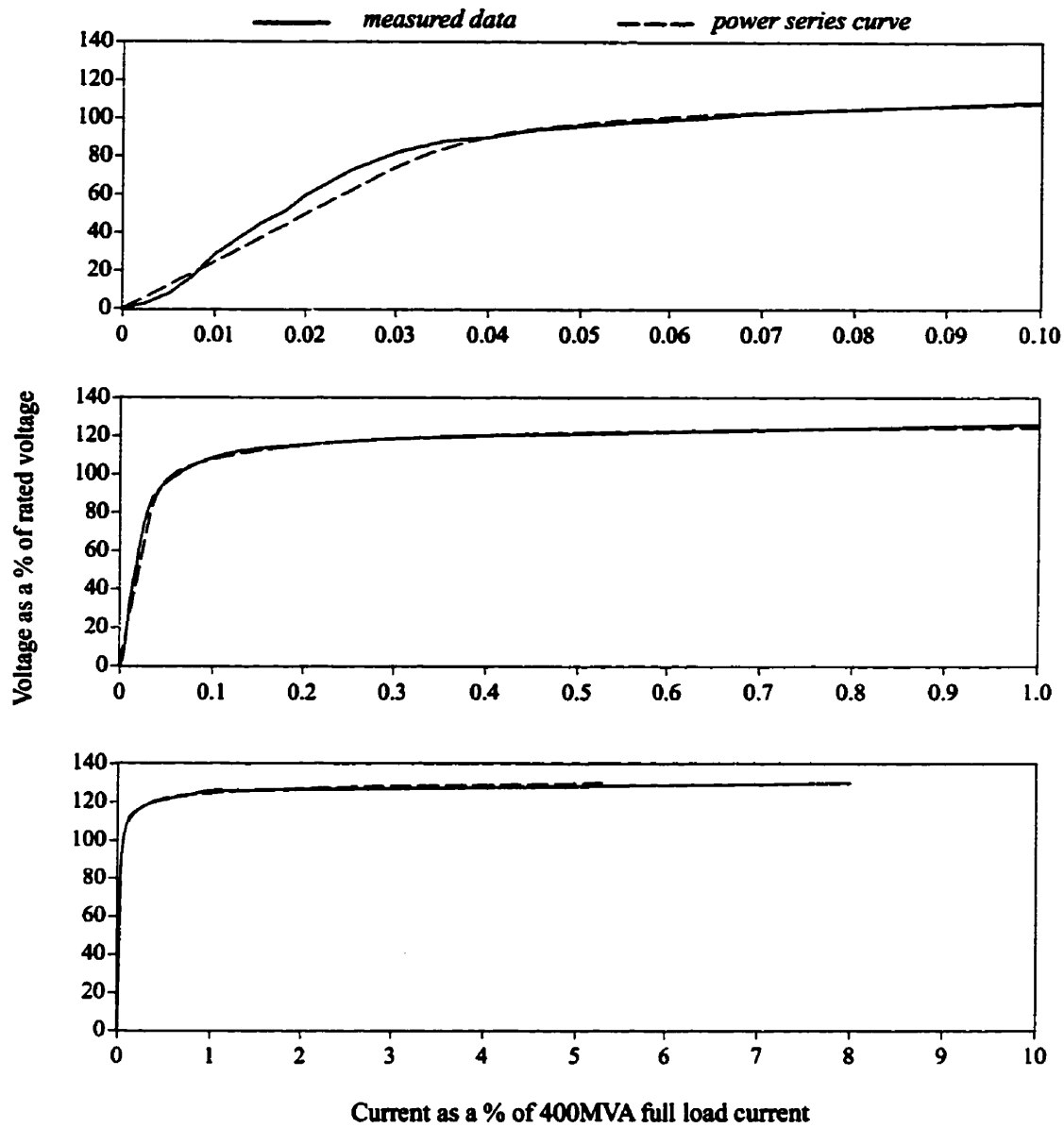


Figure 2.3 : Power series curve representation of magnetization characteristics

$$k_1 = 3.99654 \times 10^{-6} i_{FL} \left(\frac{\omega}{V_R} \right) \quad \alpha_1 = 1$$

$$k_2 = 1.76417 \times 10^{-6} i_{FL} \left(\frac{\omega}{V_R} \right)^{15} \quad \alpha_2 = 15$$

$$k_3 = 1.40763 \times 10^{-8} i_{FL} \left(\frac{\omega}{V_R} \right)^{57} \quad \alpha_3 = 57$$

where ω = frequency in rad/s
 i_{FL} = 400MVA full load current
 V_R = rated voltage (rms)

(2.21)

Figure 2.3 shows the magnetization characteristics obtained for the 230/500/46kV 240/400MVA/phase transformer at Dorsey for 60 Hz frequency. The vertical axis shows rms voltage as a percentage of rated voltage and the horizontal axis shows the rms current as a percentage of full load current. The two graphs show the actual data and the calculated power series curve. The values of k_i 's and α_i 's for the graph in Figure 2.3 are given by Equation 2.21 .

The "Reluctance" S_n of the magnetic core of the transformer is defined for convenience in this study in terms of flux linkage λ_n , rather than the flux, as in equation 2.22

$$i_{n,r} = S_n \lambda_n \quad (2.22)$$

Hence S_n may be expressed as in equation 2.23

$$S_n = \sum k_i \lambda_i^{\alpha_i - 1} \quad (2.23)$$

Since the values of k_i 's and α_i 's have been based on rms measurements ($V_{rms}-I_{rms}$ curve) they cannot be used with instantaneous values of i and λ . There are some methods to convert $V_{rms}-I_{rms}$ to instantaneous or peak values [14][12]. All these methods are applicable only for modelling saturation characteristics in piecewise linear sections and are not suitable for power series curve representation of saturation characteristics.

The following heuristic approach is used to modify k_i 's and α_i 's. Note that there will be no difference in the coefficient k_i when it is converted into an instantaneous value. This is because we chose $\alpha_i = 1$, which describes the linear portion of the relationship between voltage and current and hence there is no change in the proportionality coefficient whether it is instantaneous, peak or rms value.

For the first step, the coefficients k_i 's and indices α_i 's previously obtained from logarithmic plots of measured characteristics are used to give an estimated saturation characteristic of i and λ . The rms current is then calculated using this saturation characteristic with a sinusoidal input voltage V_{rms} of varying magnitude at rated frequency. Using these new values of V_{rms} and I_{rms} , a new curve was drawn. Then a similar logarithmic

analysis is done on this new curve and a new set of coefficients (k_{i-new}) is found keeping indices (α_i) as before. Then a new coefficient for the second term of eqn 2.23 is found by multiplying the original coefficient (k_{2-orig}) of the second term by the ratio k_{2-orig} / k_{2-new} . With this modification the new $V_{rms}-I_{rms}$ curve falls within close proximity to the measured curve over the region dominated by first and second terms of the power series. This procedure is repeated until the characteristic described by the power series coincides with the measured characteristics over the region dominated by the first and second terms.

Then a similar process is done for the coefficient of the third term of the power series. Figure 2.4 shows rms voltage as a percentage of rated voltage vs. rms current as a percentage of 400MVA full load current for different stages of converting coefficients into instantaneous values.

After determining new coefficients k_i 's to suit instantaneous values, S_n can be represented as in equation 2.24

$$S_n = k_1 + \sum k_i \lambda_i^{\alpha_i - 1} \quad \text{where } \alpha_i \neq 1 \quad (2.24)$$

The portion of reluctance which is represented by k_1 in eqn. 2.24 can be represented as an inductor across a winding. The advantage of representing it as an inductance in a time domain simulation is that current drawn by it in the present time step is based on the voltage at the present time step.

Note that although coefficients k_i 's and indices α_i 's can be found to get the relationship between $i_{m,n}$ and λ_n , computations are done using values of B rather than λ to avoid numerical problems when handling powers of very large or very small numbers.

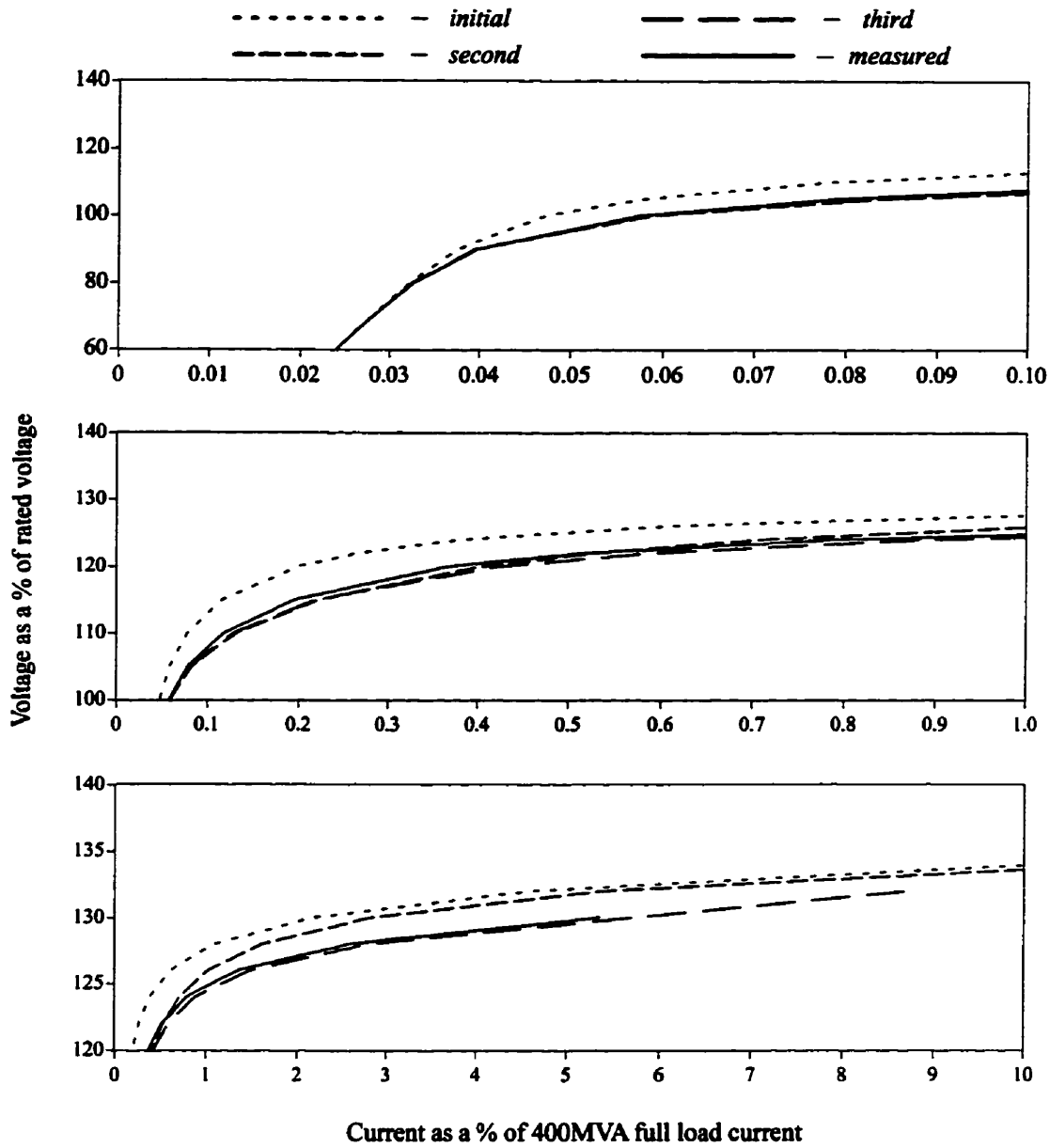


Figure 2.4 :Conversion of rms values into instantaneous values

The instantaneous current of the non-linear current due to magnetization characteristics are given by

$$i_{mag(NL)} = S'_n B_0 \lambda \quad \text{and} \quad (2.25)$$

$$S'_n = \sum B_i (B_0 \lambda)^{\alpha_i} \quad \text{where } \alpha_i \neq 1$$

$$\text{where } B_0 = \frac{1}{N A} \quad \text{and} \quad B_i = \frac{l}{N} K_i$$

This is accompanied by a linear inductance L_{mag} which represents the linear portion of the magnetization current.

$$L_{mag} = \frac{1}{k_1} = \frac{NNA}{l K_1} = \frac{1}{B_0 B_1} \quad (2.26)$$

2.1.3.2 CORE LOSSES

There are two forms of losses which occur in the transformer core;

1. eddy current loss
2. hysteresis loss

At steady state conditions eddy current loss linearly increases with approximately B^2 whereas hysteresis loss varies with approximately B^β . Thus the loss current may be written as

$$i_{c,n} = k_h V_n^{\beta-1} + \frac{V_n}{R_e} \quad (2.27)$$

where k_h is a proportionality constant for the hysteresis current, β is the Steinmetz index and R_e is the eddy current resistance. R_e and k_h will in general be frequency dependent but at present they are set to a value suitable for fundamental frequency. At present β is set to 1.6 which is typical.

Because of the linear relationship between current representing the eddy current loss and the voltage, the eddy current loss can be modelled by a resistance across the winding. But the hysteresis loss current component has to be represented as a current source.

The value of R_e can be shown

$$R_e = \frac{N^2 A}{l} \frac{12\rho}{c^2} \quad (2.28)$$

where N is the number of turns in the coil, A is the cross sectional area of the core, l is the mean length of the flux path, c is the thickness of the lamination and ρ is the resistivity of the material.[18]

2.1.4 OVERALL MODEL FOR THE TRANSFORMER CORE

Considering all the above facts discussed in sections 2.1.3.1 and 2.1.3.2, the transformer core can be represented as in Figure 2.5.

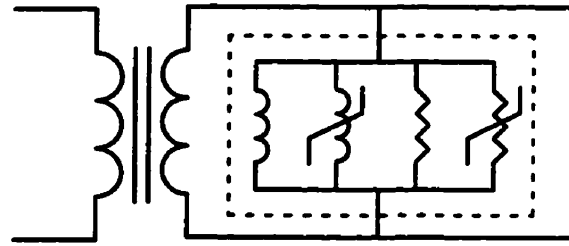


Figure 2.5 :Basic Model for the Transformer Core

Hysteresis loss current and the non-linear magnetizing current due to flux dependent reluctance are represented as a current source, giving the equivalent circuit as shown in Figure 2.6.

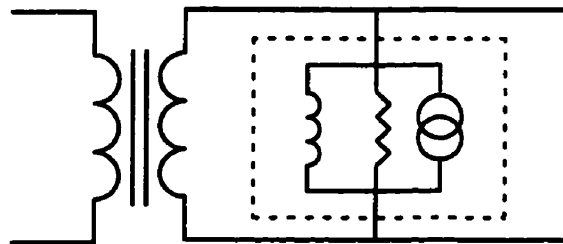


Figure 2.6 : Final Model of the Transformer Core

A flow chart of the simplified algorithm for calculating non-linear current is given in the appendix A.

2.1.5 DIFFERENT TRANSFORMER CONFIGURATIONS

The main difference which affects the transformer half cycle saturation between different transformer configurations is the magnetic flux path taken by zero sequence flux and non-zero sequence flux. If the zero sequence flux path is the same as the positive and negative sequence flux path, then the magnetization characteristics are the same

for all sequences. Then the core can be modelled by attaching a simple core model to any one of the windings.

If the zero sequence flux path is different from the positive and negative sequence flux path, then a complex core model can be developed by adding an extra winding and connecting core models corresponding to different limbs of the transformer in an appropriate way according to the principle of duality between electric and magnetic circuits.[18]

2.1.5.1 SINGLE PHASE UNITS

Single phase transformer cores can be of two types; shell form or core form. These two forms are illustrated in figure 2.7 . In the shell form the coils are wound in the centre limb whereas in the core form the coils are wound on two side limbs.

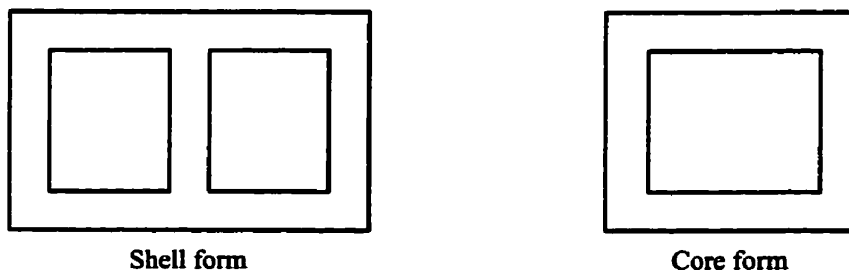


Figure 2.7 : Shell form and Core form Single Phase Transformers

A single phase unit, or a three phase transformer comprised of single phase units whether it is core type or shell type should behave in a similar fashion on exposure to GIC. The single factor linking these two types of transformer is that the magnetic circuit of the core accommodates zero sequence flux and its path is the same as that of positive and negative sequence flux. Therefore saturation characteristics of zero sequence are the same as that of positive and negative sequence. This is the most simple model of possible transformer configurations. Figure 2.8 shows the single phase multi winding transformer model for cases where zero sequence flux shares the same path with positive and negative

sequence fluxes. Three phase transformers made up of single phase units can be assembled from this by connecting them appropriately.

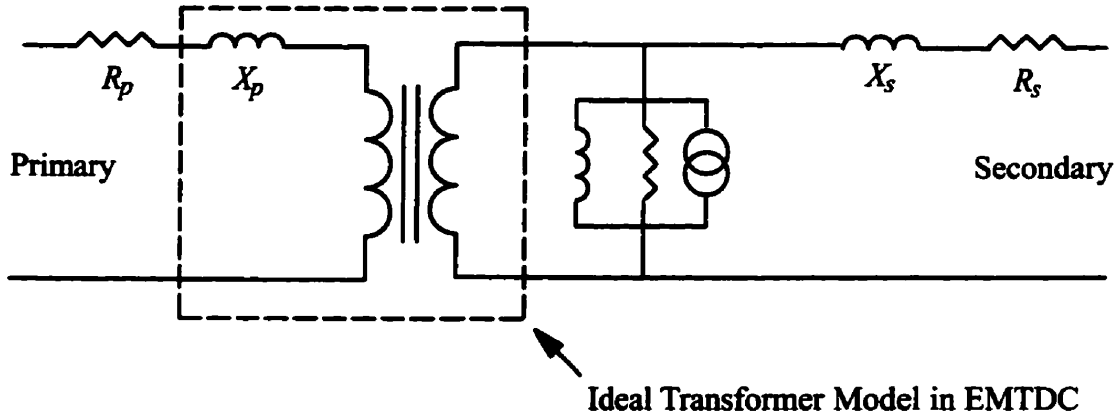


Figure 2 .8 : Single Phase Model of a Transformer

2.1.5.2 THREE PHASE CONVENTIONAL TRANSFORMERS

A typical three phase shell form transformer core is shown in figure 2.9 [19][20]. Three phase coils are wound on three middle limbs with the coils in the middle limb wound in the opposite direction to the other two. Usually the cross sectional areas of the yokes and the outer limbs are half of that of main limbs. In the case of zero sequence flux, zero sequence flux produced by two sets of coils shares the two middle yokes giving a higher zero sequence flux density in the middle yokes.

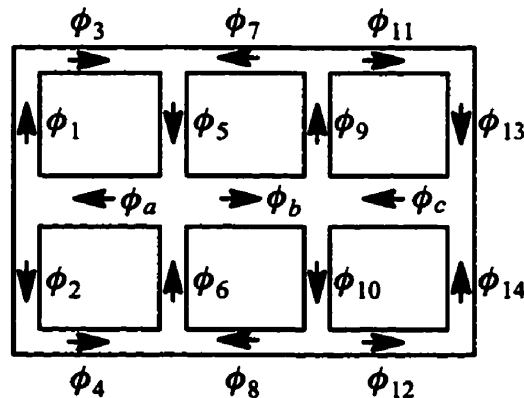


Figure 2.9 : Three phase conventional transformer core configuration

In a case like this where the paths taken by different sequence fluxes are different, a core model can be developed by making an additional winding and connecting them with different core elements which represent the limbs and yokes in the transformer core in an appropriate way according to the principle of duality between magnetic and electric circuits.

The magnetic equivalent circuit for the transformer core configuration shown above can be represented as in figure 2.10.

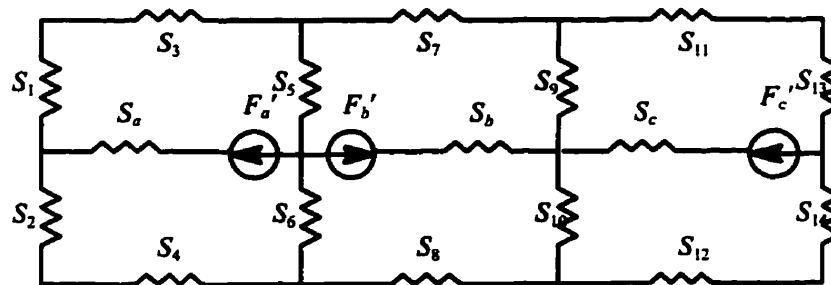


Figure 2.10 : Equivalent magnetic circuit of the three phase conventional transformer

In a magnetic equivalent circuit, around any closed path, the total magnetomotive force of the windings is equal to the sum of the products of reluctance and flux.

$$\sum F = \sum S \phi \quad (2.29)$$

The continuity of magnetic flux in the magnetic field is represented by equating the sum of the fluxes entering any junction of magnetic paths in the equivalent circuit to zero.

$$\sum \phi_{\text{into junction}} = 0 \quad (2.30)$$

For the above circuit using the symmetry of the circuit between the upper and lower half,

$$\begin{aligned}
\phi_n &= \phi_{n+1} \\
S_n &= S_{n+1} \\
F_n &= F_{n+1}
\end{aligned}
\quad \text{for } n = 1, 3, 5, 7, 9, 11, 13 \tag{2.31}$$

Using the equation 2.29 ,

$$\begin{aligned}
F_a' &= S_a \phi_a + S_1 \phi_1 + S_3 \phi_3 + S_5 \phi_5 \\
F_b' &= S_b \phi_b + S_9 \phi_9 + S_7 \phi_7 + S_5 \phi_5 \\
F_c' &= S_c \phi_c + S_9 \phi_9 + S_{11} \phi_{11} + S_{13} \phi_{13}
\end{aligned}
\tag{2.32}$$

Using the equation 2.30 we have,

$$\begin{aligned}
\phi_a &= \phi_1 + \phi_2 \\
\phi_1 &= \phi_3 \\
\phi_5 &= \phi_3 + \phi_7 \\
\phi_a + \phi_b &= \phi_5 + \phi_6 \\
\phi_9 &= \phi_7 + \phi_{11} \\
\phi_b + \phi_c &= \phi_9 + \phi_{10} \\
\phi_{11} &= \phi_{13} \\
\phi_c &= \phi_{13} + \phi_{14}
\end{aligned}
\tag{2.33}$$

Equation 2.32 can be rewritten as,

$$\begin{aligned}
F_a' &= F_a + F_1 + F_3 + F_5 \\
F_b' &= F_b + F_9 + F_7 + F_5 \\
F_c' &= F_c + F_9 + F_{11} + F_{13}
\end{aligned}
\tag{2.34}$$

Let us consider each of these magnetomotive force components to be produced by corresponding components of current in N–turn coils. These current components are then related by the expression

$$\begin{aligned}
i_a' &= i_a + i_1 + i_3 + i_5 \\
i_b' &= i_b + i_9 + i_7 + i_5 \\
i_c' &= i_c + i_9 + i_{11} + i_{13}
\end{aligned}
\tag{2.35}$$

Suppose all fluxes link an N–turn coil. Then corresponding voltages produced in the coils can be related by using equation 2.33 as follows.

$$\begin{aligned}
e_a &= e_1 + e_2 \\
e_1 &= e_3 \\
e_5 &= e_3 + e_7 \\
e_a + e_b &= e_5 + e_6 \\
e_9 &= e_7 + e_{11} \\
e_b + e_c &= e_9 + e_{10} \\
e_{11} &= e_{13} \\
e_c &= e_{13} + e_{14}
\end{aligned}
\tag{2.36}$$

Also using the symmetry we have,

$$\begin{aligned}
e_n &= e_{n+1} \\
i_n &= i_{n+1}
\end{aligned}
\quad \text{for } n = 1, 3, 5, 7, 9, 11, 13
\tag{2.37}$$

This gives us an equivalent circuit as shown in figure 2.11 .

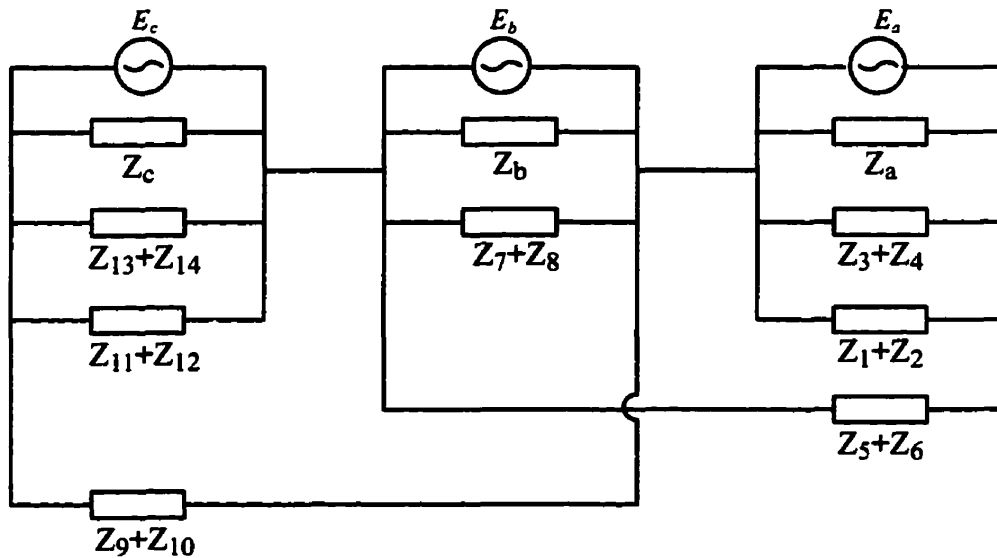


Figure 2.11 : Equivalent Circuit for 3 phase Conventional Transformer

The three voltages are applied to the circuit by adding another three phase winding and connecting the windings and the elements in series as shown in the equivalent circuit. The elements correspond to the actual limbs in the transformer. Each element is subjected to a voltage corresponding to the flux passing through the corresponding limb of the transformer core. Therefore eddy current loss resistance and hysteresis current source can be incorporated into this model. This makes each circuit element in the equivalent circuit

correspond to a parallel combination of resistor, inductor and a current source as marked in dotted lines in figure 2.6 .

2.1.5.3 THREE PHASE FIVE LIMB TRANSFORMERS

Core configuration of a typical three phase five limb transformer is shown in figure 2.12 . The coils are wound on the three middle limbs and no coils are wound on the two outside limbs. The cross sectional area of an outer limb is usually half of that of a main limb and the cross sectional area of yokes are about 70% of that of a main limb.

The zero sequence flux flows through the outside limbs thus making them susceptible to saturation due to zero sequence flux. The main limbs provide a path for all fluxes irrespective of the sequence of the flux.

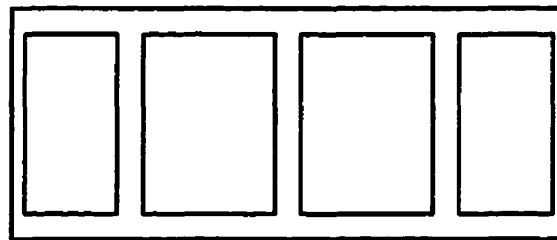


Figure 2.12 : Three phase Five limb transformer core configuration

Doing a similar analysis as for the conventional transformer, we can develop an equivalent electric circuit for a three phase five limb transformer. The equivalent circuit is shown in the figure 2.13 .

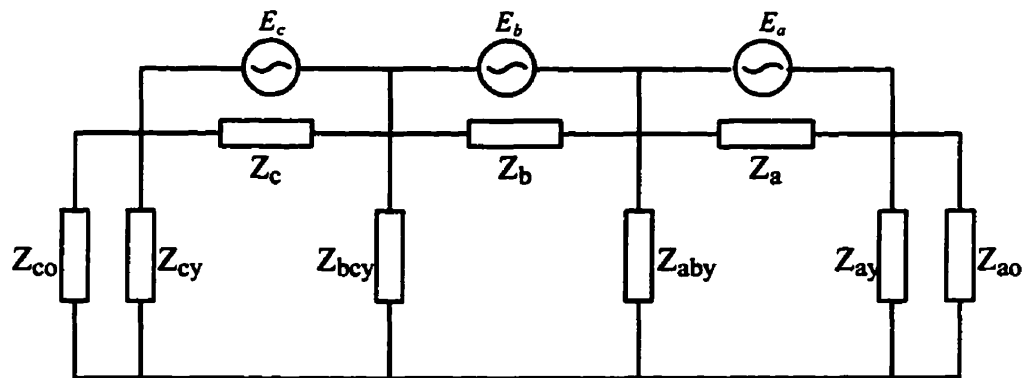


Figure 2 .13 : Equivalent Circuit for 3 phase 5 limb Transformer

2.1.5.4 THREE PHASE THREE LIMB TRANSFORMERS

Core configuration of a typical three phase three limb transformer is shown in figure 2.14. The coils are wound in the three vertical limbs. There is no low reluctance flux path for the zero sequence flux.

More accurate equivalent circuits can be developed if the flux paths outside the core material are considered. For this study flux paths outside magnetic material are not considered since this is the least affected transformer core configuration due to GIC.

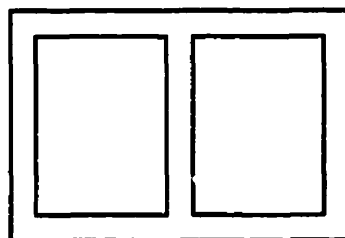


Figure 2 .14 : Three phase Three limb transformer core configuration

Doing a similar analysis as for the conventional transformer, we can develop an equivalent electric circuit for a three phase three limb transformer. The equivalent circuit is shown in the figure 2.15.

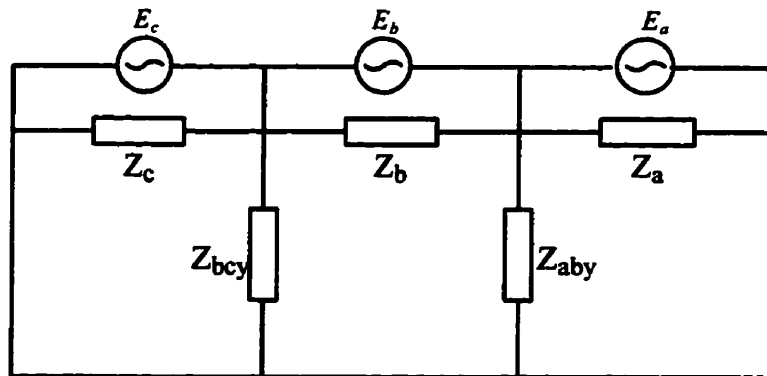


Figure 2 .15 : Equivalent Circuit for 3 phase 3 limb Transformer

2.2 TRANSMISSION LINES

Modelling of transmission lines plays an important role in studying the effects of GIC since transmission line response is frequency dependent. Since GIC gives rise to harmonics, proper representation of transmission lines for a wide frequency spectrum is very important. There are two methods used in modelling transmission lines in electromagnetic transient programs.

1. Bergeron model
2. Marti's frequency dependent line model

In order to appreciate the concept of a distributed transmission line, a single conductor overhead transmission line is considered. Multi phase and mutually coupled transmission lines follow similar concepts.

2.2.1 BERGERON MODEL

Let us first consider a lossless transmission line. Lossy transmission lines can be derived from the lossless model with certain assumptions. For a lossless line,

$$-\frac{\partial v}{\partial x} = L \frac{\partial i}{\partial t} \quad (2.38)$$

$$-\frac{\partial i}{\partial x} = C \frac{\partial v}{\partial t}$$

where L = inductance per unit length
 C = capacitance per unit length
 v = voltage
 i = current
 t = time
 x = distance along the line

d'Alembert's solution to equation 2.38 is;

$$v(x, t) = Z_c (f_1(x - at) - f_2(x + at)) \quad (2.39)$$

$$i(x, t) = f_1(x - at) + f_2(x + at)$$

$$\text{where phase velocity } a = \frac{1}{\sqrt{LC}}$$

$$\text{characteristic impedance } Z_c = \sqrt{\frac{L}{C}}$$

rearranging the equation 2.39 ,

$$v(x, t) + Z_c i(x, t) = 2 Z_c f_1(x - at) \quad (2.40)$$

$$v(x, t) - Z_c i(x, t) = -2 Z_c f_2(x + at)$$

From equation 2.40 it is clear, that an observer moving at velocity a along the line will see the quantity $v + Z_c i$ constant, because for that person, $x - at$ is constant.

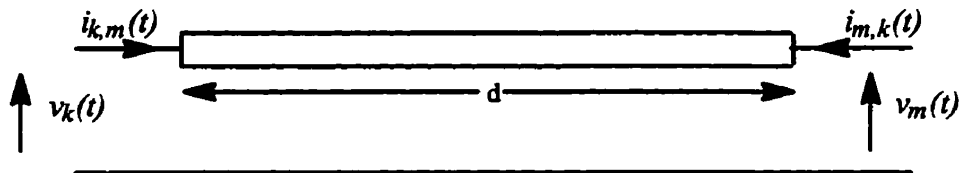


Figure 2.16 : A lossless transmission line

Let the observer leave m at time $t - \tau$ and arrive at k at time t , where $t = d/a$, d being the line length. Thus,

$$v_m(t - \tau) + Z_c i_{m,k}(t - \tau) = v_k(t) - Z_c i_{k,m}(t) \quad (2.41)$$

rearranging equation 2.41 ,

$$i_{k,m}(t) = \frac{1}{Z_c} v_k(t) + I_k(t - \tau) \quad (2.42)$$

$$\text{where } I_k(t - \tau) = -\frac{1}{Z_c} v_m(t - \tau) - i_{m,k}(t - \tau)$$

similarly,

$$i_{m,k}(t) = \frac{1}{Z_c} v_m(t) + I_m(t - \tau) \quad (2.43)$$

$$\text{where } I_m(t - \tau) = -\frac{1}{Z_c} v_k(t - \tau) - i_{k,m}(t - \tau)$$

Thus we have the Norton representation of the transmission line as shown in figure 2.17 .

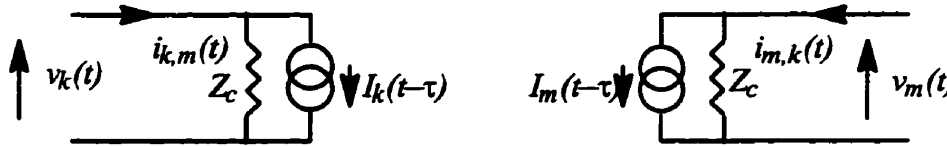


Figure 2.17 : Norton representation of the lossless transmission line

For a lossy transmission line, this method can be modified to include the total series resistance R of the transmission line for a given frequency. It is assumed that the conductance to the ground is negligible. This could be easily implemented by dividing the line section into two equal sections and having a one fourth of R in series with the Norton equivalent circuit as shown in figure 2.18 .

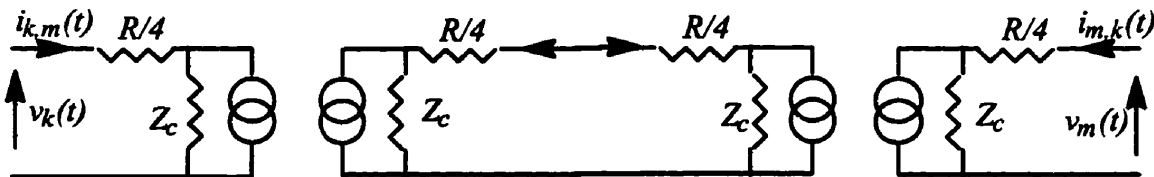


Figure 2.18 : Development of Norton representation for a lossy transmission line

The Norton representation shown in figure 2.18 can be simplified into that shown in figure 2.19 .

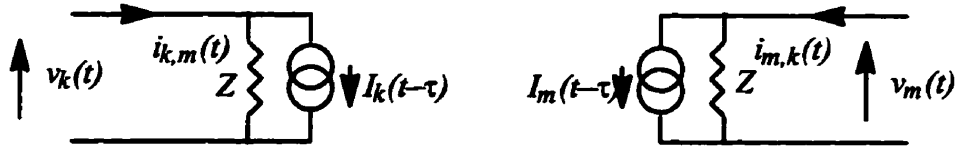


Figure 2.19 : Norton representation of the lossless transmission line

The values of $I_k(t-\tau)$, $I_m(t-\tau)$ and Z shown in figure 2.19 are given by following equations 2.44 .

$$I_k(t-\tau) = \frac{(1+h)}{2} \left[-\frac{1}{Z} v_m(t-\tau) - i_{m,k}(t-\tau) \right] + \frac{(1-h)}{2} \left[-\frac{1}{Z} v_k(t-\tau) - i_{k,m}(t-\tau) \right]$$

$$I_m(t-\tau) = \frac{(1+h)}{2} \left[-\frac{1}{Z} v_k(t-\tau) - i_{k,m}(t-\tau) \right] + \frac{(1-h)}{2} \left[-\frac{1}{Z} v_m(t-\tau) - i_{m,k}(t-\tau) \right]$$

$$\text{where } h = \frac{Z_c - R/4}{Z_c + R/4}$$

$$Z = Z_c + R/4$$

However, the above expressions are approximate only for a fixed frequency. When a transmission line is transiently disturbed it will oscillate with various frequencies depending on its length and terminating network. The lowest natural frequency of the line and the system usually dominates. Transmission line resistance at its normal steady state frequency and also at its dominating natural frequency can be found if that frequency is known or can be estimated.

In EMTDC, both the above line resistances are used. Low and steady state frequencies are filtered through the transmission line resistance found at steady state frequency. Transient and higher frequencies of oscillation are filtered through the line resistance found at a selected higher frequency [11].

Though this way of representing the transmission line is very simple, the drawback is that it is only accurate for one frequency. All the higher harmonics are assumed to have a higher series resistance than that of the operating frequency. But the higher resistance is assumed as constant for all the higher frequencies.

With proper selection of frequencies for operating frequency and higher frequency, this gives a good representation of transmission line especially for fundamental steady state and transient studies. But for studying the effects of GIC which involve a larger frequency spectrum in the steady state this representation is not sufficient.

2.2.2 MARTI MODEL

The other widely used transmission line model was developed by Marti and was derived using a different approach. To understand, consider a transmission line in the frequency domain, then the voltages and currents at both ends are related as shown in equation 2.45 .

$$V_k = \text{Cosh } \gamma l V_m - Z_c \text{ Sinh } \gamma l I_m \quad (2.45)$$

$$I_k = \frac{1}{Z_c} \text{ Sinh } \gamma l V_m - \text{Cosh } \gamma l I_m$$

$$\text{where } \gamma = \sqrt{Z Y}$$

$$Z_c = \sqrt{\frac{Z}{Y}}$$

$$l = \text{length}$$

The forward and backward propagation functions can be defined as,

$$B_k(\omega) = V_k(\omega) - Z_c I_k(\omega) \quad (2.46)$$

$$B_m(\omega) = V_m(\omega) - Z_c I_m(\omega)$$

$$F_k(\omega) = V_k(\omega) + Z_c I_k(\omega)$$

$$F_m(\omega) = V_m(\omega) + Z_c I_m(\omega)$$

The forward and backward propagation functions can be shown to be related as in equation 2.47 .

$$B_k(\omega) = A_1(\omega) F_m(\omega) \quad (2.47)$$

$$B_m(\omega) = A_1(\omega) F_k(\omega)$$

$$\text{where propagation function } A_1(\omega) = e^{-\gamma l}$$

$F_k(\omega)$ and $F_m(\omega)$ in equation 2.46 can be simplified to

$$F_k(\omega) = V_k(\omega) + E_k(\omega) \quad (2.48)$$

$$F_m(\omega) = V_m(\omega) + E_m(\omega)$$

$$\text{where } E_k(\omega) = I_k(\omega) Z_c(\omega)$$

$$E_m(\omega) = I_m(\omega) Z_c(\omega)$$

Since $Z_c(\omega)$ is the response of a linear network, the time domain representation of equations 2.47 and 2.48 can be found by means of Inverse Fourier Transform, that is,

$$b_k(t) = v_k(t) - e_k(t) = a_1(t) * f_m(t) \quad (2.49)$$

$$b_m(t) = v_m(t) - e_m(t) = a_1(t) * f_k(t)$$

$$\text{where } e_k(t) = z_c(t) * f_k(t)$$

$$e_m(t) = z_c(t) * f_m(t)$$

Equation 2.49 defines the equivalent circuit shown in figure 2.20.



Figure 2.20 : Frequency dependence model in the time domain

The propagation function $a_1(t)$ in the time domain can be expressed as

$$a_1(t) = p(t - \tau) \quad (2.50)$$

where $p(t)$ has the same shape as $a_1(t)$ but displaced τ time units from the origin.

In the frequency domain $A_1(\omega)$ can then be expressed as

$$A_1(\omega) = P(\omega) e^{-j\omega\tau} \quad (2.51)$$

The function $P(\omega)$ can be approximated by rational function of the form

$$P(s) = \sum_{i=1}^{i=m} \frac{k_i}{s + \beta_i} \quad (2.52)$$

Therefore in the time domain $a_1(t)$ becomes

$$a_1(t) = \sum_{i=1}^{i=m} k_i e^{-\beta_i(t-\tau)} \quad (2.53)$$

with $a_I(t)$ in the form given in equation 2.53, and the convolutions in equation 2.49 can be solved by recursive integration methods. Since $a_I(t) = 0$ for $t < \tau$

$$b_k(t) = \int_{\tau}^{\infty} f_m(t-u) a_i(u) du \quad (2.54)$$

Introducing equation 2.53,

$$b_k(t) = \sum_{i=1}^m b_{k,i}(t) \quad (2.55)$$

$$\text{where } b_{k,i}(t) = \int_{\tau}^{\infty} f_m(t-u) k_i e^{-\beta_i(t-\tau)} du$$

The integral in equation 2.55 can be broken into two parts.

$$\begin{aligned} b_{k,i}(t) &= \int_{\tau}^{\tau+\Delta t} f_m(t-u) k_i e^{-\beta_i(t-\tau)} du + \int_{\tau+\Delta t}^{\infty} f_m(t-u) k_i e^{-\beta_i(t-\tau)} du \quad (2.56) \\ &= \int_{\tau}^{\tau+\Delta t} f_m(t-u) k_i e^{-\beta_i(t-\tau)} du + e^{-\beta_i \Delta t} b_{k,i}(t-\Delta t) \end{aligned}$$

The first integral of equation 2.56 can be evaluated numerically using the trapezoidal rule. After some algebraic manipulations it can be shown that,[12]

$$b_k(t) = \sum_{i=1}^m \left[g_i b_{k,i}(t-\Delta t) + c_i f_m(t-\tau) + d_i f_m(t-\tau-\Delta t) \right] \quad (2.57)$$

$$\begin{aligned} \text{where } g_i &= e^{-\beta_i \Delta t} \\ h_i &= \frac{1-g_i}{\beta_i \Delta t} \\ c_i &= \frac{k_i}{\beta_i} (1-h_i) \\ d_i &= -\frac{k_i}{\beta_i} (g_i-h_i) \end{aligned}$$

Similar derivation can be made to solve $b_m(t)$. The solutions of $e_k(t)$ and $e_m(t)$ can be found by using the same approach.

The function $Z_c(\omega)$ can be approximated as,

$$Z_c(s) = k_o + \sum_{i=1}^m \frac{k_i}{s + \alpha_i} \quad (2.58)$$

Using equation 2.58, $e_k(t)$ can be solved as,

$$e_k(t) = R_k i_k(t) + e_{k,e}(t - \Delta t) + e_{k,c}(t - \Delta t) \quad (2.59)$$

$$\text{where } R_k = k_0 + \sum_{i=1}^m p_i$$

$$e_{k,c}(t - \Delta t) = \sum_{i=1}^m q_i i_k(t - \Delta t)$$

$$e_{k,e}(t - \Delta t) = \sum_{i=1}^m m_i e_{k,i}(t - \Delta t)$$

$$m_i = e^{-a_i \Delta t}$$

$$n_i = \frac{1 - m_i}{a_i \Delta t}$$

$$p_i = \frac{k_i}{a_i} (1 - n_i)$$

$$q_i = -\frac{k_i}{a_i} (m_i - n_i)$$

Similarly $e_m(t)$ can be found. From equations 2.57 and 2.59, the equivalent circuit of figure 2.20 can be simplified as shown in figure 2.21.



Figure 2.21 : Equivalent circuit in the time domain

Using elementary circuit transformations, this equivalent circuit can be transformed into the circuit of figure 2.22, which is compatible with electromagnetic transients programs.

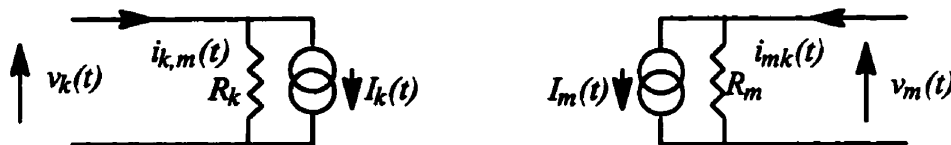


Figure 2.22 : Norton representation of the frequency dependent transmission line

The values of the current sources are given by,

$$i_k(t) = \frac{e_{k,c}(t - \Delta t) + e_{k,e}(t - \Delta t) + b_k(t)}{R_k} \quad (2.60)$$

$$i_m(t) = \frac{e_{m,c}(t - \Delta t) + e_{m,e}(t - \Delta t) + b_m(t)}{R_m}$$

The equivalent circuit in figure 2.22 can be solved by recording the past history values of equation 2.60 .

This method gives a better representation for a wider frequency spectrum and is therefore better for studying the effects of GIC.

2.2.3 MUTUALLY COUPLED TRANSMISSION LINES

So far what we have discussed are transmission lines with one conductor or mode only. Generally transmission lines consist of several mutually coupled phases or conductors. These have to be broken into modes. Each mode can be treated as a single phase transmission line. This method allows mutually coupled transmission lines to be modelled.

This is achieved by transforming the phase quantities to mode quantities using a matrix diagonalization method making each mode independent of other modes. Then the transmission line model is applied to these modes. An inverse transformation is done to convert the modal quantities back to phase quantities for Norton current injection in the electromagnetic transient program.

2.3 SIMULATION OF EARTH SURFACE POTENTIAL

During a GIC event, Earth Surface Potential (ESP) varies at a frequency in the millihertz range. Therefore for normal power frequency considerations, ESP can be treated as a dc voltage. Therefore the ESP effect can be simulated by a dc voltage source connected to the transformer neutral of value such that the injected current reaches the desired value. It should be noted that not only the transformer neutral, but other system

components connected to the ground in the vicinity of the transformer neutral should also be fed with the same magnitude dc voltage source to simulate Geomagnetically Induced Currents. Otherwise dc currents or GIC will circulate within the same subsystem rather than flowing in the transmission line.

It should be noted that the methodology of using ESP as the driving force for GIC is not considered valid today, as it provides accurate results only if the electric field caused by electrojet currents is uniform. This is not the case in reality. However for simulation purposes, the essential feature is to produce a current of particular magnitude by some means or other. Therefore a dc voltage source can be used provided it is chosen to produce the predetermined level of GIC current.

Chapter 3

Validity of the models

3.1 RESPONSE OF THE TRANSFORMER CORE

To investigate how the transformer core model behaves under normal conditions, a simple test system as shown in Figure 3.1 is used.

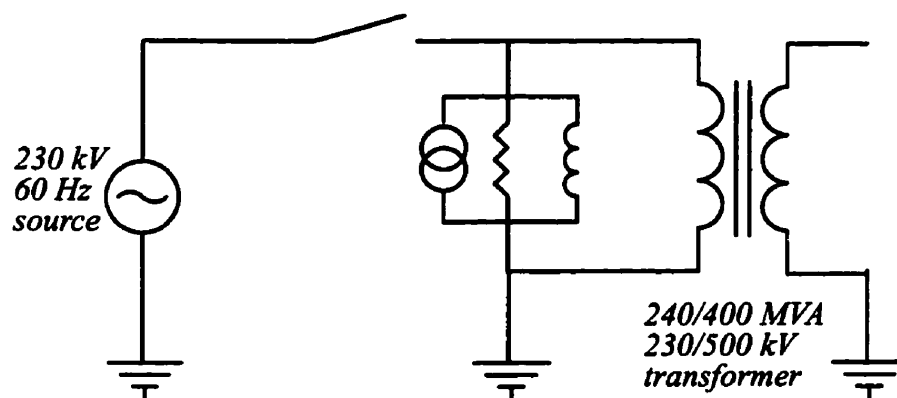


Figure 3.1 : Test system used to investigate the response of the core model

Figure 3.2 shows the magnetizing current of the transformer when it was energized from the 230kV side. Figure 3.3 shows the flux linkage – current loop obtained at this no load condition.

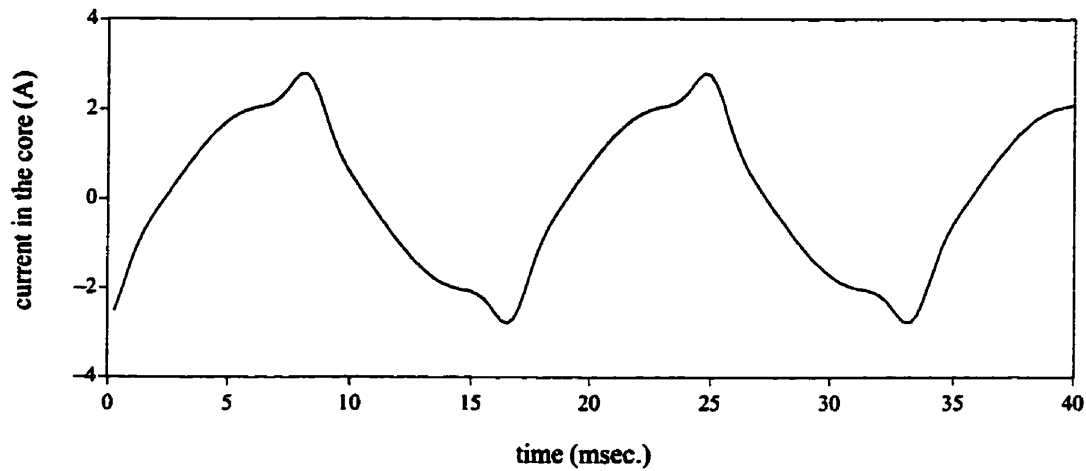


Figure 3 .2 : Transformer core current referred to the 230 kV side at no load conditions

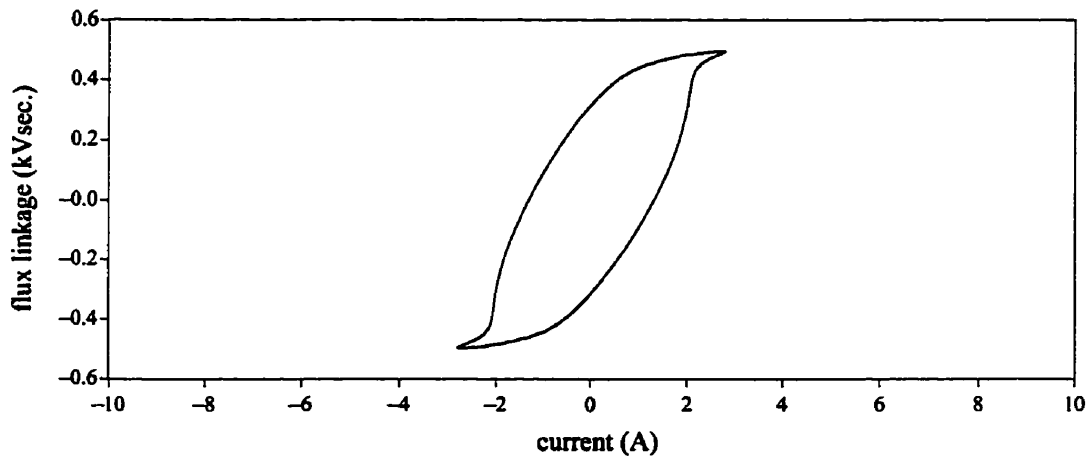


Figure 3 .3 : Flux Linkage – Current loop referred to the 230 kV side during no load condition

Both figures show the typical characteristics of transformer exciting current and flux linkage – current characteristics. Figure 3 .4 show the inrush current experienced by the transformer when it was energized by the 230kV side. This also follows a typical inrush current characteristic.

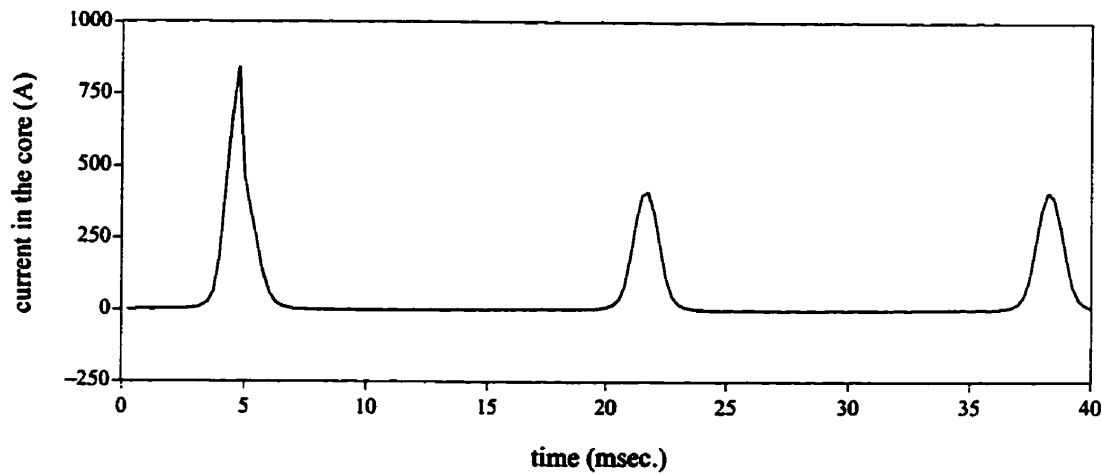


Figure 3 .4 : Transformer core current referred to 230 kV side during energization of the transformer

3.2 INITIAL SIMULATIONS

Test models were developed for eight different transformer configurations. They are namely: star–star and star–delta configurations for three single phase banks, three phase five limb transformers, three phase conventional transformers[19][20] and three phase three limb transformers. Simulations were done for a system as shown in Figure 3 .5 .

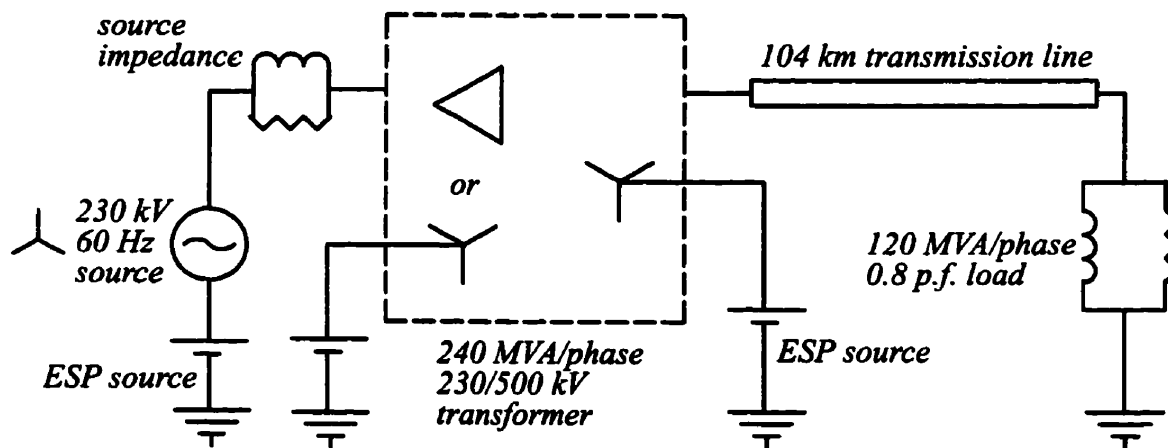


Figure 3 .5 : System used in initial simulations

The test system consists of a 230kV, 60Hz source with an equivalent source impedance represented by a parallel combination of 5.79Ω and 11.3mH feeding a 240MVA

per phase 230/500kV transformer. The 500kV side of the transformer is feeding a 120MVA per phase 0.8 lagging power factor load represented by a parallel combination of a resistor and an inductor. The 500kV side transformer neutral is connected to a dc source which represents Earth Surface Potential applied on the transformer.

The following sections describe how the test models for various transformer configurations behaved under GIC conditions.

3.2.1 DELTA-STAR THREE SINGLE PHASE BANK MODEL

Figure 3.6 shows both 230kV and 500kV side line currents and also 500kV side phase voltage when there is a flow of 100A GIC in the 500kV side neutral. As expected there is half cycle saturation and due to this there is some distortion in the waveforms.

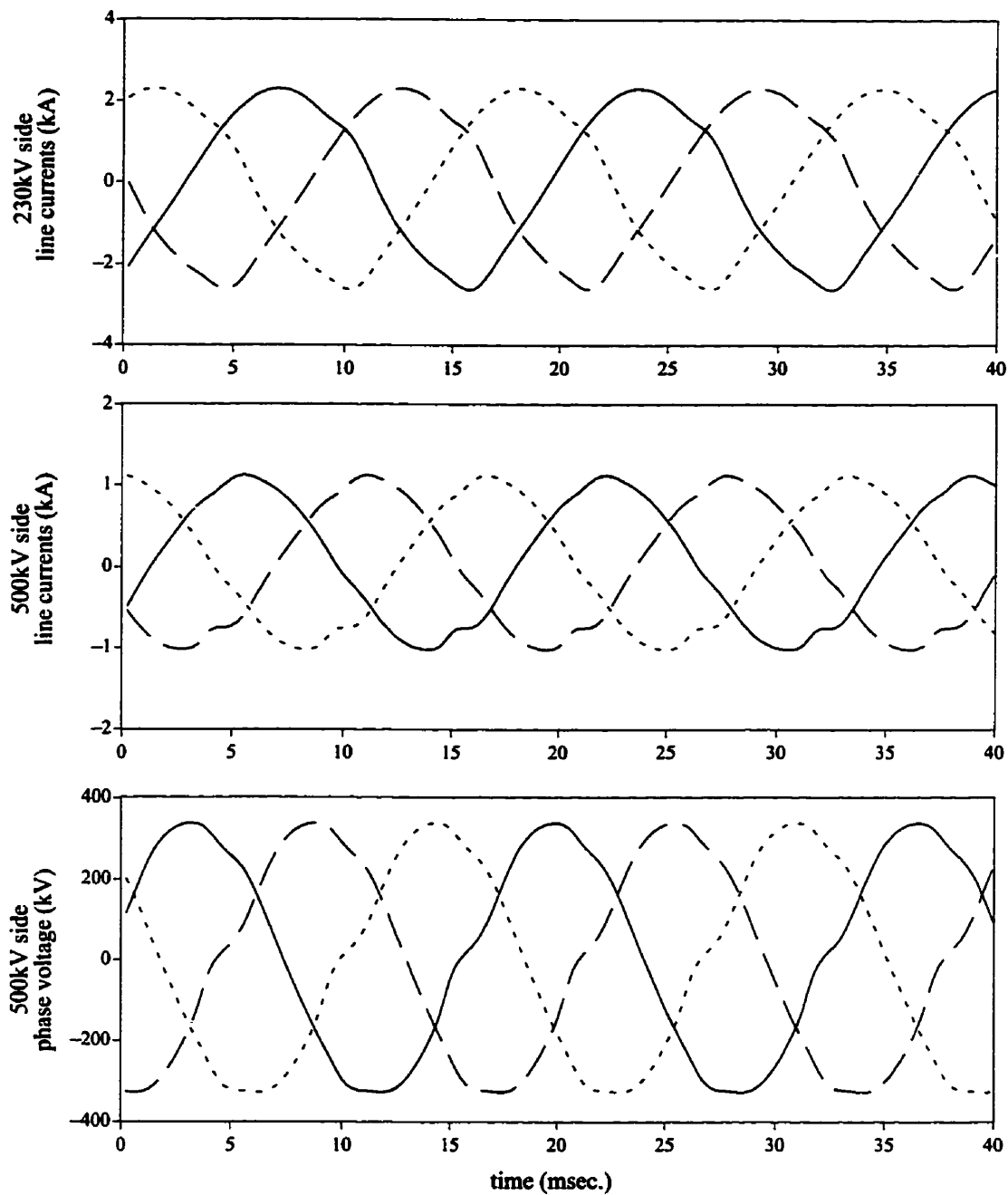


Figure 3 .6 : Line Currents and Phase Voltages in the three single phase bank of delta-star transformer for 100A GIC.

3.2.2 STAR-STAR THREE SINGLE PHASE BANK MODEL

As in the delta-star transformer, the three phase bank of single phase transformers under star-star configuration also gives rise to half cycle saturation under GIC

conditions. Here zero sequence impedances are different than the delta–star configuration and hence the waveforms are different than those obtained for the star–delta case. Figure 3.7 describes how a star–star transformer configured with three single phase banks behaves under 100A of GIC in it's 500kV side neutral.

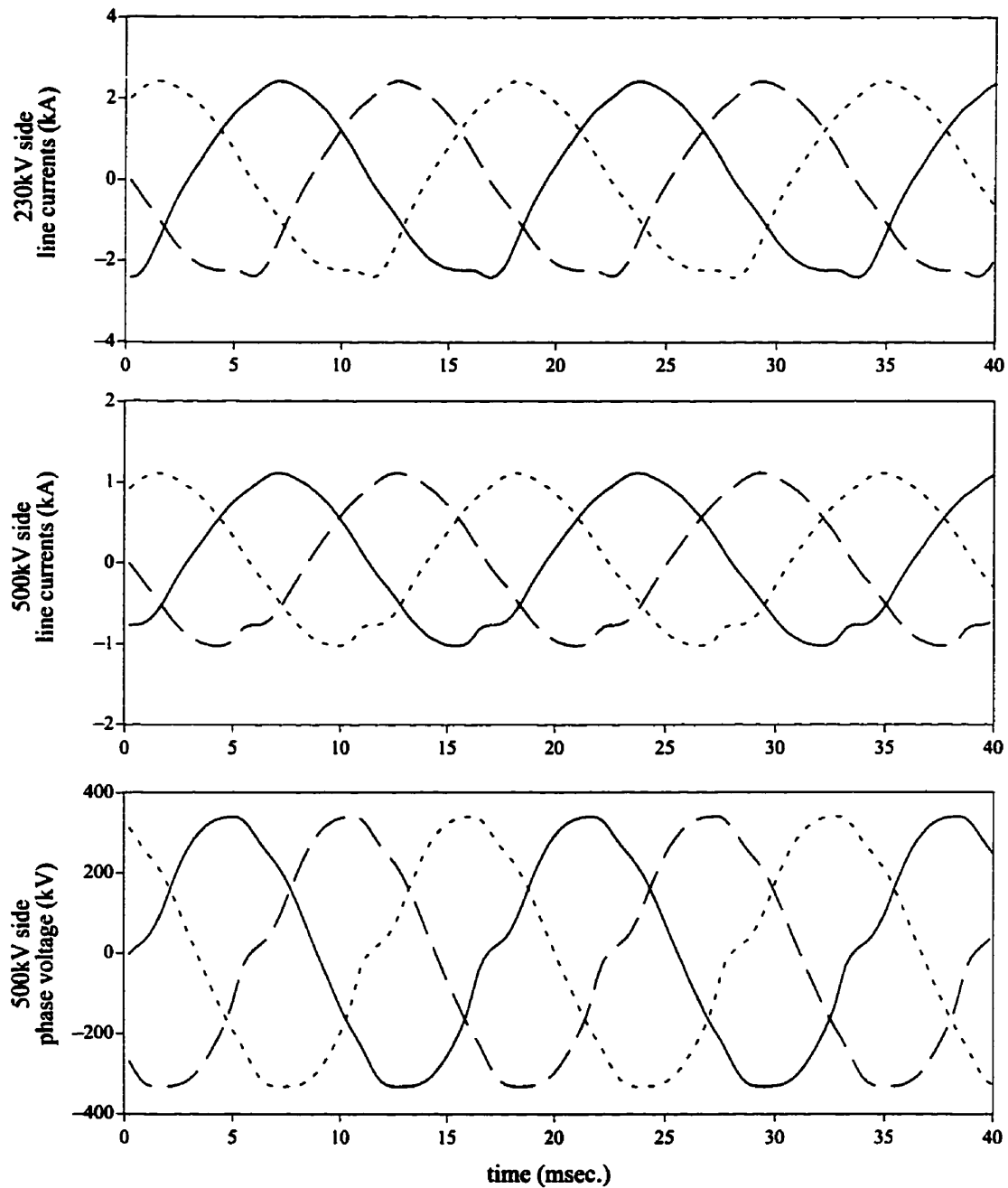


Figure 3.7 : Line Currents and Phase Voltages in the three single phase bank of star–star transformer for 100A GIC.

Figures 3.8 and 3.9 show the harmonic response of the line current on the 500kV side of a single phase bank of a three phase transformer for star–star and delta–star configurations. The harmonics are classified according to their sequence.

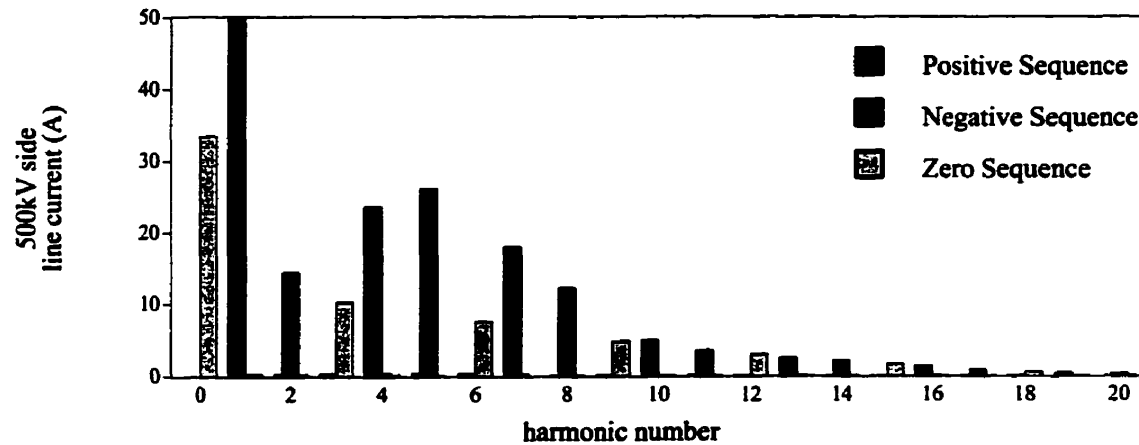


Figure 3.8 : Fourier Analysis of the line current on the 500 kV side of a single phase bank of a 3 phase transformer for star–star configuration

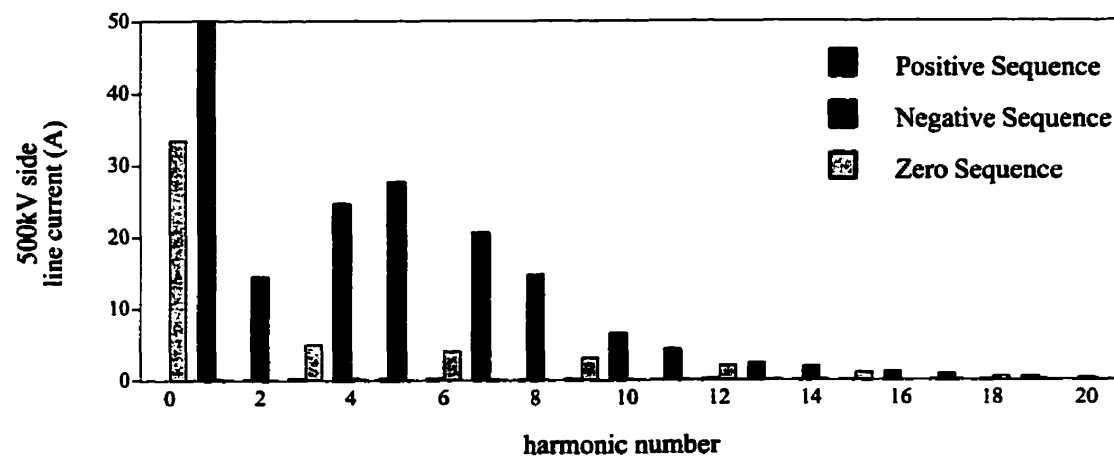


Figure 3.9 : Fourier Analysis of the line current on the 500 kV side of a single phase bank of a 3 phase transformer for delta–star configuration

The waveforms of the three phases are very similar in shape. This is due to the fact that all three phases are subjected to the same saturation behaviour. This is further explained by distribution of harmonics according to their sequence. The harmonic distribution for star–star and delta–star is almost the same except for the zero sequence. The delta–star configuration provides less zero sequence harmonics in the 500kV side due to the

additional path provided by the delta winding. The average total harmonic distortion factor for the preceding waveforms is about 4.6%.

3.2.3 THREE PHASE CONVENTIONAL STAR-STAR TRANSFORMER

Figure 3 .10 shows how a conventional three phase star-star transformer behaves when 100A of GIC flows in its neutral. Line current and Phase voltage of the high voltage side and the line current in the low voltage side are presented in this figure.

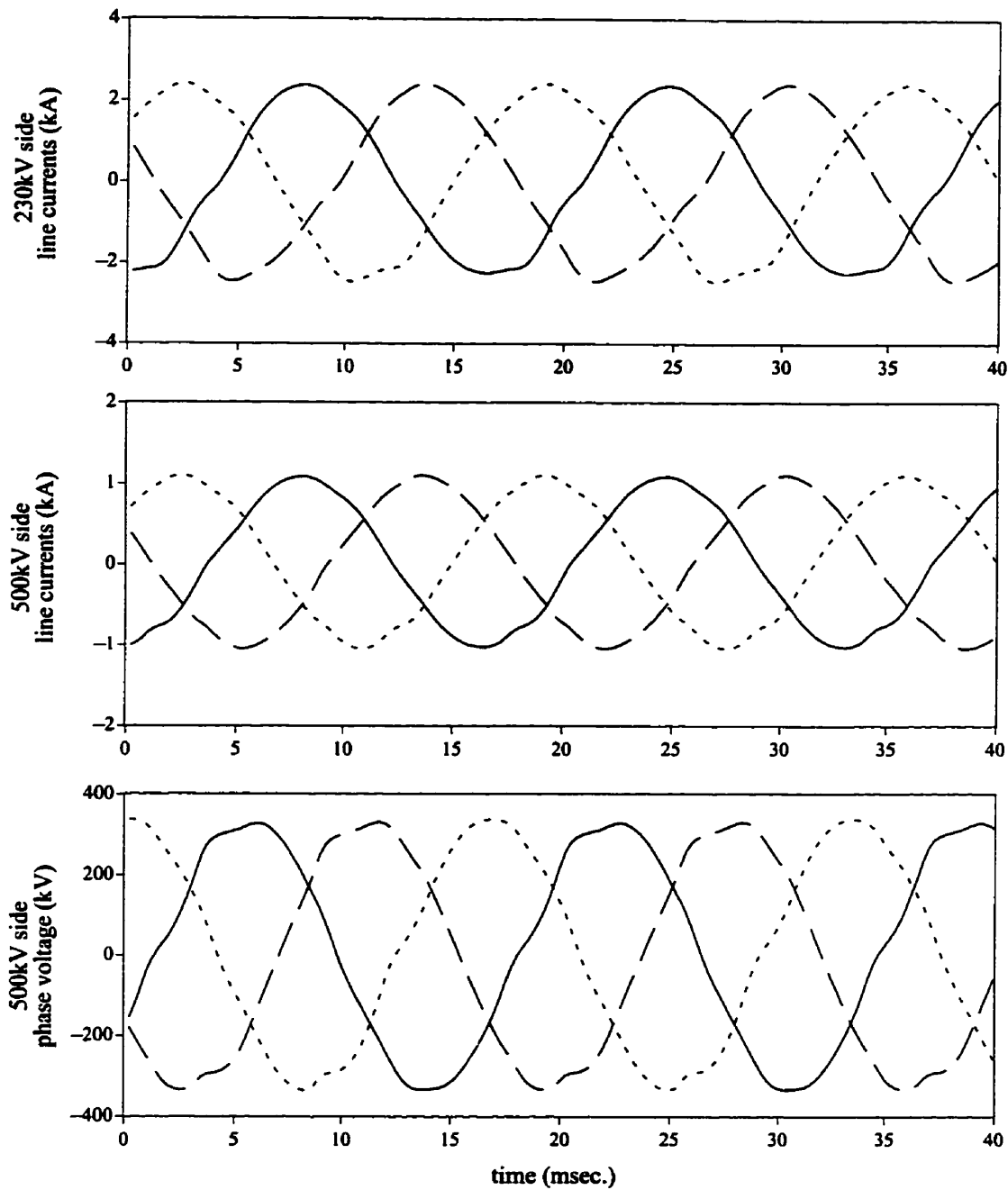


Figure 3 .10 : Line Currents and Phase Voltages in the three phase conventional star–star transformer for 100A GIC.

3.2.4 THREE PHASE CONVENTIONAL DELTA–STAR TRANSFORMER

Figure 3 .11 shows both the 230kV and 500kV side line currents and also the 500kV side phase voltage when there is a flow of 100A GIC in the 500kV side neutral.

As expected there is half cycle saturation and due to this there is some distortion in the waveforms. The delta winding provides an additional path for zero sequence currents and less zero sequence currents appear in the 500kV side line currents.

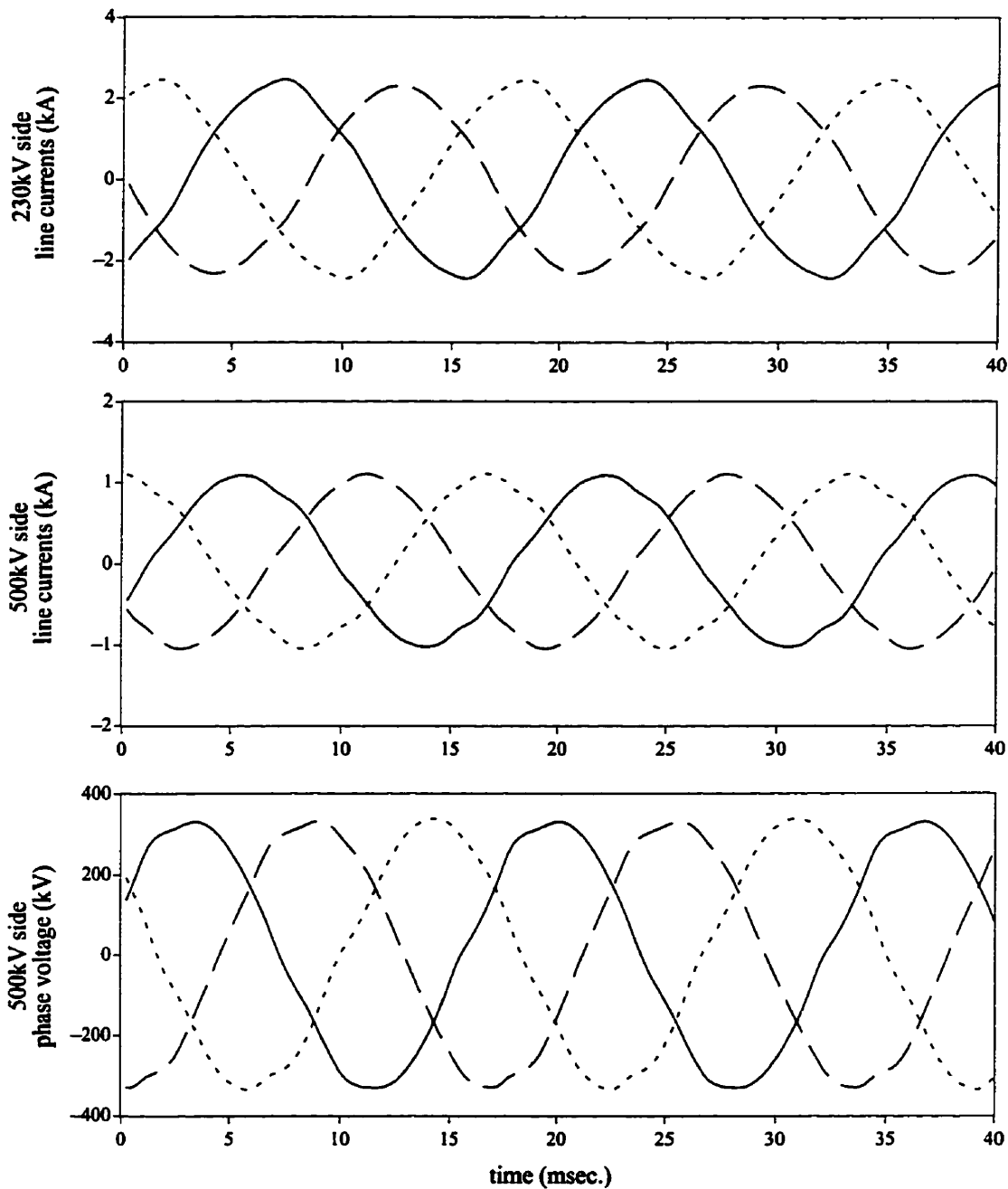


Figure 3 .11 : Line Currents and Phase Voltages in the three phase conventional delta-star transformer for 100A GIC.

Figures 3.12 and 3.13 show the Fourier analysis of the 500kV side line current for a three phase conventional transformer when subjected to a 100A of GIC in its neutral. Fourier analysis is presented for both star-star and delta-star configurations and the analyses are classified according to their sequence components.

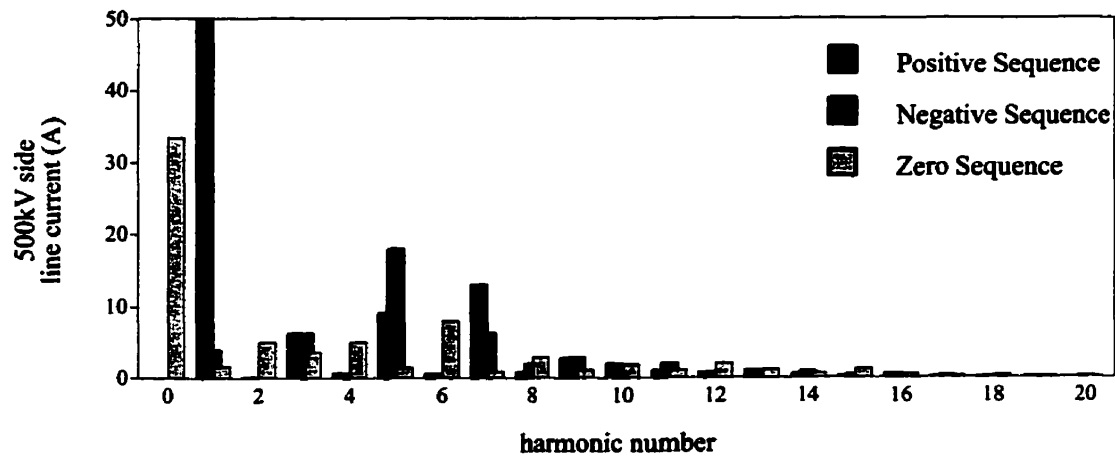


Figure 3.12 : Fourier Analysis of the line current on 500 kV side of a 3 phase conventional star-star transformer

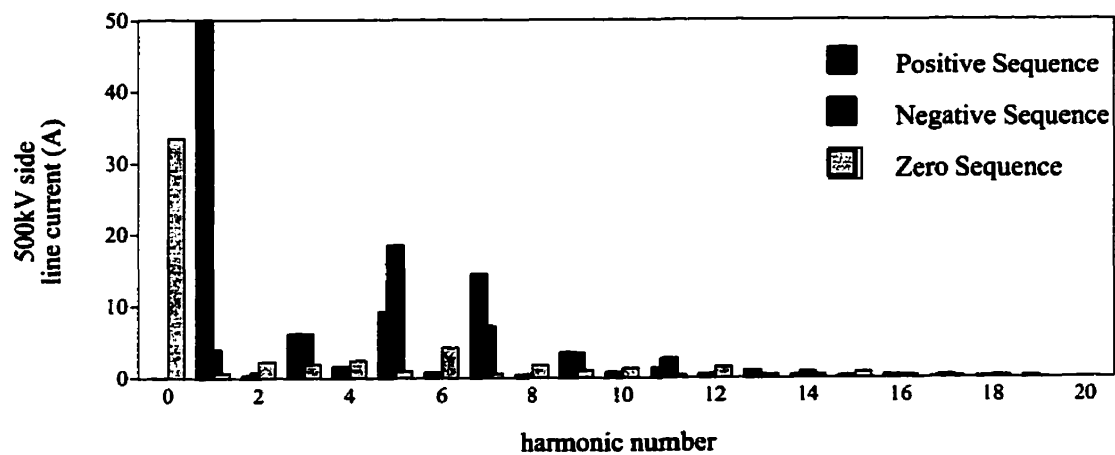


Figure 3.13 : Fourier Analysis of the line current on 500 kV side of a three phase delta-star conventional transformer

Unlike in the previous case of a three phase transformer made of single phase transformer units, this provides non-traditional sequences of harmonic components. For example there is a considerable amount of negative sequence fundamental, third harmonic and seventh harmonic components. This is due to the fact that the effect of the saturation of

the limbs in the transformer core on individual phases is not the same. The average total harmonic distortion factor for the above two cases is 2.84%.

3.2.5 THREE PHASE FIVE LIMB STAR-STAR TRANSFORMER

Figure 3 .14 shows how a five limb three phase star-star transformer behaves when 100A of GIC flows in its neutral. Line current and Phase voltage of the high voltage side and the line current in the low voltage side are presented in this figure.

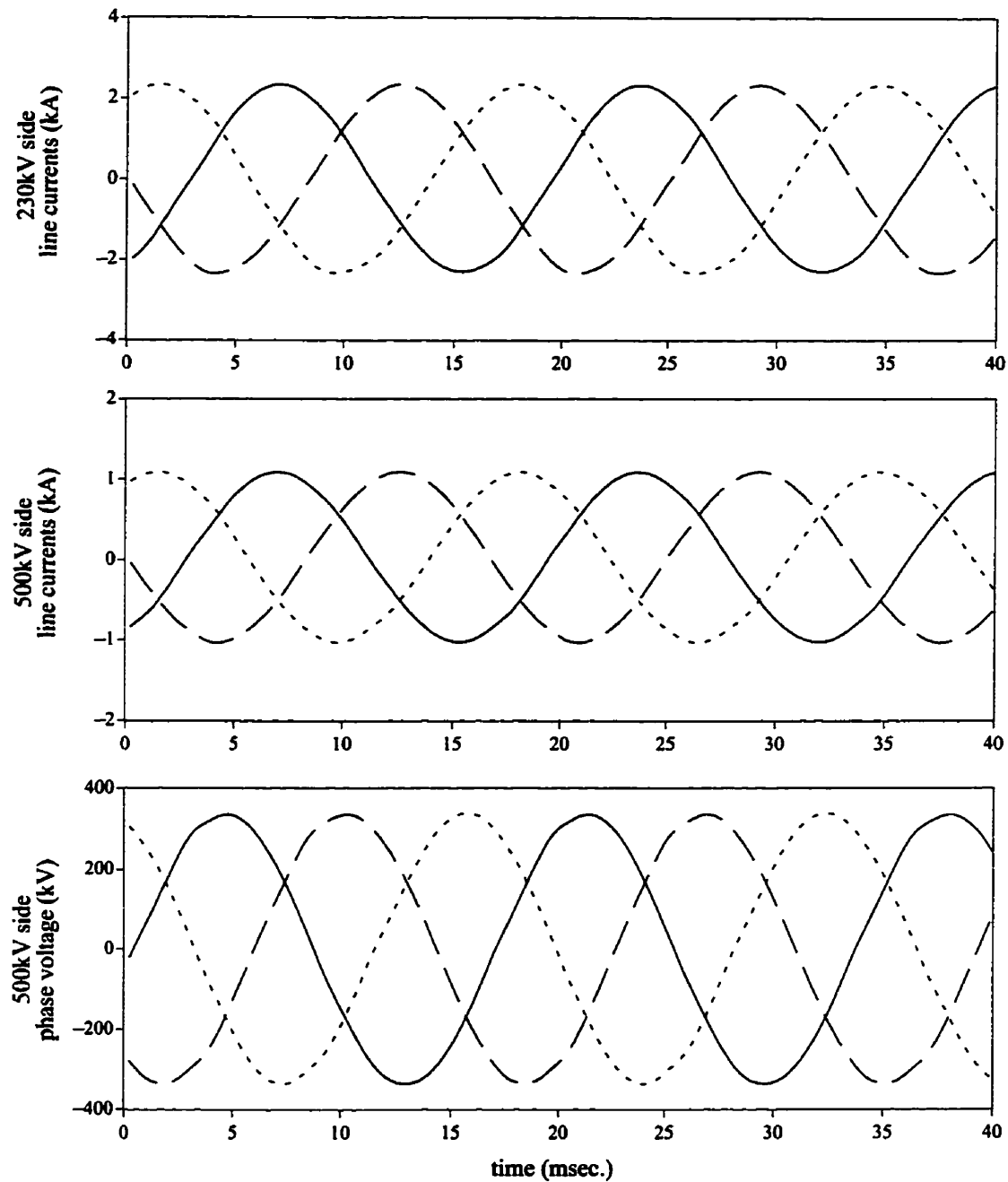


Figure 3 .14 : Line Currents and Phase Voltages in the three phase five limb star-star transformer for 100A GIC

3.2.6 THREE PHASE FIVE LIMB DELTA-STAR TRANSFORMER

Figure 3 .15 shows both the 230kV and 500kV side line currents and also the 500kV side phase voltage when there is a flow of 100A GIC in the 500kV side neutral.

As expected there is half cycle saturation and due to this there is some distortion in the waveforms. The delta winding provides an additional path for zero sequence currents and less zero sequence current appears in the 500kV side line currents.

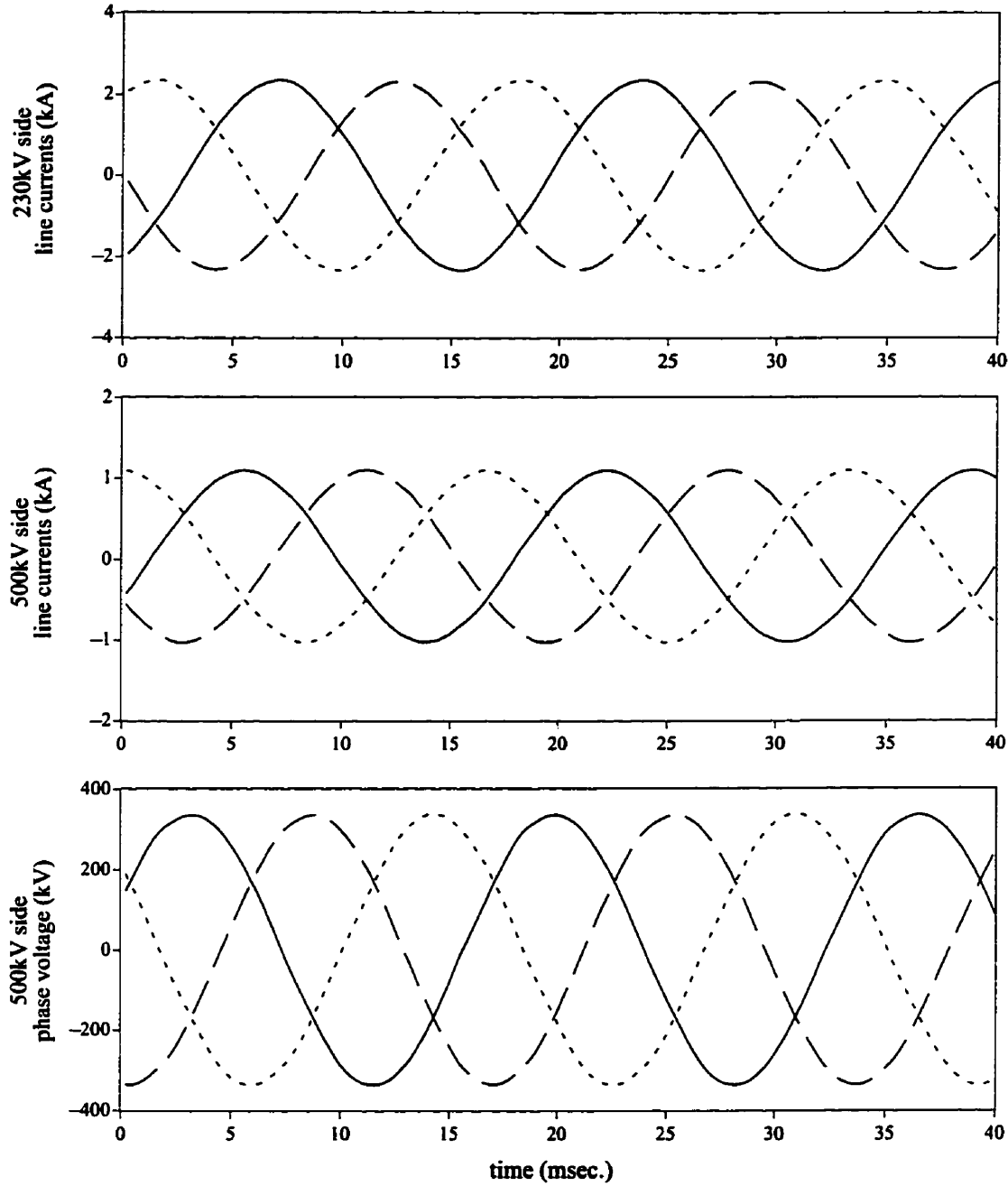


Figure 3 .15 : Line Currents and Phase Voltages in the three phase five limb delta-star transformer for 100A GIC.

Figures 3.16 and 3.17 show the Fourier analysis of the 500kV side line current for a three phase conventional transformer when subjected to 100A of GIC in its neutral. Fourier analysis is presented for both star–star and delta–star configurations and the analyses are classified according to their sequence components.

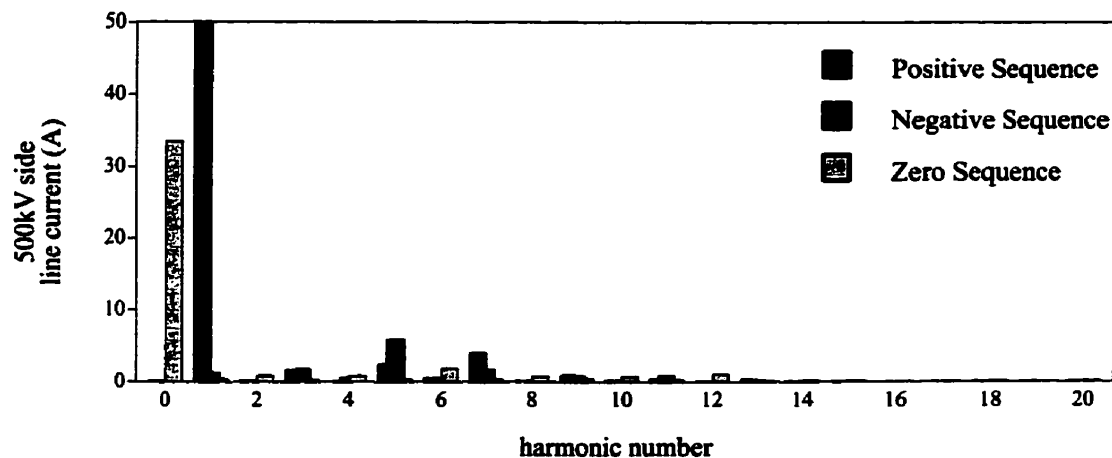


Figure 3.16 : Fourier Analysis of the line current on 500 kV side of a three phase five limb star–star transformer

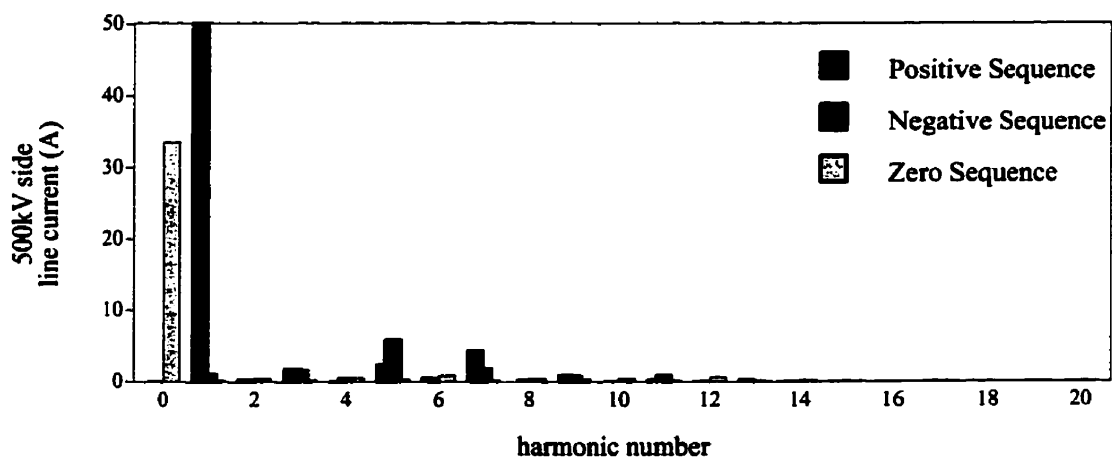


Figure 3.17 : Fourier Analysis of the line current on 500 kV side of a three phase five limb delta–star transformer

Unlike the previous case of a three phase transformer consisting of single phase transformer units, this provides non–traditional sequences of harmonic components. For example there is a considerable amount of positive sequence fifth and third harmonic components. This is due to the fact that the effect of the saturation of the limbs in the

transformer core on individual phases is not the same. The average total harmonic distortion factor for the above two cases is 0.84%.

3.2.7 THREE PHASE THREE LIMB STAR-STAR TRANSFORMER

Figure 3.18 shows how a three limb three phase star-star transformer behaves when 100A of GIC flows in its neutral. Line current and Phase voltage of the high voltage side and the line current in the low voltage side are presented in this figure. As expected there is no half cycle saturation due to the non existence of a low reluctance flux path for zero sequence flux.

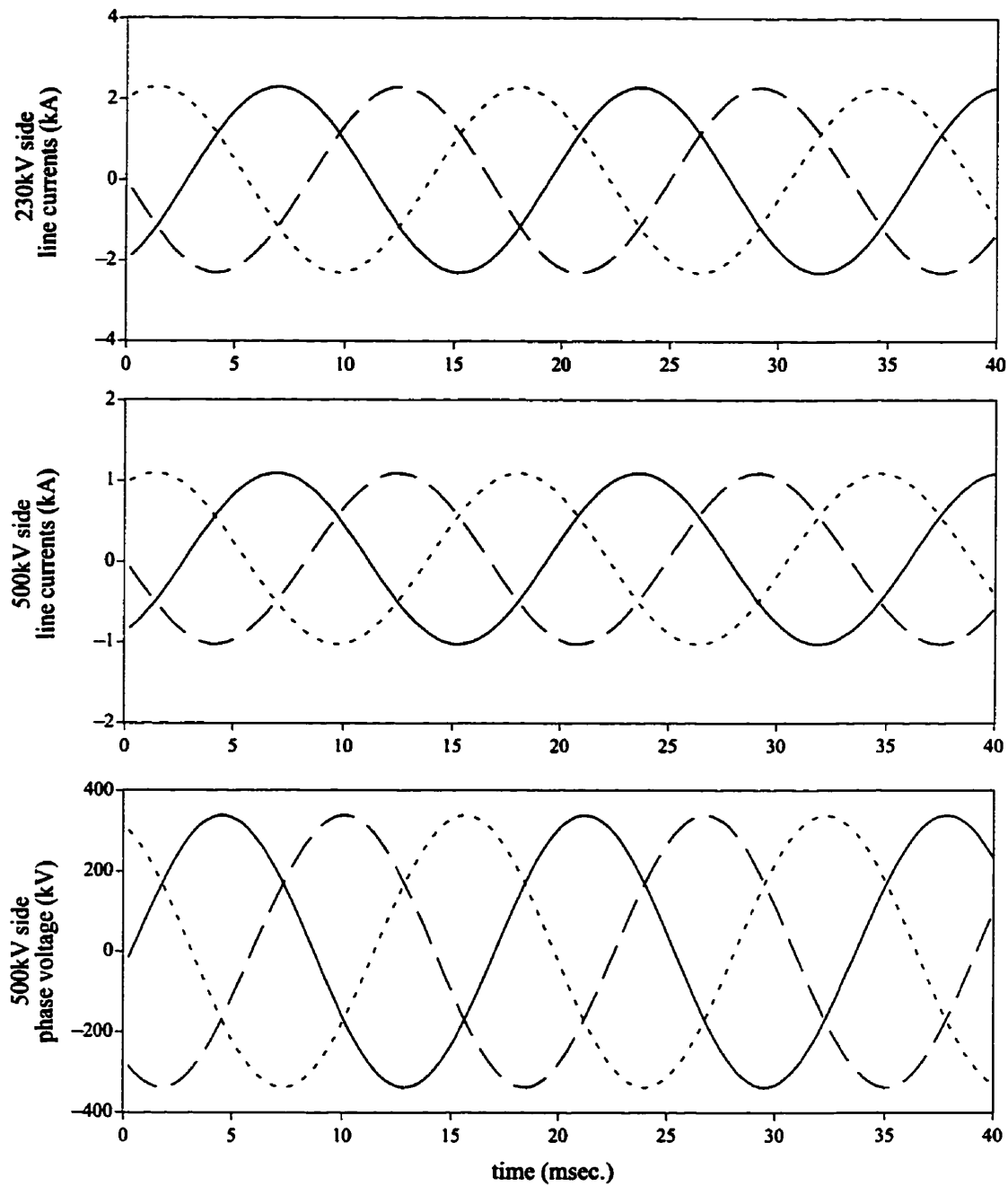


Figure 3 .18 : Line Currents and Phase Voltages in the three phase three limb star–star transformer for 100A GIC.

3.2.8 THREE PHASE THREE LIMB DELTA–STAR TRANSFORMER

Figure 3 .19 shows both the 230kV and 500kV side line currents and also the 500kV side phase voltage when there is a flow of 100A GIC in the 500kV side neutral.

As expected there is no half cycle saturation due to the non existence of low reluctance flux path for zero sequence flux.

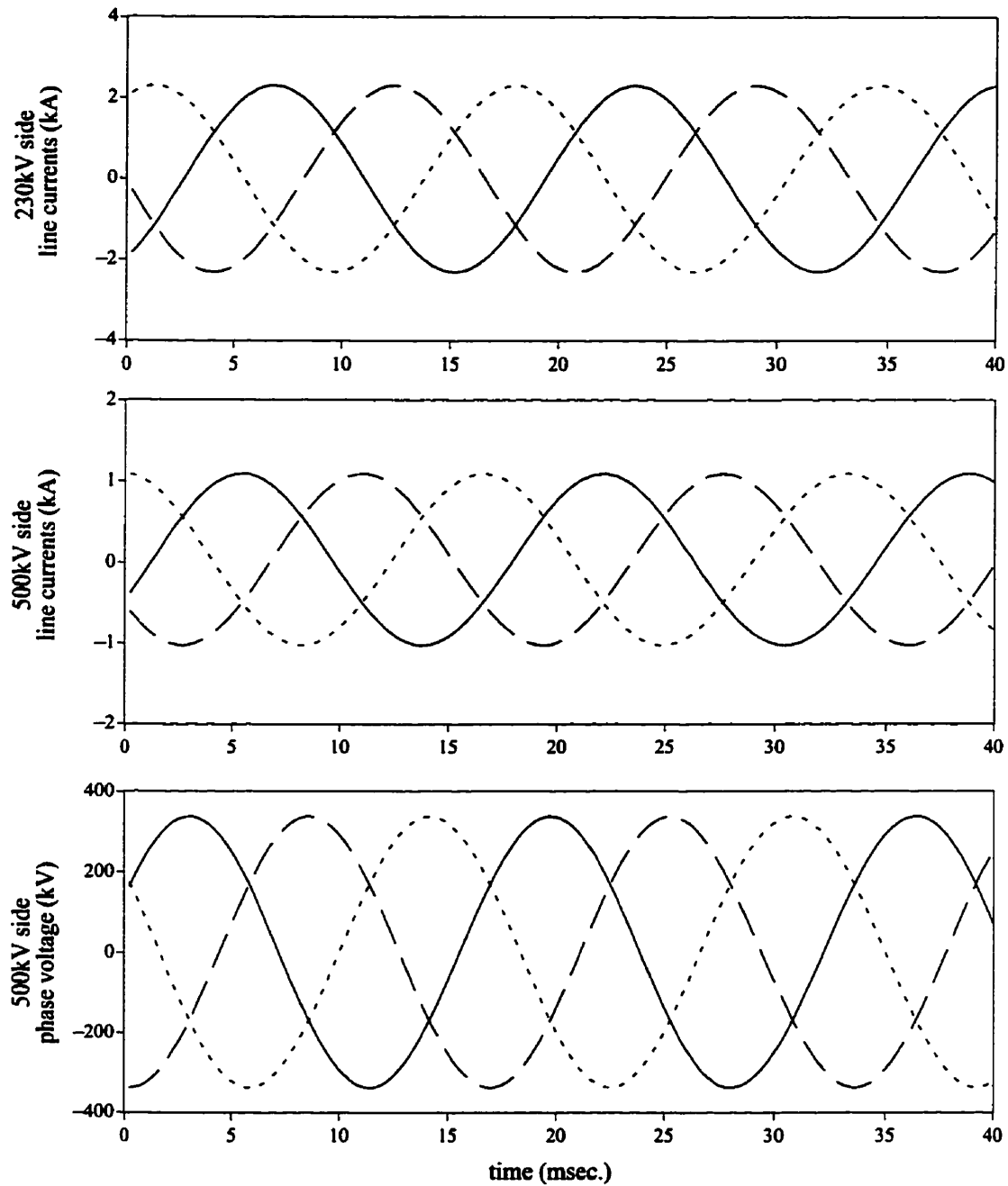


Figure 3 .19 : Line Currents and Phase Voltages in the three phase three limb delta-star transformer for 100A GIC.

Figures 3 .20 and 3 .21 show the Fourier analysis of the 500kV side line current for a three phase conventional transformer when subjected to a 100A of GIC in its

neutral. Fourier analysis is presented for both star–star and delta–star configurations and the analyses are classified according to their sequence components.

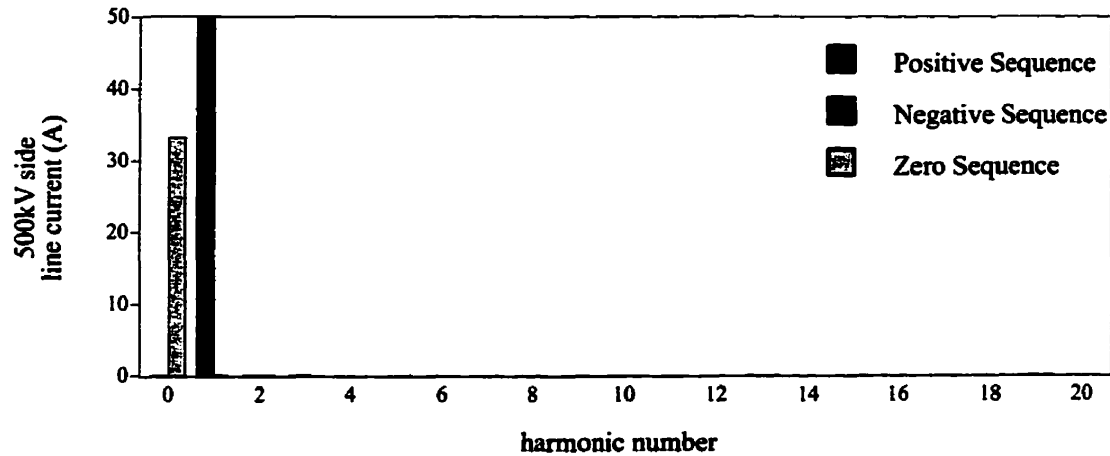


Figure 3 .20 : Fourier Analysis of the line current on 500 kV side of a three phase three limb star–star transformer

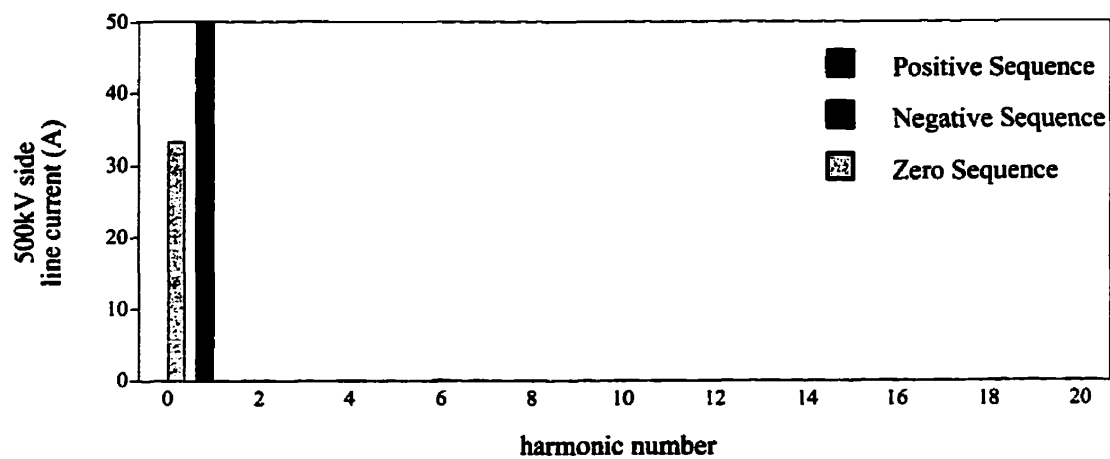


Figure 3 .21 : Fourier Analysis of the line current on 500 kV side of a three phase three limb star–star transformer

Since there is no saturation due to the zero sequence GIC applied, the transformers do not get saturated. The harmonic analysis of the current waveform shows that it does not contain any harmonics.

3.3 COMPARISON WITH RECORDED EVENTS

To prove the validity of the model, it is necessary to compare the recorded waveforms with simulated waveforms for the same conditions. Two sets of recordings with significant distortion are chosen for this purpose.

The recordings were taken at the 500kV substation at Dorsey. This 500 kV transmission line system connects three utility companies; Manitoba Hydro, Northern States Power and Minnesota Power. The recordings were taken at the 500kV side of the 720/1200 MVA transformer. A detailed description of the 500 kV transmission line system is provided in the following chapter. A single line diagram of the system is shown in figure 4.1 .

3.3.1 EVENT ON SEPTEMBER 10, 1992

On the 10th of September 1992 the recently installed Sunburst recorder[21] at the Dorsey substation took a snapshot of the 500kV line voltage and current of the secondary side of the current and voltage transformers. The time of the recording was 03.26 GMT and the corresponding GIC in the transformer neutral was 45A. The power flow out of Dorsey was 102.5 MW and -147.5 MVar. Figures 3.22 and 3.23 show the recorded and simulated waveforms of line currents in the 500 kV side respectively.

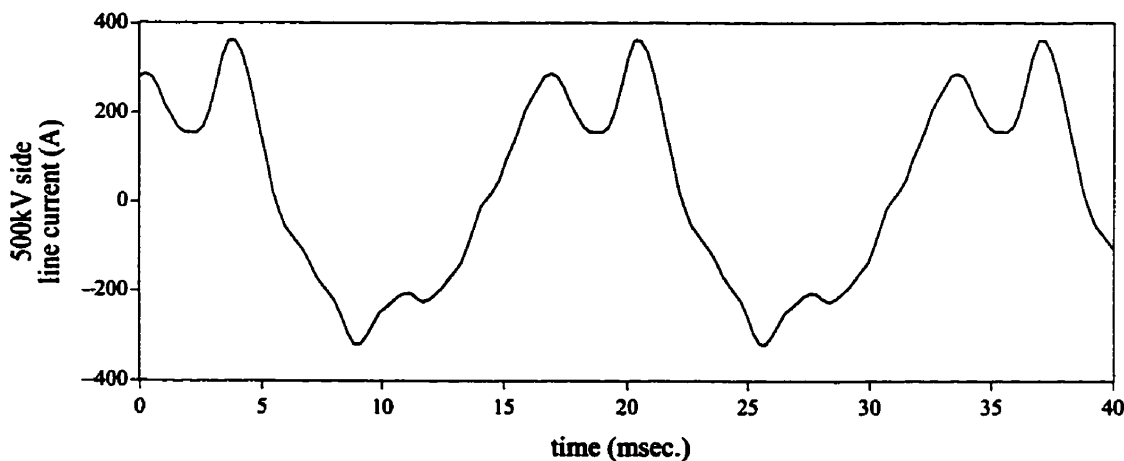


Figure 3.22 : Recorded line current on 500 kV side at Dorsey

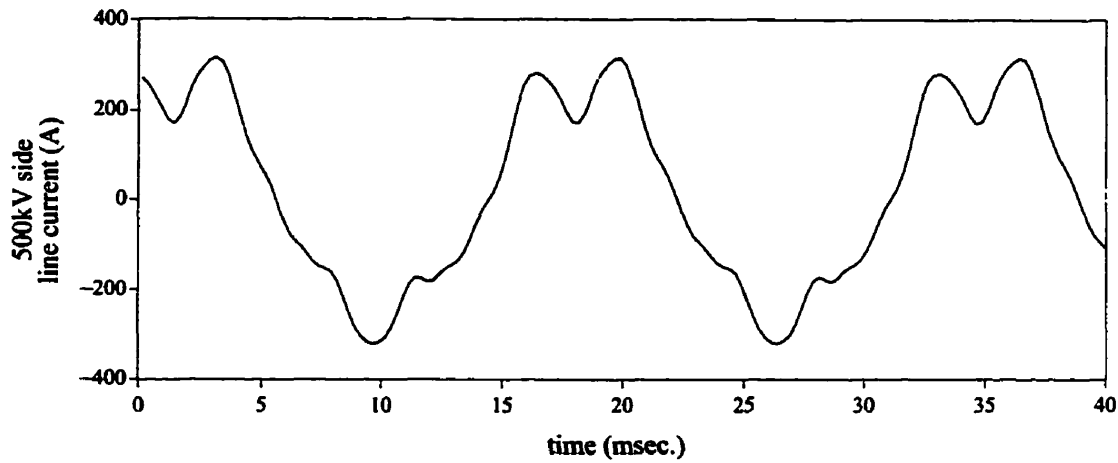


Figure 3 .23 : Simulated line current on 500 kV side at Dorsey

The analysis of the recorded line current shows that it has a peak-to-peak magnitude of 681.2 A with an absolute maximum peak of 361.8 A. It also has a fundamental component of 284.1 A peak with a total harmonic distortion factor of 31.5 %. Similar analysis on the simulated waveform shows that it has a peak-to-peak magnitude of 628.2A with an absolute maximum peak of 319.8 A. It also has a fundamental component of 277.8A with a total harmonic distortion factor of 24.3 %.

The basic shapes of the two waveforms are similar with two peaks in the upper half of the wave, the second larger than the first, and a single peak followed by a ripple in the lower half cycle.

The corresponding voltage waveforms are presented next with Figure 3 .24 showing the recorded waveforms and Figure 3 .25 showing the simulated waveform of the 500 kV side.

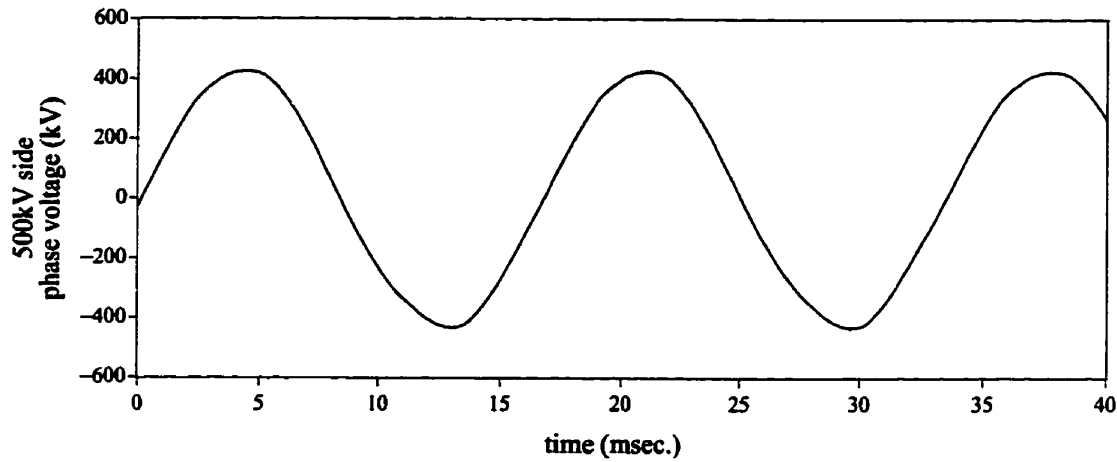


Figure 3 .24 : Recorded voltage waveform on 500 kV side at Dorsey

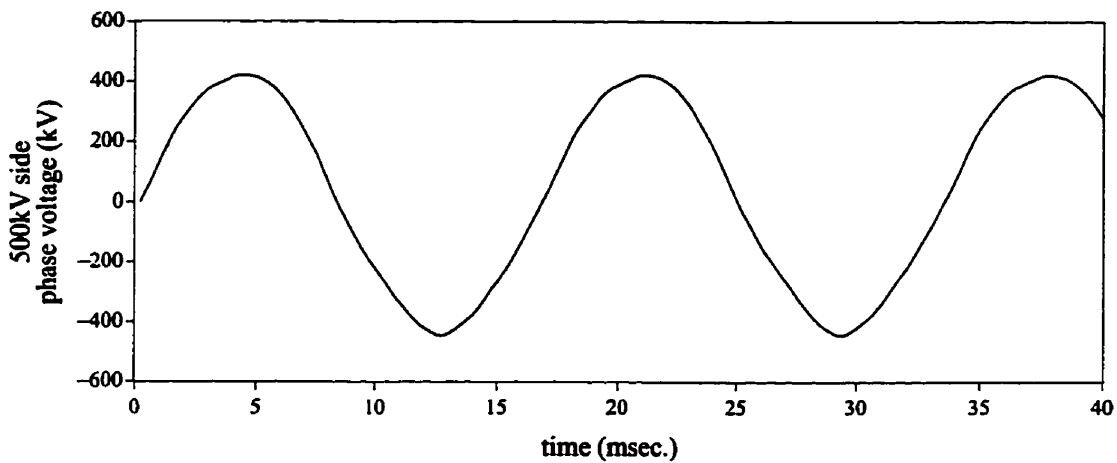


Figure 3 .25 : Simulated voltage waveform on 500 kV side at Dorsey

The voltage waveforms have very little distortion due to the low harmonic impedance of the Dorsey source. In fact, the harmonic distortion factor is only 2.9% for both voltage waveforms. The recorded waveform has a peak-to-peak magnitude of 860.4 kV with an absolute maximum peak of 433.2 kV. It also has a fundamental component with a peak of 429.4 kV . The corresponding figures for the simulated waveform are 869.5 kV, 445.9 kV and 429.8 kV respectively.

3.3.2 EVENT ON OCTOBER 5, 1993

On the 5th of October 1993 the Sunburst recorder at the Dorsey substation took a snapshot of the 500kV line voltage and current of the secondary side of the current and voltage transformers. The time of the recording was 04.59 GMT and the corresponding GIC in the transformer neutral was 30A. The power flow out of Dorsey was -53.2 MW and -137.1 MVar. The power flow out of Forbes was -100.1 MW and -34.8 MVar. Figures 3.26 and 3.27 show the recorded and simulated waveforms of line currents in the 500 kV side respectively.

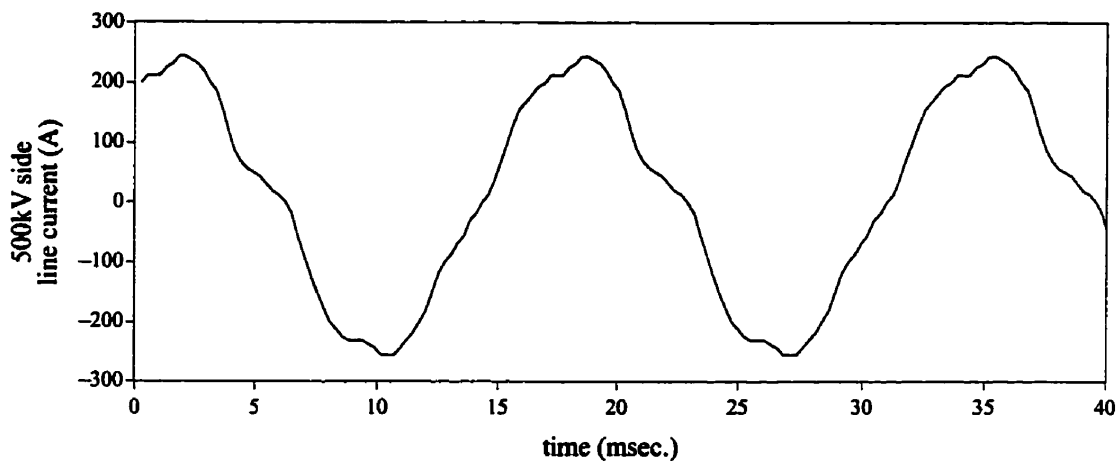


Figure 3.26 : Recorded line current on 500 kV side

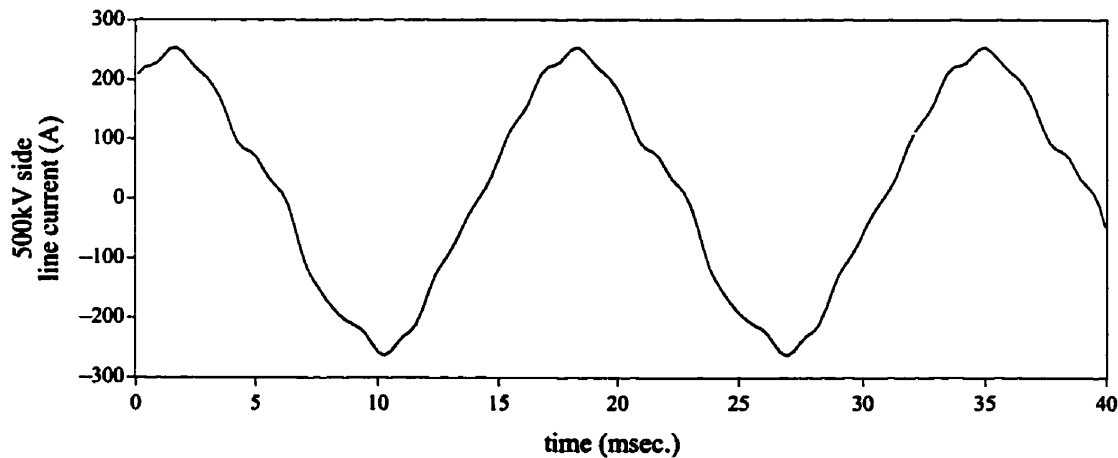


Figure 3.27 : Simulated line current on 500 kV side

The peak-to-peak magnitude of the recorded current waveform is 492.4A with an absolute maximum of 247.9A whereas the corresponding values for the simulated waveform are 514.5A and 259.4A respectively. The recorded waveform has a rms value of 167.87A with a fundamental rms component of 167.16A whereas the simulated waveform has a rms value of 167.58A with a fundamental rms component of 166.95A. The total harmonic distortion factors of the recorded and the simulated waveforms are 9.26% and 8.59% respectively.

The harmonic analysis of the two waveforms are shown in the Figure 3.28. The harmonic composition of the two waveforms are more or less the same. The significant differences are shown only in the 3rd and 5th harmonics. The 3rd harmonic in the simulated waveform is more than that of the recorded waveform and the 5th harmonic in the simulated waveform is less than that of the recorded waveform.

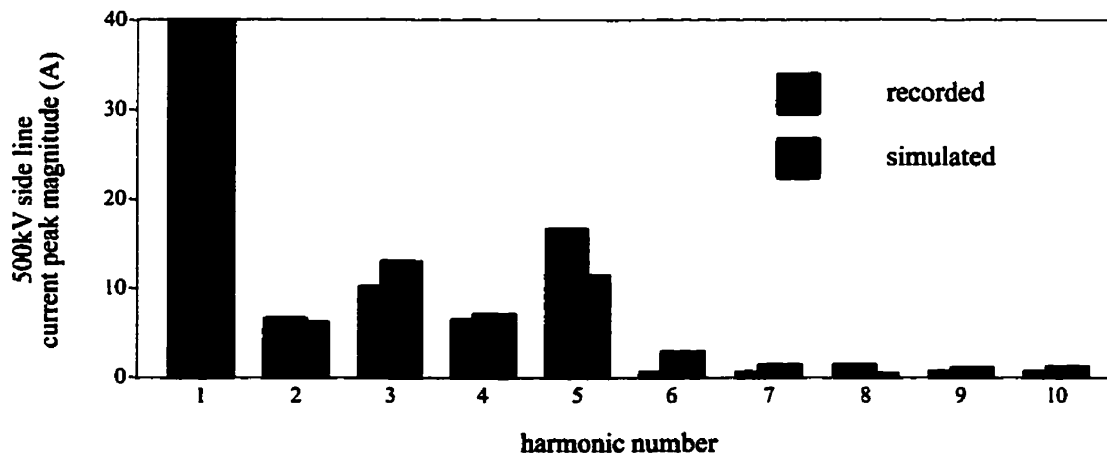


Figure 3.28 : Harmonic composition of recorded and simulated current waveforms

The voltage waveforms associated with the waveforms are not presented here since they are more or less harmonic free as in the case described in the previous subsection 3.3.1.

3.4 CONCLUSIONS

3.4.1 SUSCEPTIBILITY OF DIFFERENT TRANSFORMER CONFIGURATIONS TO GIC

Looking at the Fourier analysis of the waveforms obtained for different transformer configurations, susceptibility of transformers to GIC can be listed in the following descending order.

1. Single phase transformers
2. Three phase shell form conventional transformers
3. Three phase five limb transformers
4. Three phase three limb transformers

This observation agrees with the experimental results obtained by Takasu et. al. [22] and Kappenman [23]. A theoretical analysis done by McNutt [20] also agrees with this observation.

3.4.2 DIFFERENCES IN RECORDED AND SIMULATED WAVEFORMS

The differences between the recorded and simulated waveforms can be attributed to several reasons. The ESP difference between Forbes and Chisago was assumed to be zero since there was no information to decide otherwise. The other unknown was the history of the GIC current at Dorsey. The history is important since the bias flux in the transformer builds up very slowly when the d.c. current in the windings is held constant. Apart from making it impossible to know the exact state of the bias when given the GIC value at any given instant, this slow build up results in very long times for empty simulations before the steady state is reached. Simulation runs are usually accelerated towards the steady state by some means and in the present case this is achieved by starting the runs with a remanent flux in the same direction as the bias.

Given a more precise information about the conditions at the time of recordings, the ESP distribution and with perhaps more detail of the source at Dorsey converter station, it is probable that the simulation could be improved still further. Nonetheless it was decided to proceed with the present model to investigate numerous other system currents and voltages.

Chapter 4

Dorsey–Forbes–Chisago 500kV system

4.1 DESCRIPTION OF THE SYSTEM

This 500kV transmission line system connects three utility companies as shown in Figure 4.1. The northern section of the system is 528km long and it connects Manitoba Hydro's Dorsey HVDC Converter station to Northern States Power's Forbes substation. The southern section of the system is 220km long and it connects Forbes substation to Minnesota Power's Chisago substation.

Three phase shunt reactors with sizes 225 MVars, 300 MVars and 150 MVars are installed in the Dorsey, Forbes and Chisago substations respectively. Neutral reactors with sizes 425 Ω , 325 Ω and 1250 Ω are located in Dorsey, Forbes and Chisago respectively. The Dorsey–Forbes section is transposed at 4 locations and Forbes–Chisago section is transposed at 3 locations along the route.

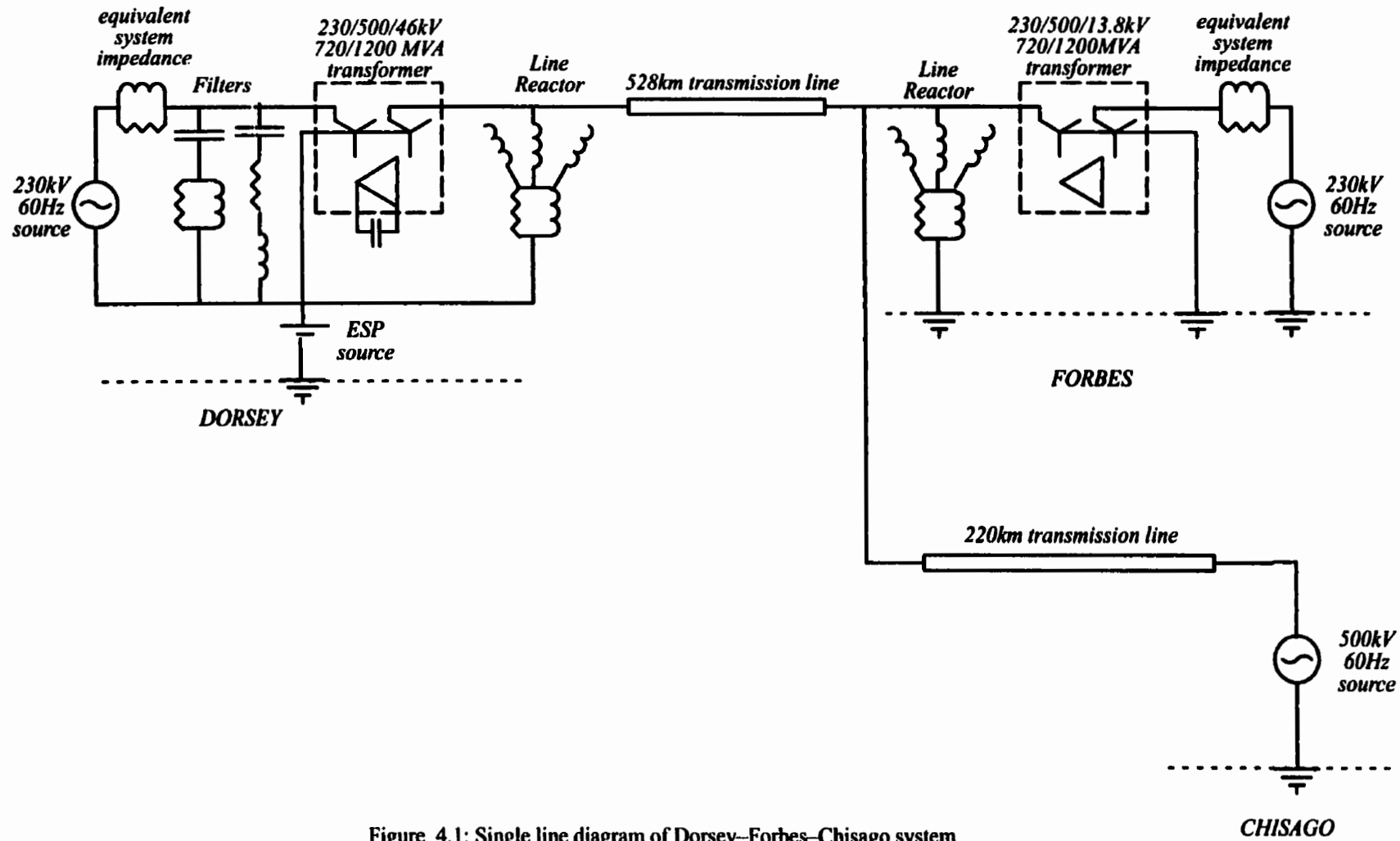


Figure 4.1: Single line diagram of Dorsey-Forbes-Chisago system

The auto-transformer at Dorsey consists of three single phase units and each separate unit is a two winding transformer. The windings are connected to form a 230/500/46kV three phase unit with the 230kV and 500kV windings connected as an auto-transformer. The 230kV and 500kV windings are star connected and grounded whereas the 46kV winding is connected as a delta winding. The transformer is rated for 720MVA without cooling and 1200MVA with cooling. The auto-transformer at Forbes is a similar one with the exception that the tertiary winding is rated for only 13.8kV.

In the Dorsey Substation, filters are connected on the 230kV side to minimize the harmonics introduced by the HVDC converter station. There is also a delta connected bank of capacitors of 15.3 μ F each connected to the 46kV tertiary winding. For the simulations, an Earth Surface Potential is applied between Dorsey and Forbes forcing a GIC current to go into the transformer neutral at Dorsey and to go through the northern section of the transmission line finally leaving the system at Forbes transformer neutral.

Several assumptions were made in the modelling, sometimes due to lack of data and sometimes to make the system simpler. The Chisago subsystem is represented as a 500kV source with an internal inductance, though in reality transformers and reactors are present. It is assumed further that the transformer at Forbes follows the same saturation characteristics as that of the Dorsey transformer.

It was assumed that the ESP difference between Forbes and Chisago is negligible compared with that between Dorsey and Forbes. The northern section of the 500 kV line is closer to the north pole giving rise to higher ESP gradient than the southern section. Furthermore the northern section runs in NW-SE direction whereas the southern section runs mainly in N-S direction thus giving less ESP gradient in the southern section than the northern section. The geographical layout of the transmission line is given in Figure 4.2 .[24]

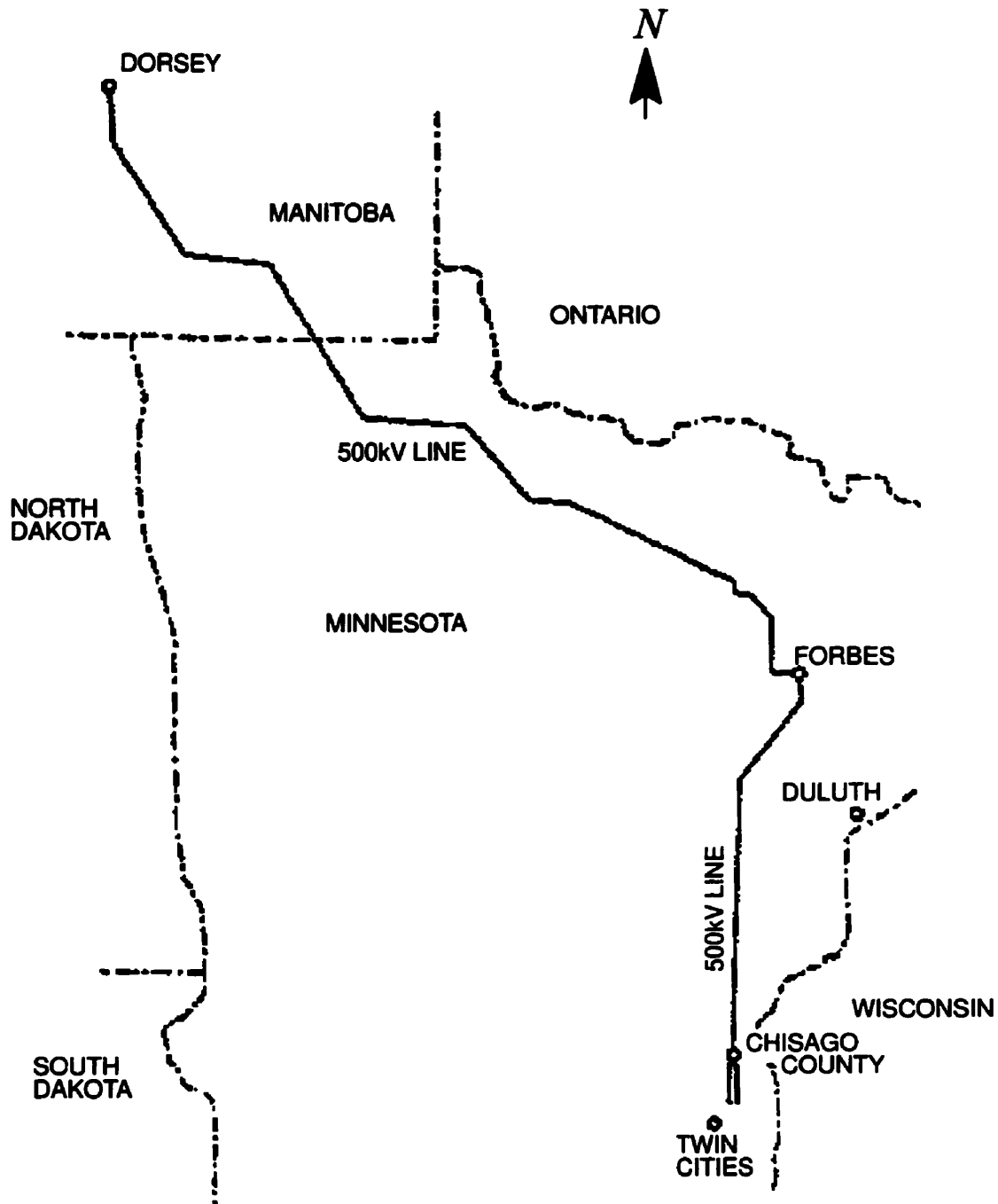


Figure 4 .2 : Geographical layout of the 500 kV transmission line

4.2 WORST CASE SCENARIO

The maximum recorded GIC flow for the Dorsey–Forbes line was 105 A per phase at the Dorsey end [25][26]. This occurred in 1982 before the Sunburst recorder was

installed and no waveform recordings are available for this event. The predicted maximum GIC flow for this line is 223 A per phase on the 500 kV side at Dorsey [25].

4.3 SIMULATIONS AT DIFFERENT CONDITIONS

For this presentation, two GIC levels are chosen; one at the recorded maximum GIC level, and one typical level below the maximum recorded. Occasionally another GIC level which is more than the recorded maximum but less than the maximum predicted was also chosen for some comparisons.

These simulations are carried out for two different power flow conditions; one is a typically high power flow and the other a relatively low power flow. These pre-GIC power flows are described in the tables 4 .1 and 4 .2 respectively.

Table 4 .1 : Pre-GIC system conditions for high power flow study – 500kV side

	DORSEY	FORBES	CHISAGO
Voltage (kV)	521.4	503.1	506.1
Angle (degrees)	0.0	-39.8	-51.5
current (A)	1209.0	397.1	796.4
Active Power (MW)	1062.0	-280.7	-698.1
Reactive Power (MVar)	251.4	202.9	-6.2

Table 4 .2 : Pre-GIC system conditions for low power flow study – 500kV side

	DORSEY	FORBES	CHISAGO
Voltage (kV)	534.4	519.8	506.4
Angle (degrees)	0.0	-0.76	0.98
Current (A)	96.6	192.2	299.4
Active Power (MW)	39.0	-110.7	107.5
Reactive Power (MVar)	-80.5	-133.0	-239.5

The voltage and current waveforms at the 500 kV side for the two different power flow conditions selected are presented in this chapter. The corresponding system quantities at the 230 kV side are presented in appendix B and follow a similar pattern.

4.3.1 A TYPICAL HIGH POWER FLOW

Two simulations are presented here with the typical high power flow conditions described in table 4.1. The GIC flows are taken as 50 A per phase and 105 A per phase (which is the maximum recorded).

When the transformers at both ends were saturated due to the applied ESP, the system conditions changed to that shown in Table 4.3 assuming that the sources were kept constant. The fundamental components of the voltage and the current, relative phase of the fundamental component of the voltage and the active and reactive power produced by fundamental components are given in the table.

Table 4.3 : System conditions after saturation for high power flow

	50A GIC			105A GIC		
	DORSEY	FORBES	CHISAGO	DORSEY	FORBES	CHISAGO
Voltage (kV)	515.7	497.9	503.9	509.7	491.9	501.6
Angle (degrees)	0.0	-40.0	-51.8	0.0	-40.2	-52.0
current (A)	1200.0	376.7	789.7	1190.0	355.7	782.3
Active Power (MW)	1043.0	-271.5	-689.0	1022.0	-262.4	-678.3
Reactive Power (MVar)	249.0	178.3	17.75	246.1	151.8	42.8

There is an increased reactive power demand from the transformers due to the saturation. At 50A GIC condition, the voltages at Dorsey, Forbes and Chisago dropped by 1.1%, 1.0% and 0.4% respectively due to the increased reactive power demand. The voltage drops were increased to 2.2%, 2.2% and 0.9% when the GIC flow was increased to 105A.

There are a number of definitions in use for reactive power during distorted conditions [27]. Emmanuel recommends separate treatment of fundamental and harmonic reactive power [28]. A definition of reactive power limited to the fundamental frequency positive sequence voltage and current components has a distinct advantage in effective application of the reactive power relationships discussed in this study. Because only fundamental currents have significant impact on the system voltage profile, the narrow definition is used here. Also this definition is consistent with the analysis tools used by the utility industry [27].

The net reactive power consumed at the Dorsey end by the transformers and tertiary capacitors combined is increased by 64.2 MVar at 50 A GIC per phase and it further increased to 128.3 MVar when the GIC level was increased to 105 A as described in the Table 4.4.

Table 4.4 : Reactive Power Flow at Dorsey for high power flow

	230kV side	500kV side	Net consumed
Before saturation	331.6	251.4	80.2
low GIC	393.4	249.0	144.4
maximum recorded GIC	454.6	246.1	208.5

It can be observed that the active power flow is dropped due to the drop in the voltages. Active power flowing out of Dorsey dropped by about 1.8% at low GIC conditions due to the change in magnitudes of the voltages. The active power flow drop increased to 3.8% at maximum recorded GIC conditions.

4.3.1.1 WAVEFORMS IN 500KV SIDE

Figure 4.3 shows the simulated voltage waveforms on the 500kV side of the Dorsey transformer when the transformers at Dorsey and Chisago were fully saturated due to the GIC currents of 50 A and 105 A.

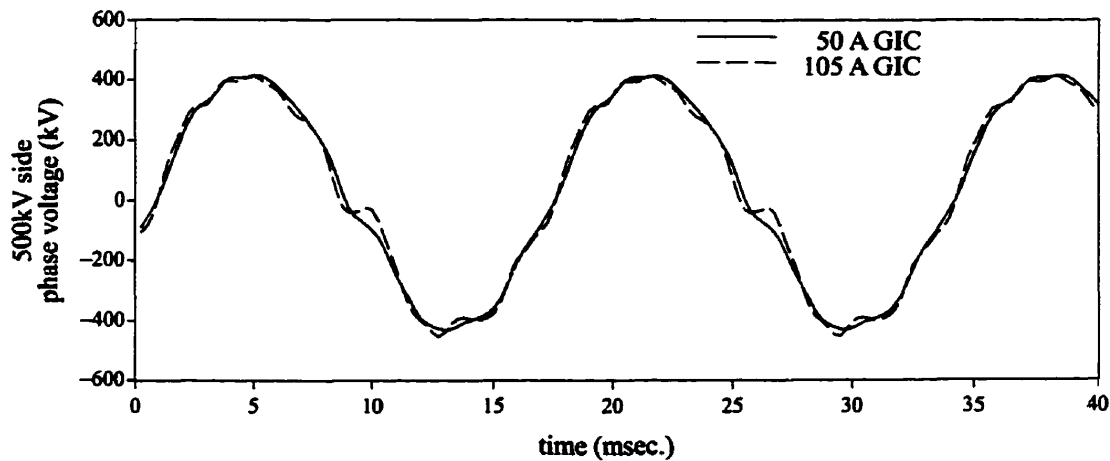


Figure 4.3 : Voltage waveforms on 500 kV side of Dorsey at high power flow

The rms magnitude, the maximum and the minimum peaks of the voltage waveforms are given in table 4.5. The Fourier analysis of these waveforms is shown in Figure 4.4.

Table 4.5 : Details on the 500kV side phase voltage

	50A GIC	105A GIC
rms magnitude (kV)	298.7	297.1
maximum peak (kV)	415.7	416.1
minimum peak (kV)	-431.0	-452.7

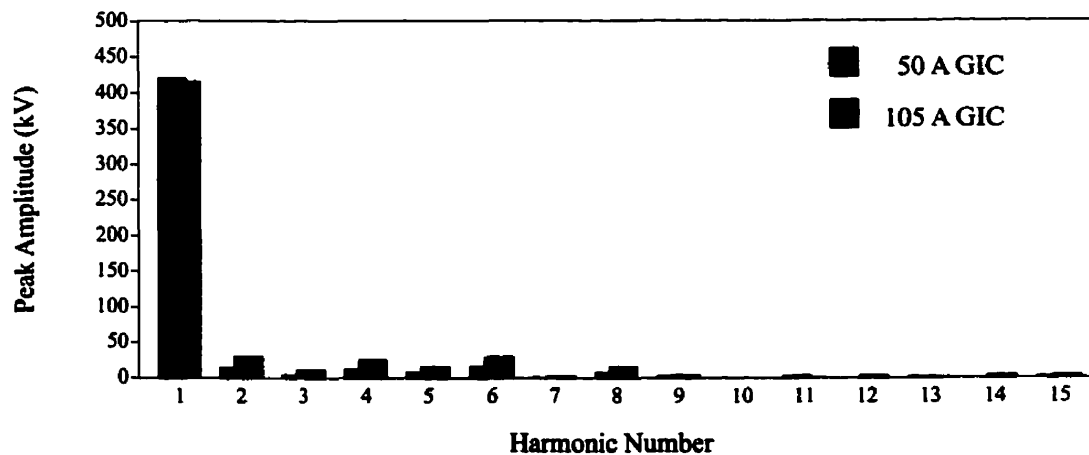


Figure 4.4 : Fourier analysis of 500 kV voltage waveforms at high power flow

The most prominent harmonic component is the 6th followed by the 2nd and 4th. The waveform has a total harmonic distortion factor of 6.56% at 50A per phase GIC and 13.13% at 105 A per phase GIC.

Figure 4.5 shows the corresponding current waveforms in the 500kV side when the transformers at both ends are saturated due to the applied 50A per phase GIC and 105 A per phase GIC.

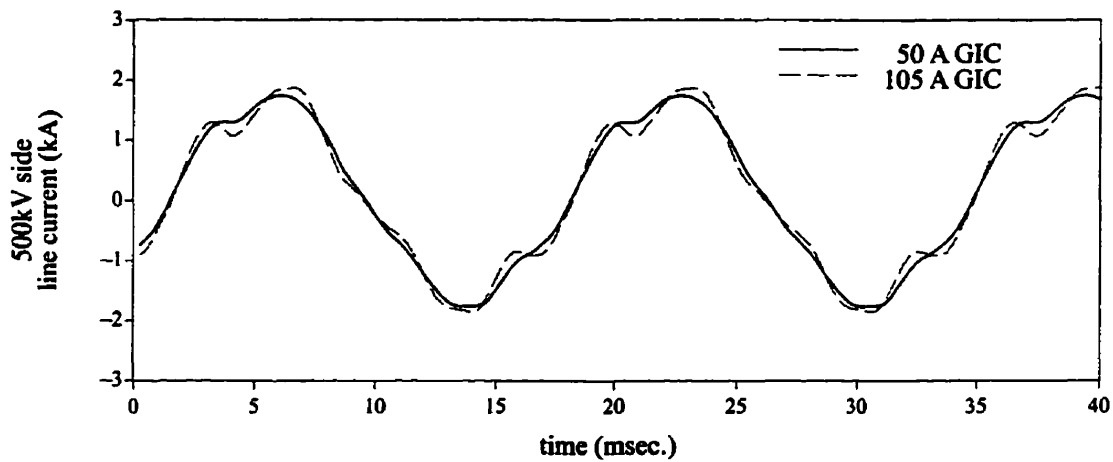


Figure 4.5 : Current waveforms on 500 kV side of Dorsey at high power flow

The details of the current waveforms such as rms magnitude, maximum and minimum peaks are given in table 4.6. The Fourier analysis of the waveforms is shown in Figure 4.6.

Table 4.6 : Details on the 500kV side line current

	50A GIC	105A GIC
rms magnitude (A)	1204.5	1209.8
maximum peak (A)	1750.0	1871.0
minimum peak (A)	-1770.0	-1861.0

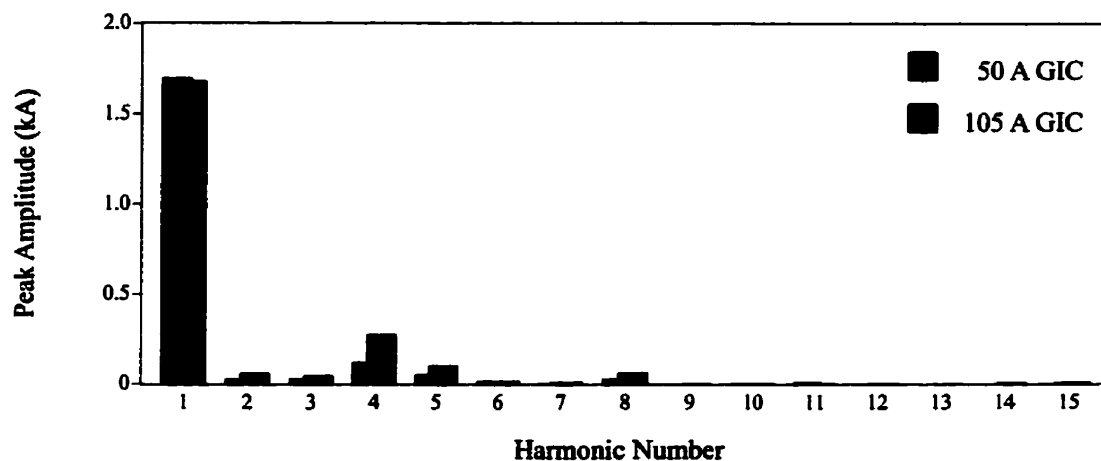


Figure 4 .6 : Fourier analysis of 500 kV current waveforms at high power flow

The most prominent harmonic component is the 4th followed by the 5th. The waveforms obtained for 50 A per phase GIC and 105 A per phase GIC have a total harmonic distortion factor of 8.36% and 18.27% respectively.

4.3.2 A TYPICAL LOW POWER FLOW

Two simulations are presented here with the typical low power flow conditions described in table 4.2 . The GIC flows are taken as 50 A per phase or 150A in the transformer neutral and 105 A per phase or 315A in the transformer neutral which is the maximum recorded.

When the transformers at both ends were saturated due to the applied ESP, the system conditions changed to that shown in Table 4.7 assuming that the sources were kept constant.

Table 4 .7 : System conditions after saturation for high power flow

	50A GIC			105A GIC		
	DORSEY	FORBES	CHISAGO	DORSEY	FORBES	CHISAGO
Voltage (kV)	528.4	514.3	504.1	521.6	507.7	501.5
Angle (degrees)	0.0	-0.78	0.95	0.0	-0.74	1.02
current (A)	96.8	210.1	274.6	95.2	234.2	248.0
Active Power (MW)	38.7	-110.0	106.4	36.7	-110.8	108.3
Reactive Power (MVar)	-79.7	-151.4	-214.9	-77.8	-173.5	-186.3

There is an increased reactive power demand from the transformers due to the saturation. At 50A GIC, the voltages at Dorsey, Forbes and Chisago dropped by 1.1%, 1.0% and 0.5% respectively due to the increased reactive power demand. The voltages were further dropped by 2.4%, 2.3% and 1.0% when the GIC flow was increased to 105A.

The net reactive power consumed at the Dorsey end by the transformers and capacitors in the tertiary winding is increased by 62.0 MVar at 50 A per phase GIC and it further increased to 124.6 MVar when the GIC level was increased to 105 A per phase as described in the Table 4 .8 .

Table 4 .8 : Reactive Power Flow at Dorsey

	230kV side	500kV side	Net consumed
Before saturation	-120.1	-80.5	-39.6
low GIC	-57.3	-79.7	22.4
maximum recorded GIC	7.2	-77.8	85.0

It can be observed that the active power flow is dropped due to the drop in the voltages and the power lost due to harmonic currents. Active power flowing out of Dorsey dropped by about 0.8% at low GIC conditions and it dropped by about 5.9% at maximum recorded GIC conditions.

4.3.2.1 WAVEFORMS ON THE 500KV SIDE

Figure 4.7 shows the simulated voltage waveform on the 500kV side of the Dorsey transformer when transformers at Dorsey and Forbes were fully saturated due to the 50A and 105A per phase GIC.

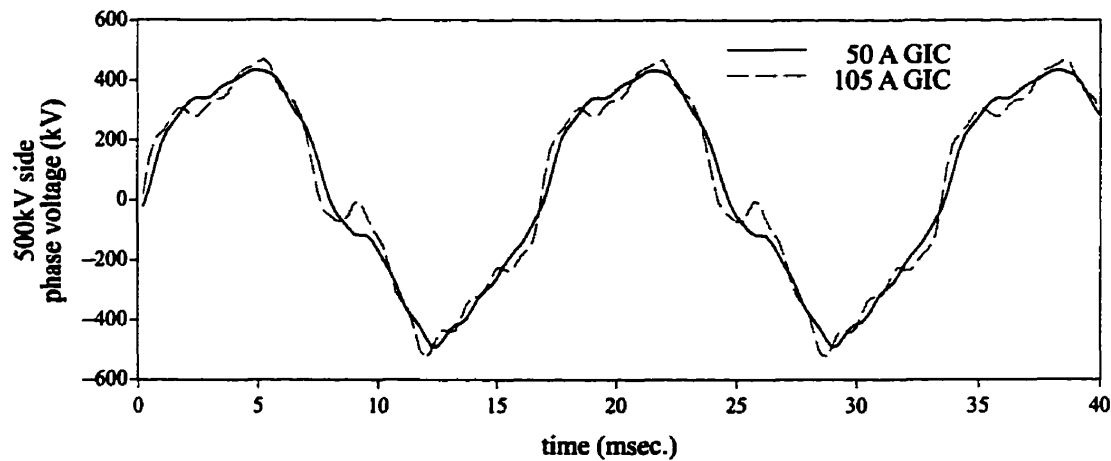


Figure 4.7 : Voltage waveform on 500 kV side of Dorsey at low power flow

The details of the 500kV side phase voltage such as rms magnitude, maximum and minimum peak values for both waveforms are given in table 4.9 . The Fourier analysis of these waveforms is shown in Figure 4.8 .

Table 4.9 : Details on the 500kV side phase voltage

	50A GIC	105A GIC
rms magnitude (kV)	307.2	308.4
maximum peak (kV)	434.5	470.1
minimum peak (kV)	-492.9	-520.9

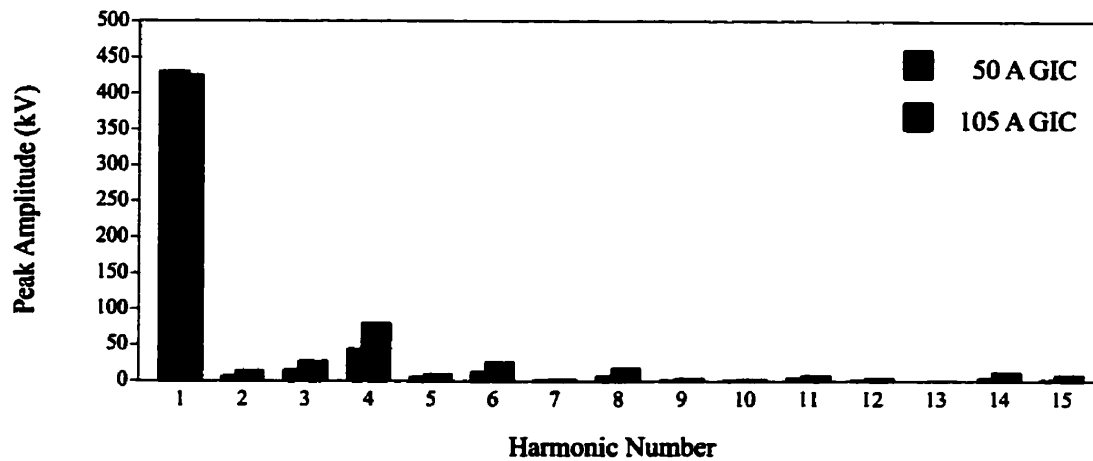


Figure 4.8 : Fourier analysis of 500 kV voltage waveforms at low power flow

For both waveforms, the most prominent harmonic component is the 4th followed by the 3rd and 6th. The waveform at 50A per phase GIC has a total harmonic distortion factor of 11.70% and that at 105A per phase GIC has a THD factor of 22.10%.

Figure 4.9 shows the corresponding current waveforms in the 500kV side when the transformers at both ends are saturated due to the applied GIC.

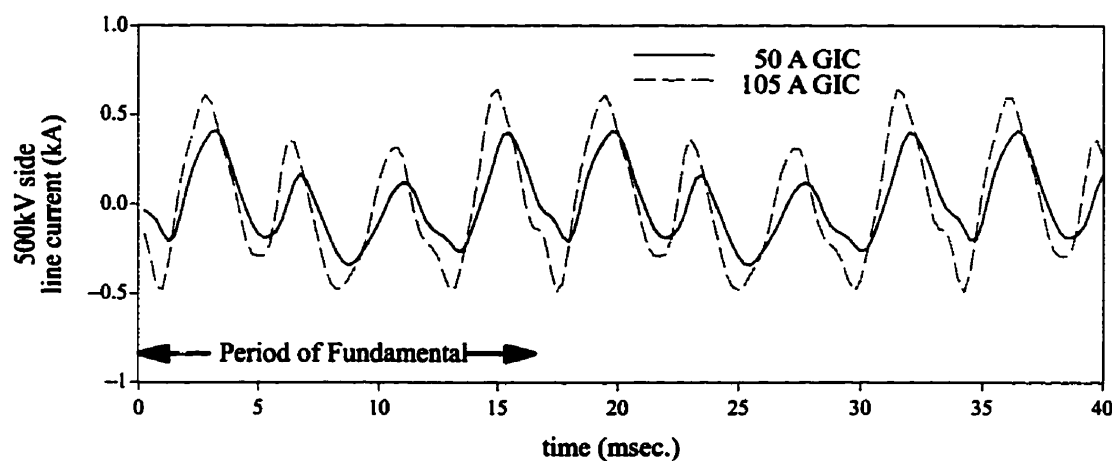


Figure 4.9 : Current waveforms on 500 kV side of Dorsey at low power flow

The details of the waveforms of the 500kV side line currents for the two different GIC conditions considered are given in table 4.10. The Fourier analysis of the two waveforms are shown in Figure 4.10.

Table 4 .10 : Details on the 500kV side line current

	50A GIC	105A GIC
rms magnitude (A)	205.8	328.8
maximum peak (A)	412.5	650.8
minimum peak (A)	-342.7	-495.6

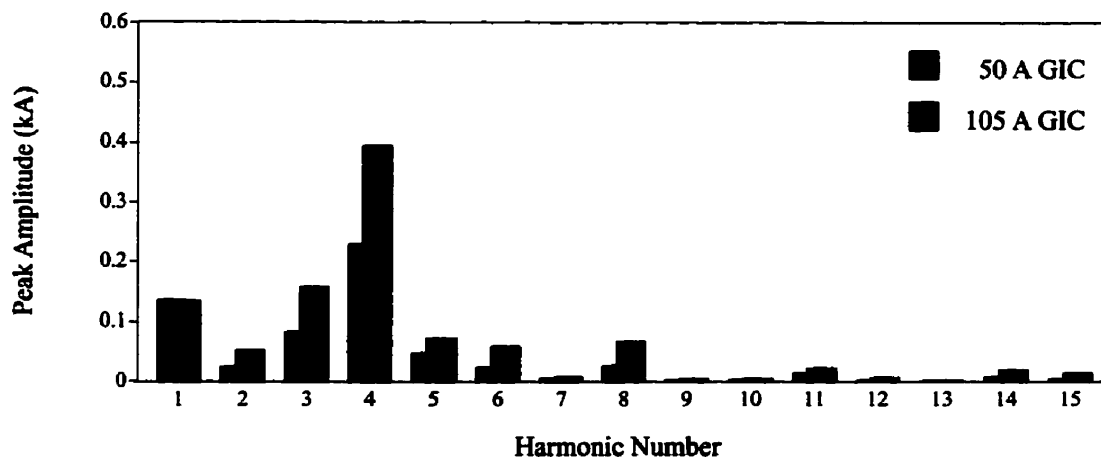


Figure 4 .10 : Fourier analysis of 500kV current waveforms at low power flow

When the power flow is low, there are harmonic components in the current which are greater than the fundamental component. The most prominent harmonic component is the 4th followed by the 3rd and 5th. The 4th harmonic component in the current at low GIC conditions and the 4th and 3rd harmonic components in the current at maximum recorded GIC conditions are more than the corresponding fundamental components in the current. The waveform at low GIC conditions has a total harmonic distortion factor of 185.48% whereas the waveform at maximum recorded GIC conditions has a THD factor of 331.22%.

4.4 EFFECT OF GIC ON DISTORTIONS AND HARMONICS

This subsection describes the effects on harmonics due to a change in applied GIC. The harmonic composition of the line currents and phase voltages at the 500 kV side is presented for different GIC levels.

Figure 4.11 shows the harmonic composition of the 500 kV line currents at Dorsey for different GIC levels for a typical high power flow whereas Figure 4.12 shows the harmonic composition of the 500 kV line current for a different GIC under a typical low power flow condition.

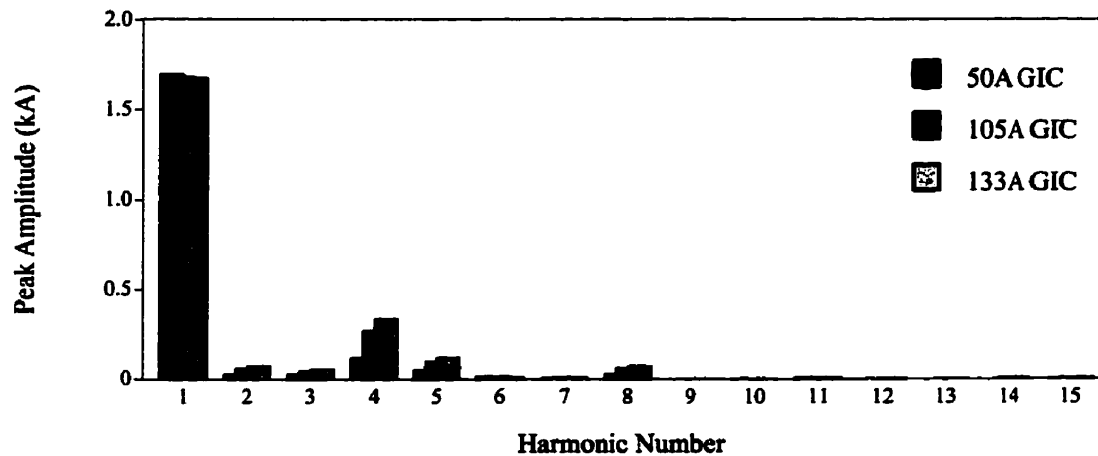


Figure 4.11 : Fourier analysis of 500 kV side currents with a typical high power flow

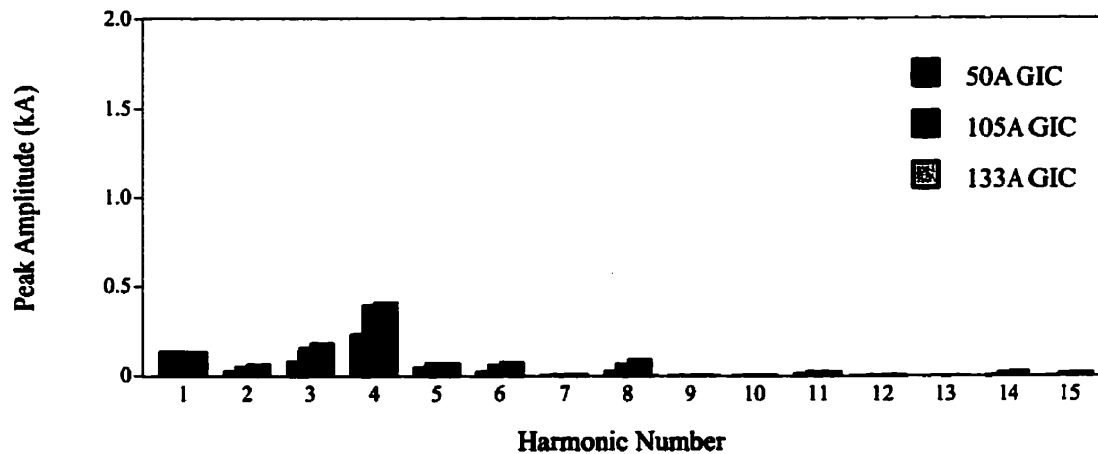


Figure 4.12 : Fourier analysis of 500 kV side currents with a typical low power flow

It is clear that the pattern of harmonic composition for a particular power flow remains more or less the same, but the magnitudes of harmonics other than the fundamental increase with the increase of the level of GIC. There is a slight decrease in the magnitude of the fundamental component with the increase of the GIC.

Figure 4 .13 shows the total harmonic distortion of the 500 kV line current for different GIC levels for the two different power flows considered.

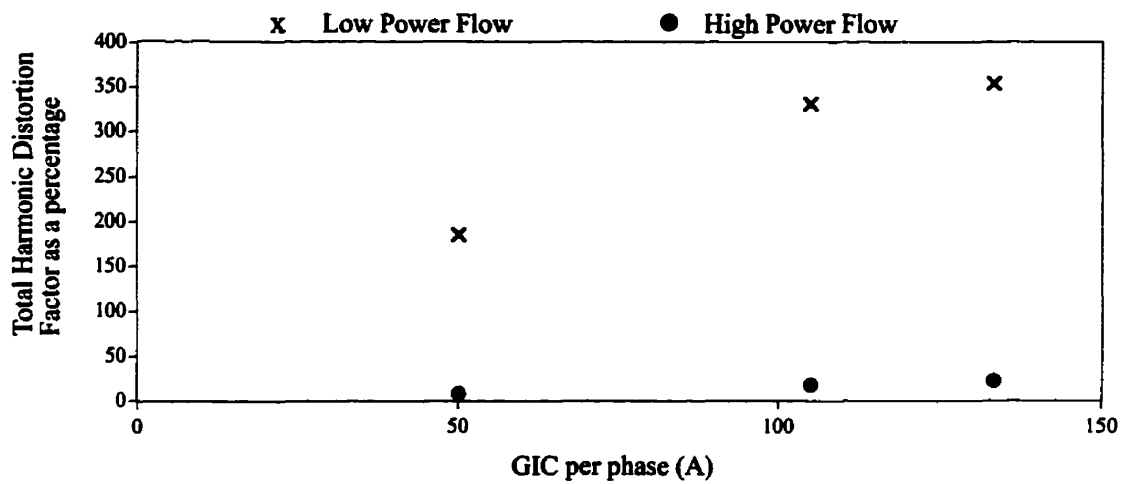


Figure 4 .13 : THD Factor of 500 kV side currents

The total harmonic distortion of the waveforms increases with the applied level of GIC, but the distortion factor for the waveform obtained during a low power flow condition is much more than that obtained during a high power flow condition for the same GIC level. This is to be expected due to the decreased level of the fundamental.

A similar analysis is done on the 500 kV side voltage waveforms and the results are presented in appendix B . The difference in THD factors for low and high power flow conditions is not as high as in the current waveforms. This is to be expected since the level of the fundamental is more or less the same unlike in the current.

4.5 EFFECT OF POWER FLOW ON HARMONICS

This subsection describes the effects on harmonics due to the change of power flow for a given GIC. The harmonic composition of the line currents and phase voltages at the 500 kV side is presented for different power flow conditions.

Figures 4.14 and 4.15 show the harmonic composition of the 500 kV line currents and voltage respectively for the two different power flow conditions considered at the maximum recorded GIC level. The harmonic analysis done for waveforms obtained at two other GIC levels are presented in appendix B.

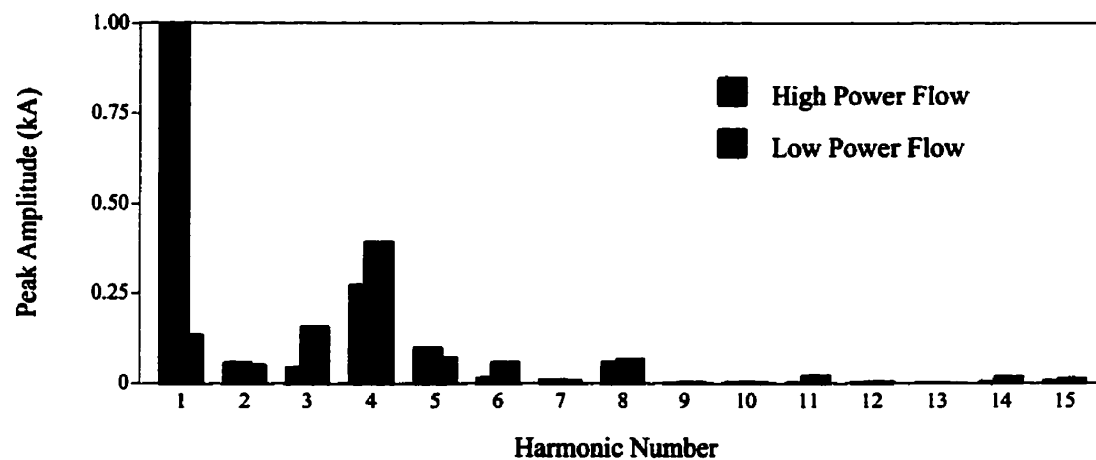


Figure 4.14 : Fourier analysis of 500 kV side currents at Dorsey with 105A GIC per phase

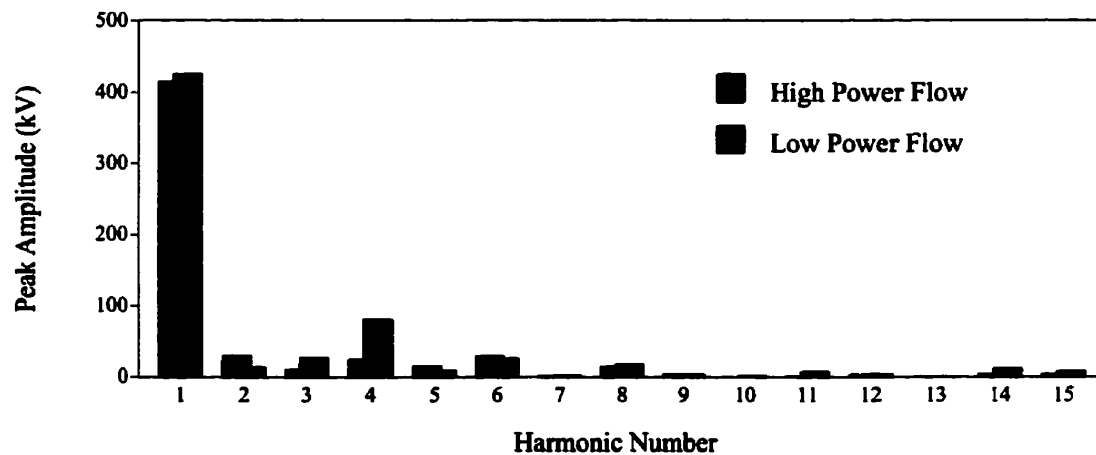


Figure 4.15 : Fourier analysis of 500 kV side phase voltages at Dorsey with 105A GIC per phase

It can be seen that the magnitudes of the harmonic currents are more or less the same irrespective of the level of power flow for any given level of GIC. In fact, the harmonic magnitudes are slightly more in the case of low power flow condition. This could be due to the fact that the voltage applied to the transformers is slightly more in the low power flow case. Out of all the waveforms considered, it is clear that the most prominent harmonic is the 4th harmonic.

Figures 4.16 and 4.17 show the total harmonic distortion factor as a function of the current in the 500 kV side for 500 kV line current and phase voltage respectively. The Total Harmonic Distortion factor of the waveforms for the three different GIC levels are presented.

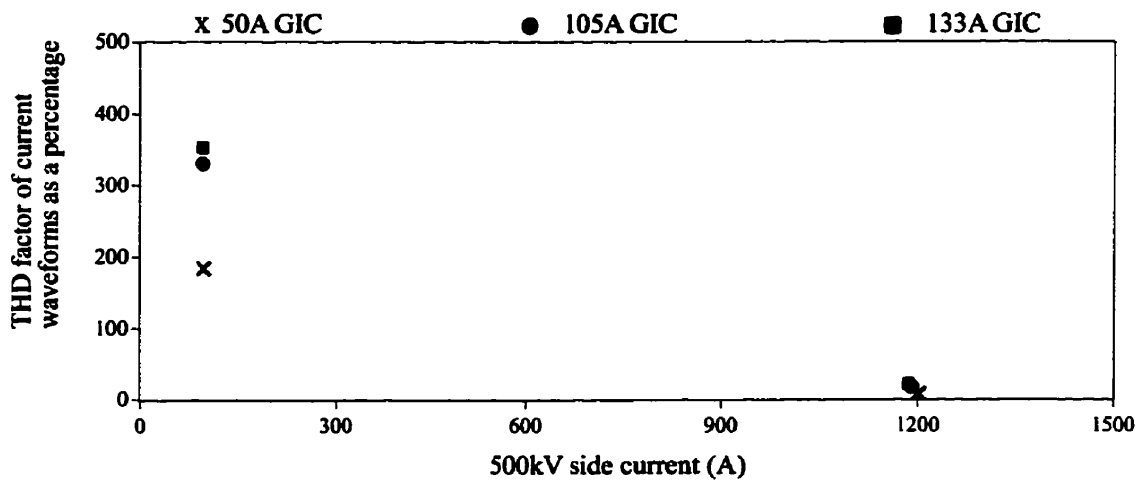


Figure 4.16 : Harmonic Distortion of current with the Load Flow

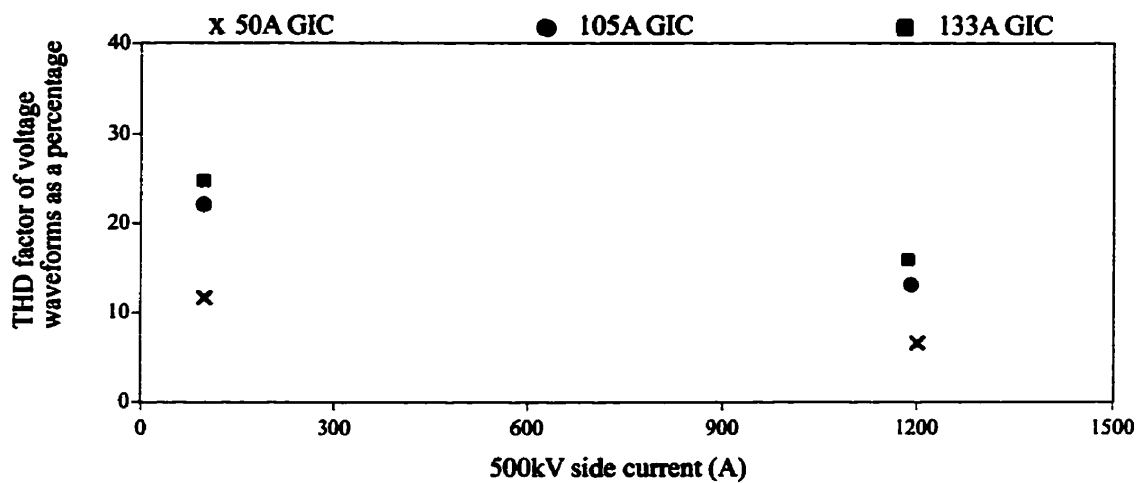


Figure 4 .17 : Harmonic Distortion of voltage with the Load Flow

It can be observed that the total harmonic distortion decreases as the level of power flow increases. It can also be observed that the distortion of the current waveform is much more than the distortion of the voltage waveform.

4.6 CONCLUSIONS

It is seen from tables 4 .4 and 4 .8 that the increase in reactive power consumption of the transformer for a given GIC is more or less the same irrespective of the amount of power flow. The slight difference is due mainly to the difference in reactive power consumption in the leakage inductance for different power flow conditions. Otherwise, reactive power drawn by the transformer due to half cycle saturation due to a specific amount of GIC is more or less the same irrespective of the power flow, provided the voltage applied to the transformers is more or less the same. This is usually true.

It is also seen that the 4th harmonic is the most prominent harmonic for a number of system waveforms during GIC conditions.

The magnitude of the harmonics in various waveforms increases with the amount of GIC. The relationship between harmonic magnitudes with the GIC is roughly linear. The magnitude of the harmonics is more or less the same or slightly decreases with

an increase in power flow. It can be concluded that by decreasing the amount of power flow during a geomagnetic storm, the likelihood of a protection system malfunction increases due to the increased distortions in the waveforms. But the whole system could be made stable since the loss of power is small in the event of a false trip.

More waveforms related to the studies presented in this section are given in appendix B .

Chapter 5

Dorsey–Forbes–Chisago after series compensation

5.1 DESCRIPTION OF THE SYSTEM

For the studies of the Dorsey–Forbes–Chisago system after series compensation, the same system described in 4.1 is used with a detailed 230 kV system. In the previous work, the 230 kV system was included as an equivalent source.

In addition to the 500 kV line, two 230 kV transmission lines from Dorsey connect to Northern States Power. These two lines run almost parallel to the 500 kV line. The two lines are 141 km and 187 km long. The longer line connects Dorsey to Moranville and the shorter one connects Dorsey to Drayton.

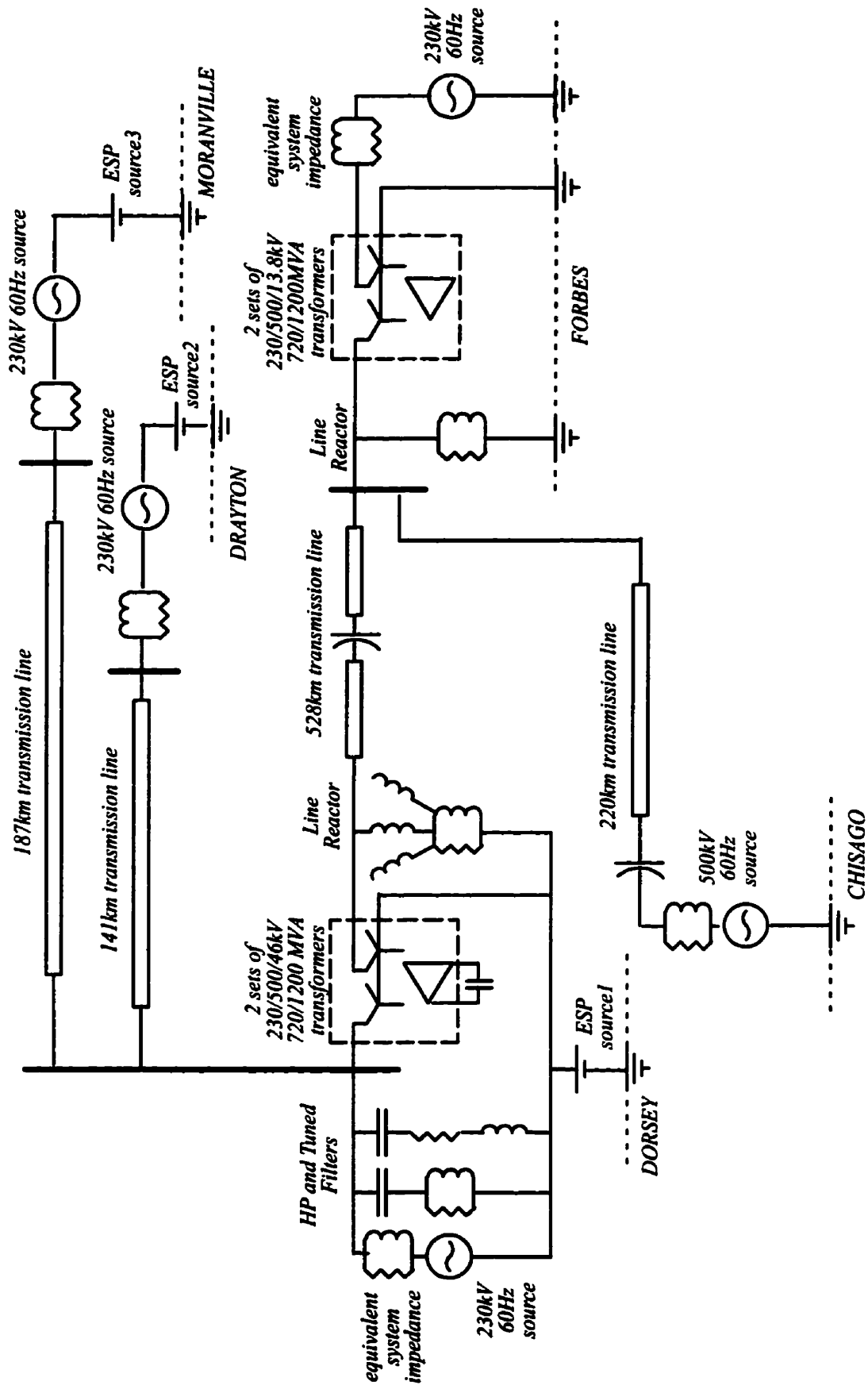


Figure 5.1: Single line diagram of Dorsey-Forbes-Chisago system after series compensation

The northern section of the 500 kV transmission line is 50% series compensated at the second transposition location 193km from Dorsey. The southern section is series compensated at Chisago. The transformers at Dorsey, Forbes and Chisago were doubled to match the increased power capacity of the transmission line.

The 230 kV Dorsey–Moranville transmission line runs almost parallel to the 500 kV Dorsey–Forbes transmission line in a NW–SE direction. Therefore the ESP gradient at Dorsey–Moranville was assumed the same as that of the Dorsey–Forbes line. The 230 kV Dorsey–Drayton lies almost in a N–S direction. Thus the ESP gradient at Dorsey–Drayton line was assumed as 12.86% of that of Dorsey–Forbes line based on the previous studies done by Albertson [7]. The converter transformers at Dorsey were also considered since part of the GIC that flows in the 230 kV system flows through their neutrals.

A single line diagram of the Drayton–Moranville–Dorsey–Forbes–Chisago system used in the simulation is shown in the Figure 5.1. Geographical layout of the system is shown in the Figure 5.2.

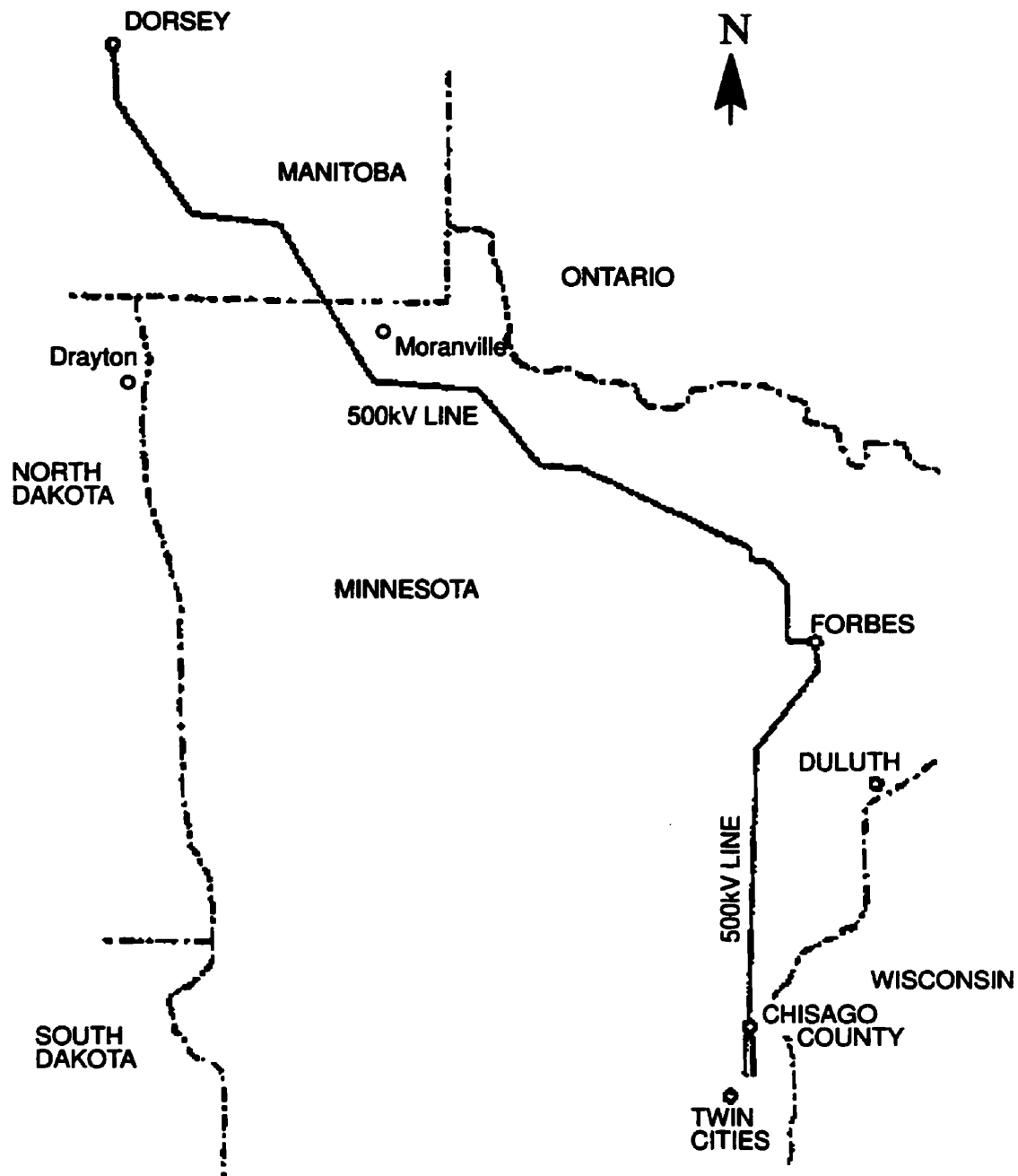


Figure 5.2 : Geographical layout of the 500 kV transmission line

5.2 SIMULATIONS UNDER DIFFERENT CONDITIONS

Simulations for two different power flows are studied and also two different ESP levels are chosen. The Earth Surface Potentials at various substations are chosen so that

one ESP gradient is the same as that which caused the maximum recorded GIC flow in the 500 kV transmission line before it was series compensated, and the other ESP gradient is the one which would have given the predicted maximum GIC [25][33]. The two different power flows are; one typical low power flow and one typical high power flow.

Tables 5.1 and 5.2 show the pre-GIC system conditions of the 500 kV and 230 kV sides respectively for the low power flow study whereas tables 5.3 and 5.4 show the pre-GIC system conditions of the 500 kV and 230 kV sides respectively for the high power study.

Table 5.1 : Pre-GIC system conditions for low power flow study – 500kV side

	DORSEY	FORBES	CHISAGO
Voltage (kV)	510.9	500.4	496.4
Angle (degrees)	0.0	-5.2	-11.2
current (A)	355.0	166.7	435.2
Active Power (MW)	266.6	123.6	-353.2
Reactive Power (MVar)	-166.1	-74.9	-123.4

Table 5.2 : Pre-GIC system conditions for low power flow study – 230kV side

	DORSEY	DRAYTON	MORANVILLE
Voltage (kV)	233.1	232.9	234.6
Angle (degrees)	0.8	-3.8	-3.7
current (A)		163.4	119.8
Active Power (MW)		-65.9	-48.4
Reactive Power (MVar)		3.0	5.6

Table 5 .3 : Pre-GIC system conditions for high power flow study – 500kV side

	DORSEY	FORBES	CHISAGO
Voltage (kV)	497.4	495.9	503.0
Angle (degrees)	0.0	-29.9	-47.4
current (A)	1610.0	609.6	1167.0
Active Power (MW)	1387.0	-255.8	-1009.0
Reactive Power (MVar)	32.0	456.8	127.1

Table 5 .4 : Pre-GIC system conditions for high power flow study – 230kV side

	DORSEY	DRAYTON	MORANVILLE
Voltage (kV)	230.2	226.8	224.2
Angle (degrees)	4.4	-19.8	-9.3
current (A)		835.5	360.4
Active Power (MW)		-316.5	-139.9
Reactive Power (MVar)		87.1	2.9

5.2.1 A TYPICAL LOW POWER FLOW

Two simulation studies at a typical low power flow are studied here. The two earth surface potentials are chosen as one that gave the maximum recorded GIC before series compensation and the other that would have given the maximum predicted GIC for this particular system.

Tables 5.5 and 5.6 show the post-GIC system conditions of the 500 kV and 230 kV sides respectively when the transformers at Dorsey are fully saturated due to the applied ESP that corresponds to both the maximum recorded and maximum predicted GIC levels.

Table 5.5 : Post-GIC system conditions for low power flow study – 500kV side

	MAXIMUM RECORDED ESP			MAXIMUM PREDICTED ESP		
	DORSEY	FORBES	CHISAGO	DORSEY	FORBES	CHISAGO
Voltage (kV)	509.6	500.0	496.3	508.0	499.4	496.3
Angle (degrees)	0.0	-5.2	-11.3	0.0	-5.3	-11.3
current (A)	358.1	165.6	433.9	361.4	164.4	432.1
Active Power (MW)	266.4	123.6	-353.0	265.6	123.7	-352.5
Reactive Power (MVar)	-170.0	-72.8	-120.5	-174.7	-70.2	-117.0

Table 5.6 : Post-GIC system conditions for low power flow study – 230kV side

	MAXIMUM RECORDED ESP			MAXIMUM PREDICTED ESP		
	DORSEY	DRAYTON	M'VILLE	DORSEY	DRAYTON	M'VILLE
Voltage (kV)	232.4	232.6	234.2	231.6	232.3	233.7
Angle (degrees)	0.8	-3.8	-3.7	0.8	-3.8	-3.7
current (A)		163.3	119.6		163.0	119.4
Active Power (MW)		-65.8	-48.3		-65.6	-48.1
Reactive Power (MVar)		-1.5	-4.9		21.4	-4.1

The voltages at all the substations dropped very slightly. The voltage drops at maximum recorded ESP level are; Dorsey by 0.3%, Forbes by 0.1%, Drayton by 0.1% and Moranville by 0.2%. The corresponding voltage drops were increased to 0.6%, 0.2%, 0.3% and 0.4% respectively when the ESP level was increased to the maximum predicted. There was no GIC flowing in the 500kV line due to the high resistance for dc created by series capacitors in the line. There is a 15A per phase GIC flowing in the 230kV side of the 230/500kV transformer at Dorsey. This current increased to 31A when the ESP was increased to the maximum predicted. This 31A per phase GIC matches with the maximum predicted GIC flow in the low voltage side of Dorsey [33]. The active power flowing out from Dorsey dropped slightly, as does the active power received at other substations. The

reactive power flow out of the 500kV side of Dorsey dropped slightly but the reactive power flow out from Forbes, Chisago, Drayton and Moranville increased slightly.

5.2.1.1 WAVEFORMS ON THE 500KV SIDE

Figures 5.3 and 5.4 show the simulated phase voltage and the line current on the 500 kV side when the transformers are fully saturated due to the GIC created by the applied ESP.

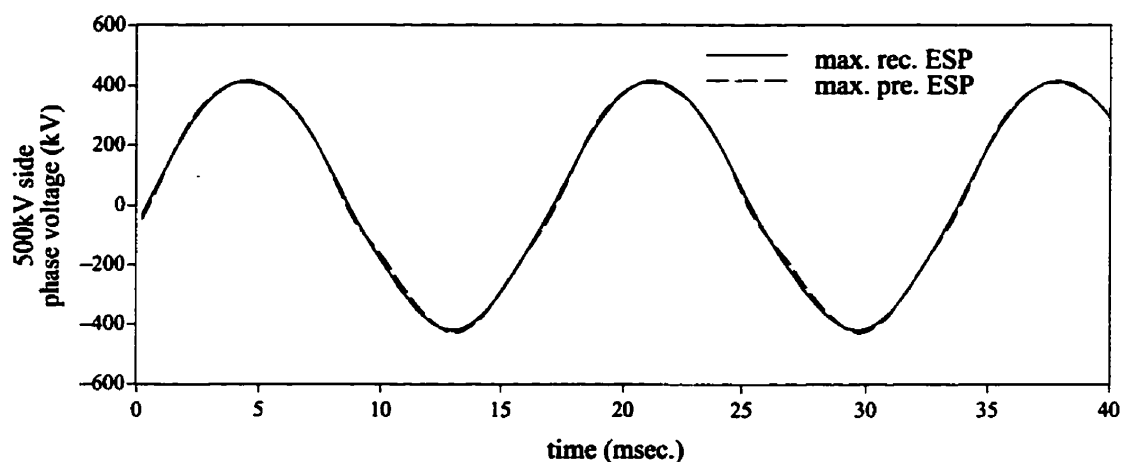


Figure 5.3 : Voltage waveform on 500 kV side of Dorsey at low power flow

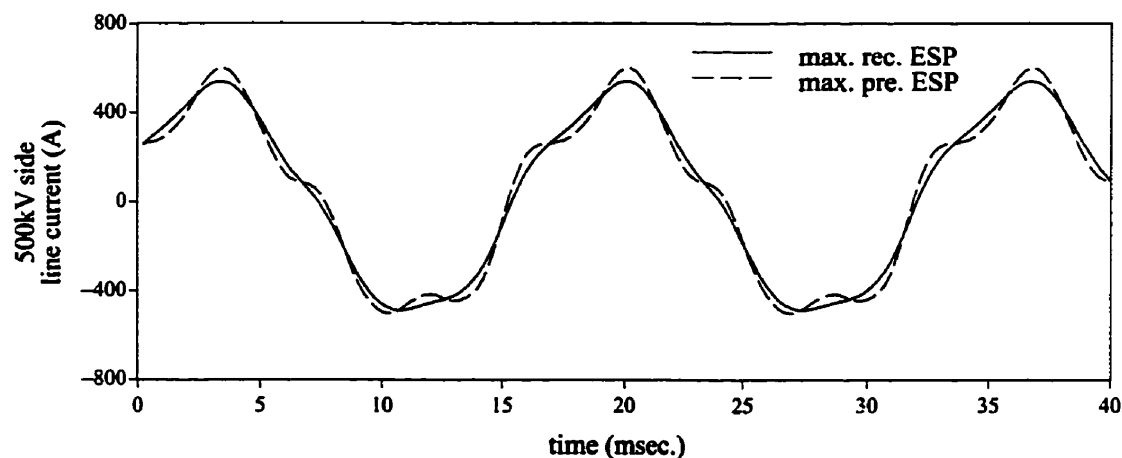


Figure 5.4 : Current waveforms on 500 kV side of Dorsey at low power flow

Tables 5.7 and 5.8 show the rms magnitudes, maximum and minimum peak values of the two waveforms shown in the two preceding figures.

Table 5 .7 : The details on the 500 kV side voltage at Dorsey after saturation

	Max. Rec. GIC	Max. Pred. GIC
rms magnitude (kV)	294.9	294.2
maximum peak (kV)	415.4	413.5
minimum peak (kV)	-421.3	-428.9

Table 5 .8 : The details on the 500 kV side current at Dorsey after saturation

	Max. Rec. GIC	Max. Pred. GIC
rms magnitude (A)	358.5	366.8
maximum peak (A)	540.1	600.2
minimum peak (A)	-490.4	-508.1

The Fourier analysis of the 500kV side voltage and current waveforms at Dorsey are shown in Figures 5 .5 and 5 .6 respectively.

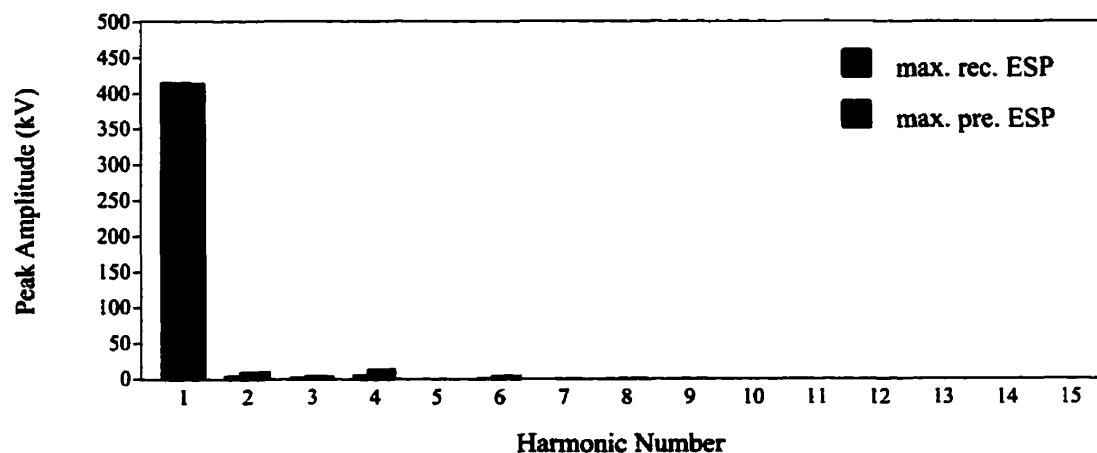


Figure 5 .5 : Fourier analysis of 500kV side voltage waveforms at low power flow

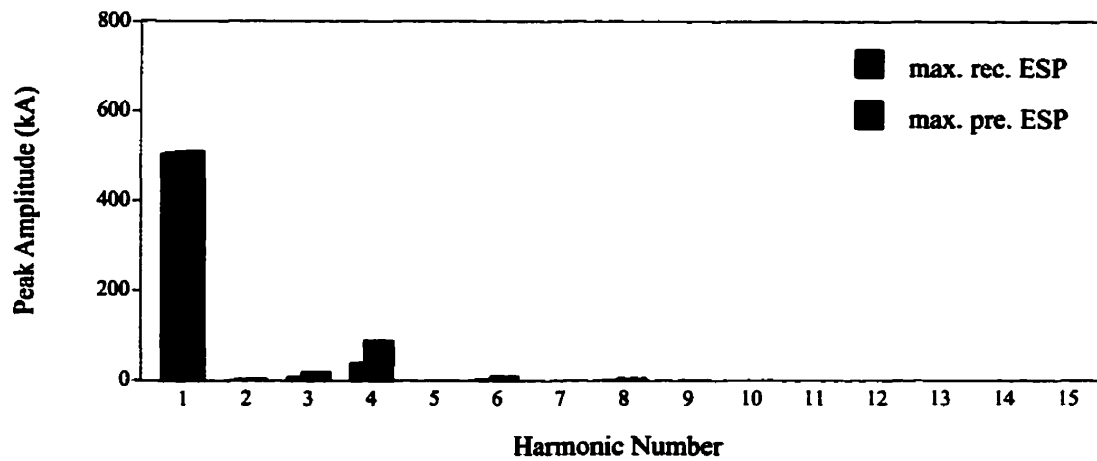


Figure 5 .6 : Fourier analysis of 500kV side current waveforms at low power flow

The distortions of the waveforms are much less compared to the distortions of the waveforms obtained for pre-compensated study. The voltage waveform has a THD factor of 1.96% and 4.45% at maximum recorded and maximum predicted ESP conditions respectively. The corresponding figures for the current waveform are 7.96% and 18.16%. The most prominent harmonic for both the waveforms is the 4th harmonic.

5.2.1.2 WAVEFORMS ON THE 230KV SIDE

Figures 5.7 and 5.8 show the simulated phase voltage and the line current on the 230 kV side when the transformers are fully saturated due to the GIC created by the applied ESP.

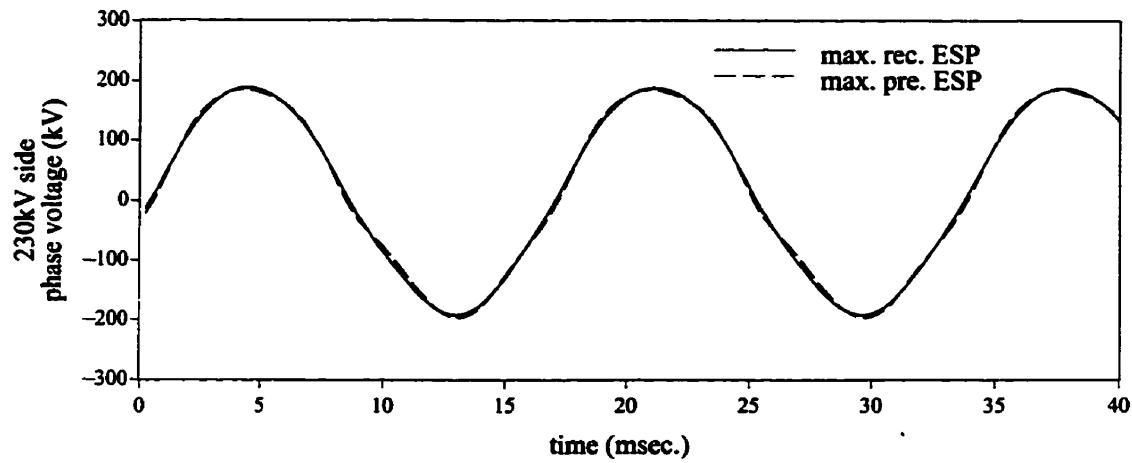


Figure 5.7 : Voltage waveforms on the 230 kV side at Dorsey at low power flow

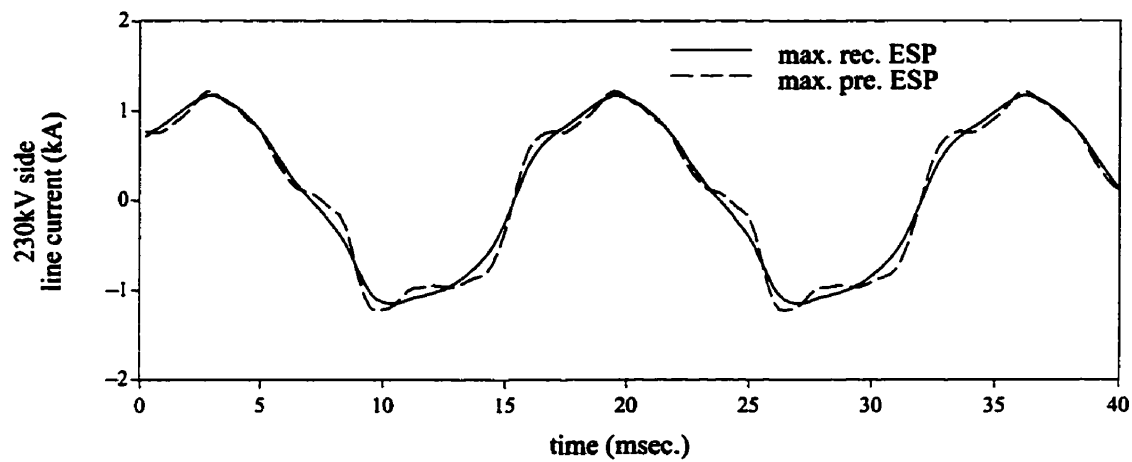


Figure 5.8 : Current waveforms on the 230 kV side of Dorsey at low power flow

Tables 5.9 and 5.10 show the rms magnitudes, maximum and minimum peak values of the two waveforms shown in the two preceding figures.

Table 5.9 : The details on the 230 kV side voltage after saturation

	Max. Rec. GIC	Max. Pred. GIC
rms magnitude (kV)	134.5	134.2
maximum peak (kV)	188.5	186.7
minimum peak (kV)	-193.0	-197.4

Table 5 .10 : The details on the 230 kV side current at Dorsey after saturation

	Max. Rec. GIC	Max. Pred. GIC
rms magnitude (A)	819.7	829.0
maximum peak (A)	1178.0	1230.0
minimum peak (A)	-1154.0	-1238.0
per phase GIC (A)	15.0	31.0

The Fourier analysis of the 230kV side voltage and current waveforms are shown in Figures 5.9 and 5.10 respectively.

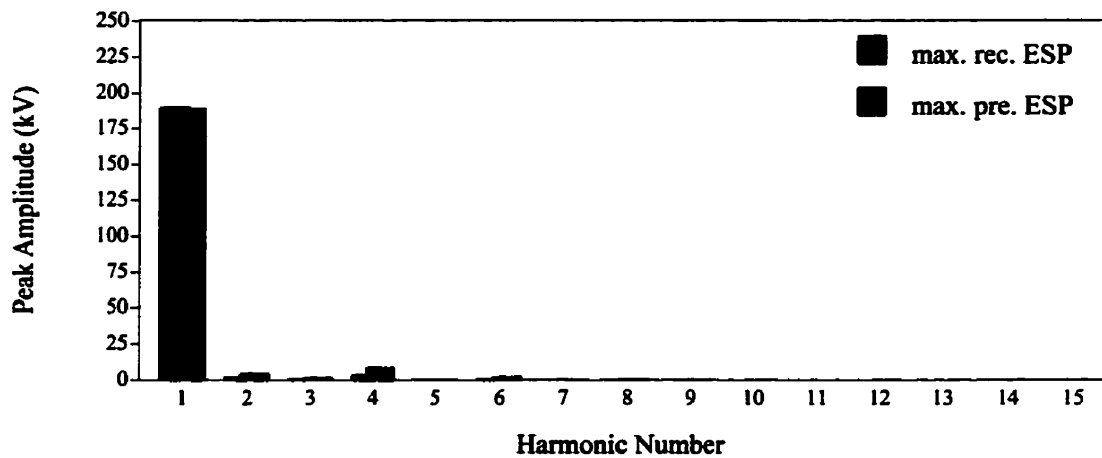


Figure 5.9 : Fourier analysis of 230kV voltage waveforms at low power flow

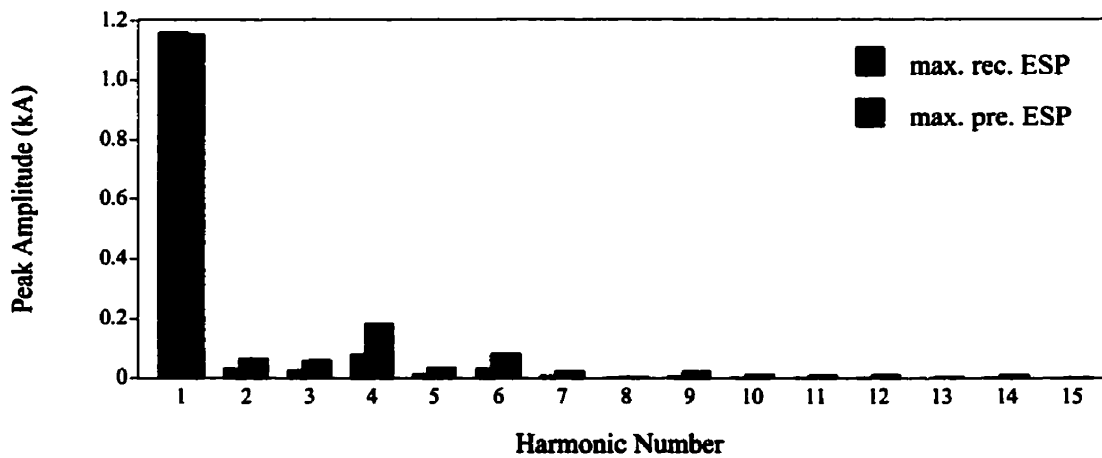


Figure 5.10 : Fourier analysis of 230kV side current waveforms at Dorsey at low power flow

The THD factors of the two voltage waveforms at the 230 kV side is 2.36% and 5.39% respectively for maximum recorded ESP and maximum predicted ESP conditions. The corresponding figures for the current waveforms are 8.33% and 19.57%. For all the waveforms, the most prominent harmonic is the 4th harmonic.

5.2.1.3 CURRENT WAVEFORMS IN 230KV FEEDERS

Figures 5.11 and 5.12 show the waveform of the current flowing to Drayton and Moranville respectively.

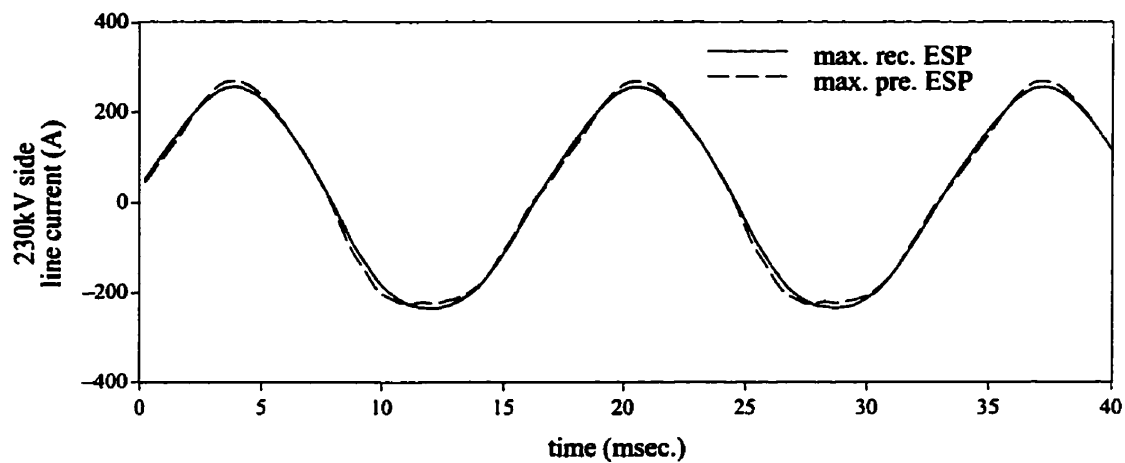


Figure 5.11 : Current on Dorsey-Drayton line at Dorsey at low power flow

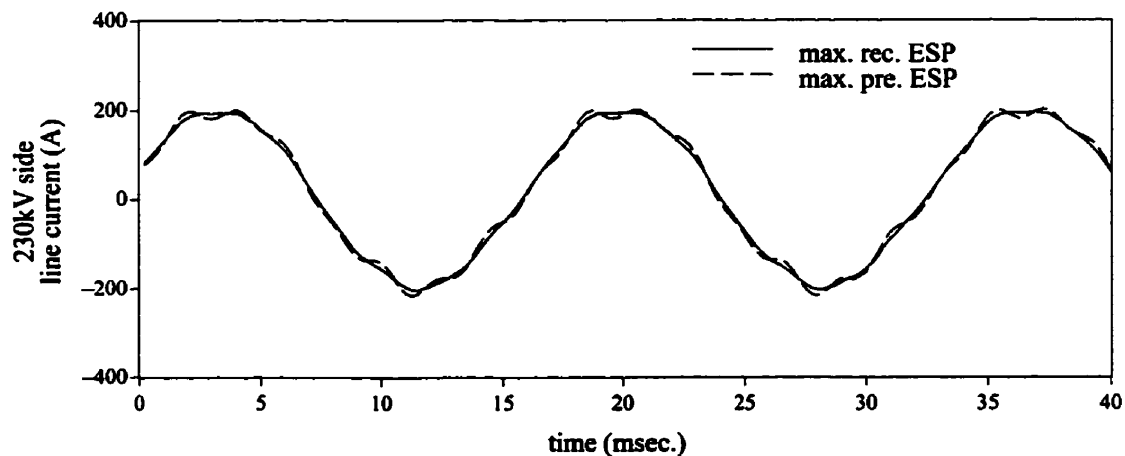


Figure 5.12 : Current on Dorsey-Moranville line at Dorsey at low power flow

Table 5.11 shows the rms and peak values of the current flowing to Drayton at Dorsey whereas table 5.12 shows the corresponding values of the current flowing to Moranville at Dorsey.

Table 5.11 : The details on the current flowing to Drayton after saturation

	Max. Rec. GIC	Max. Pred. GIC
rms magnitude (A)	174.7	176.6
maximum peak (A)	255.9	268.1
minimum peak (A)	-235.5	-227.8
per phase GIC (A)	4.1	8.7

Table 5.12 : The details of the current flowing to Moranville after saturation

	Max. Rec. GIC	Max. Pred. GIC
rms magnitude (A)	140.5	141.8
maximum peak (A)	194.5	200.9
minimum peak (A)	-205.2	-217.2
per phase GIC (A)	32.8	69.7

The Fourier analysis of the current flowing to Drayton is shown in Figure 5.13 whereas Figure 5.14 shows the Fourier analysis of the current flowing to Moranville.

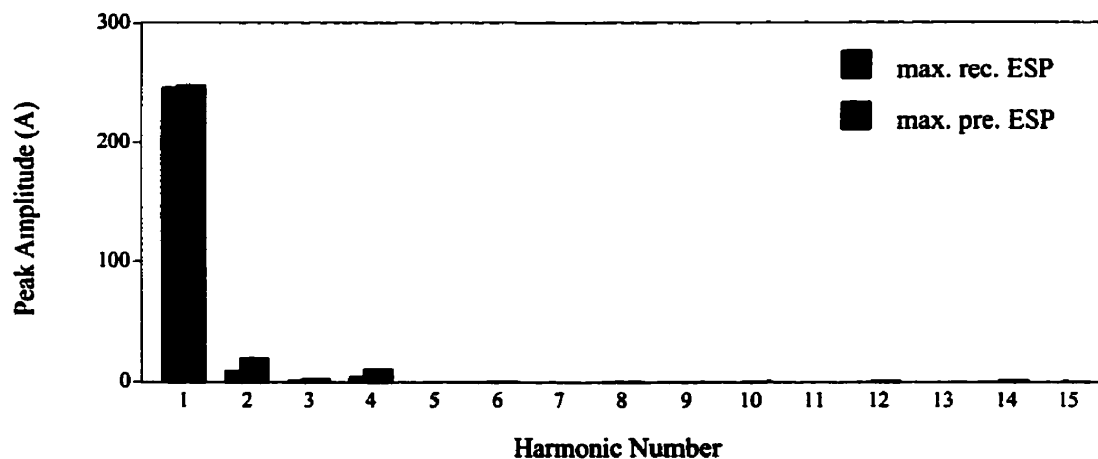


Figure 5.13 : Fourier analysis of current flowing to Drayton at low power flow

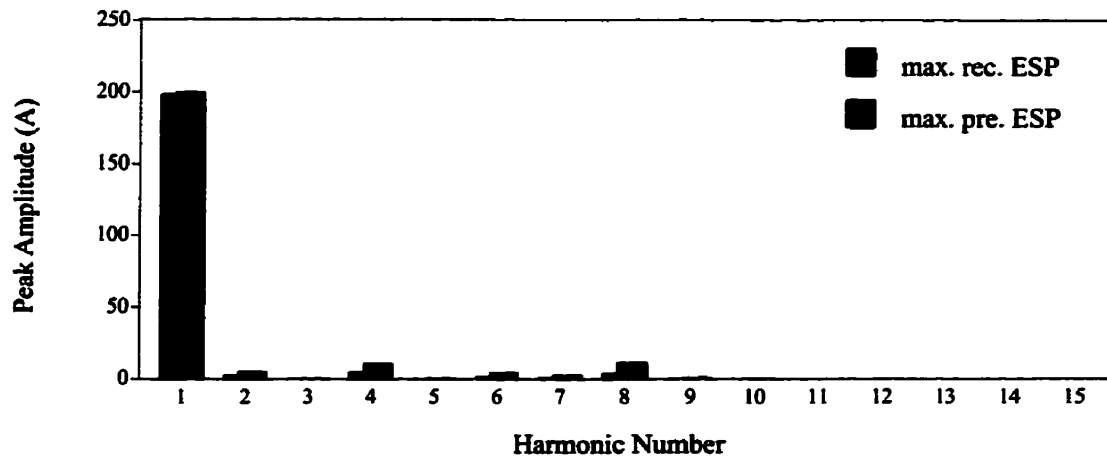


Figure 5 .14 : Fourier analysis of current flowing to Moranville at low power flow

The THD factor of the current flowing to Drayton at the 230 kV side of Dorsey is 4.18 % and 9.06% respectively for the waveform at maximum recorded ESP and maximum predicted ESP. The most prominent harmonic is the 2nd harmonic followed by the 4th.

The THD factors of the two waveforms of the current flowing to Moranville at the 230 kV side of Dorsey are 3.41% and 8.76% respectively for the maximum recorded ESP and the maximum predicted ESP conditions. The most prominent harmonic is 4th harmonic followed by the 8th and the 2nd.

5.2.2 A TYPICAL HIGH POWER FLOW

Two simulation studies at a typical high power flow are studied herefor the same GIC levels as in the low power flow case (5 .2 .1) . The two earth surface potentials chosen are the one that gave the maximum recorded GIC before series compensation and the other that would have given the maximum predicted GIC for this particular system.

Tables 5.13 and 5.14 show the post-GIC system conditions of the 500 kV and 230 kV sides respectively when the transformers at Dorsey are fully saturated due to the applied ESP.

Table 5 .13 : Post–GIC system conditions for high power flow study – 500kV side

	MAXIMUM RECORDED ESP			MAXIMUM PREDICTED ESP		
	DORSEY	FORBES	CHISAGO	DORSEY	FORBES	CHISAGO
Voltage (kV)	496.0	495.5	503.0	494.3	495.0	503.0
Angle (degrees)	0.0	–30.0	–47.4	0.0	–30.0	–47.4
current (A)	1610.0	610.8	1165.0	1610.0	612.1	1162.0
Active Power (MW)	1383.0	–254.3	–1006.0	1378.0	–252.4	–1004.0
Reactive Power (MVar)	28.0	458.3	129.3	22.9	460.1	131.8

Table 5 .14 : Post–GIC system conditions for high power flow study – 230kV side

	MAXIMUM RECORDED ESP			MAXIMUM PREDICTED ESP		
	DORSEY	DRAYTON	M'VILLE	DORSEY	DRAYTON	M'VILLE
Voltage (kV)	229.5	226.6	232.8	228.7	226.3	223.2
Angle (degrees)	4.5	–19.8	–9.3	4.5	–19.8	–9.4
current (A)		835.2	360.2		834.7	359.8
Active Power (MW)		–315.6	–139.6		–314.5	–139.1
Reactive Power (MVar)		88.4	3.6		90.6	4.3

The voltages at all the substations dropped very slightly. The voltage drops at the maximum recorded ESP level are; Dorsey by 0.3%, Forbes by 0.1%, Drayton by 0.1% and Moranville by 0.2%. The voltage drops at the maximum predicted ESP level are; Dorsey by 0.6%, Forbes by 0.2%, Drayton by 0.2% and Moranville by 0.4%. There was no GIC flowing in the 500kV line due to the high resistance for dc created by series capacitors in the line. There is a 15A per phase GIC flowing in the 230kV side of the 230/500kV transformer at Dorsey. This current increased to 31A when the ESP level was increased to the maximum predicted. This 31A per phase GIC matches with the maximum predicted GIC flow in the low voltage side of Dorsey [33]. The active power flowing out from Dorsey dropped slightly. So does the active power received at other substations. The reactive power flow out of the

500kV side of Dorsey dropped slightly but the reactive power flow out from Forbes, Chisago, Drayton and Moranville increased slightly.

5.2.2.1 WAVEFORMS IN 500KV SIDE

Figures 5.15 and 5.16 show the simulated phase voltage and the line current on the 500 kV side respectively when the transformers are fully saturated due to the GIC created by the applied ESP.

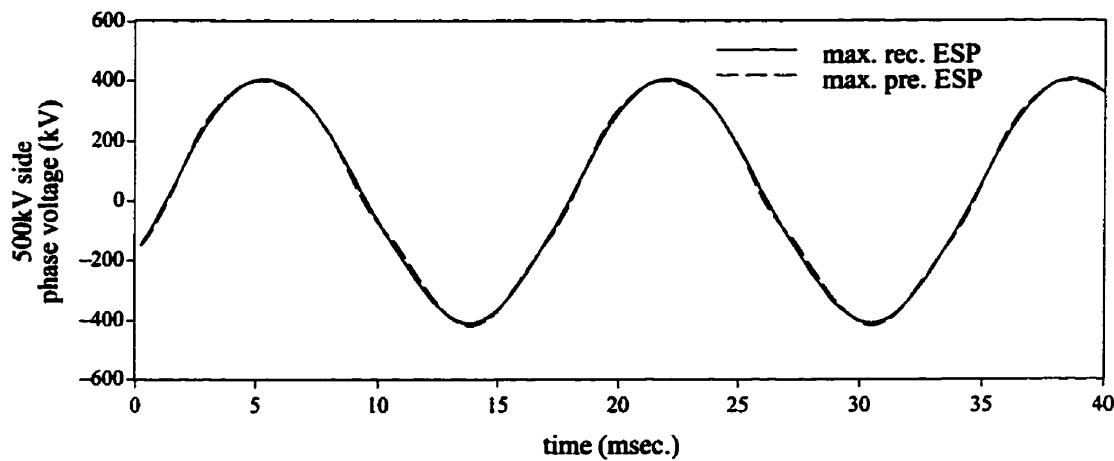


Figure 5.15 : Voltage waveforms on 500 kV side at high power flow

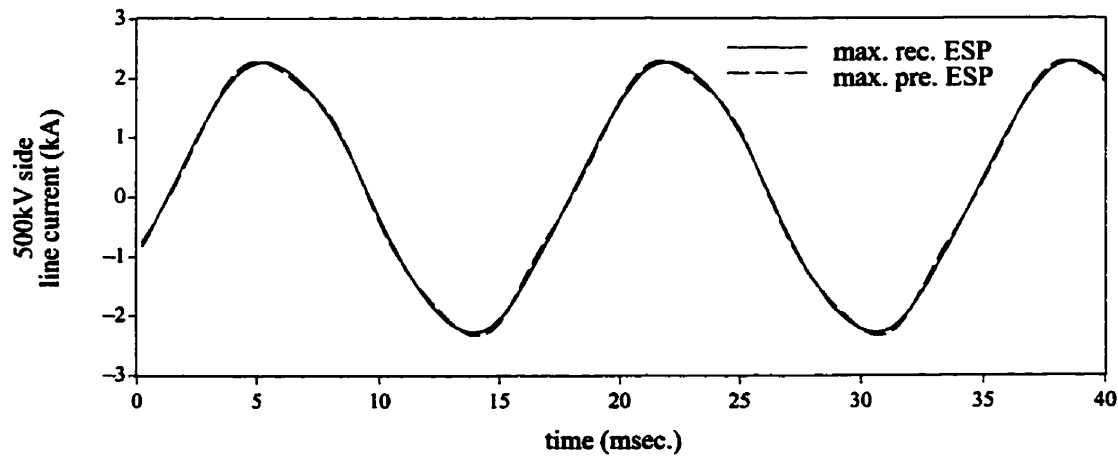


Figure 5.16 : Current waveforms on 500 kV side of Dorsey at high power flow

Tables 5.15 and 5.16 show the rms magnitudes, maximum and minimum peak values of the two waveforms shown in the two preceding figures.

Table 5 .15 : The details on the 500 kV side voltage after saturation

	Max. Rec. GIC	Max. Pred. GIC
rms magnitude (kV)	286.9	286.9
maximum peak (kV)	404.0	400.0
minimum peak (kV)	-411.7	-419.4

Table 5 .16 : The details on the 500 kV side current after saturation

	Max. Rec. GIC	Max. Pred. GIC
rms magnitude (A)	1610.6	1609.1
maximum peak (A)	2293.0	2305.0
minimum peak (A)	-2304.0	-2340.0

The Fourier analysis of the 500 kV side voltage and current waveforms are shown in Figures 5 .17 and 5 .18 respectively.

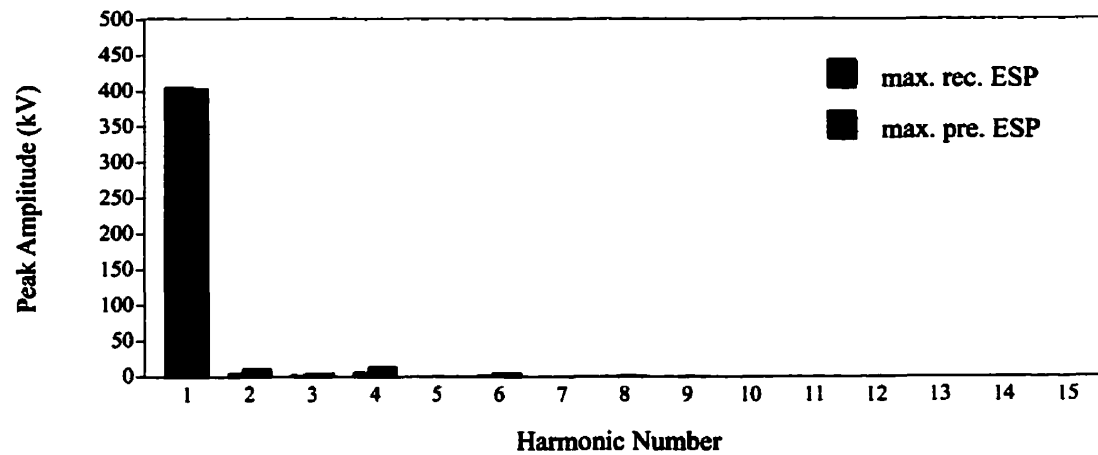


Figure 5 .17 : Fourier analysis of 500kV voltage waveforms at high power flow

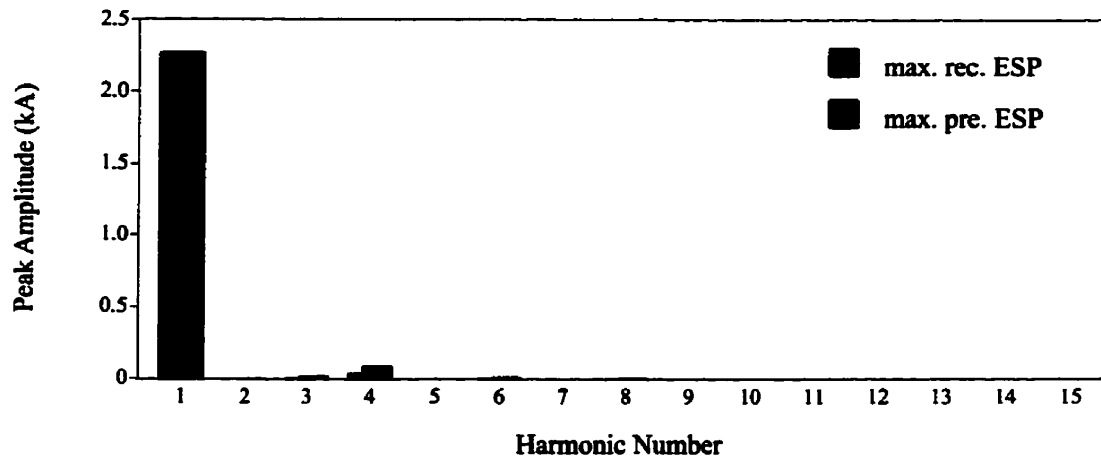


Figure 5 .18 : Fourier analysis of 500kV current waveforms at high power flow

The distortions of the waveforms are much less compared to the distortions of the waveforms obtained for the pre-compensated study. The voltage waveform has a total harmonic distortion factor of 1.99% and 4.08% at maximum recorded and maximum predicted ESP conditions respectively. The corresponding figures for the current waveform are 1.75% and 4.08%. For both waveforms, the most prominent harmonic is the 4th harmonic.

The waveforms on the 230 kV side follow a similar pattern. The distortions in them are also less in this high power flow condition. The voltage and current waveforms on the 230kV side are presented in appendix C .

5.2.2.2 CURRENT WAVEFORMS IN 230KV FEEDERS

Figure 5 .19 shows the waveforms of the current flowing to Moranville at Dorsey at a typical high power flow for two different GIC conditions when the transformers are fully saturated due to the applied ESP.

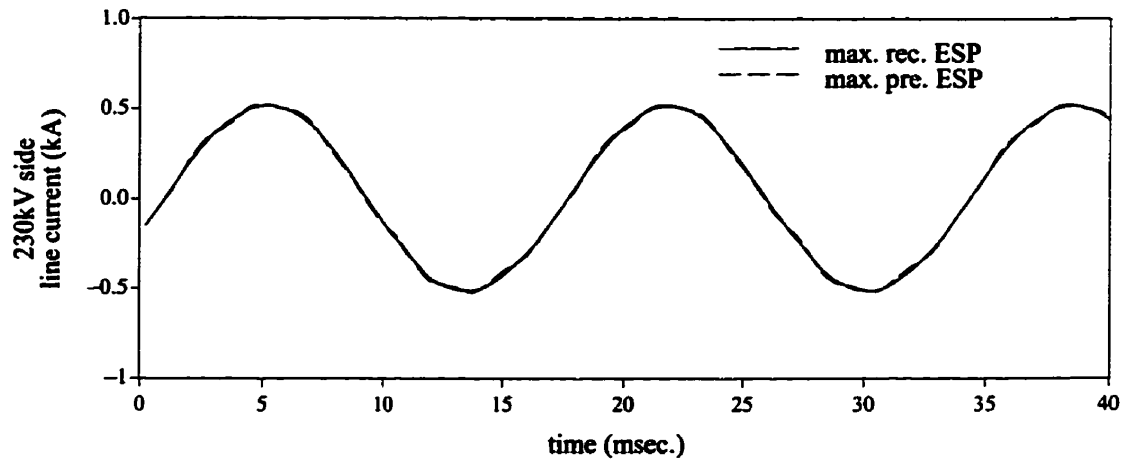


Figure 5 .19 : Current on Dorsey–Moranville line at Dorsey at high power flow

Table 5 .17 shows the rms magnitudes, maximum and minimum peak values of the two waveforms shown in the Figure 5 .19 .

Table 5 .17 : The details on the current flowing to Moranville after saturation

	Max. Rec. GIC	Max. Pred. GIC
rms magnitude (A)	364.6	366.3
maximum peak (A)	519.6	522.9
minimum peak (A)	-516.5	-520.8
per phase GIC (A)	32.8	69.7

Figure 5 .20 show the Fourier analysis of the waveforms shown in the Figure 5 .19 .

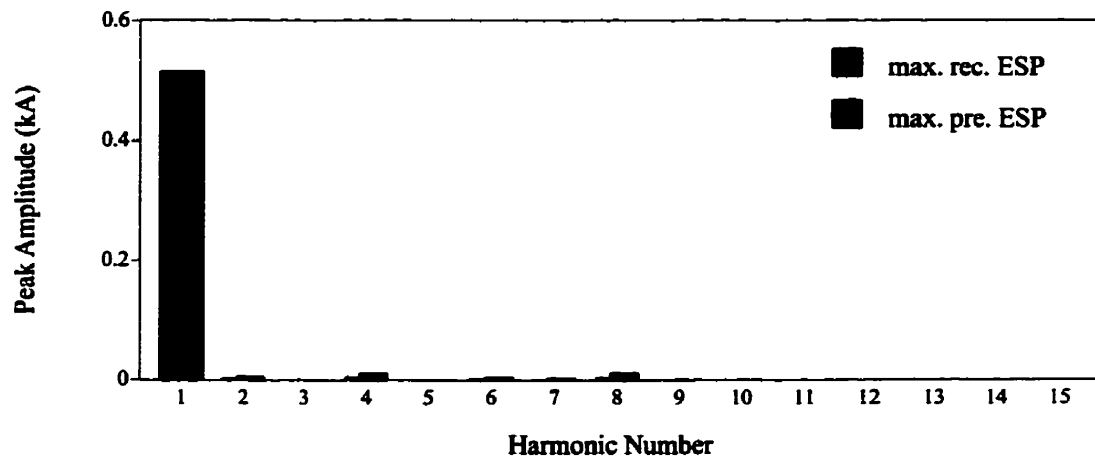


Figure 5.20 : Fourier analysis of current flowing to Moranville at high power flow

At low ESP conditions, the THD factor of the current flowing to Moranville at the 230 kV side of Dorsey is 1.29% whereas the corresponding figure at maximum predicted ESP conditions is 3.37%. The prominent harmonics are the 4th and the 8th.

The current flowing to Drayton shows less distortions as in the low power flow case. They are presented in appendix C .

5.3 CONCLUSIONS

Series compensation of the 500kV line completely blocks the GIC flow in the 500kV line. But there is still a small amount of GIC which flows through the 230kV side of the transformers at Dorsey. During the series compensation upgrade an additional set of transformers were also introduced in order to facilitate the increased power flow. This gives a further decreased GIC current per phase per transformer. Thus the effects of GIC are further reduced.

However, there is still some distortion of waveforms because of the small amount of GIC passing through the 230kV side of the transformer. At the maximum predicted ESP conditions, some waveforms have THD factors close to 20%. This could be even more if the power flow is less than the presented case of low power flow.

The 230kV transmission line to Moranville carries more GIC than the line to Drayton mainly due to the fact that there is a high ESP gradient along the line to Moranville.

More waveforms related to the studies presented in this chapter are presented in appendix C .

Chapter 6

Protection Considerations

6.1 CURRENT IN HARMONIC FILTERS

At the Dorsey converter station, there are filters tuned to the 5th, 7th, 11th and 13th harmonics. In addition there are high pass filters to filter out higher harmonics generated at the converter station. These high pass filters also provide the additional reactive power demand by the converter station. When the transformers are saturated due to the GIC, the harmonics produced will flow through these harmonic filters since it has a low impedance path.

6.1.1 HIGH PASS FILTER CURRENTS

6.1.1.1 BEFORE SERIES COMPENSATION AT MAXIMUM RECORDED ESP

Figures 6.1 and 6.2 show the current passing through the equivalent high pass filter for the high power flow and low power flow conditions respectively. These

simulated waveforms occur when the transformers are fully saturated at the maximum recorded GIC level.

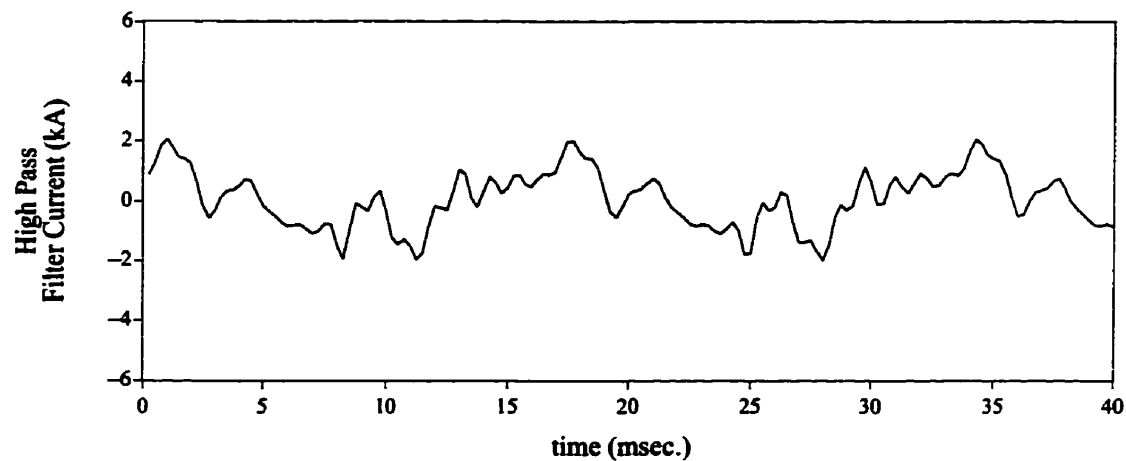


Figure 6.1 : High Pass Filter current at Dorsey with 105A GIC per phase and with a high power flow

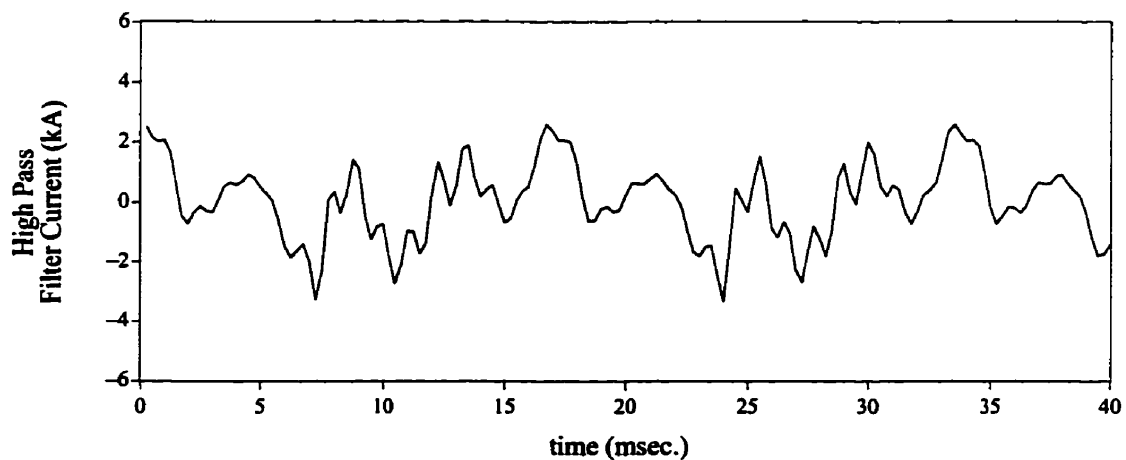


Figure 6.2 : High Pass Filter current at Dorsey with 105A GIC per phase and with a low power flow

The high pass filter current at high power flow conditions has a rms magnitude of 937.7 A with a maximum positive peak of 2045 A and a maximum negative peak of -1993 A whereas the high pass filter current at low power flow conditions has a rms magnitude of 1270 A with a positive peak of 2586 A and negative peak of -3338 A.

Figure 6.3 shows the harmonic composition of the high pass filter currents at two different power flows and at the maximum recorded GIC level.

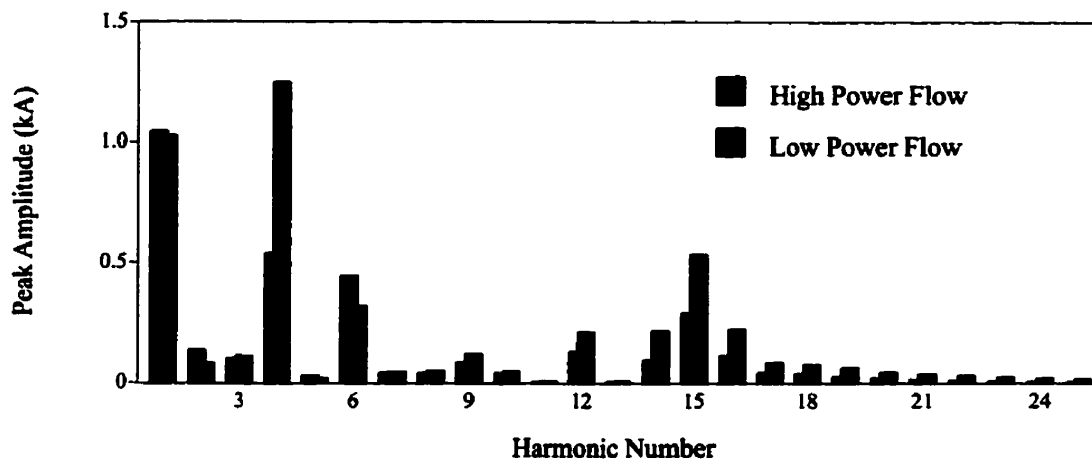


Figure 6.3 : Fourier analysis of high pass filter current waveforms at 105A GIC per phase on 500kV side

The harmonic composition follows more or less the same pattern irrespective of the level of power flow. The most dominant harmonic is the 4th harmonic. In the low power flow case, the 4th harmonic is even bigger than the fundamental. Other noticeable harmonics are the 6th, 15th, 12th, 14th and 16th.

Looking at the harmonic analysis of the high pass filter current waveforms in figure 6.3, it is very clear that a lot of harmonics non characteristic to a HVDC converter station exist in these currents. In fact, characteristic harmonics in these waveforms are very minimal due to the presence of filters tuned for those harmonics. There is a significant portion of fundamental component in these waveforms. This is due to the fact that the high pass filters at the Dorsey end are also used to give voltage support at Dorsey. The ratios of the total rms magnitude to that of the fundamental component is 126.7% and 174.7% for high power flow and low power flow conditions respectively when the GIC flow is 105A per phase. These values change to 136.5% and 195.2% respectively when the GIC flow is increased to 133A per phase.

At both GIC levels considered, it is clear that more harmonic currents flow through the high pass filter when the power flow is low. Table 6.1 shows the analysis of high pass filter currents obtained at maximum recorded GIC conditions.

Table 6 .1 : Analysis of high pass filter currents at different power flows before series compensation

power flow	I_{rms}	I_{1-rms}	I_{rms} / I_{1-rms} as a %age	positive peak	negative peak	rms based on max.peak	$I_{peak-rms} / I_{rms}$ as a %age
high	938	740	126.7	2045	-1993	1409	150.2
low	1270	727	174.7	2586	-3338	2360	185.9

If the waveforms are assumed to be sinusoidal and if the rms magnitude is derived from the absolute peak magnitude, then rms values are 1409A and 2360A respectively for high and low power flow conditions. These figures are 50.2% and 85.9% more than the actual rms magnitude of their corresponding waveforms for high and low power flow conditions respectively.

Therefore, if these high pass filters are protected by an overcurrent measurement based on peak detection, it would see a very high increase in the apparent rms value. This could trip the filters unnecessarily.

6.1.1.2 AFTER SERIES COMPENSATION AT MAXIMUM PREDICTED ESP

Figure 6 .4 shows the current going through the high pass filter at high power flow conditions when the transformers are fully saturated due to the applied ESP which is set to the maximum predicted.

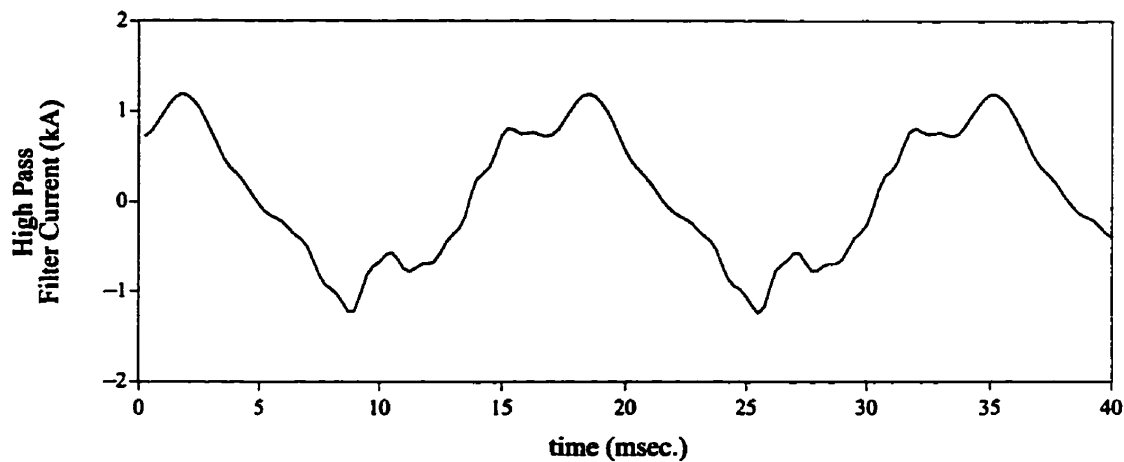


Figure 6.4 : High Pass Filter current at Dorsey with a high power flow

The high pass filter current has a rms magnitude of 714.7 A , a positive peak of 1191 A and a negative peak of -1242 A. Figure 6.5 shows the current going through the high pass filter at low power flow conditions when the transformers are fully saturated due to the GIC created by the same ESP.

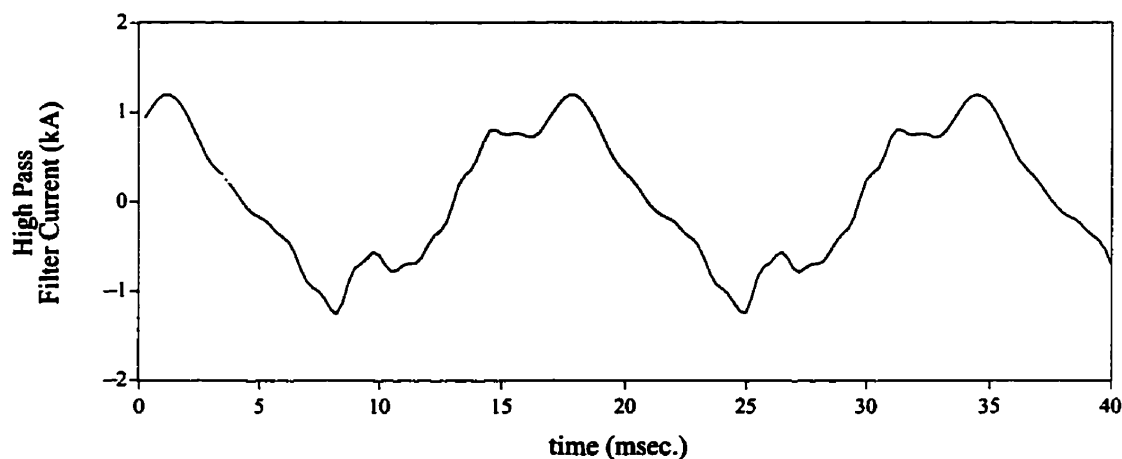


Figure 6.5 : High Pass Filter current at Dorsey at low power flow

The high pass filter current has a rms magnitude of 722.4 A , a positive peak of 1201 A and a negative peak of -1254 A. The Fourier analysis of these two waveforms are shown in Figure 6.6 .

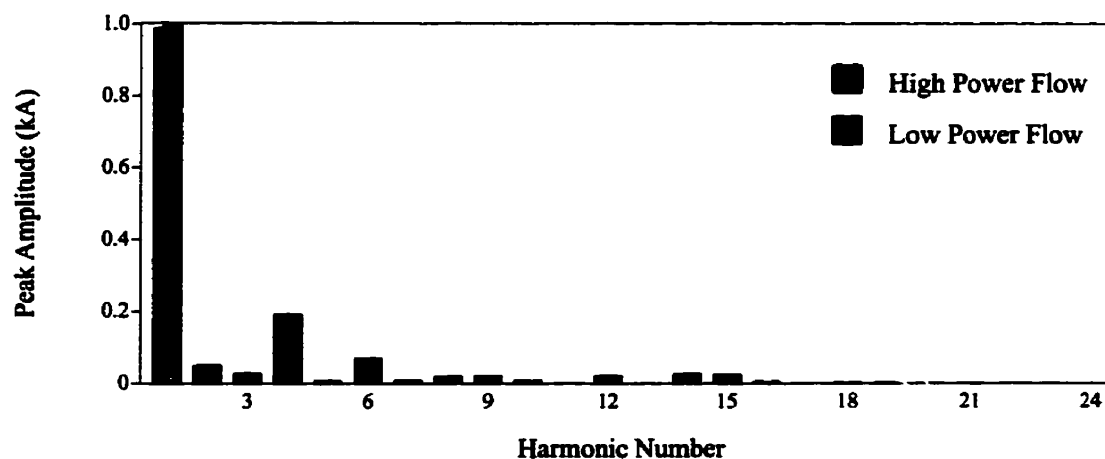


Figure 6 .6 : Fourier analysis of currents in high pass filter

The harmonic composition is almost the same irrespective of the level of power flow for this low saturation condition. The most dominant harmonic is the 4th harmonic. Other noticeable harmonics are the 6th and 2nd.

Table 6 .2 shows the analysis of the high pass filter currents obtained at the maximum predicted GIC conditions for two different power flows.

Table 6 .2 : Analysis of high pass filter currents at different power flows after series compensation

power flow	I_{rms}	I_{1-rms}	I_{rms} / I_{1-rms} as a %age	positive peak	negative peak	rms based on max.peak	$I_{peak-rms} / I_{rms}$ as a %age
high	715	699	102.3	1191	-1242	878	122.8
low	722	707	102.1	1201	-1254	887	122.8

If the waveforms are assumed to be sinusoidal and if the rms magnitude is derived from the absolute peak magnitude, the waveforms see magnitudes 878A and 887A respectively for high and low power flow conditions. These figures are 22.8% more than the actual rms magnitude of their corresponding waveforms for both high and low power flow conditions.

Therefore, if these high pass filters are protected by an overcurrent measurement based on peak detection, the protection device would see an increase in the apparent rms value. This could trip the filters unnecessarily.

6.1.2 CURRENT IN TUNED FILTERS

The tuned filters at the Dorsey converter station were introduced in two stages. In the first stage four tuned filters tuned to the 5th, 7th, 11th and 13th harmonics were introduced for the 6 pulse bridge installed. Another set of 11th and 13th tuned harmonic filters were introduced in the second stage for the 12 pulse bridge installed.

6.1.2.1 BEFORE SERIES COMPENSATION AT MAXIMUM RECORDED ESP

Figure 6.7 shows the current going through one of the 13th harmonic tuned filters installed in the second stage when the power flow is high and the GIC is 315 A.

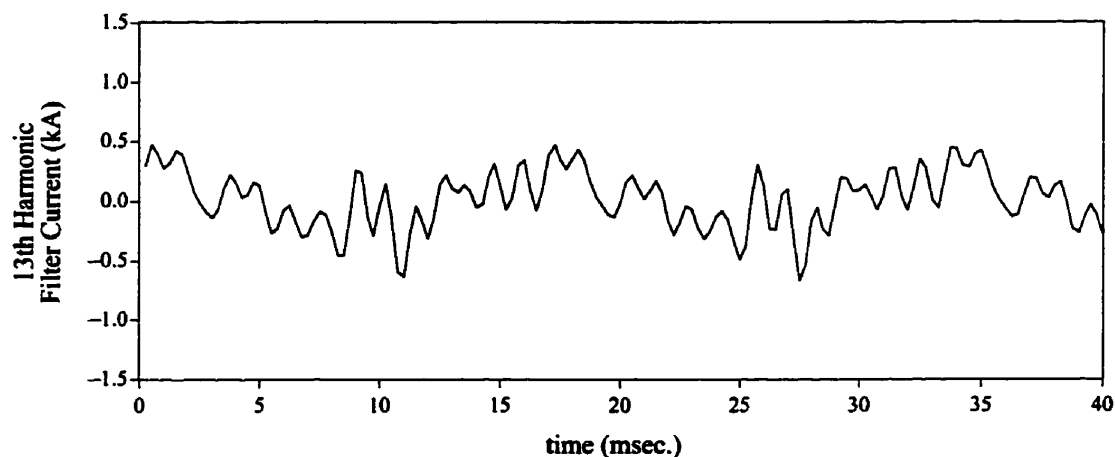


Figure 6.7 : 13th Harmonic Filter current at Dorsey with 105A GIC per phase and with a high power flow

The current waveform has a rms magnitude of 239 A with a positive peak of 470.8 A and a negative peak of -682.6 A. The 13th harmonic component of the current flowing through the filter is 38.3 A. Figure 6.8 shows the current going through the same filter at the same GIC level when the power flow is low.

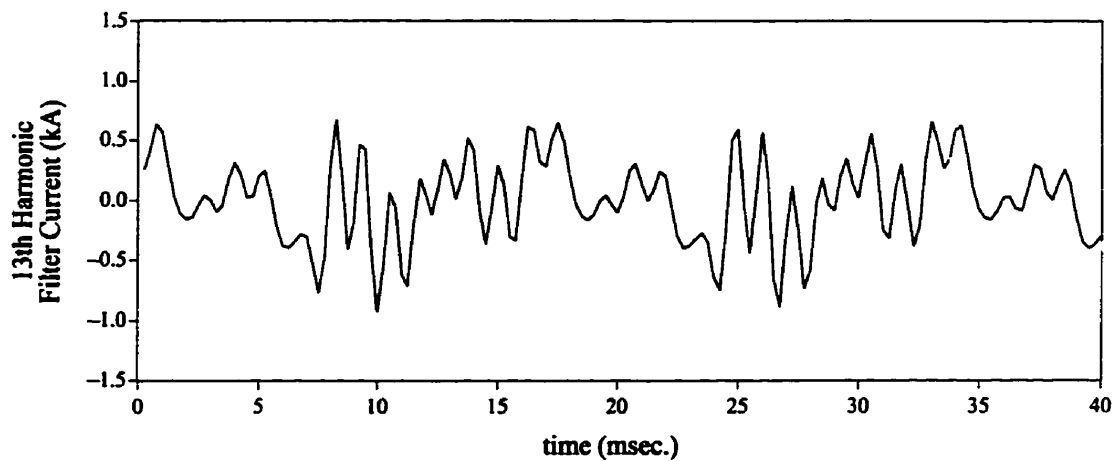


Figure 6.8 : 13th Harmonic Filter current at Dorsey with 105A GIC per phase and with a low power flow

The current waveform has a rms magnitude of 357.1 A with a positive peak of 666.5 A and a negative peak of 926.7 A. The 13th harmonic component flowing through the filter has a magnitude of 48.2 A. Figure 6.9 shows the Fourier analysis of the two current waveforms flowing through the same tuned filter for the two different power flow conditions.

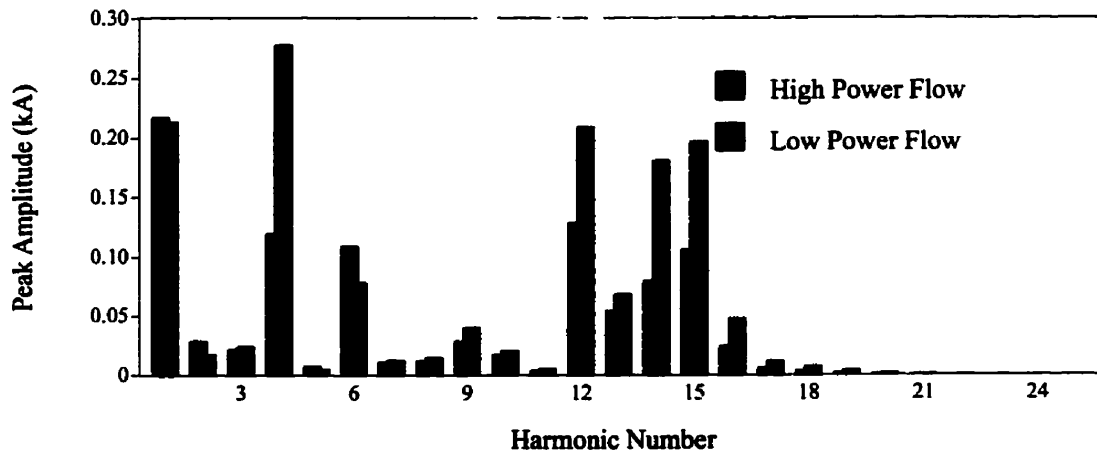


Figure 6.9 : Fourier analysis of currents in 13th harmonic filter before compensation

In both cases, the significant harmonics are the 4th, 6th, 12th, 13th, 14th and 15th. In the high power flow case, the dominant harmonic is the 12th. But in low power flow

case, the 4th harmonic became the dominant harmonic. In the latter case, the 4th harmonic is even bigger than the fundamental component in that current.

Figure 6 .10 shows the waveform of the current flowing through the 5th harmonic tuned filter which was installed at the first stage. The waveform is taken at high power flow conditions and at a 315 A GIC level.

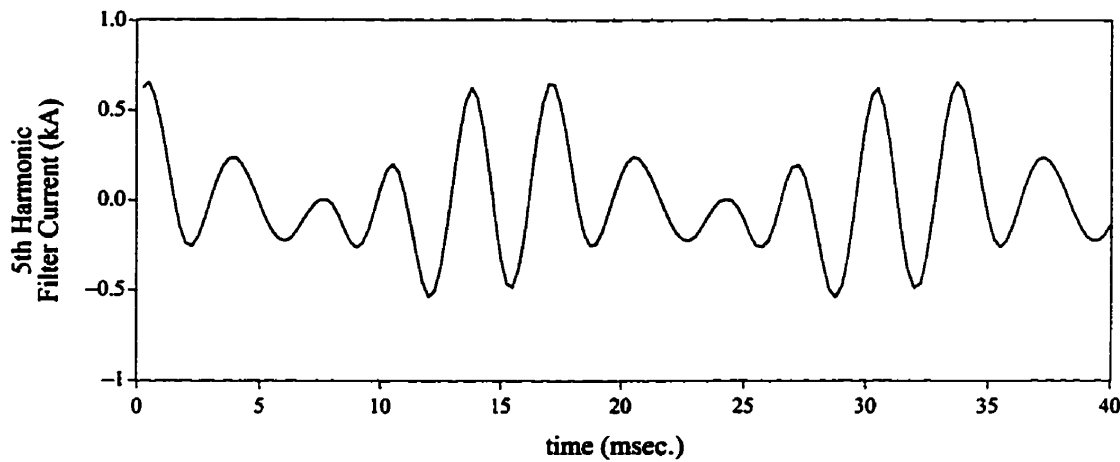


Figure 6 .10 : 5th Harmonic Filter current at Dorsey with 105A GIC per phase and with a high power flow

The current waveform has a rms magnitude of 294.5 A with a positive peak of 658.7 A and a negative peak of -539.2 A. The 5th harmonic component flowing through the filter is 237.6 A. Figure 6 .11 shows the current flowing in the same filter when the power flow was changed to the low power flow condition described before.

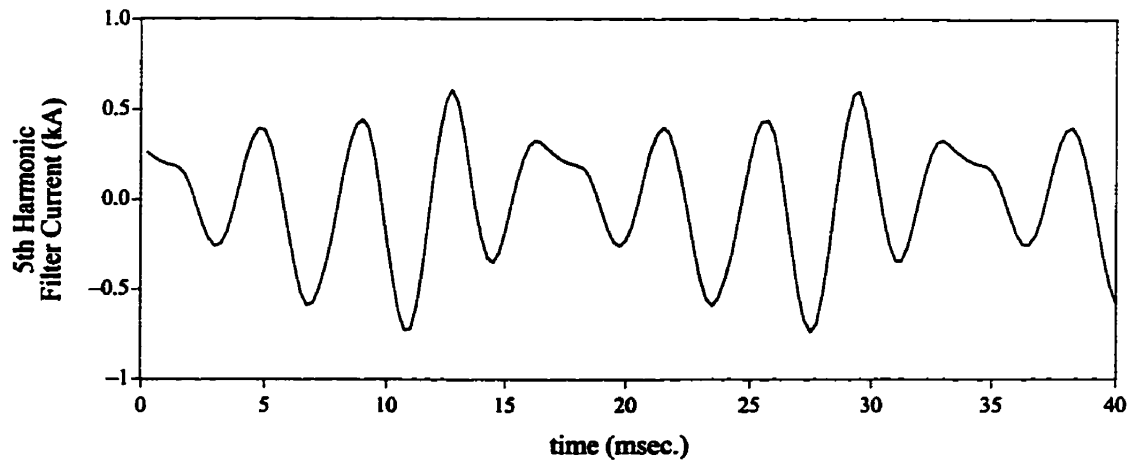


Figure 6 .11 : 5th Harmonic Filter current at Dorsey with 105A GIC per phase and with a low power flow

The current waveform has a rms magnitude of 340.3 A with a positive peak of 609.9 A and a negative peak of -738.2 A. The 5th harmonic component flowing through the filter is 154.5 A. Figure 6 .12 shows the Fourier analysis of the two current waveforms flowing through the same tuned filter for the two different power flow conditions.

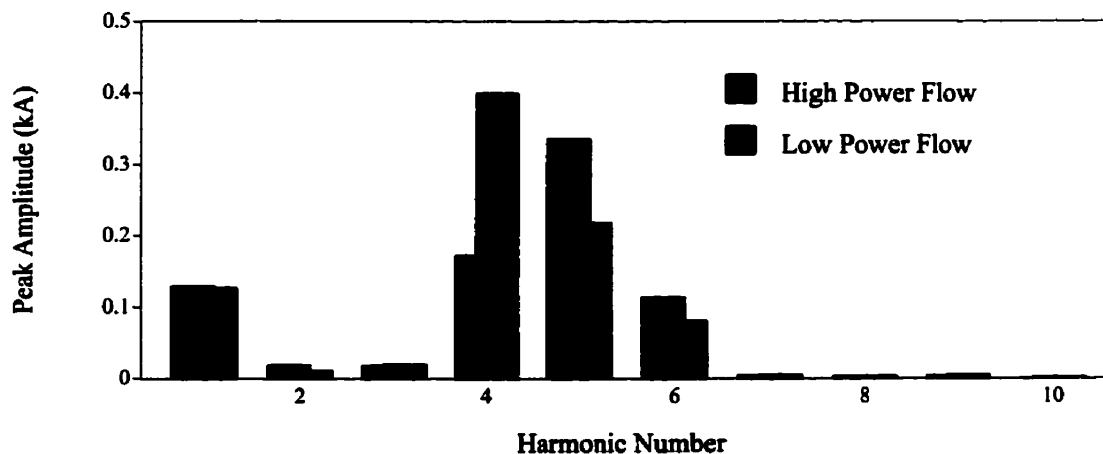


Figure 6 .12 : Fourier analysis of currents in 5th harmonic filter before compensation

In both cases, the significant harmonics are the 4th, 5th and 6th. In the high power flow case, dominant harmonic is the 5th. But in the low power flow case, the 4th harmonic became the dominant harmonic. In both cases, the 4th and 5th harmonics are bigger than the corresponding fundamental component.

Tables 6.3 and 6.4 show the detailed analysis of currents flowing through tuned filters for both high power flow and low power flow conditions respectively. The analysis was done for the waveforms obtained for 105 A GIC per phase condition. The tables give the details of the rms magnitude of the current waveform with their positive and negative peak values, the rms magnitudes of the fundamental frequency component and the tuned frequency component and also the rms magnitude of the combined fundamental and tuned frequency components.

Table 6.3 : Analysis of currents through the tuned harmonic filters for a high power flow

Tuned Filter	Positive Peak (A)	Negative Peak (A)	RMS (A)	RMS of fundamental component (A)	RMS of tuned frequency component (A)	RMS of fundamental and tuned frequency components (A)	RMS of harmonics other than fundamental and tuned frequency components (A)
5	658.7	-539.2	294.5	91.8	237.7	254.8	147.7
7	286.0	-403.3	176.8	45.9	153.1	159.8	75.6
11	270.7	-195.5	103.8	69.7	30.3	76.0	70.7
13	148.2	-237.5	79.6	49.8	22.4	54.6	57.9
11	766.9	-595.4	313.1	218.2	48.2	223.5	219.3
13	470.8	-682.6	239.0	154.0	38.3	158.7	178.7

Table 6 .4 : Analysis of currents through the tuned harmonic filters for a low power flow

Tuned Filter	Positive Peak (A)	Negative Peak (A)	RMS (A)	RMS of fundamental component (A)	RMS of tuned frequency component (A)	RMS of fundamental and tuned frequency components (A)	RMS of harmonics other than fundamental and tuned frequency components (A)
5	609.9	-738.2	340.3	90.2	154.5	178.9	289.5
7	354.5	-408.3	200.0	45.1	171.7	177.5	92.1
11	374.8	-309.3	144.8	68.5	49.0	84.2	117.8
13	231.5	-319.9	117.8	48.9	28.1	56.4	103.4
11	1046.0	-974.7	430.6	214.4	71.0	225.9	366.6
13	665.5	-927.3	357.1	151.2	48.2	158.7	319.9

From the analysis of the harmonic content of the current flowing in the tuned filters as illustrated by the tables 6 .3 and 6 .4 , it is clear from the last column of the tables, that the total harmonic content of frequencies other than the fundamental and the tuned frequency is significant. It is appropriate to consider the ratios between the rms magnitude of the waveform with the rms magnitude of combined fundamental component and the tuned frequency component since those two frequencies are the frequencies that are expected to flow in the tuned filters at normal operating conditions. The ratios of the rms magnitude of the waveform to the rms magnitude of the combined fundamental and the tuned frequency varies between 111% to 150% in the case of the high power flow condition. It varies between 113% to 225% in the case of low power flow condition. The harmonic content of frequencies other than the fundamental and the tuned frequency is more when the power flow is low.

Table 6 .5 shows an analysis of the apparent increase of magnitudes seen if the rms magnitudes are derived from peak values of the waveforms for both high and low power flow conditions.

Table 6.5 : Apparent increase of rms magnitudes when based on peak values

Tuned Filter	high power flow				low power flow			
	max. abs. peak (A)	rms based on peak (A)	rms (A)	apparent increase %	max. abs. peak (A)	rms based on peak (A)	rms (A)	apparent increase %
5	658.7	465.8	294.5	58.2	738.2	522.0	340.3	53.4
7	403.3	285.2	176.8	61.6	408.2	288.6	200.0	44.3
11	270.7	191.4	103.8	84.4	374.8	265.0	144.8	83.0
13	237.5	167.9	79.6	110.9	319.9	226.2	117.8	92.0
11	766.9	542.3	313.1	73.2	1046.0	739.6	430.6	71.8
13	682.6	482.7	239.0	102.0	927.3	655.7	357.1	83.6

6.1.2.2 AFTER SERIES COMPENSATION AT MAXIMUM PREDICTED ESP

Figure 6.13 shows the current passing through the 13th harmonic filter installed in the second stage, when the potential difference between Dorsey and Forbes is set to the same potential difference that would have produced the maximum predicted GIC before the series compensation.

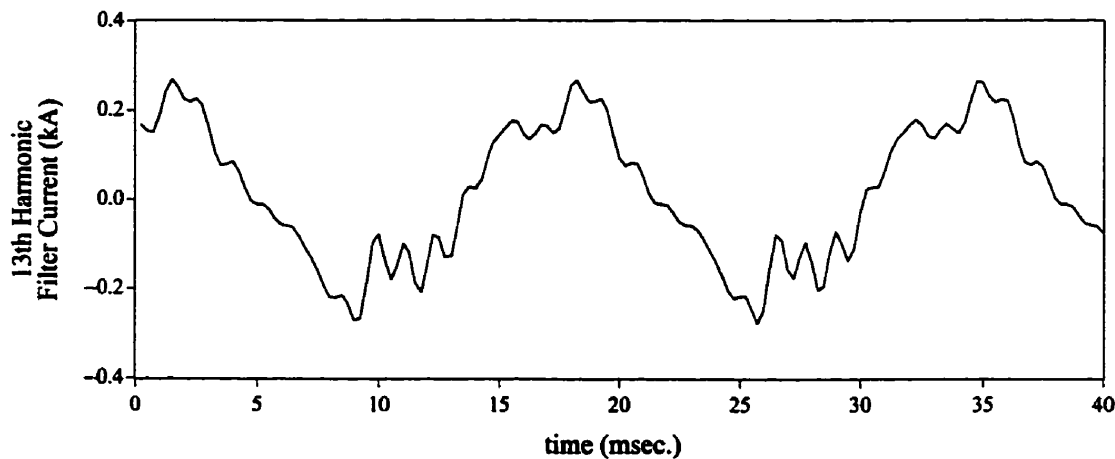


Figure 6.13 : 13th Harmonic Filter current at Dorsey with 105A GIC per phase and with a high power flow

The waveform has a rms magnitude of 151.0 A with a positive peak magnitude of 268.3 A and a negative peak magnitude of -276.7 A.

Figure 6.14 shows the current passing through the 13th harmonic filter installed in the second stage, when the potential difference between Dorsey and Forbes is set to the same potential difference that would have produced the maximum predicted GIC before the series compensation. This waveform was obtained at low power flow conditions.

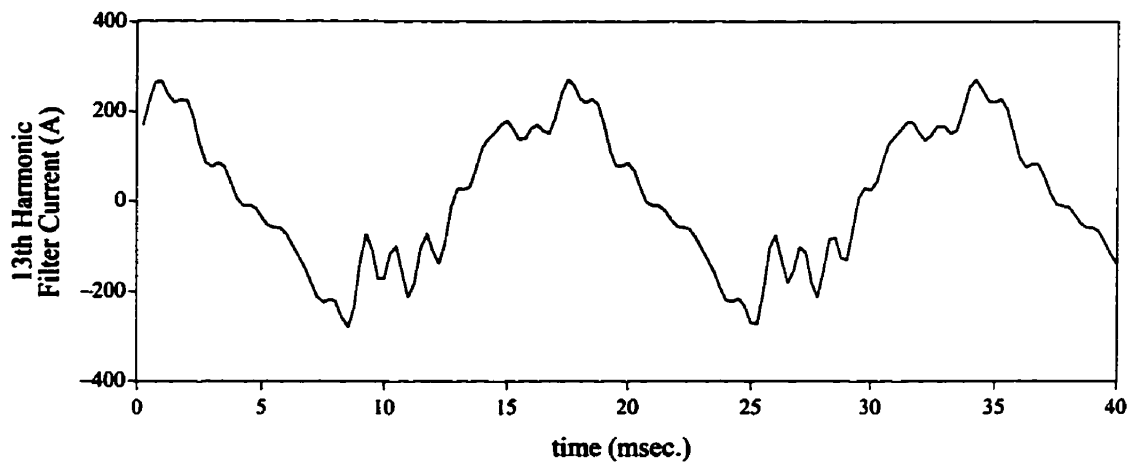


Figure 6.14 : 13th Harmonic Filter current at Dorsey

The waveform has a rms magnitude of 152.6 A with a positive peak magnitude of 270.5 A and a negative peak magnitude of -279.8 A. The Fourier analysis of these waveforms are shown in the Figure 6.15.

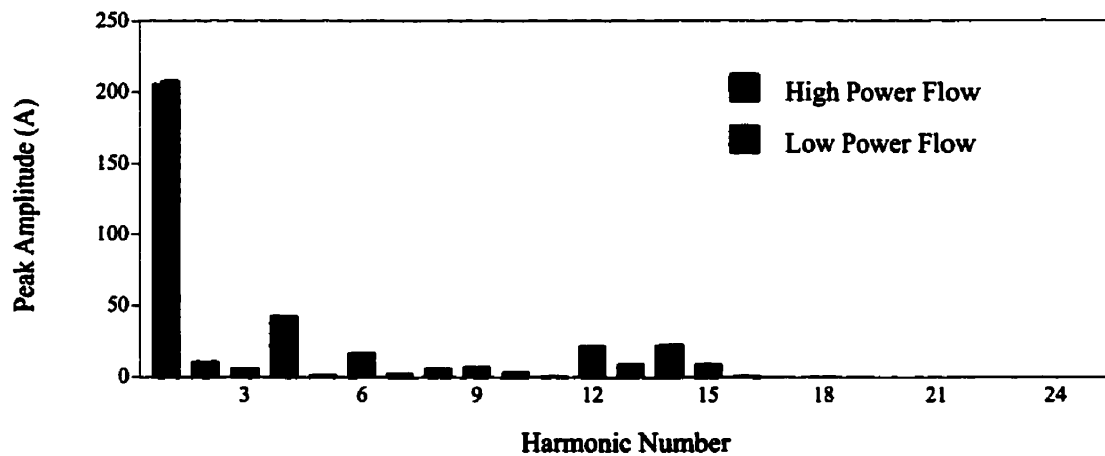


Figure 6.15 : Fourier analysis of currents in 13th harmonic filter after compensation

The current passing through the 13th harmonic tuned filter contains mostly fundamental and a significant contribution from the 4th harmonic. It also has slight contributions from the 6th, 12th and 14th harmonics. The harmonic compositions of both waveforms are almost the same irrespective of the level of power flow.

Figure 6 .16 shows the current passing through the 5th harmonic tuned filter at high power flow conditions when the transformers are fully saturated due to the applied ESP.

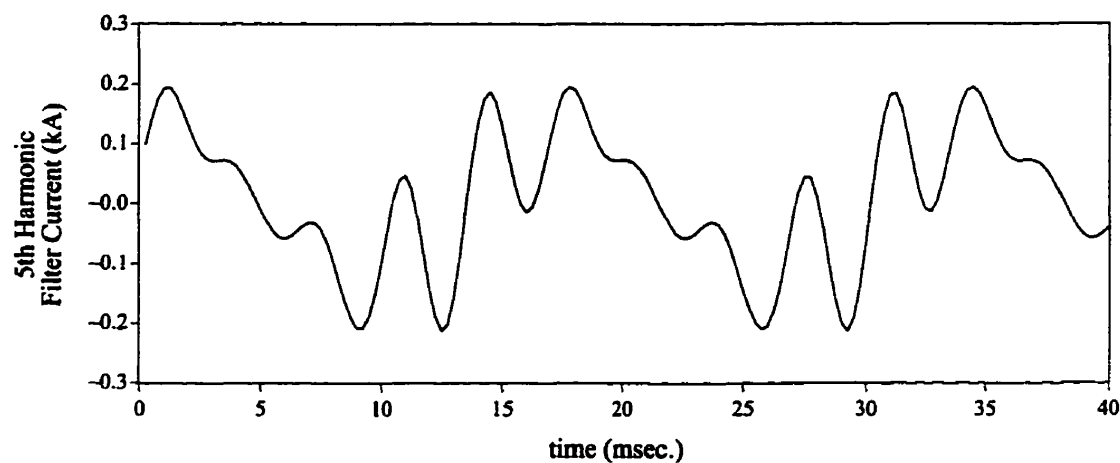


Figure 6 .16 : 5th Harmonic Filter current at Dorsey with 105A GIC per phase and with a high power flow

The waveform of the current going through the 5th harmonic filter is highly distorted. It has an rms magnitude of 113.7 A with a positive peak of 195.5 A and a negative peak of -212.4 A.

Figure 6 .17 shows the current passing through the 5th harmonic tuned filter during the low power flow condition when the transformers are fully saturated due to the applied ESP.

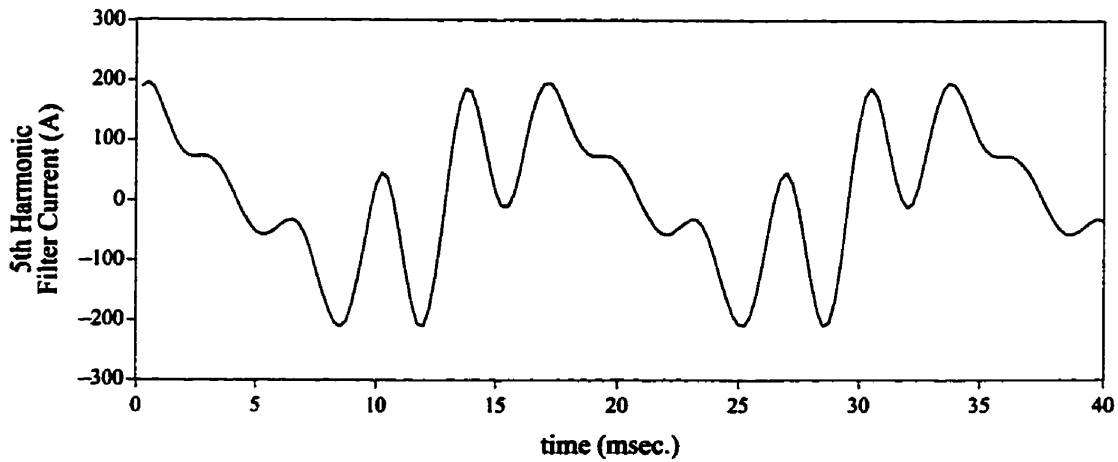


Figure 6 .17 : 5th Harmonic Filter current at Dorsey

The waveform of the current going through the 5th harmonic filter is highly distorted. It has an rms magnitude of 114.3 A with a positive peak of 196.8 A and a negative peak of -212.7 A. The Fourier analysis of these waveforms is shown in figure 6 .18 .

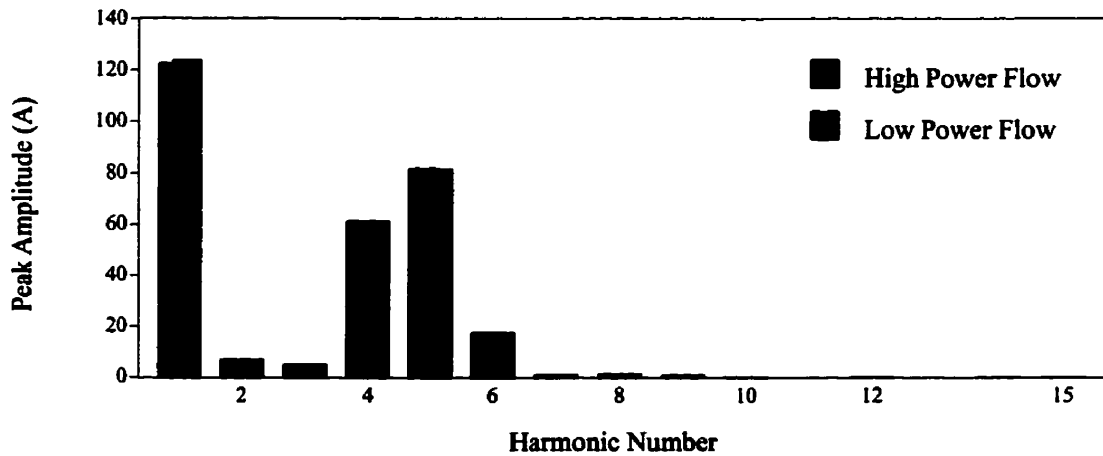


Figure 6 .18 : Fourier analysis of currents in 5th harmonic filter after compensation

The waveforms contain not only the fundamental and the tuned 5th harmonic, they contain a lot of 4th harmonic and a significant amount of 6th, 2nd and 3rd harmonic components. At this low saturation condition, the harmonic composition of both waveforms is almost the same irrespective of the power flow.

Table 6 .6 and Table 6 .7 show the results of analysis of the currents going through the tuned filters when the transformers are fully saturated due to the applied ESP at

high and low power flow conditions respectively. The analysis was done for the waveforms obtained for the maximum predicted ESP condition. The tables give the details of the rms magnitude of the current waveform with their positive and negative peak values, the rms magnitudes of the fundamental frequency component and the tuned frequency component and also the rms magnitude of the combined fundamental and tuned frequency components.

Table 6.6 : Analysis of currents through the tuned harmonic filters for a high power flow

Tuned Filter	Positive Peak (A)	Negative Peak (A)	RMS (A)	RMS of fundamental component (A)	RMS of tuned frequency component (A)	RMS of fundamental and tuned frequency components (A)	RMS of harmonics other than fundamental and tuned frequency components (A)
5	195.5	-212.4	113.7	86.7	58.1	104.4	45.1
7	110.5	-110.2	57.4	43.4	34.1	55.2	15.8
11	124.7	-118.0	68.4	65.9	6.7	66.2	17.2
13	84.2	-90.9	48.9	47.0	3.7	47.2	12.9
11	378.5	-356.7	213.3	206.1	10.6	206.4	53.8
13	268.3	-276.7	151.0	145.5	6.3	145.6	40.0

Table 6.7 : Analysis of currents through the tuned harmonic filters for a low power flow

Tuned Filter	Positive Peak (A)	Negative Peak (A)	RMS (A)	RMS of fundamental component (A)	RMS of tuned frequency component (A)	RMS of fundamental and tuned frequency components (A)	RMS of harmonics other than fundamental and tuned frequency components (A)
5	196.8	-212.7	114.3	87.7	57.8	105.0	45.1
7	111.4	-111.1	57.9	43.8	34.3	55.6	15.9
11	125.7	-119.1	69.1	66.6	6.7	66.9	17.3
13	85.0	-92.1	49.7	47.6	3.7	47.7	13.0
11	381.2	-360.1	215.6	208.5	10.7	208.7	54.0
13	270.5	-279.8	152.6	147.1	6.4	147.2	40.3

At this low saturation condition, the fundamental frequency component and the tuned frequency component make up the major portion of the current going through the tuned filters.

Table 6.8 shows an analysis of the apparent increase of magnitudes seen if the rms magnitudes are derived from peak values of the waveforms for both high and low power flow conditions.

Table 6.8 : Apparent increase of rms magnitudes when based on peak values

Tuned Filter	high power flow				low power flow			
	max. abs. peak (A)	rms based on peak (A)	rms (A)	apparent increase %	max. abs. peak (A)	rms based on peak (A)	rms (A)	apparent increase %
5	212.4	150.2	113.7	32.1	212.7	150.4	114.3	31.6
7	110.5	78.1	57.4	36.1	111.4	78.8	57.9	36.1
11	124.7	88.2	68.4	28.9	125.7	88.9	69.1	28.7
13	90.9	64.3	48.9	31.5	92.1	65.1	49.7	31.0
11	378.5	267.6	213.3	25.5	381.2	269.5	215.6	25.0
13	276.7	195.7	151.0	29.6	279.8	197.8	152.6	29.6

There is an apparent increase of about 30%, if the rms magnitudes were derived from the peak magnitudes of the waveforms irrespective of the level of power flow. This could change at a higher level of saturation but it is very unlikely since the presented data is simulated under maximum predicted ESP conditions which is approximately twice the level of the maximum recorded level.

6.1.3 SUMMARY

From the analysis of waveforms of currents going through the harmonic filters at maximum recorded GIC level before series compensation the following

observations can be made. A significant portion, sometimes a major portion, of the waveform is comprised of harmonics which are uncharacteristic to a DC converter station. Comparison of peak values and rms magnitudes of the waveforms show that peak detection overcurrent protection schemes are not suitable for harmonic filters when GIC is present. A peak detection method can give a false indication 210% from the actual rms magnitude at maximum recorded GIC level. Another observation is that the peak detection method gives a larger error in the 11th and 13th harmonic filters than the 5th and 7th harmonic filters.

After series compensation, the level of saturation was greatly reduced due to the increased resistance to dc due to the series capacitors in the GIC path. Therefore the amount of harmonic distortion is less even at maximum predicted ESP level which is more than twice the maximum recorded ESP level. The contribution of the uncharacteristic harmonics in currents going through the harmonic filters is low. The error of calculating rms based on peak value is about 30% even at the maximum predicted ESP conditions.

It should be noted that these waveforms do not contain the harmonic currents generated at the converter station. This is because the converter station is modelled as an equivalent AC source. Actual harmonic currents of 5th, 7th, 11th and 13th harmonics are different than the simulated waveforms. This difference is small at the low power flow condition since the characteristic harmonic currents produced by the HVDC converter station at low power flow is much smaller[29]. All the other harmonics will remain more or less the same.

6.2 INSTRUMENT TRANSFORMER RESPONSE

Instrument transformers are used to transform large magnitude voltages and currents to smaller magnitudes for metering and protection devices. Voltage transformers (VT) or Capacitive Voltage Transformers (CVT) are used for voltage transformation whereas Current Transformers (CT) are used for current transformation. This section looks into the effects of GIC on these instrument transformers.

6.2.1 CURRENT TRANSFORMER RESPONSE

Current Transformer ratios for protection systems are determined by the available load current. But the physical size of the transformer core is determined by the available fault current. When this axiom is followed, it is unlikely that the CT saturates before the saturation of the power transformer where the physical size of the core is determined by the available fault current.

To investigate the effect of GIC on CTs under no fault GIC conditions, a model of the CT on the 500 kV line[17] is fed with the waveforms obtained for the maximum recorded GIC level. A 15 VA 0.85 power factor burden at 5 A is used as the burden for the CT. The CT burden is small giving a slow rate of build up of dc bias. But the steady state dc bias of the CT is not affected by the size or the power factor of the burden.

Figure 6.19 shows the CT response to the 500 kV line current obtained for the maximum recorded GIC conditions and at low power flow conditions before series compensation. The two waveforms presented are the input current referred to the secondary and the output current of the CT for the burden chosen.

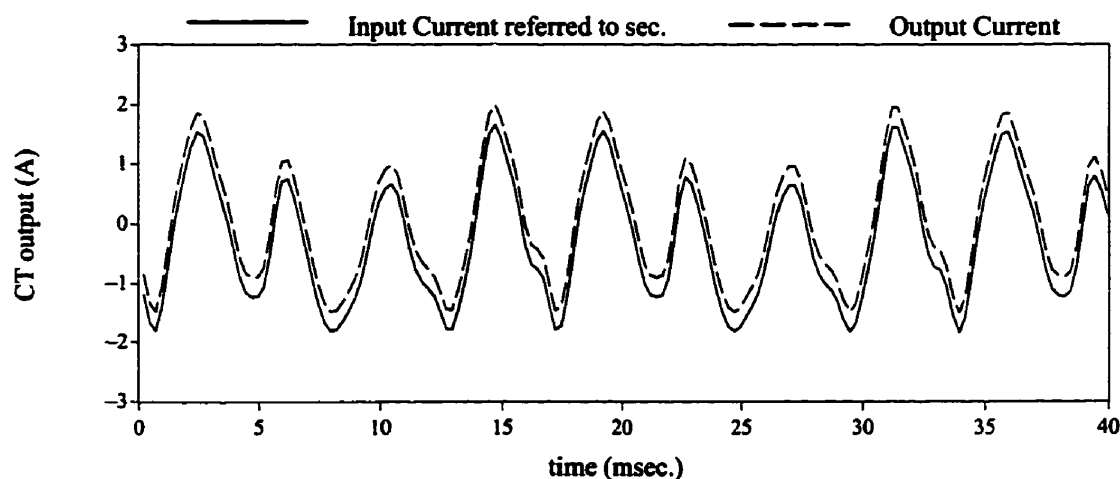


Figure 6.19 : CT Response for 105A GIC per phase, low power case

Both waveforms follow the same pattern. The GIC current in the input waveform is not transformed to the secondary. The difference between the two waveforms

is the magnetising current referred to the secondary of the CT. Figure 6 .20 shows the harmonic magnitudes of both waveforms.

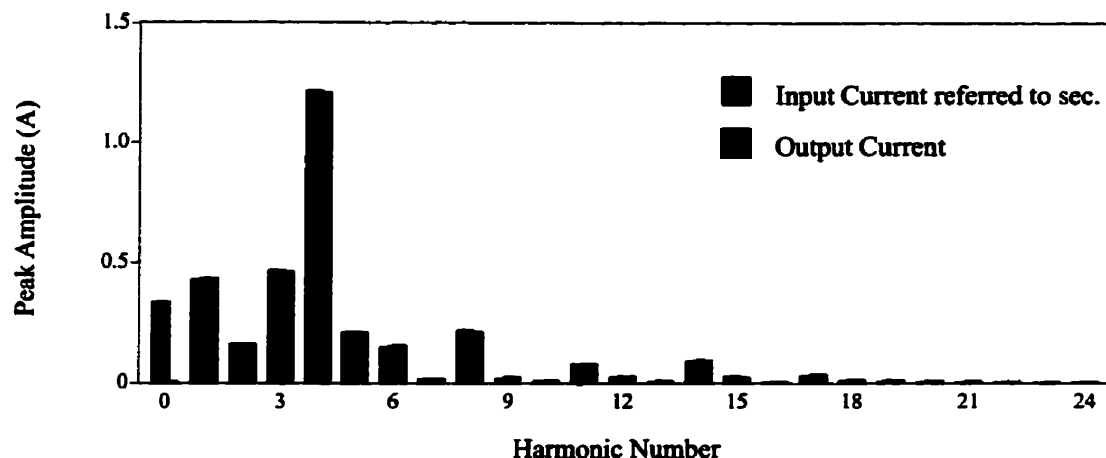


Figure 6 .20 : Magnitude of the harmonics in current waveforms at low power flow

There is hardly any difference in harmonic magnitudes. In fact the difference in magnitudes for different harmonics was always less than 6 mA. Figure 6 .21 shows the phase shift of harmonics when the waveform is transformed through the CT.

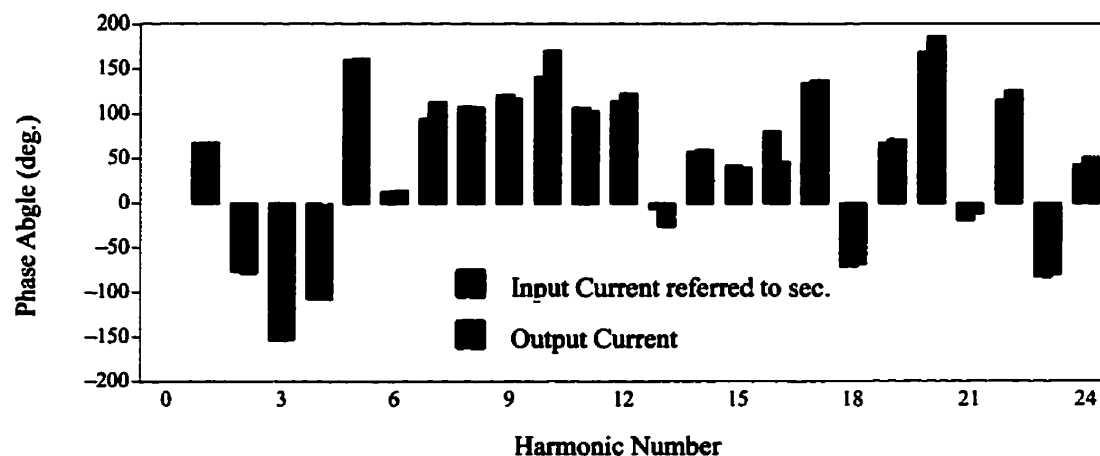


Figure 6 .21 : Phase of the harmonics in current waveforms at low power flow

For all the harmonics whose magnitudes are greater than 12 mA the phase shift compared to the input waveform is less than 2 degrees. It is clear that the distortions caused by the non-linearity of the CT is very insignificant compared to the distortions caused by the non-linearity of power transformers under no fault GIC conditions.

Figures 6.22 and 6.23 show the flux density and the magnetizing core current of the current transformer for the low power flow conditions respectively.

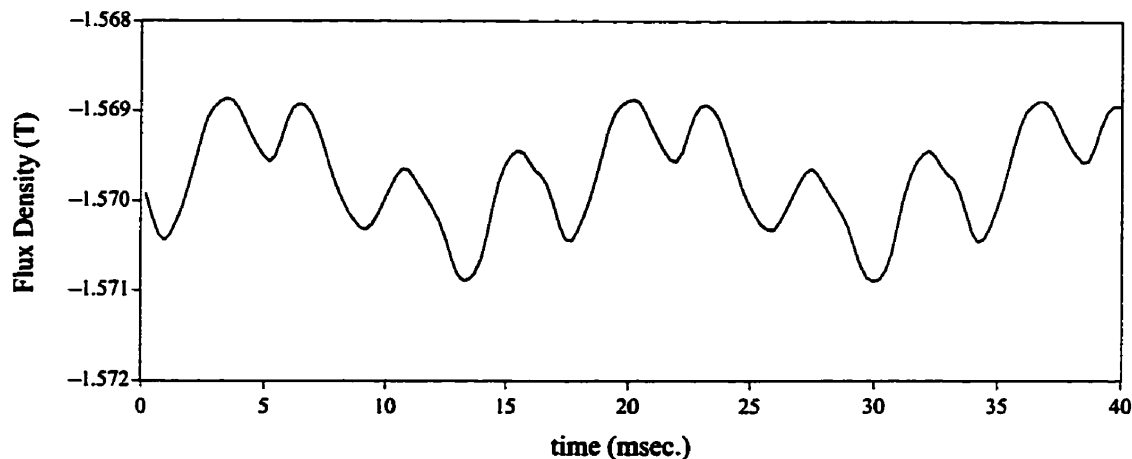


Figure 6.22 : Flux Density of the CT for 105A GIC per phase, low power case

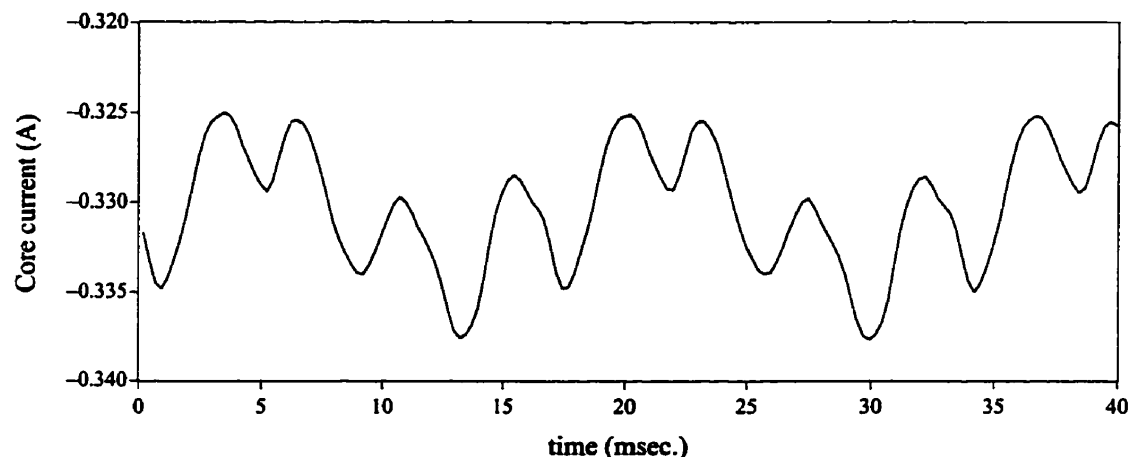


Figure 6.23 : Core current of the CT for 105A GIC per phase, low power case

The current transformer operates at a higher flux density due to the GIC current in the input waveform.

Figure 6.24 shows the CT response to the 500 kV line current obtained for the maximum recorded GIC conditions and at the high power flow condition before the series compensation. The two waveforms presented are the input current referred to the secondary and the output current of the CT for the burden chosen.

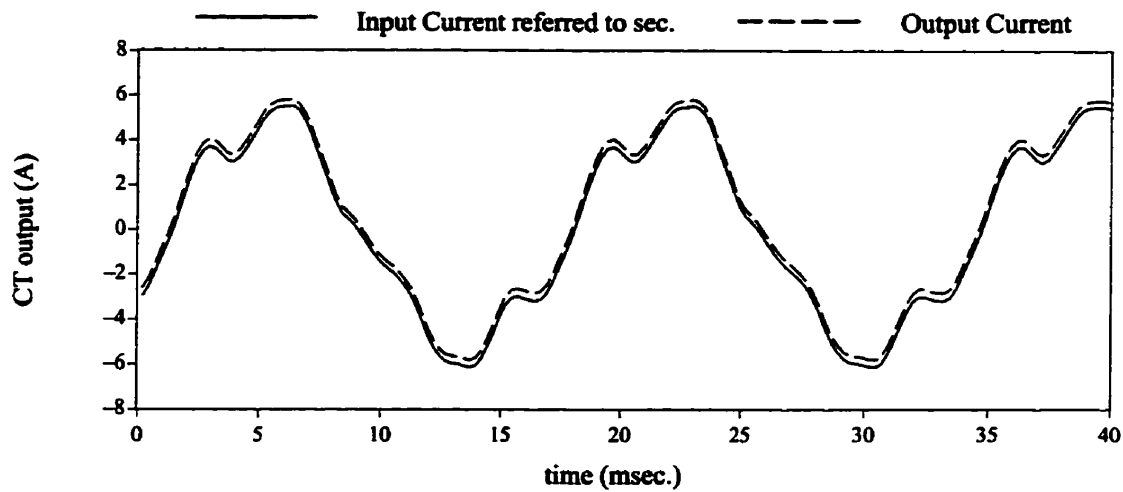


Figure 6 .24 : CT Response for 105A GIC per phase high power case

Both waveforms follow the same pattern. The GIC current in the input waveform is not transformed to the secondary. Figure 6 .25 shows the harmonic magnitudes of both waveforms.

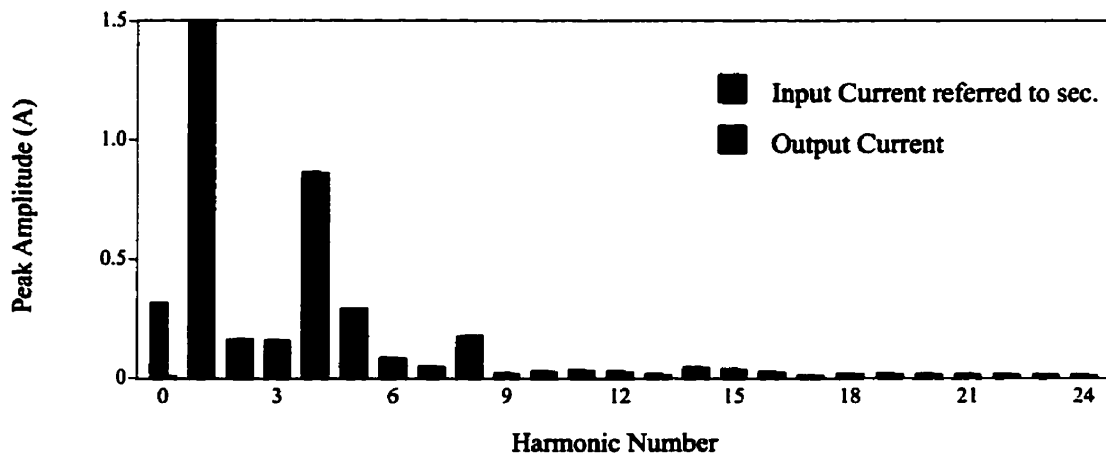


Figure 6 .25 : Magnitude of the harmonics in current waveforms at high power flow

There is hardly any difference in magnitudes. In fact the difference in magnitudes for different harmonics was always less than 6 mA. Figure 6 .26 shows the phase shift of harmonics when the waveform is transformed through the CT.

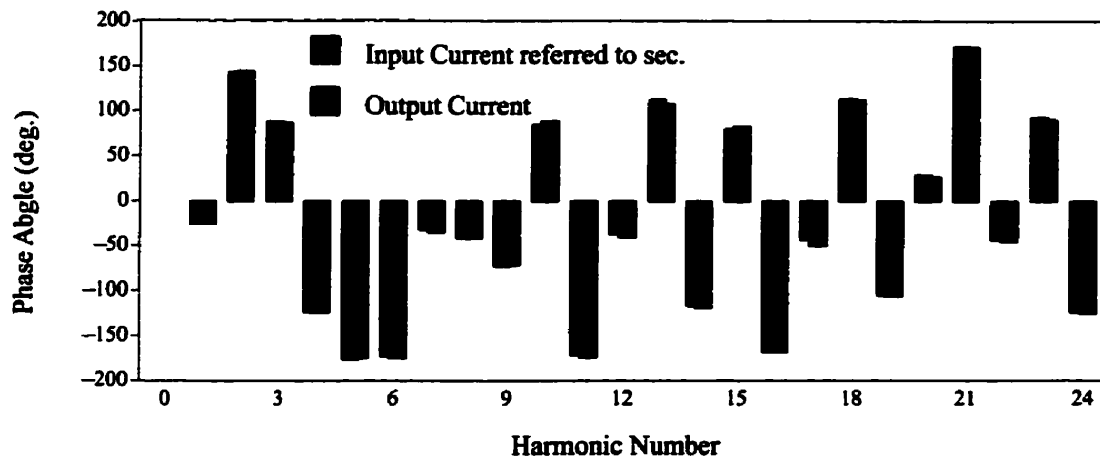


Figure 6 .27 : Phase of the harmonics in current waveforms at high power flow

For all the harmonics whose magnitudes are greater than 50 mA the phase shift compared to the input waveform is less than 2 degrees. It is clear that the distortions caused by the non-linearity of the CT are very insignificant compared to the distortions caused by the non-linearity of the power transformers under no fault GIC conditions.

Figures 6 .28 and 6 .29 show the flux density and the magnetizing core current of the current transformer for the high power flow condition.

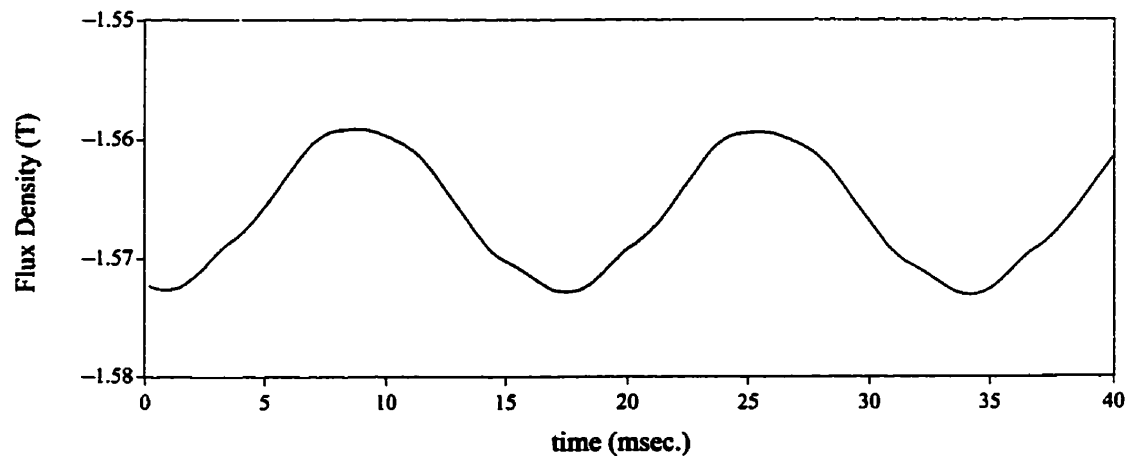


Figure 6 .28 : Flux Density of the CT for 105A GIC per phase, high power case

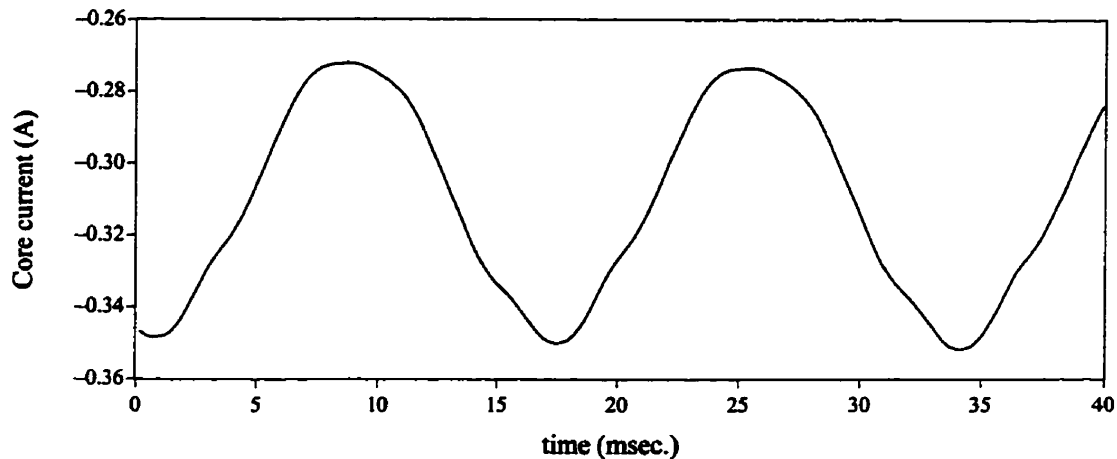


Figure 6 .29 : Core current of the CT for 105A GIC per phase high power case

By analyzing the waveforms in Figures 6 .19 – 6 .29 , it can be concluded that at steady state, the distortions introduced by current transformers are very minimal even at very high GIC levels. But if a fault occurs during a GIC event, and if that fault creates a dc bias of the current towards the same direction as the dc bias created by GIC, then the CT will saturate sooner. This might cause the relay to take a longer time to detect the fault.

6.2.2 VOLTAGE TRANSFORMER RESPONSE

Voltage transformers have such a relatively high resistance that very little of the GIC will flow in the primary winding. In addition there will be other low impedance paths in the vicinity such as grounded power transformers. Capacitively coupled Voltage transformers (CCVT) are even less susceptible to the saturation due to GIC because the capacitors will act as an open circuit for the DC current thus avoiding DC current flow to the voltage transformer of the CCVT. The effect of passing voltage waveforms through a model of the CCVT [17] was not noticeable and hence not presented here.

6.3 SEQUENCE NETWORK PROBLEMS

Modern line protection systems which utilize sequence voltage or current quantities for fault determination can be susceptible to misoperation when the protected line

currents contain harmonics generated during a GIC event. AC harmonics of the order $3n+1$, $3n+2$ and $3n$ where n is an integer have the phase sequences of positive, negative and zero respectively. Both zero and negative sequence currents are commonly used in direction comparison overcurrent schemes and in the time overcurrent backup function[25].

To investigate the behaviour of sequence filters, waveforms obtained from the high and low power flow cases at maximum recorded GIC conditions were fed into a simple sequence filter. The circuit diagram of the simple sequence filter used is shown in Figure 6.30 .

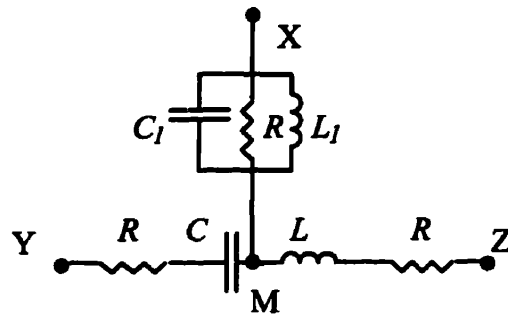


Figure 6.30 : A Simple Negative Sequence Filter

The relationship among the main circuit parameters, resistance R , capacitance C and inductance L is given by equation 6.1 .

$$\sqrt{3}R = \frac{1}{\omega C} = \omega L \quad (6.1)$$

Given R , the values of inductance L_1 and capacitance C_1 are chosen according to the quality factor. The relationship among them with resistance R and quality factor of the filter Q is given by equation 6.2 .

$$\frac{R}{Q} = \omega L_1 = \frac{1}{\omega C_1} \quad (6.2)$$

If three voltages V_X , V_Y and V_Z whose frequency is ω are applied to X, Y and Z then using Kirchoff's current law,

$$\frac{V_X - V_M}{R} + \frac{V_Y - V_M}{2R \angle -60} + \frac{V_Z - V_M}{2R \angle 60} = 0 \quad (6.3)$$

This can be re-written as,

$$V_M = \frac{V_X + 0.5 V_Y \angle 60 + 0.5 V_Z \angle -60}{1 + 0.5 \angle 60 + 0.5 \angle -60} \quad (6.4)$$

It can be shown that V_M becomes zero when balanced three phase voltages are applied to the points X, Y and Z with the sequence A, C and B thus giving voltage across X and M as the voltage applied to X. It also can be shown that if the phase sequence is reversed, then V_M will be the same as V_X thus giving zero voltage across X and M.

Figure 6.31 shows the output of a positive sequence filter for the 500 kV side currents obtained for 105 A GIC per phase, high power case before the series compensation. To get the positive sequence output the same filter shown in Figure 6.30 is used with the reversed phase sequence. Outputs were taken for different quality factors of the filter.

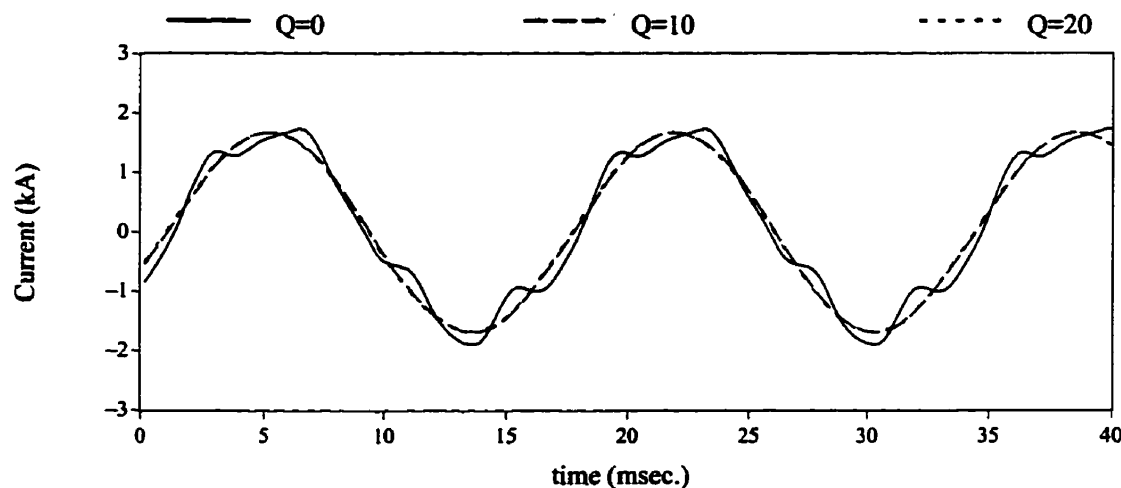


Figure 6.31 : Positive Sequence Output for 315A GIC high power case

The three waveforms were taken at three different quality factors 0, 10 and 20 . The rms magnitudes of the waveforms for the quality factors 0, 10 and 20 are 1207.8 A, 1191.6 A and 1190.7 A respectively. If the sequence components were calculated after filtering digitally though a FFT, then the positive sequence magnitude is 1190.3 A.

Figure 6.32 shows the negative sequence output using the same filter. The waveforms fed in were the 500 kV line currents obtained for high power flow, 105 A GIC per phase condition before the series compensation.

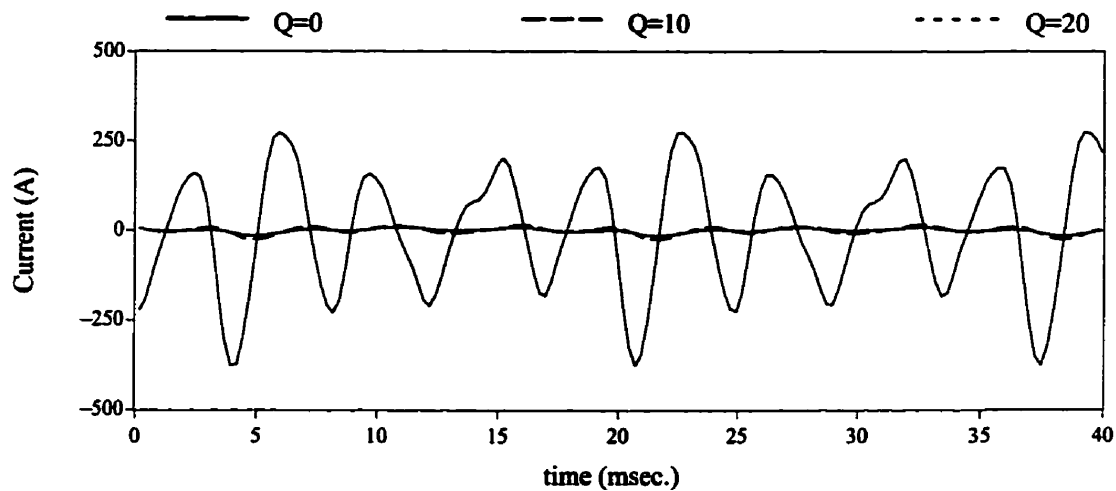


Figure 6.32 : Negative Sequence Output for 105A GIC per phase, high power case

The three waveforms were taken at three different quality factors. The rms magnitudes of the output waveforms for the quality factors 0, 10 and 20 are 160.7 A, 9.5 A and 5.8 A. It is clear that the rms magnitude is very dependant on the quality factor. The negative sequence component obtained through FFT filtering and then calculating gives the magnitude as 3.7 A.

Figure 6.33 shows the zero sequence output of the 500 kV line current obtained for high power flow, maximum recorded GIC conditions. To obtain the zero sequence, the three waveforms were added and fed into a tuned filter.

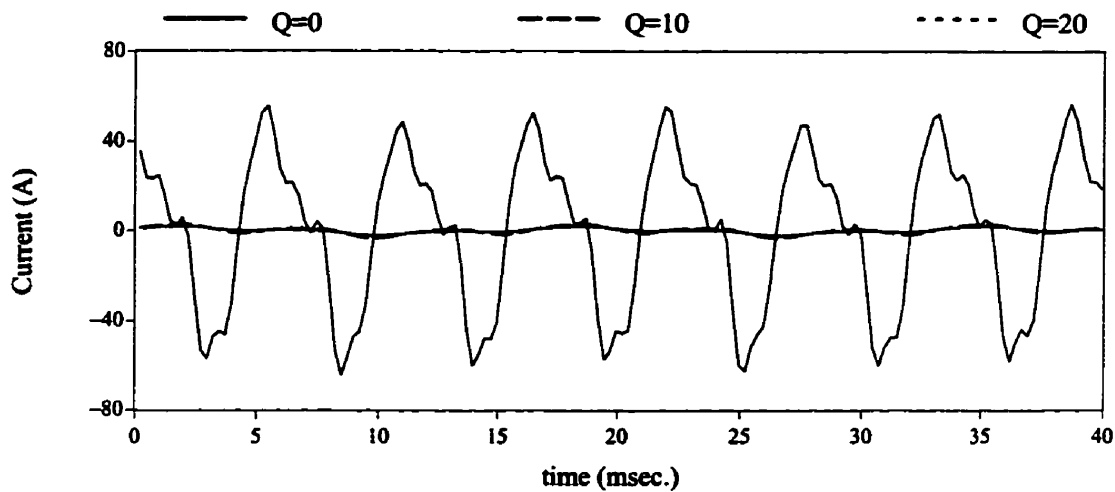


Figure 6.33 : Zero Sequence Output for 105A GIC per phase, high power case

The rms magnitudes of the output waveforms for the quality factors 0, 10 and 20 are 34.9 A, 1.58 A and 1.12 A. It is clear that the rms magnitude is very dependant on the quality factor. The zero sequence component obtained by filtering the waveforms digitally by a FFT and then calculating gives the magnitude as 1.06 A.

Figure 6.34 shows the positive sequence output of the filter when fed with the 500 kV current waveforms obtained for low power flow maximum recorded GIC conditions.

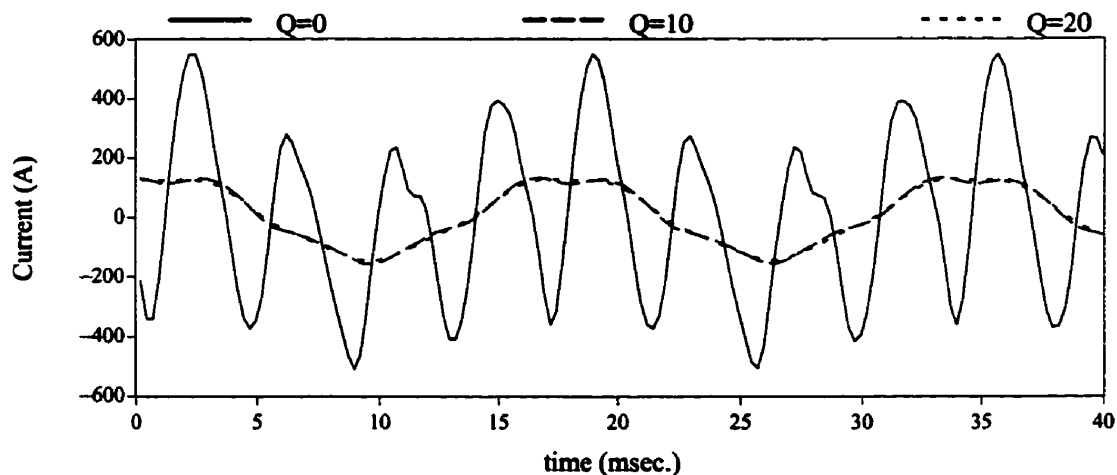


Figure 6.34 : Positive Sequence Output for 315A GIC low power case

With a quality factor of 0, the rms magnitude of the output waveform of the filter is 281.9 A. When the quality factor increased to 10, the rms magnitude decreased to

96.6 A. With a quality factor of 20, it decreased further to 95.6 A. If the input current waveforms were subjected to a FFT and then sequence components were derived, then the rms magnitude is 95.2 A.

Figure 6 .35 shows the negative sequence output using the same filter. The waveforms fed in were the 500 kV line currents obtained for low power flow, 105 A GIC per phase condition.

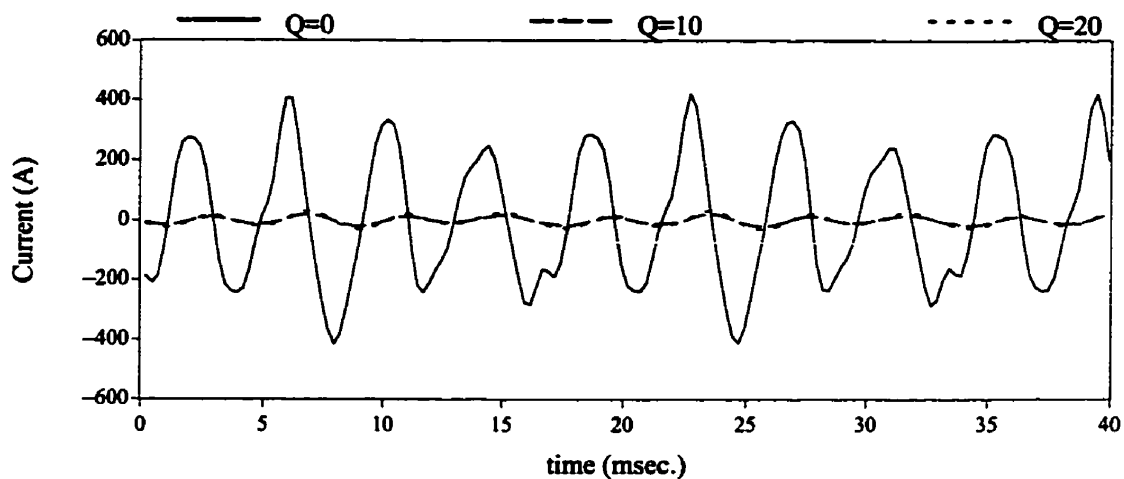


Figure 6 .35 : Negative Sequence Output for 105A GIC per phase, low power case

The output waveforms obtained for three quality factors 0, 10 and 20 gives the rms magnitudes as 216.6 A, 11.15A and 5.63 A respectively. Using a FFT to filter the individual waveforms and then calculating the sequence components gives the rms magnitude of negative sequence as 0.48 A.

Figure 6 .36 shows the zero sequence output waveforms obtained by adding the waveforms together and then feeding through a tuned filter.

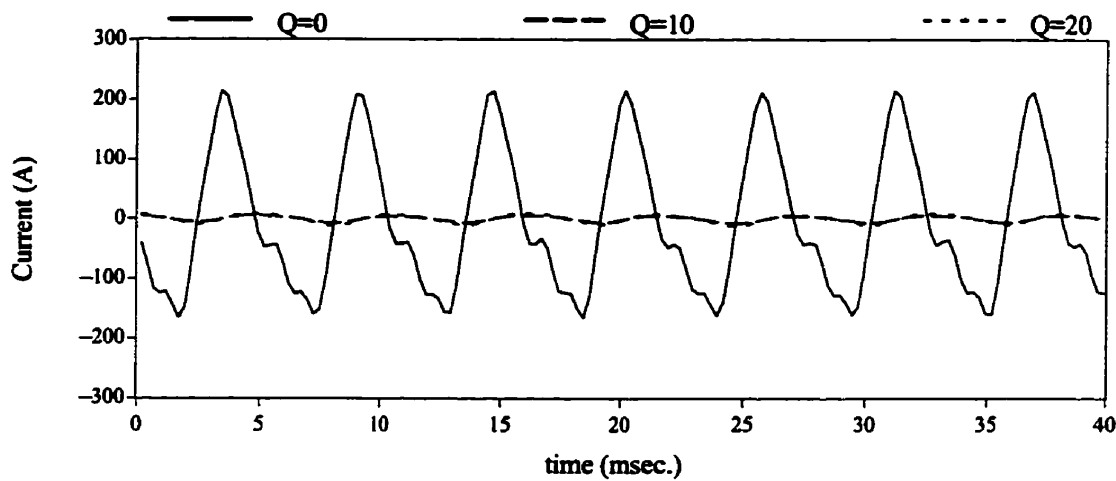


Figure 6 .36 : Zero Sequence Output for 105A GIC per phase, low power case

The rms magnitudes of the output waveforms for the quality factors 0, 10 and 20 are 118.5 A, 4.27 A and 2.17 A respectively. It is clear that the dependency on the quality factor of the filter is very high . Zero sequence component obtained through a FFT gives the magnitude as 0.39 A.

In the high power flow case, a quality factor of 20 gives a reasonable accuracy for all the sequence components. But in the low power flow case, only the positive sequence filter gives a reasonable accuracy at quality factor 20. In the low power flow simulation, where the harmonic components in the current are more than the fundamental component, negative and zero sequence filters give a very poor accuracy. From these results it can be concluded that if analog filters are used to extract sequence components, then it could give rise to an unnecessary trip during GIC conditions.

To see the effects of harmonics on a simple analog sequence filter, different harmonics were injected into the filter and the output responses were taken. Figure 6 .37 shows the effect of positive sequence harmonic signals on the positive sequence filter (or negative sequence harmonics on negative sequence filter) whereas Figure 6 .38 shows the effect of negative sequence harmonic signals on the positive sequence filter (or positive sequence harmonics on negative sequence filter).

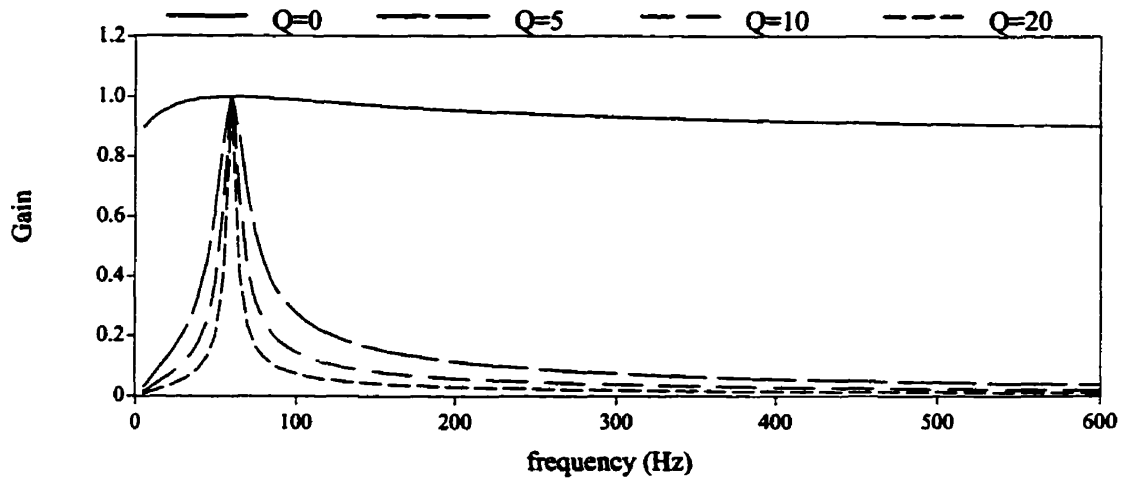


Figure 6 .37 : Effect of positive sequence harmonics on positive sequence filter

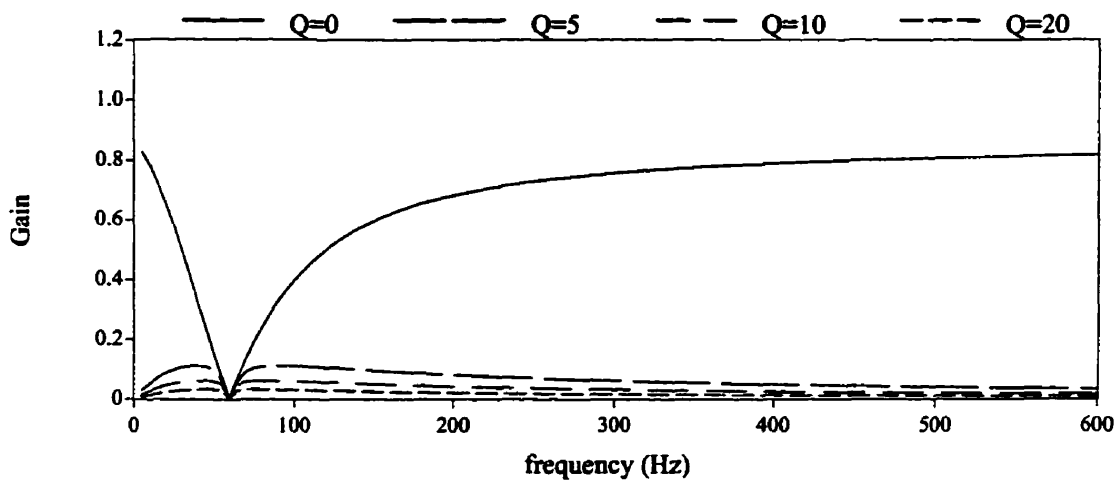


Figure 6 .38 : Effect of negative sequence harmonics on positive sequence filter

Since there is a significant gain at lower order harmonics even at higher quality factors, a considerable amount of lower order harmonics are reflected in sequence outputs.

6.4 TRANSFORMER DIFFERENTIAL PROTECTION

Universal transformer protection practice consists of comparing the current entering the transformer input winding with the currents leaving the secondary windings. There are, however, two well known instances where the differential criteria will indicate

a fault condition although none exists. These are the presence of inrush current and over excitation.

The present or most popular design practice is to measure second or fifth harmonic content in the differential current in order to probe for an inrush or an over excitation condition. Should the ratio of harmonic component magnitude over differential current magnitude exceed a minimum threshold, a blocking signal will prevent the protection from operating.

Figures 6.39 and 6.40 show the transformer differential current obtained for maximum recorded GIC conditions for high and low power flow conditions respectively.

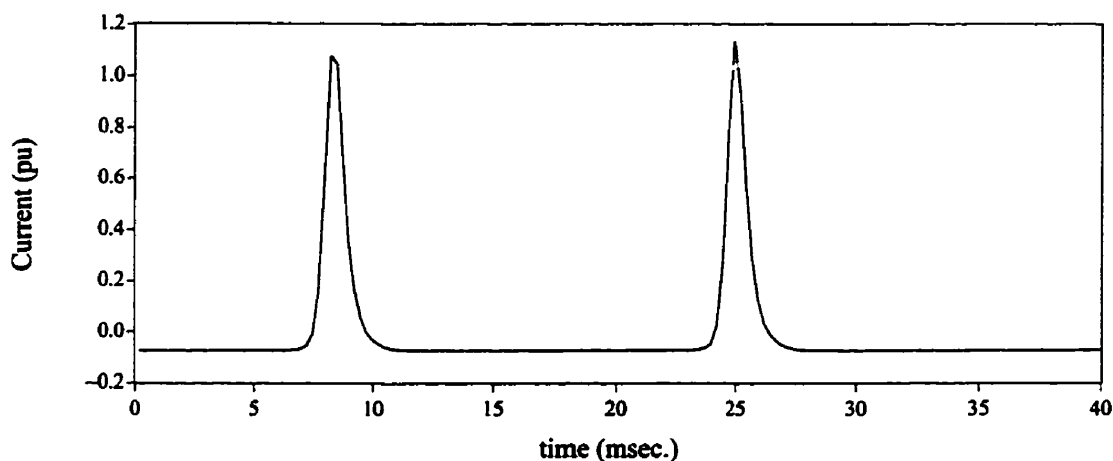


Figure 6.39 : Transformer differential current seen from CT for 105A GIC per phase, high power case

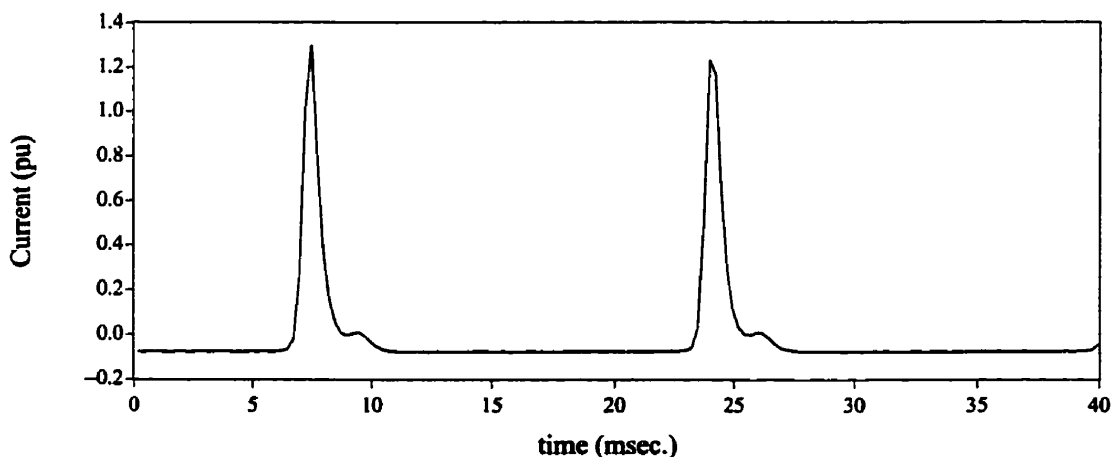


Figure 6.40 : Transformer differential current seen from CT for 105A GIC per phase, low power case

The corresponding Fourier analysis of the waveforms obtained for high and low power flow situations are shown in Figures 6 .41 and 6 .42 respectively.

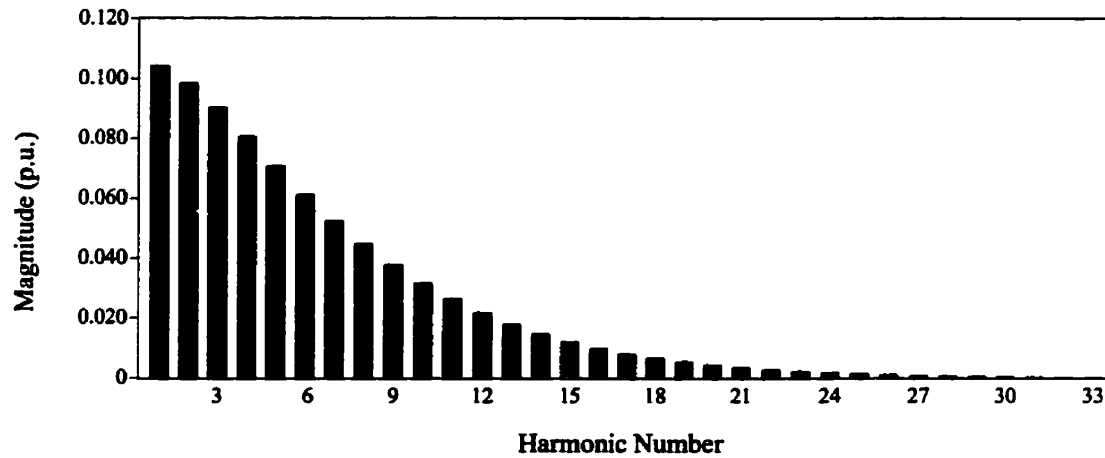


Figure 6 .41 : Fourier analysis of differential current at high power flow

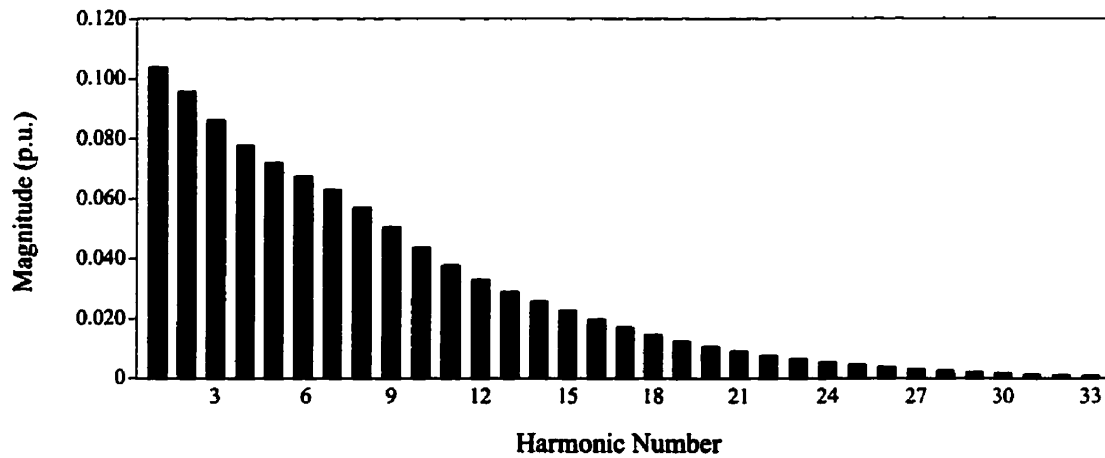


Figure 6 .42 : Fourier analysis of differential current at low power flow

For both low power flow and high power flow cases, there is a fundamental component of 0.104 per unit based on 400 MVA in the transformer differential current. The second harmonic components are 0.099 per unit and 0.096 per unit for high and low power flow conditions respectively. In both cases, the second harmonic component is more than 90% of the fundamental. The 5th harmonic components are 0.071 p.u. and 0.072 p.u. for high and low power flow cases respectively. The fifth harmonic component is more than 65% of the fundamental for both cases. The second harmonic restraint is normally set to 15% of

the fundamental[30][31]. The second harmonic component in the differential current of a transformer during an internal fault is usually less than 5% of the fundamental[31]. Since there is a large amount of second harmonic component in the differential current (way above the threshold of 15% of the fundamental in the no fault condition), there is a need to investigate whether GIC induced 2nd harmonic currents have a significant effect during an internal fault situation.

Chapter 7

Conclusions

Transformer models for different transformer configurations were developed with reasonable accuracy to study the protection problems due to saturation of the transformers. Single phase transformers are the most susceptible to GIC whereas three phase three limb transformers are the least susceptible to GIC. Three phase conventional transformers seem to be more susceptible to GIC than the three phase five limb transformers. This observation verifies experimental results obtained before[22][23]. Unfortunately today's transmission systems with large power flow capabilities contain single phase transformers to maintain the reliability economically. The test system used in this study also contains single phase transformers.

The results obtained using the models are shown to be in close agreement with recorded GIC events in the Dorsey–Forbes–Chisago 500kV system. The model derived for the Dorsey–Forbes–Chisago system was then used to study the voltages and currents in the system for different conditions. Several power flow conditions and several GIC conditions were studied. System conditions at maximum recorded GIC level were presented

for two different power flow conditions. Unfortunately there are no recorded line current or voltage waveforms for this maximum recorded GIC event. The predicted maximum GIC for this system is roughly twice the maximum recorded GIC level. The effects at an ESP level corresponding to the maximum predicted GIC is studied on a revised model of the Dorsey–Forbes–Chisago system since it was series compensated recently.

Before series compensation, line currents show more distortions than the phase voltages at both low and high power flow conditions. It is also seen that the fundamental reactive power consumed by the transformers is more or less the same irrespective of the power flow. The slight difference mainly comes from different reactive power consumption by leakage inductance. Otherwise, reactive power drawn by transformers due to half cycle saturation due to a specific amount of GIC is more or less the same irrespective of power flow provided the level of energization of transformers is more or less the same which is usually true.

The distortions of the waveforms increase with the amount of GIC as expected. The relationship between harmonic magnitudes with the GIC is roughly linear. At the low power flow conditions, the distortions of the waveforms are higher for the same GIC level than the distortions of the waveforms obtained at high power flow. With the decrease of power flow, harmonic distortions increase. Current waveforms show a higher rate of increase than the voltage waveforms. It can be said that by decreasing the amount of power flow during a geomagnetic storm, the likelihood of a protection system maloperation increases due to the increased distortions in the waveforms. But the whole system would be more stable since the possible loss of power is less.

Series compensation of the 500kV line greatly reduces the effects of GIC on the system since it blocks the GIC flows completely in the 500kV line. But there is still a small amount of GIC flow in the 230kV side of the transformers at Dorsey. Another reason for smaller effects is the introduction of an additional set of transformers. It gives a further

decreased GIC current per phase per transformer. Thus the effects of GIC on the transformer and hence the overall effects are further reduced.

However, there is still some distortion of the waveforms because of the small amount of GIC passing through the 230kV side of the transformer. At the maximum predicted ESP conditions, some waveforms have THD factors close to 20%. This could be even more if the power flow is further reduced.

The 230kV transmission line to Moranville carries more GIC than the line to Drayton mainly because it has a higher ESP gradient along the line. The Dorsey–Moranville line lies in a direction of NW–SE whereas Dorsey–Drayton line lies in a direction of N–S thus giving a higher ESP gradient on Dorsey–Moranville line.

Both before and after series compensation, the most prominent harmonic in the system during GIC conditions is the 4th harmonic. Before the series compensation, the line current obtained at low power flow conditions has more 4th harmonic than even the fundamental component.

Before the series compensation, a significant portion of the currents flowing in the harmonic filters was comprised of harmonics which are uncharacteristic to a DC converter station. Comparison of the peak values of the waveforms and actual rms magnitudes of them show that the peak detection scheme to evaluate the current is not suitable for harmonic filters when GIC is present. A peak detection method can give a false indication of as high as 210% of the actual rms magnitude at maximum recorded GIC level.

After series compensation, the level of saturation was greatly reduced due to the increased resistance for dc. Therefore the amount of harmonic distortion is less even at the maximum predicted ESP level which is more than twice the maximum recorded ESP level. The contribution of uncharacteristic harmonics in currents going through harmonic filters is low. The error in evaluating current based on peak current is about 30% even at the maximum predicted ESP conditions.

Series compensation and the addition of another set of transformers greatly reduces the effects of GIC. But still there is a possibility of maloperation of protection schemes due to the distortion created by half cycle saturation. The risk seems to be higher during low power flow conditions.

Investigation of instrument transformer response during GIC events shows that voltage transformers are immune to saturation because of higher resistance for dc in VT's and CCVT's. At steady state operation during GIC events, current transformers also perform very satisfactorily mostly because the physical dimensions of the magnetic cores of the CT's are determined by available fault current and not by load current and hence a load current with GIC would not drive the CT deep into saturation. It was seen that the distortion introduced by CT saturation is very minimal even at high GIC levels. But if a fault occurs and if that fault creates a dc bias of the current towards the same direction as the dc bias created by GIC, then the CT will saturate sooner. This might cause the relay to take a longer time to detect the fault.

Modern line protection schemes which utilize sequence components for fault determination can be susceptible to misoperation when the protected line currents contain harmonics generated during a GIC event. Both zero and negative sequence currents are commonly used in direction comparison overcurrent schemes and in time overcurrent backup functions. Feeding of waveforms obtained during a GIC event into a generic sequence filter shows that unless the output is filtered through a tuned or a low pass filter with a very high quality factor, it could produce sequence component magnitudes which are much more than the actual values. This could cause the protection devices to misoperate. This could be either an unnecessary trip or a blocking of a necessary trip signal.

Universal transformer protection practice consists of comparing the current entering the transformer input winding with the currents leaving the secondary windings. However in the presence of inrush current or over excitation this criteria is violated. Present

design practice is to measure the second or fifth harmonic content in the differential current in order to probe for an inrush or an over excitation condition. Should the ratio of harmonic component magnitude over differential current magnitude exceed a minimum threshold, a blocking signal will prevent the protection device from operating. Investigation of transformer differential current obtained at maximum recorded GIC level before series compensation shows that the transformer differential current during no fault condition has a second harmonic component much more than the typical threshold limit. The operation of differential protection during an internal fault under GIC conditions needs to be further investigated.

To summarize the conclusions,

1. Transformer models for different transformer configurations were developed with reasonable accuracy.
2. The results obtained using the models are shown to be in close agreement with the recorded GIC events.
3. The simulation results could be used to assess the protective relay settings in the system.
4. The distortions of the waveforms increase with the amount of GIC. They also increase with the decrease of power flow. By decreasing the power flow in the event of a GIC, the likelihood of protection system maloperation increases. But the whole power system would be more stable since the loss of power is small in the event of a false trip.
5. Series compensation greatly reduces (not completely) the effects of GIC in the system.
6. The 4th harmonic is the most prominent harmonic in the system under GIC conditions.
7. Peak detection algorithms used to measure magnitude are not suitable under GIC conditions.
8. Voltage transformers do not show any effects under GIC and the effects of Current transformers are negligible compared to the effects introduced by saturation of power transformers.
9. Analog sequence filters could produce erroneous outputs in the event of GIC and could cause protection schemes to misoperate.
10. There is a need to investigate the effects of GIC induced second harmonic currents on transformer differential protection schemes during an internal fault situation.

References

- [1] Syun-Ichi Akasofu, "The Dynamic Aurora", *Scientific American*, May 1989.
- [2] John G. Kappenman, Vernon D. Albertson, "Bracing for the Geomagnetic Storms", *IEEE spectrum*, March 1990.
- [3] V. D. Albertson, "Geomagnetic Disturbance Causes and Power System Effects", Panel Session on Effects of Geomagnetic Disturbances on Power Systems, PES Summer Meeting, California, July 1989.
- [4] V. D. Albertson, "General Overview: Geomagnetic Storms and Electric Power System Effects", EPRI Conference on Geomagnetically Induced Currents, Palo Alto, California, November 1989.
- [5] W. F. Davidson, "The Magnetic Storm of March 24, 1940—Effects in the Power System", *Edison Electric Institute Bulletin*, July 1940, pp 365,366,374
- [6] "Faults and Failures", *IEEE Spectrum*, June 1989, p. 16
- [7] V. D. Albertson, "Modelling and analysis of GIC", EPRI Conference on Geomagnetically Induced Currents, Palo Alto, California, November 1989.
- [8] V. D. Albertson, J. A. Van Baelen, "Electric and Magnetic Field at the Earth's Surface Due to Auroral Currents", *IEEE Trans.*, Vol. PAS-89, No. 2, April 1970,
- [9] J. N. Towle, F. S. Prabhakara, J. Z. Ponder, "Geomagnetic Effects Modelling for the PJM Interconnection System, Part 1 – Earth Surface Potential Computation", *IEEE PES Summer Meeting*, San Diego, California, July–August 1991.
- [10] G. B. Rackliffe, J. C. Crouse, J. R. Legro, V. J. Kruse, "Simulation of Geomagnetic Currents Induced in Power System by Magnetohydrodynamic Electromagnetic Pulses", *IEEE Trans. on Power Delivery*, Vol. 3, No. 1, January 1988.
- [11] Manitoba HVDC Research Centre, "EMTDC User's Manual", 1988.
- [12] H. W. Dommel, I. I. Dommel, "Transients Program User's Manual", April 1986.
- [13] Glenn W. Swift, "Power Transformer Core Behavior Under Transient Conditions", *IEEE Trans.*, Vol. PAS-90, No.5, September/October 1971
- [14] Washington L. A. Neves, Hermann W. Dommel, "On Modelling of Iron Core Nonlinearities", paper presented at IEEE/PES 1992 Winter Meeting, 92 WM 176–8 PWRS
- [15] C. F. T. Widger, "Representation of magnetisation curves over extensive range by rational fraction approximations", *IEE proc.* 116, No. 1, January 1969.

- [16] J. R. Lucas, "Representation of magnetisation curves over a wide region using a non-integer power series", *International Journal of Electrical Engineering Education*, Vol. 25, 1988
- [17] J. R. Lucas, P. G. McLaren, W. W. L. Keerthipala, R. P. Jayasinghe, "Improved Simulation Models for Current and Voltage Transformers in Relay Studies", *IEEE Transactions on Power Delivery*, Vol. 7, No. 1, January 1992, p 155
- [18] Gordon R. Slemon, "Magnetolectric Devices, Transducers, Transformers, and Machines", John Wiley & Sons. Inc., 1966
- [19] R. A. Walling, A. H. Khan, "Solar-Magnetic Disturbance Impact on Power System Performance and Security ", EPRI conference on "Geomagnetically Induced Currents", Burlingame, California, November 1989.
- [20] William J. McNutt, " The Effect of GIC on Power Transformers ", Panel Discussion on Geomagnetic Storm Effects, IEEE PES Summer Meeting 1990, Minneapolis, July 17, 1990.
- [21] Robert J. Leshner, Joseph W. Porter, Richard T. Byerly, "SUNBURST – A Network of GIC Monitoring Systems ", IEEE Trans. on Power Delivery, Vol. 9, No. 1, January 1994.
- [22] Nobuo Takasu, Tetsuo Oshi, Fumhiko Miyawki, Sadamu Saito, Yasuo Fujiwara, "Experimental Analysis of DC Excitation of Transformers by Geomagnetically Induced Currents", IEEE PES Summer Meeting 1993, 93 SM 393-9 PWRD
- [23] John G. Kappenman, " Field Tests to Measure Large Power Transformer Behaviour to GIC Excitation ", EPRI conference on Geomagnetically Induced Currents, November 8-10, 1989, Burlingame, CA.
- [24] V. D. Albertson, "Modelling and Analysis of GIC", EPRI conference on Geomagnetically Induced Currents, November 8-10, 1989, Burlingame, CA
- [25] J. G. Kappenman, D. L. Carson, G. A. Sweezy, "GIC effects on relay and CT performance", EPRI conference on "Geomagnetically Induced Currents", Burlingame, California, November 1989.
- [26] "geomagnetic induced current effect on SVC operation", CEA report No. CEA ST-316, May 1989.
- [27] R. A. Walling, A. H. Khan, "Characteristic of Transformer exciting-current during geomagnetic disturbances", IEEE PES Winter Meeting 1991, 91 WM 095-0 PWRD
- [28] A. E. Emmanuel, " Powers in nonsinusoidal situations – a review of definitions and physical meanings", IEEE PES Winter Meeting 1990, Atlanta, Georgia, February 4-8, 1990.
- [29] J. Arrillaga, "High Voltage Direct Current Transmission", Peter Peregrinus Ltd., 1983/1988.
- [30] R. L. Sharp, W. E. Glassburn, "A Transformer Differential Relay with Second-harmonic Restraint", *AIEE Transactions Power Apparatus and Systems*, Vol. 77 Part III, Dec. 1958, pp 913-918.
- [31] A. R. van C. Warrington, "Protective Relays: Their Theory and Practice – Volume Two", Chapman & Hall Ltd., 1977, page 212, ISBN 0 412 153807

- [32] J. G. Kappenman, V. D. Albertson, N. Mohan, "Current Transformer and Relay Performance in the Presence of Geomagnetically-Induced Currents", IEEE Trans. on Power Apparatus and Systems, Vol PAS-100, No. 3, March 1981

Appendix A
Flow Charts

**A-1 ALGORITHM FOR CALCULATING THE NON-LINEAR CURRENT IN
THE CORE**

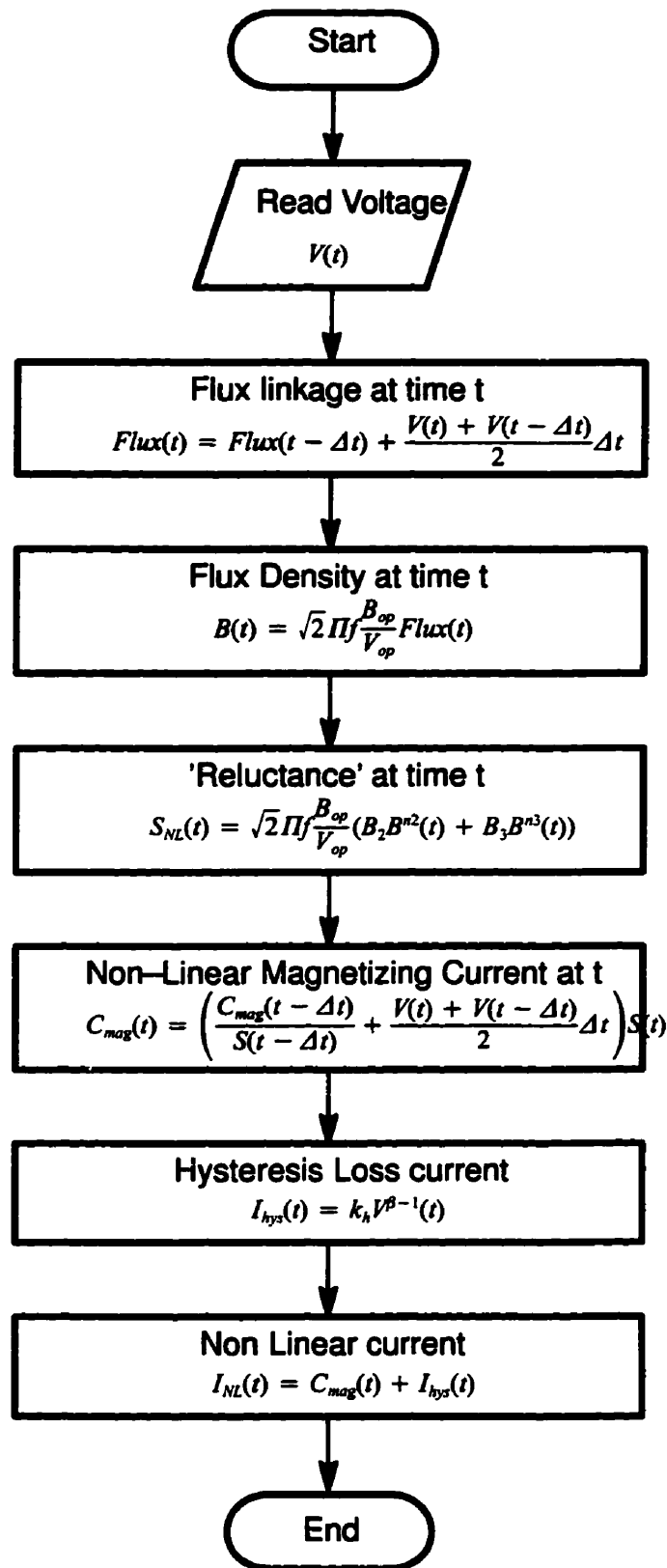


Figure A-1 : Simplified Flow Chart for Calculating Non-Linear Current

Appendix B

More details on Dorsey–Forbes–Chisago before compensation

B–1 WAVEFORMS IN 230KV SIDE – HIGH POWER FLOW

Figure B–1 shows the simulated voltage waveform on the 230kV side of the Dorsey transformer when transformers at Dorsey and Chisago were fully saturated due to the 50A and 105A per phase GIC.

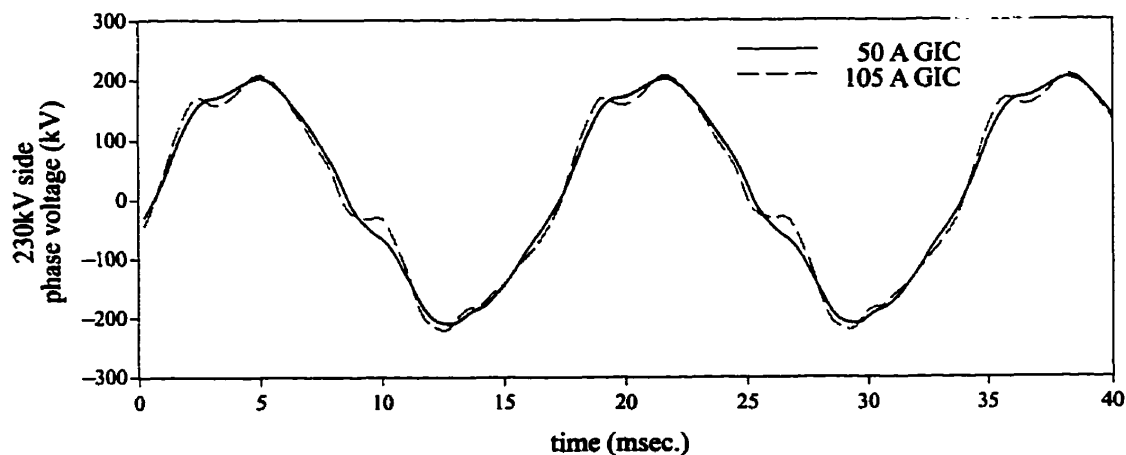


Figure B–1 : Voltage waveforms on 230 kV side at high power flow

The rms magnitudes, maximum and minimum values of the waveforms are given in table B–1 . The Fourier analysis of the waveforms are given in figure B–2 .

Table B-1 : Details on the 230 kV side phase voltage at high power flow

	50A GIC	105A GIC
rms magnitude (kV)	142.0	141.9
maximum peak (kV)	203.3	208.1
minimum peak (kV)	-210.4	-221.4

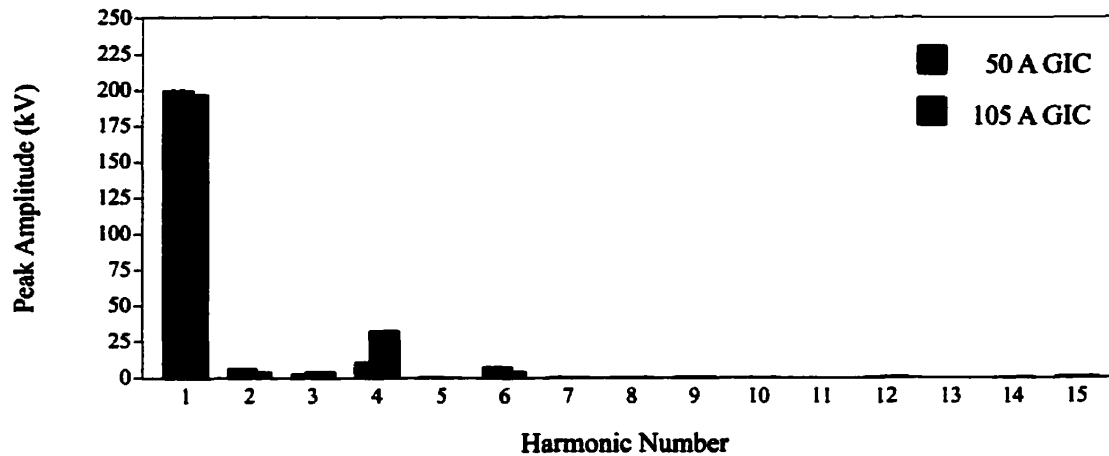


Figure B-2 : Fourier analysis of 230 kV side voltage waveform at high power flow

The most prominent harmonic component is the 4th followed by the 6th and 2nd. The waveform at 50 A per phase GIC has a total harmonic distortion (THD) factor of 7.53% and that at 105 A per phase GIC has a THD factor of 15.92%.

B-2 WAVEFORMS IN 230KV SIDE – LOW POWER FLOW

Figure B-3 shows the simulated voltage waveform on the 230kV side of the Dorsey transformer at low power flow conditions when the transformers at Dorsey and Chisago were fully saturated due to the 50A and 105A per phase GIC.

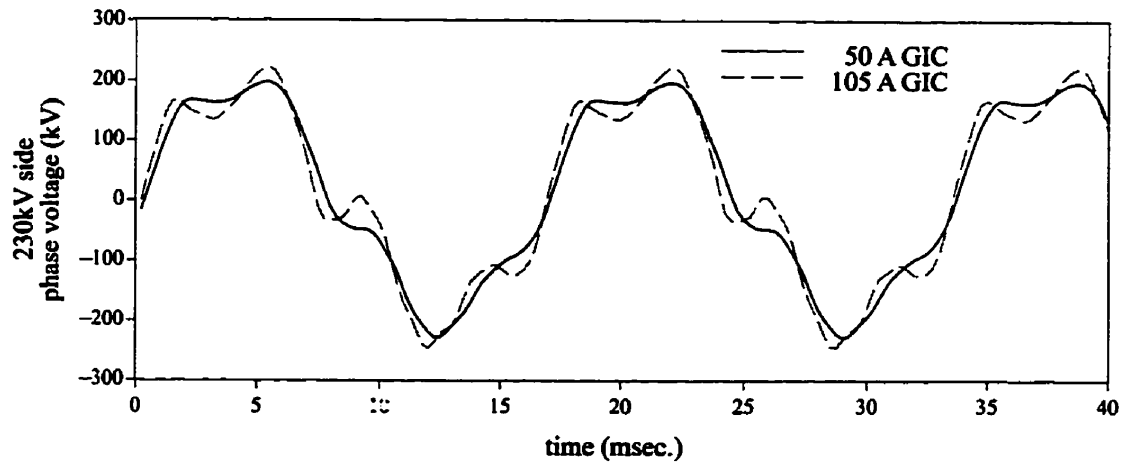


Figure B-3 : Voltage waveform on 230 kV side at low power flow

The rms magnitudes, maximum and minimum values of the waveforms are given in table B-2 . The Fourier analysis of the waveforms are given in Figure B-4 .

Table B-2 : Details on the 230 kV side phase voltage at low power flow

	50A GIC	105A GIC
rms magnitude (kV)	141.3	143.8
maximum peak (kV)	197.8	222.5
minimum peak (kV)	-229.3	-248.1

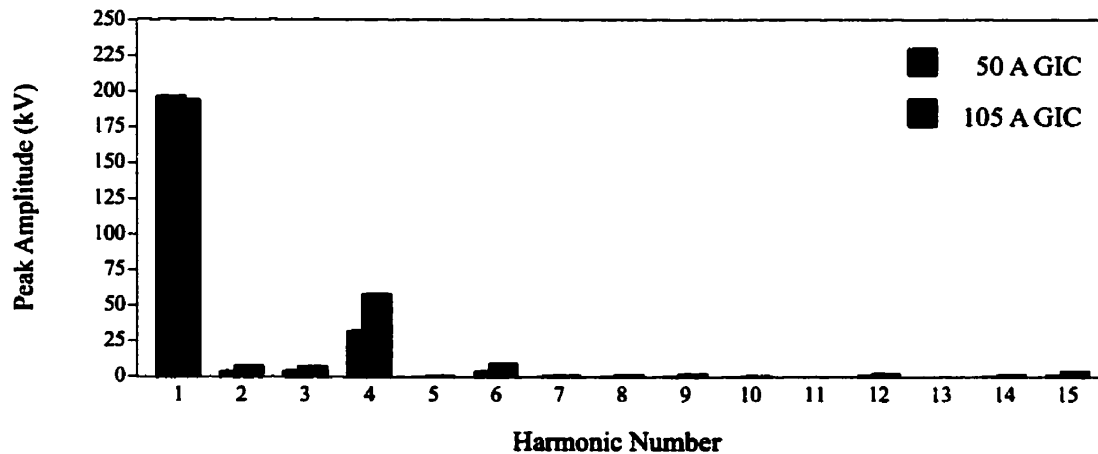


Figure B-4 : Fourier analysis of 230kV side voltage waveform at low power flow

For both waveforms, the most prominent harmonic component is the 4th harmonic. The waveform at 50A per phase GIC has a THD factor of 16.86% whereas the waveform at 105A per phase GIC has a THD factor of 30.83%.

B-3 EFFECT OF GIC ON DISTORTIONS AND HARMONICS
-VOLTAGE WAVEFORMS

Figure B-5 shows the harmonic composition of the 500 kV phase voltages for different GIC levels for a typical high power flow whereas the Figure B-6 shows the harmonic composition of the 500 kV phase voltage for different GIC under a typical low power flow condition.

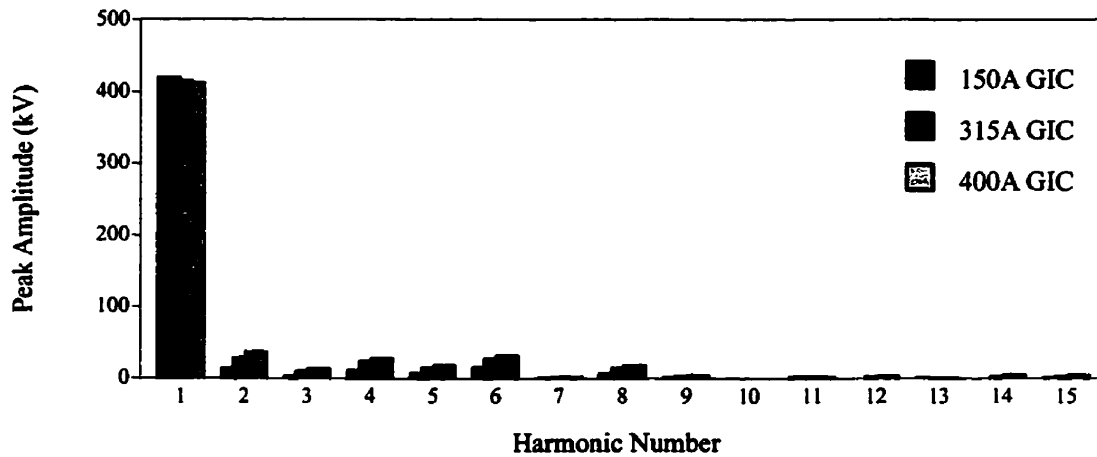


Figure B-5 : Fourier analysis of 500 kV side phase voltages with a typical high power flow

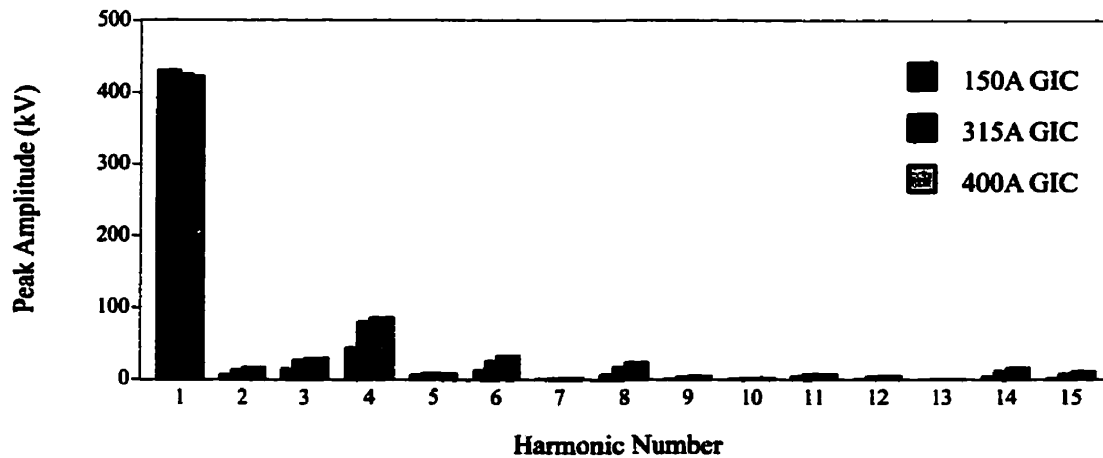


Figure B-6 : Fourier analysis of 500 kV side phase voltages with a typical low power flow

Again, It is clear that the pattern of harmonic composition for a particular power flow remains more or less the same, but the magnitudes of harmonics other than the fundamental increase with an increase of the level of GIC. The magnitude of the fundamental component decrease slightly with an increase of the amount of GIC.

Figure B-7 shows the total harmonic distortion of the 500 kV phase voltage for different GIC levels for the two different power flows considered.

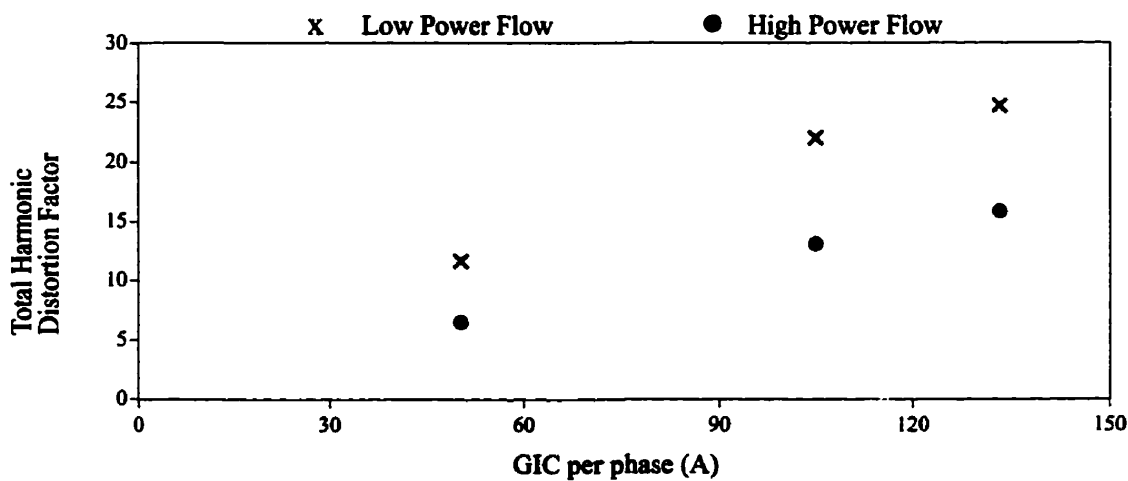


Figure B-7 : THD Factor of 500 kV side phase voltages

The Total harmonic distortion of the waveforms increase with the applied level of GIC, But the distortion factor for the waveform obtained during low power flow

condition is more than that obtained during high power flow condition for the same GIC level.

B-4 EFFECT OF POWER FLOW ON HARMONICS – WAVEFORMS AT OTHER GIC LEVELS

Figures B-8 and B-9 show the harmonic composition of the 500kV line currents for the two different power flows considered for 150A and 400A GIC levels respectively.

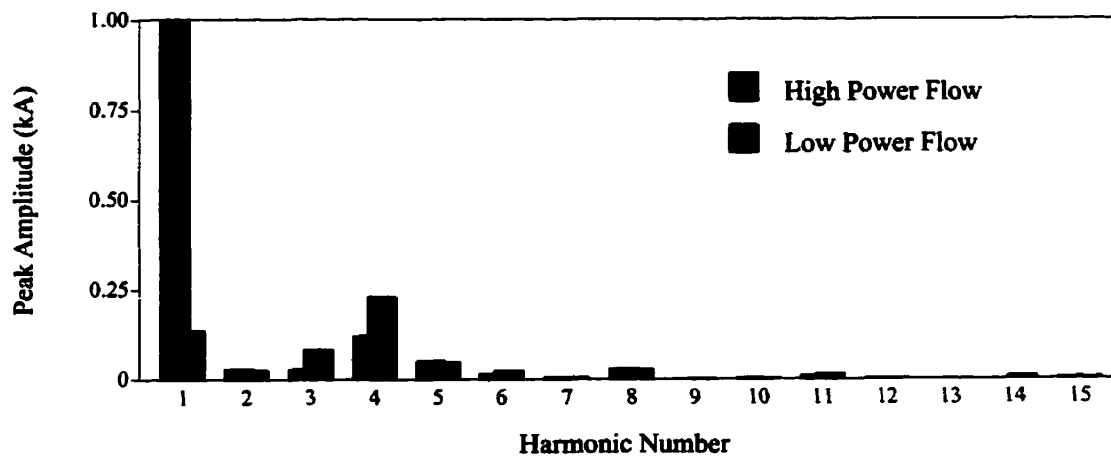


Figure B-8 : Fourier analysis of 500 kV side currents with 150A GIC

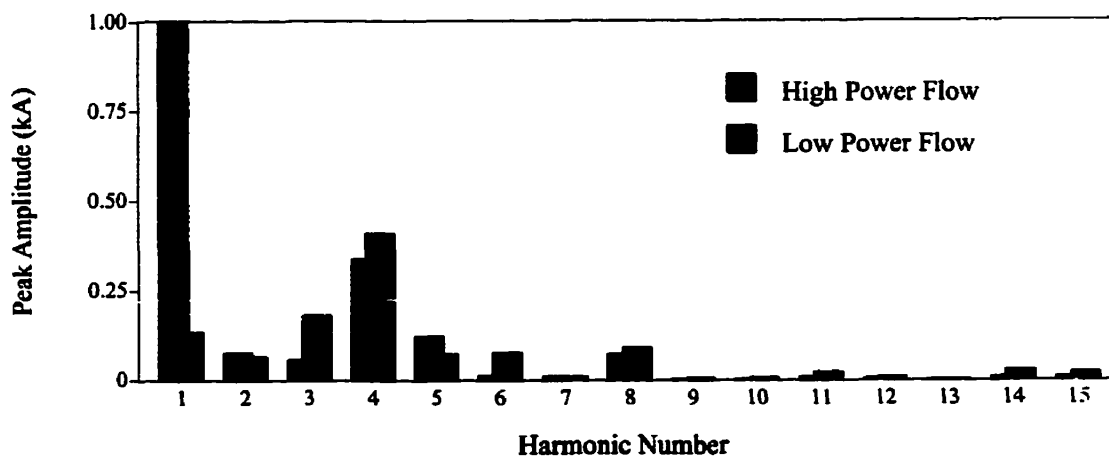


Figure B-9 : Fourier analysis of 500 kV side currents with 400A GIC

Figures B–10 and B–11 show the harmonic composition of the 500 kV phase voltages for the two different power flow conditions considered for 150A and 400A GIC levels respectively.

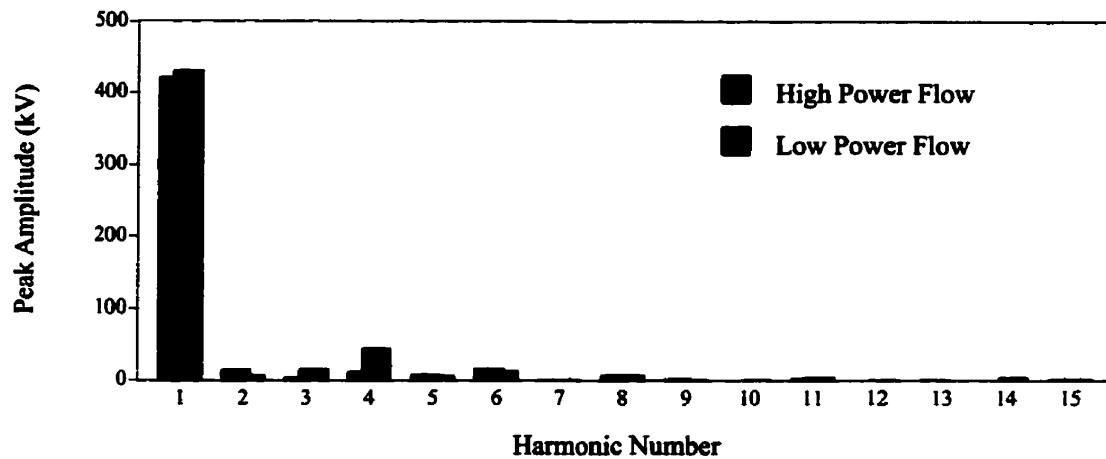


Figure B–10 : Fourier analysis of 500 kV side phase voltages with 150A GIC

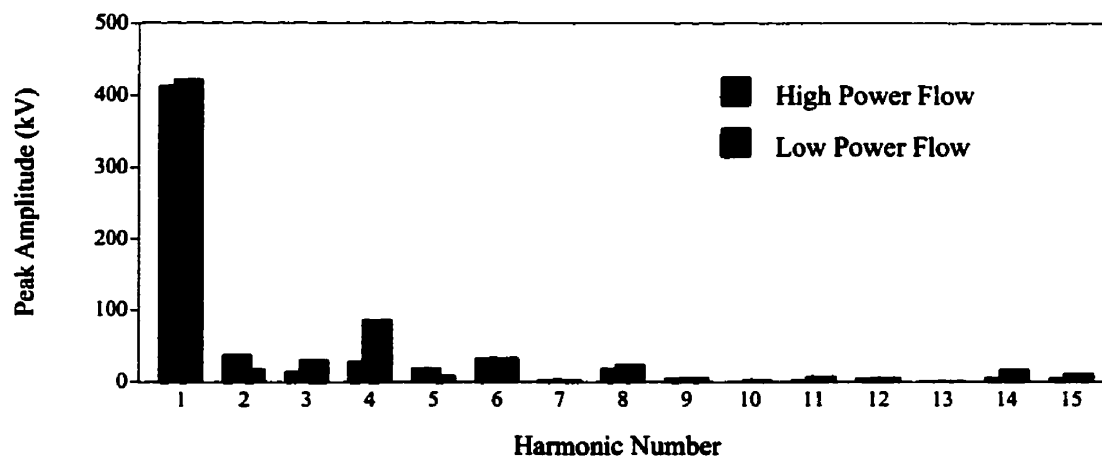


Figure B–11 : Fourier analysis of 500 kV side phase voltages with 400A GIC

Again, it is clear that the amount of dependency of harmonic magnitudes on the amount of power flow is very low. Out of all the waveforms considered, it is clear that the most prominent harmonic is the 4th harmonic.

Appendix C

More details on Dorsey–Forbes–Chisago after series compensation

C-1 WAVEFORMS IN THE 230KV SIDE – HIGH POWER FLOW

Figures C-1 and C-2 show the simulated phase voltage and the line current on the 230 kV side respectively when the transformers are fully saturated due to the GIC created by the applied ESP.

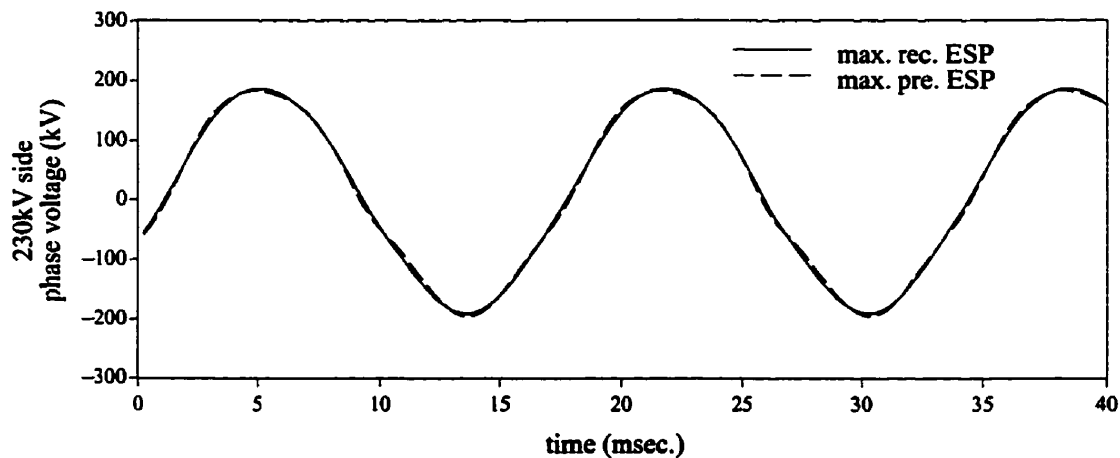


Figure C-1 : Simulated voltage waveform on the 230 kV side

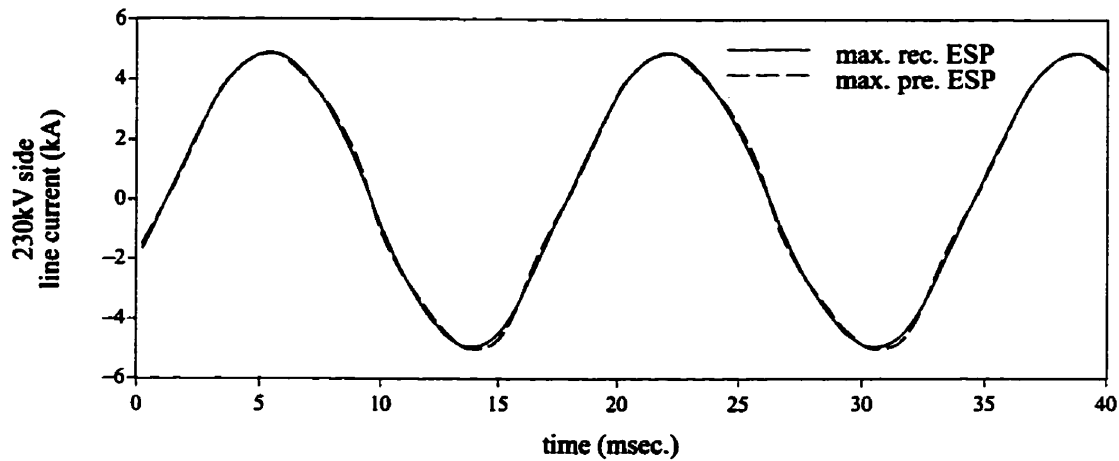


Figure C-2 : Current waveform on 230 kV side of Dorsey at high power flow

Tables C-1 and C-2 show the rms magnitudes, maximum and minimum peak values of the two waveforms shown in the two preceding figures.

Table C-1 : The details on the 230 kV side voltage after saturation

	Max. Rec. GIC	Max. Pred. GIC
rms magnitude (kV)	132.5	132.7
maximum peak (kV)	186.4	184.1
minimum peak (kV)	-190.8	-195.3

Table C-2 : The details on the 230 kV side current after saturation

	Max. Rec. GIC	Max. Pred. GIC
rms magnitude (A)	3497.0	3499.0
maximum peak (A)	4949.0	4949.0
minimum peak (A)	-4990.0	-5046.0
per phase GIC (A)	15.0	31.0

The Fourier analysis of 230kV side voltage and current waveforms are shown in Figures C-3 and C-4 respectively.

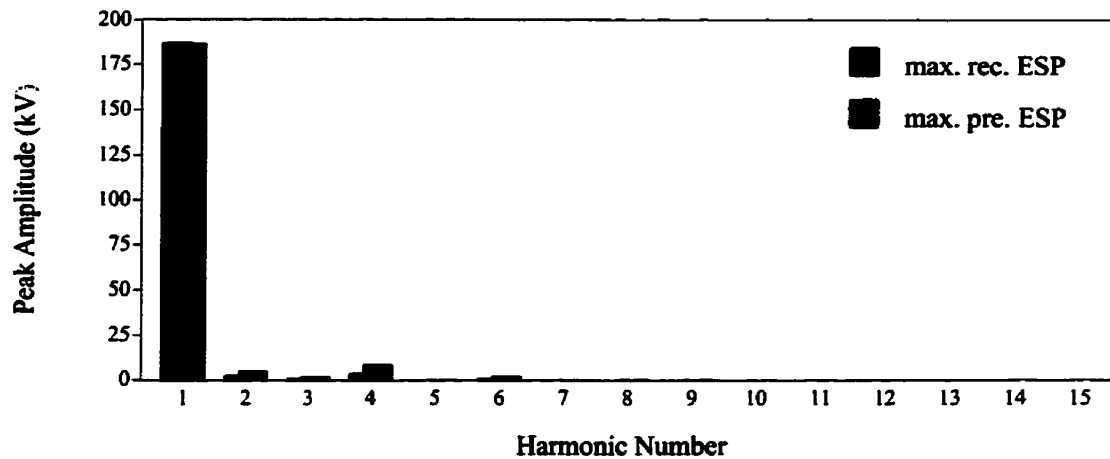


Figure C-3 : Fourier analysis of 230 kV voltage waveforms at high power flow

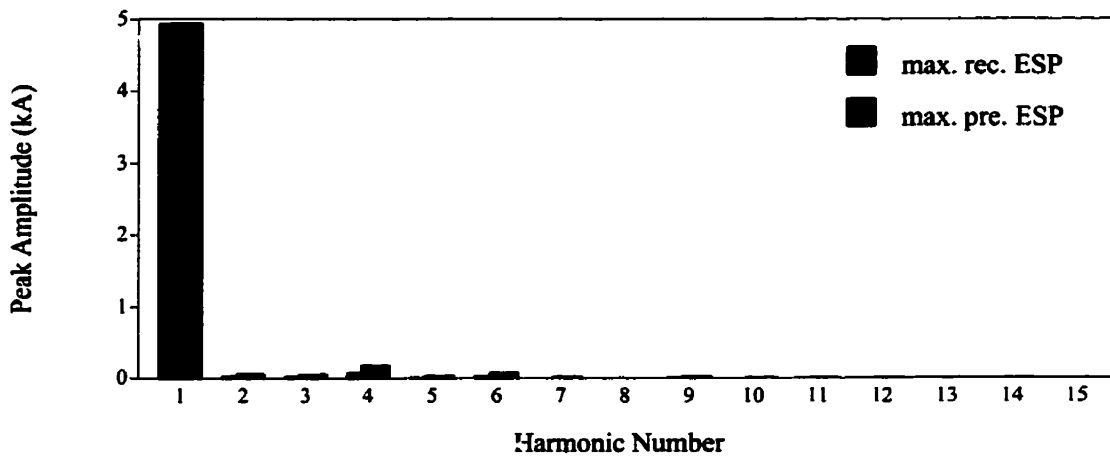


Figure C-4 : Fourier analysis of 230 kV side current waveforms at high power flow

For all the waveforms, the most prominent harmonic is the 4th harmonic. The THD factor of the voltage waveform obtained at the maximum recorded ESP conditions is 2.37% and that of the voltage waveform obtained at the maximum predicted ESP conditions is 5.47%.

The current waveforms are presented without the GIC component of current in them. The GIC components of 15A and 31A were subtracted from their respective current waveforms obtained at maximum recorded ESP conditions and maximum predicted ESP conditions.

The THD factors of the current waveforms at the 230 kV side of the transformer when the transformers at Dorsey are saturated due to the GIC created by the maximum recorded ESP conditions and maximum predicted ESP conditions respectively are 1.94% and 4.56%.

C-2 CURRENT WAVEFORMS IN 230KV FEEDERS AT HIGH POWER FLOW – CURRENT FLOWING TO DRAYTON

Figure C –5 shows the waveforms of the current flowing to Drayton at Dorsey at a typical high power flow for two different GIC conditions when the transformers are fully saturated due to the applied ESP.

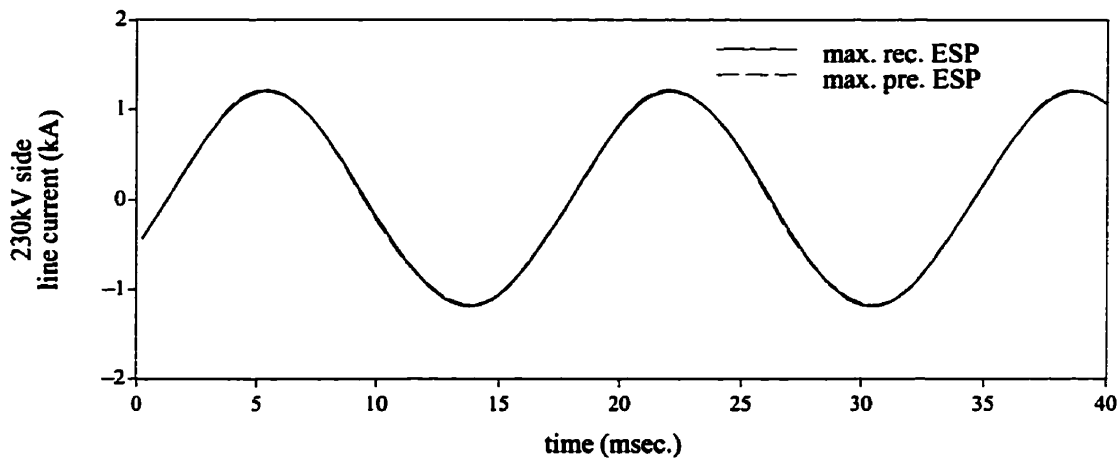


Figure C –5 : Current on Dorsey–Drayton line at Dorsey at high power flow

Table C –3 shows the maximum and minimum values, rms magnitude and the amount of per phase GIC in the waveforms shown in the preceding figure.

Table C –3 : The details on the current flowing to Drayton after saturation

	Max. Rec. GIC	Max. Pred. GIC
rms magnitude (A)	843.2	846.7
maximum peak (A)	1203.0	1213.0
minimum peak (A)	-1186.0	-1178.0
per phase GIC (A)	4.1	8.7

The Fourier analysis of the two waveforms shown in Figure C-5 are shown in Figure C-6.

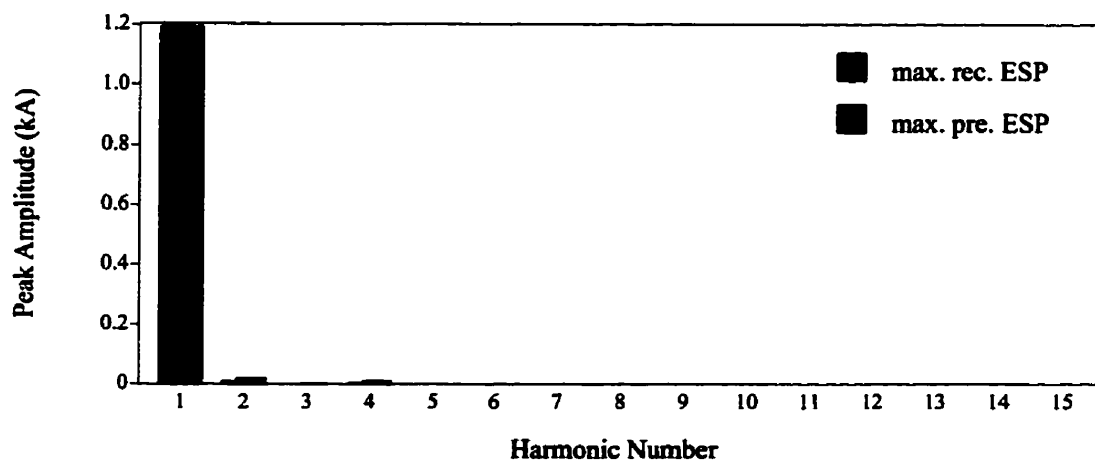


Figure C-6 : Fourier analysis of current flowing to Drayton at high power flow

The total harmonic distortion factors of the two current waveforms are 0.86% and 1.89% respectively for maximum recorded and maximum predicted conditions. The most prominent harmonic of both the waveforms is the 2nd harmonic followed by the 4th.